Adam Mickiewicz University
Faculty of Physics
Department of Biomedical Physics

Folding and aggregation of the human prion protein: biophysical studies of interactions with metal ions and the NCAM1-Aβ peptide construct

Doctoral Thesis in Physics

Maciej Gielnik

Supervisor
Prof. dr hab. Maciej Kozak
Assistant supervisor
Dr. Sebastian K. T. S. Wärmländer

Poznań 2022

Acknowledgements

I would like to express my sincere gratitude to my supervisor Prof. dr hab. Maciej Kozak. Thank you for the possibility to conduct research for my thesis at the former Department of Macromolecular Physics, current Department of Biomedical Physics, Faculty of Physics, Adami Mickiewicz University. Also thank you for the motivation, belief in me and the opportunity to perform SAXS studies at P12 beamline, PETRA III, DESY.

My assistant supervisor dr. Sebastian K. T. S. Wärmländer, thank you for the valuable suggestions involving peptide/protein titrations with metal ions. Thank you for discussion of the results despite the long distance between Poland and Sweden and for the help to visit other laboratories.

I would like to express my gratitude to Prof. Astrid Gräslund. It has been a privilege to visit your laboratory, where I had a look on metal binding experiments from a different perspective. Thank you very much!

I would like to acknowledge Prof. UG dr hab. Aneta Szymańska for peptide synthesis and Dr. Lilia Zhukova for PrP^{C} expression and purification. Without you I would not have any material to perform the experiments.

Prof. Željko Svedružić, thank you for the possibility to visit your laboratory in Croatia, expertise on molecular dynamics simulations, and access to the Croatian supercomputer Bura.

Dr. Igor Zhukov, thank you for performing NMR experiments on PrP^{C}-Zn(II) complex. Your experiments brought invaluable contribution to the PrP^{C}-Zn(II) binding phenomenon and connected all spectroscopic, scattering and computational techniques into one piece of knowledge.

Dr. Zuzanna Pietralik-Molińska, thank you very much for performing TEM and for teaching me about AFM measurements.

Dr. Michał Taube, thank you for the introduction to SAXS and for valuable discussions.

I would like to acknowledge all present and past members of the former Department of Macromolecular Physics, current Department of Biomedical Physics. Thank you for the help and good working environment.

Last but not least I would like to thank to my wife Patrycja and my mother Aleksandra for constant support during my doctoral studies, my father-in-law Zbigniew, who always believed in me, but passed away shortly before completion of my doctoral thesis, my sister Dr. Anna Gielnik for helpful discussions, and my whole family. I also thank my friends Łukasz, Zbigniew, Hubert, and Bartosz for help with maintaining a healthy work-life balance.

The work presented in this thesis was supported by the National Science Center under the project “Molecular basis of amyloidogenesis - structure and conformational dynamics of selected human PrP^C prion protein complexes with metal cations (2014/15/B/ST4/04839)”, granted to Prof. dr hab. Maciej Kozak.

NATIONAL SCIENCE CENTRE
POLAND

Abstract

Misfolding of the cellular prion protein (PrP^C) is associated with the development of fatal neurodegenerative diseases known as Transmissible Spongiform Encephalopathies (TSEs), such as Creutzfeldt-Jakob disease in humans and the corresponding “mad cow” disease in cattle. The misfolding of PrP^C is not unique process: under specific conditions all proteins can undergo structural transitions from a native soluble state into insoluble and fibrillar amyloid state. Such misfolding followed by aggregation of the proteins is connected with several different neurodegenerative diseases.

The 208-residue long human PrP^C protein consists of two structurally distinct domains: an intrinsically disordered N-terminal domain (NTD), and a structured, mainly α-helical, C-terminal domain (CTD). The NTD contains the so-called octarepeat (OR) region, which is known to bind Cu(II) and Zn(II) ions by histidine residues. Many cofactors, including metal ions, seem to play an important role in PrP^C misfolding. Here, I have used multiple complementary biophysical methods to investigate the structural effects of Cu(II) and Zn(II) binding to the human full-length PrP^C protein, and to the isolated OR peptide.

Circular dichroism (CD) spectroscopy suggest that OR peptide binds up to four Cu(II) ions, and up to two Zn(II) ions. At sub-stoichiometric concentrations, both metal ions induce polyproline type II helix to β-turn transitions in the OR peptide secondary structure, whereas stoichiometric concentrations of the metal ions seem to induce formation of an antiparallel β-sheet secondary structure. Molecular dynamics (MD) simulations of the isolated OR peptide together with bound metal ions indicate formation of hairpin structures with antiparallel β-sheet properties. Direct addition of Zn(II) ions to the OR peptide results in binding of the amyloid-specific dyes such as Thioflavin T and Congo Red, indicating amyloid formation. After incubation of the OR peptide with Zn(II) ions, imaging with atomic force microscopy (AFM) and transmission electron microscopy (TEM) revealed the presence of fibrillar

structures. X-ray diffraction (XRD) analysis identified the amyloid-specific cross-β structure. Hence, binding of Cu(II) and Zn(II) ions to the OR peptide may induce formation of fibrillar amyloid structures.

For the full-length human PrP^C protein, binding of Zn(II) to the OR region results in an intra-domain interaction between the NTD and CTD. CD spectroscopy suggest loss of α-helical secondary structure upon Zn(II) binding, possibly at helices 2 and 3 from the CTD, together with formation of β-turn secondary structures, probably around the Zn(II) ion. Fluorescence and CD spectroscopy titrations suggest a low micromolar apparent dissociation constant for the PrP^C·Zn(II) complex, which makes such interactions possible under physiological conditions. MD simulations of the PrP^C·Zn(II) complex indicate stabilization of α-helix 3, while small angle X-ray scattering (SAXS) data suggest an overall more compact conformation of the Zn(II)-bound PrP^C protein. As Zn(II) binding to PrP^C favorites intra-domain interactions and stabilization of α-helix 3, Zn(II) might have an inhibitory effect on PrP^C aggregation or fibrillation.

Furthermore, I have investigated a possible inhibitory effect of a bioengineered NCAM1-Amyloidβ (NCAM1-Aβ) peptide on PrP^C aggregation and fibrillation. PrP^C and NCAM1-Aβ peptide alone formed fibrillar structures. However when incubated together up to three days only small aggregate clumps were observed. The results suggest a direct interaction between the PrP^C and NCAM1-Aβ molecules, resulting in inhibition of PrP^C aggregation, probably involving hydrophobic forces.

Streszczenie

Proces nieprawidłowego fałdowania komórkowej formy białka prionowego (PrP^C), jest związany z rozwojem śmiertelnych chorób neurodegeneracyjnych znanych jako pasażowalne encefalopatie gąbczaste, do których należy choroba Creutzfeldta-Jakoba występująca u ludzi lub choroba „szalonych krów” występująca u bydła. Proces ten nie jest zjawiskiem wyjątkowym: w odpowiednich warunkach wszystkie białka mogą ulec zmianie strukturalnej z dobrze rozpuszczalnego stanu natywnego do nierozpuszczalnego i włóknistego stanu amyloidowego. Takie błędne fałdowanie białek połączone z ich agregacją związane jest również z kilkoma innymi chorobami neurodegeneracyjnymi.

Ludzkie białko PrP^C jest zbudowane z 208 aminokwasów i składa się z dwóch strukturalnie różnych domen: nieustrukturyzowanej domeny N-terminalnej (DNT) oraz ustrukturyzowanej, głównie α-helikalnej, domeny C-terminalnej (DCT). DNT posiada ośmioaminokwasową powtarzającą się sekwencję (ang. octarepeat, OR), która poprzez reszty histydynowe wiąże jony metali Cu(II) i Zn(II). Wiele kofaktorów, włączając w to jony metali, wpływa na błędne fałdowanie białka PrP^C. W niniejszej pracy zastosowałem różnorodne, komplementarne metody biofizyczne do zbadania strukturalnych skutków wiązania jonów Cu(II) i Zn(II) przez ludzkie białko PrP^C oraz przez peptyd zawierający sekwencję OR.

Wyniki spektroskopii dichroizmu kołowego (ang. circular dichroism, CD) sugerują, że peptyd OR wiąże cztery jony Cu(II) oraz dwa jony Zn(II). Bliskie stechiometrycznym stężenia jonów obu metali wywołują zmianę helisy poliprolinowej typu II w zwrot β, natomiast stechiometryczne stężenia obu jonów metali wywołują powstanie antyrównoległych arkuszy β. Symulacje dynamiki molekularnej peptydu OR związanego z jonami metalu wskazują formowanie struktur spinek do włosów posiadających antyrównoległe arkusze β. Bezpośrednie dodanie jonów Zn(II) do peptydu OR skutkuje wiązaniem barwników, charakterystycznych dla włókien amyloidowych takich jak tioflawina T oraz czerwień Kongo. Po inkubacji peptydu OR z jonami Zn(II) obrazowanie z

zastosowaniem mikroskopii sił atomowych oraz transmisyjnej mikroskopii elektronowej ujawniło obecność włóknistych struktur. Charakterystyczny obraz dyfrakcji promieniowania rentgenowskiego wykazał obecność poprzecznych arkuszy β, typowych dla włókien amyloidowych. W związku z powyższym wiązanie jonów Cu(II) i Zn(II) przez peptyd OR może prowadzić do powstania struktur amyloidowych.

W przypadku ludzkiego białka PrP^C wiązanie jonów Zn(II) przez region OR skutkuje oddziaływaniem pomiędzy DNT i DCT. Spektroskopia CD wskazuje na utratę struktury α-helikalnej na skutek wiązania jonów Zn(II), prawdopodobnie w obrębie helisy drugiej i trzeciej, zlokalizowanych w DCT, oraz powstanie zwrotów β, prawdopodobnie dokoła związanego jonu Zn(II). Wyniki miareczkowania z zastosowaniem spektroskopii fluorescencji oraz CD sugerują, że pozorna stała dysocjacji dla kompleksu $PrP^C\cdot Zn(II)$ mieści się w granicy niskich stężeń mikromolowych, przez co można wnioskować, że takie oddziaływanie jest możliwe w warunkach fizjologicznych. Symulacje dynamiki molekularnej dla kompleksu $PrP^C\cdot Zn(II)$ wskazują stabilizację trzeciej α-helisy, podczas gdy wyniki małokątowego rozpraszania promieniowania rentgenowskiego sugerują bardziej kompaktowe zwinięcie białka PrP^C związanego z cynkiem. Jako że wiązanie cynku do białka PrP^C faworyzuje oddziaływanie międzydomenowe i stabilizuje trzecią α-helisę, cynk może hamować proces agregacji lub tworzenia włókien amyloidowych przez białko PrP^C.

Ponadto zbadano wpływ zaprojektowanego peptydu NCAM1-Aβ na agregację i tworzenie włókien amyloidowych przez ludzkie białko PrP^C. Białko PrP^C i peptyd NCAM1-Aβ same tworzą struktury amyloidowe, jednak ich wspólna inkubacja przez trzy dni skutkowała powstaniem wyłącznie niewielkich agregatów. Uzyskane wyniki sugerują bezpośrednie oddziaływanie peptydu NCAM1-Aβ z ludzkim białkiem prionowym, prawdopodobnie poprzez oddziaływania hydrofobowe, oraz inhibicję agregacji białka PrP^C.

List of papers

List of papers included in the thesis

I. Gielnik, M.; Pietralik, Z.; Zhukov, I.; Szymańska, A.; Kwiatek, W. M.; Kozak, M. PrP (58–93) Peptide from Unstructured N-Terminal Domain of Human Prion Protein Forms Amyloid-like Fibrillar Structures in the Presence of Zn 2+ Ions. RSC Advances 2019, 9 (39), 22211–22219.

II. Gielnik, M.; Szymańska, A.; Dong, X.; Jarvet, J.; Svedružić, Ž. M.; Gräslund, A.; Kozak, M.; Wärmländer, S. K. T. S. The Prion Protein Octarepeat Domain Forms Transient β-sheet Structures Upon Residue-Specific Cu(II) and Zn(II) Binding. Manuscript. Preprint available at bioRxiv, 2021.

III. Gielnik, M.; Taube, M.; Zhukova, L.; Zhukov, I.; Wärmländer, S. K. T. S.; Svedružić, Ž.; Kwiatek, W. M.; Gräslund, A.; Kozak, M. Zn(II) Binding Causes Interdomain Changes in the Structure and Flexibility of the Human Prion Protein. Scientific Reports 2021, 11 (1), 21703.

IV. Gielnik, M.; Zhukova, L.; Zhukov, I.; Gräslund, A.; Kozak, M.; Wärmländer, S. K. T. S. The Engineered Peptide Construct NCAM1-Aβ Inhibits Aggregation of the Human Prion Protein (PrP). Acta Biochimica Polonica (accepted). Preprint available at bioRxiv, 2021.

List of papers not included in the thesis

V. Marcinkowski, M.; Pilžys, T.; Garbicz, D.; Piwowarski, J.; Mielecki, D.; Nowaczyk, G.; Taube, M.; Gielnik, M.; Kozak, M.; Winiewska-Szajewska, M.; Szołajska, E.; Dębski, J.; Maciejewska, A. M.; Przygońska, K.; Ferenc, K.; Grzesiuk, E.; Poznański, J. Effect of Posttranslational Modifications on the Structure and Activity of FTO Demethylase. IJMS 2021, 22 (9), 4512.

Contents

1. Introduction

Scrapie is a Transmissible Spongiform Encephalopathy (TSE) – a fatal neurodegenerative disease of sheep and goats[1]. Up to the early 80's of the last century it was believed that scrapie is caused by a strain of slow viruses[2]. In 1982 Stanley Prusiner gathered all the available pieces of information and published a review in the *Science* Magazine, where he proposed that the infectious agent responsible for the development of scrapie might be a prion protein. The term prion was defined as "small proteinaceous infectious particles which are resistant to inactivation by most procedures that modify nucleic acids"[3]. The resistance to inactivation included UV radiation, ionizing radiation and treatment with formalin or heat. The term prion is still used today and it refers to a "proteinaceous infectious particle that lack nucleic acid"[2].

What is special about prions? According to the central dogma of molecular biology stated by Francis Crick, information cannot flow from one protein to another. At that time in the 1950's, there was a lack of evidence and lack of a mechanism for such signal transduction[4]. Nevertheless, a flow of information from protein to protein is present in TSEs. The normal, cellular form of the prion protein (PrP^C) is expressed in the central nervous system (CNS)[5]. In TSEs, this mainly α-helical and well soluble transmembrane protein undergoes a structural transition into an aggregated isoform, denoted as PrP^{Sc}. PrP^{Sc} isoform acts as a template and induces refolding of PrP^C into PrP^{Sc} form. This process results in accumulation of the insoluble, aggregated PrP^{Sc} isoform in the CNS causing spongiform degeneration[2].

Misfolding of the PrP^C protein is not limited to scrapie in sheep or goats. This fatal process is associated with at least seven diseases occurring in different animals species, and at least eight different diseases in humans, including Cruetzfeldt-Jacob disease (CJD) and Gerstmann-Sträussler-Scheinker syndrome (GSS)[6,7]. PrP^C misfolding is an ambiguous process, as different prion strains can originate from the same protein and result in different clinical symptoms, attributed to distinct diseases[8,9]. PrP^{Sc} can be transmitted between species[10], particularly to humans, which was prominent in the 1990's during the bovine spongiform encephalopathy (BSE) epidemy in the UK[11]. Prion diseases are rare, and affect approximately one person per million[12]. However, prion-like mechanisms of protein misfolding and aggregation have also been attributed to other neurodegenerative disorders[13]. This includes self-aggregation of the α-synuclein protein in Parkinson's disease[14], the amyloid-β (Aβ) and tau proteins in Alzheimer's disease[15], and the islet amyloid polypeptide in type 2 diabetes[16].

The prion protein binds different divalent transition metal ions, including Cu(II) and Zn(II). Such behavior suggests, that the physiological function of PrP^C is likely connected with metal ion binding[17–19]. This suggests a role for PrP^C in metal ion homeostasis, and metal ion imbalance has been suggested to be part of the pathology of prion diseases[19–21]. However, exactly how metal binding to PrP^C might be connected with TSEs is still unknown.

So far, no drug or treatment procedures have been approved to cure or reduce the symptoms of TSEs. Studies on bio-engineered cell-penetrating peptide constructs have shown that such constructs can reduce the amount of PrP aggregates in neuronal cell cultures, inoculated with different prion strains[22,23]. The molecular mechanisms underlying this effect are, however unknown.

Biophysics is a discipline in the field of physical science and applies techniques commonly used in physics to investigate properties of biological systems. In particular, biophysical techniques have been useful for the characterization of intrinsically disordered proteins (IDPs) and proteins with intrinsically disordered regions (IDRs), including PrP[24]. In this work, I have used several complementary biophysical methods to characterize the binding of Zn(II) and Cu(II) ions to PrP^C, and to investigate how such binding affects the protein's folding and aggregation properties. I have also investigated if the bio-engineered $NCAM1_{1\text{-}19}\text{-}A\beta_{16\text{-}20}$ peptide construct can inhibit PrP^{Sc} formation *in vitro*. Answering these questions may give valuable clues for understanding the prion diseases.

1.1. Structure of the human prion protein

The primary structure of human PrP^{C}, i.e. its sequence, is encoded by the *PRNP* gene[25,26] located in the short arm of chromosome 20[27]. The PrP^{C} sequence is encoded as a single exon, which eliminates the possibility of PrP^{Sc} formation by alternative RNA splicing[25]. The initial PrP^{C} precursor is a 253-residue long protein that undergoes posttranslational modifications to yield the 208 amino acids long mature PrP^{C} form (Fig. 1, A). The posttranslational modifications in details include: (i) formation of a disulfide bond between Cys179 – Cys214[28], (ii) cleavage of the 22-residue long N-terminal signal sequence responsible for directing PrP^{C} to the endoplasmic reticulum (ER)[25,29], (iii) removal of 23 C-terminal residues in the ER with (iv)

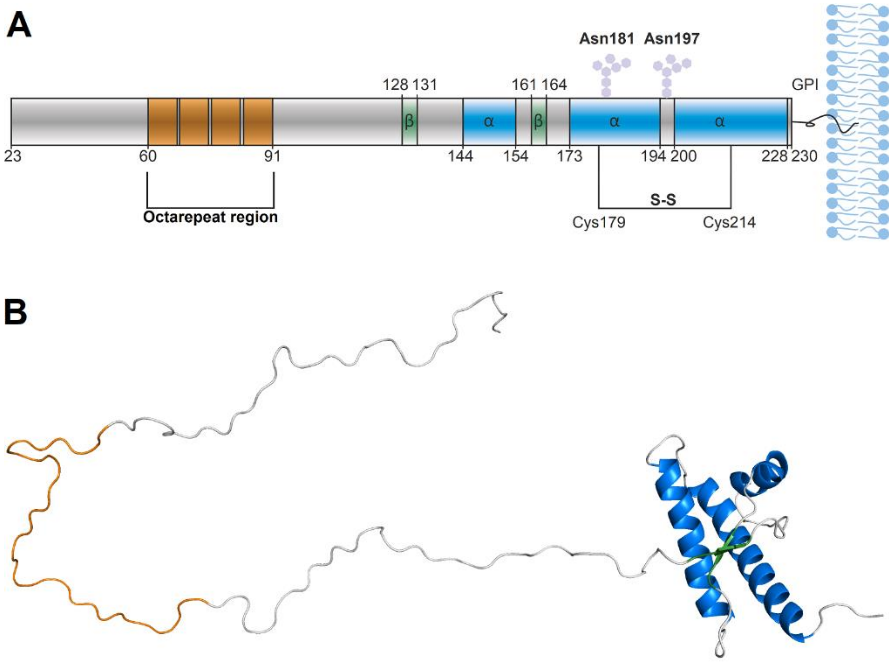

Figure 1. (A) Schematic representation of the mature human PrP^{C} protein. The OR region is shown in orange, β-strands are green, α-helices are blue, the hexagons represent glycosylation sites, S-S is a disulfide bridge, and GPI represents the glycosylphosphatidylinositol anchor. (B) Tertiary structure of human PrP^{C} with the OR region shown in orange, β-strands in green, α-helices in blue. The figure was made in the PyMOL software (Version 2.3.0, Schrödinger, LLC., New York, USA).

attachment of a glycosylphosphatidylinositol (GPI) anchor[29,30], and finally (v) glycosylation of the two asparagine residues Asn181 and Asn197, where PrP^C can be glycosylated at both positions, one position, or none[31,32]. Another post-translational modification is endoproteolytic cleavage. PrP^C can undergo α-cleavage around His111, and β-cleavage around Tpr89[33,34].

The PrP^C molecule consists of two structurally distinct domains: the flexible and unstructured N-terminal domain (residues 23-120) and the structured C-terminal domain (residues 121-230). The N-terminal domain contains four tandem octapeptide repeats (ORs), which are important for metal binding to PrP^C. Circular dichroism studies suggest that the secondary structure of the N-terminal domain, including the OR regions, is a mixture of random coil and polyproline II helix[35–38] – a left-handed, extended helical conformation[39]. On the other hand, nuclear magnetic resonance (NMR) studies suggest that the secondary structure of the OR region is a mixture of β-turns and structured loops[40,41].

In contrast to the flexible N-terminal domain, the secondary structure of the C-terminal domain is more uniform, and the NMR spectroscopy[28] and X-ray crystallography[42] studies show similar features. The C-terminal domain consists of two short antiparallel β-strands and three α-helices (Fig. 1, B). The first β-strand comprises residues 128–131, and the second β-strand comprises residues 161–164. Residues 144–154 form the first α-helix, residues 173–194 form the second α-helix, and residues 200–228 form the third α-helix. NMR solution studies suggest that the C-terminal fragments of α-helices 2 and 3 are in equilibrium with random coil structures. Interestingly, these helical PrP^C fragments seem to form tertiary contacts with the flexible N-terminal domain, and such interaction can have an overall stabilizing effect on the protein's structure[28,43].

1.2. Function of the human prion protein

PrP^C is widely expressed in the human body, with the highest expression levels in the central nervous system, including the amygdala, prefrontal cortex, and hypothalamus[44]. In neurons, PrP^C is localized in the synaptic cleft[5]. The presence of PrP^C in synapses suggests that it is involved in synaptic transmission, or in maintenance of synaptic structure, as progressive synaptic degeneration is an early symptom of prion diseases[45].

In the first attempts to investigate the PrP^C function, specific lines of transgenic mice without the *PRNP* gene (knockouts) were generated. Results on such *PRNP* knockouts showed that PrP^C expression is required for development of TSE diseases, as the knockouts were resistant to scrapie[46]. Surprisingly, the first generation of *PRNP* knockout mice showed development similar to the control mice[47,48], although individuals with *PRNP* knockout seemed to have a disturbed circadian rhythm. Under constant darkness conditions, the daily activity of knockouts differed from the control mice. Knockouts also showed signs of sleep fragmentation[49]. Newer mouse lines lacking the *PRNP* gene showed death of Purkinje neurons, but this was probably a result of Doppel overexpression, a protein encoded by the *PRNP* gene paralogue[44,50].

Other proposed roles for PrP^C include embryo development, myelin maintenance, and cellular differentiation[44,50,51]. Bioinformatic analysis suggests that PrP^C is evolutionarily related to the Zrt-, Irt-like Protein (ZIP) family of zinc transporters, which makes PrP^C a possible player in metal ion homeostasis[52]. With the ability to bind divalent metal ions[53], the main PrP^C functions connected with metal ion homeostasis may include protection from metal-induced oxidative stress, sequestering of metal ion concentrations, or signal transduction[18,54]. Interestingly, some studies suggest that TSEs are linked to metal ion dyshomeostasis[20,21].

1.2.1. Cu(II) binding

Copper is the third most common transition metal ion in the human brain[55]. In the human body copper mainly exists in ionic form, either in the oxidized Cu(II) state or in the reduced Cu(I) state[56]. The concentration of copper ions in the synaptic cleft ranges from 1 μM to 10 μM[57], and during synapse depolarization the local copper concentrations can transiently reach up to 250 μM[58]. Free (non-bound) Cu(II) ions can catalyze a Haber – Weiss reaction:

$$\cdot O_2^- + H_2O_2 \rightarrow O_2 + \cdot OH + OH^- \qquad (1)$$

As a result, highly reactive hydroxyl radicals are formed, which can lead to the oxidative damage of nearby biomolecules[59].

Human PrP^C binds up to six Cu(II) ions *in vivo* via two regions: the OR region (involving His61, His69, His76 and His84) and the so-called non-OR region (or amyloidogenic region, involving His96 and His111). The ability to bind Cu(II) ions has been attributed to PrP^C function[60–63]. Located in the presynaptic membrane, PrP^C during synapse depolarization is directly exposed to changes in Cu(II) concentration[64]. When exposed to Cu(II) concentration of 100 μM, PrP^C undergoes endocytosis, i.e. transport from the plasma membrane into the cell[65–67]. Point mutations of histidine to glycine in the first and second octarepeat or deletion of the N-terminal domain inhibits endocytosis[65–67]. This observation suggests that even if Cu(II) can bind to the other parts of the protein, binding to the OR region might be necessary for the biological function of PrP^C[67]. Cu(II) ions stimulate PrP^C expression, which suggests direct involvement of PrP^C in copper sequestration[68]. Cu(II) binding to PrP^C is therefore an important process that prevents the formation of harmful oxygen radicals[69]. Experiments in cell cultures suggest that PrP^C has a protective role as it prevents Cu(II)-induced toxicity and PrP^C overexpression reduces oxidative damage[70]. Neuronal cells expressing the *PRNP* gene are also more resistant to Cu(II) toxicity and oxidative stress than *PRNP* knockouts[71]. Moreover, addition of the OR peptide to neuronal cells lacking the *PRNP* gene reduces Cu(II) toxicity[71].

When investigating metal binding, there are some advantages in studying protein fragments (oligopeptides) that contain the metal-binding sites, rather than the full-length protein. The PrP^C fragments are less toxic to work with, easier and cheaper to produce, and easier to study with some techniques. Circular dichroism spectroscopy and electron paramagnetic resonance (EPR) studies indicate that peptide fragments are good models for PrP^C metal ion binding. To some extent, Cu(II) coordination in full length PrP^C is a sum of the Cu(II) coordination to the OR and amyloidogenic regions[72,73].

The OR region can bind up to four Cu(II) ions[61,62,74,75], where the binding modes depend on the Cu(II) concentration[76]. For up to 1:1 equivalents of Cu(II) ions, the OR region coordinates a single copper ion via the Nε2 atoms from the four histidine residues His61, His69, His77, and His85[76] (Figs. 1 and 2, A). Density functional theory calculations have shown that Cu(II) coordination by Nε2 atoms is favored over Nδ1 atoms[77]. In this binding mode, the OR region seems to have the highest affinity for Cu(II) ions, with reported dissociation constant (K_d) values ranging from 0.1 nM to 3 nM[78,79].

At copper concentration between 1 and 2 equivalents, the OR region binds two Cu(II) ions. The structure of this binding mode seems to be elusive, as different research groups have proposed different models. However, in all models a single Cu(II) cation is coordinated by two histidine residues. In some models the Cu(II) ion is coordinated by two Nδ1 atoms from the histidine residues and two deprotonated amide nitrogen atoms from the preceding glycine residues[80,81] (Fig. 2, B). Other models suggest that the Cu(II) ion is coordinated by one Nδ1 atom from one histidine residue, one Nε2 atom from the second histidine residue, two deprotonated amide nitrogen atoms, and one carbonyl oxygen, where one histidine residue is in axial position[75,76,78] (Fig. 2, B’). In principle both models could be correct, as the Cu(II) ions may switch between different binding configurations. In this binding mode the OR region seems to have a lower affinity for Cu(II) ions than in the binding mode with four histidine residues, as reported K_d values here are ~200 nM[78].

Above 2 equivalents of copper, up to four copper ions can be coordinated, each by one histidine Nδ1 atom, two deprotonated amide nitrogen atoms and one carbonyl oxygen from a preceding glycine residues[76,78,82] (Fig. 2, C). Even though this binding mode seems to have the weakest affinity for Cu(II) ions with reported K_d values in the 1-10 μM range[78,79], it stabilizes the Cu(II) oxidation state[76]. This stabilization prevents copper from cycling between Cu(II) and Cu(I) oxidative states and therefore prevents generation of harmful reactive oxygen species[76].

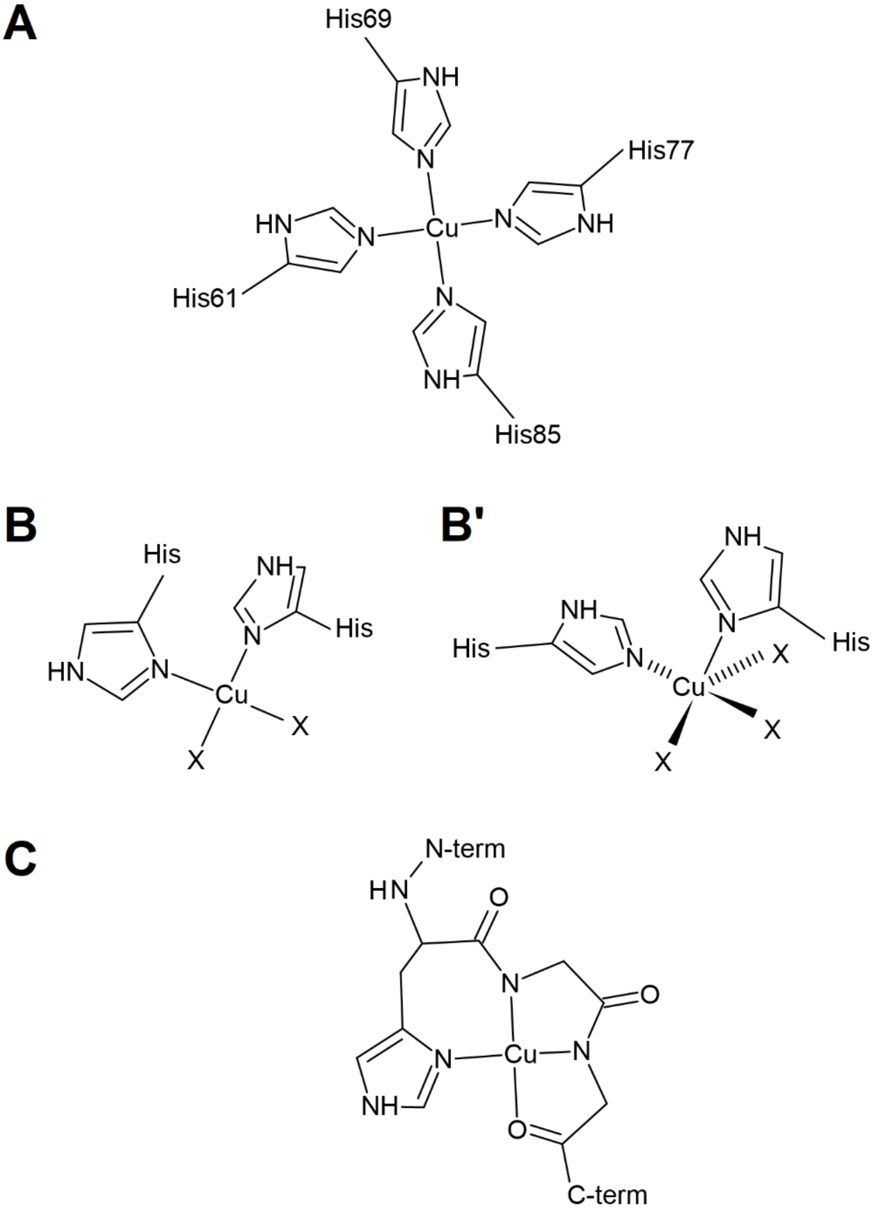

Figure 2. Copper(II) binding modes to the OR region of PrP^C. (A) Low Cu(II) occupancy binding mode[76,78]. Intermediate Cu(II) occupancy with (B) two equatorial His residues[80,81] and (B') one equatorial and one axial His residue[75,78]. X corresponds to two deprotonated amide groups, two water molecules or two deprotonated amide groups and one carbonyl group. (C) High Cu(II) occupancy[76,78,81,82]. The figure was made in ACD/ChemSketch (Version 2021.1.1, Advanced Chemistry Development, Inc., Toronto, Canada).

The secondary structure of the OR region is a mixture of random coil and PPII helix[35–37]. Binding of Cu(II) cations by the His residues should induce structural alterations within the sequence. Circular dichroism spectroscopy data suggest that the Cu(II)-bound OR region forms turns or unstructured loops wrapped around the metal ions[75]. Molecular dynamics (MD) simulations of a single Cu(II) ion bound to four Nε2 atoms from the OR domain showed a stable peptide conformation with multiple loops formed by the peptide backbone[77]. For higher metal ion:OR ratios, i.e. 4:1, the MD results suggest stacking of individual Cu(II)-bound octapeptide repeats and formation of extended structures[83].

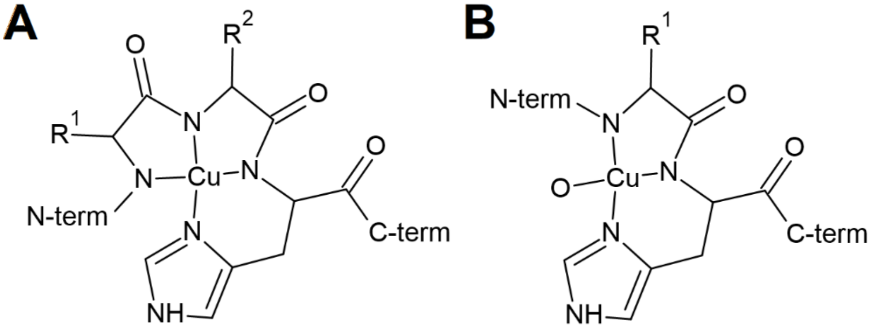

Figure 3. Cu(II) binding modes in the PrP^{C} amyloid region. (A) Cu(II) ions can be coordinated by Gly94 (R1), Thr95 (R2), His96 and Met109 (R1), Lys110 (R2), His111[84,85]. (B) A second plausible Cu(II) binding mode involves Thr95(R1), His96 and Lys(110), His111[85,86]. The O ligand represents an oxygen atom from a water molecule or carbonyl group. The figure was made in ACD/ChemSketch.

Copper binding sites are located also in the so-called non-OR domain, also known as the amyloidogenic region (residues 90-126). This region contains two histidine residues, i.e. His96 and His111. Each side chain of these histidine residues can independently bind a single Cu(II) ion[61,84–87]. In the formed complex, the Cu(II) ion is coordinated by the Nδ1 atom of the His residue together with three deprotonated amide nitrogen atoms (Fig. 3, A), or together with two deprotonated amide nitrogen atoms and one oxygen atom from a water molecule or a carbonyl group (Fig. 3, B). Out of the two histidine residues present in the amyloidogenic region, His111 appears to be preferred over His96[88]. The amyloid domain binds

Cu(II) ions with similar affinities to the intermediate Cu(II) occupancy of the OR-domain, and the reported K_d values are in the 100-250 nM range[78].

Cu(II) binding to the amyloidogenic region induces conformational changes. The isolated amyloidogenic region in solution adopts a random coil structure[87]. Cu(II) binding to His96 and His111 induces β-sheet formation[61,77,87], where the structural transition from random coil to β-sheet is directly attributed to Cu(II) coordination around His residues[61].

A related question is if Cu(II) binding alters the fold of the full-length PrP^C protein? Evans et al.[89] performed NMR experiments on full-length mouse PrP^C complexed with Cu(II) ions. In order to exclude possible binding to the amyloidogenic domain, the His95 and His110 residues (which correspond to His96 and His111 in human sequence) were mutated to tyrosine. Therefore, the added Cu(II) ions could bind only to the OR region. After addition of one Cu(II) equivalent, a decrease in resonance intensity for amino acids located in the C-terminal domain was observed. The authors concluded that Cu(II) binding to the OR domain results in interactions between the Cu(II)-bound N-terminal domain and the C-terminal domain. These intramolecular interactions affected the C-terminal part of the β1-α1 loop, the N-terminal part of α-helix 2, and the N-terminal part of α-helix 3. These observations were confirmed by MD simulations and EPR distance measurements using spin labels incorporated to specific residues[89]. It was concluded that the interaction between the Cu(II)-bound N-terminal domain and the C-terminal domain is driven by electrostatic attraction between the Cu(II) ion and the electronegative surface of the C-terminal domain[89]. The same researchers also performed mass spectrometry (MS) on cross-linked *apo* and Cu(II)-bound PrP^C, and observed the same cross-linked peptide pairs, but with different intensities. It was therefore concluded that *apo*-PrP^C and Cu(II)-bound PrP^C exist in a conformational equilibrium, and that Cu(II) ions act as a switch shifting this equilibrum[90].

Thakur et al.[91] observed similar intradomain interactions for the Cu(II)-PrP^C complex. NMR experiments on N-terminally truncated mouse PrP(90-231) protein with Cu(II) ions also suggest interactions between the β1-α1 loop and the Cu(II) binding site, however in this case metal binding was attributed to the amyloidogenic region. For full-length mouse PrP^C, addition of Cu(II) ions resulted in the disappearance of NMR peaks assigned to α-helix 2. The authors interpreted this as a result of interactions between the Cu(II)-bound OR region and α-helix 2[91].

It is still an open question if the Cu(II)-driven intradomain interaction is good or bad for the physiological role of PrP^C. Thakur et al. suggested that interaction between Cu(II)-bound His96 or His111 and α-helix 1 can be responsible for the inhibition of amyloid formation[91]. On the other hand, results provided by Younan et al.[61] indicate that Cu(II) binding can destabilize the PrP^C fold and as a result promote aggregation.

1.2.2. Zn(II) binding

Zinc, after iron, is the second most common transition metal in the human body[92]. This divalent metal ion is redox neutral and plays a crucial role as a catalytic, structural, and/or signaling component[92]. Among all the organs, the highest Zn(II) concentrations are present in the brain[93]. Under neuronal depolarization Zn(II) is released from the presynaptic into the synaptic cleft, where it can reach transient concentrations in the 100 μM – 300 μM range[94,95].

PrP^C is evolutionarily related to the ZIP family of zinc transporters, therefore its function should be connected with Zn(II) ions[52]. Indeed, PrP^C facilitates uptake of Zn(II) ions into neurons, where the Zn(II) uptake is lost in mutated PrP^C forms associated with TSE[96]. Region-specific Zn(II) content in the brain also depends on the PrP^C expression level[97]. Moreover, treatment of neuronal cell lines with 100 μM of $ZnSO_4$ stimulates endocytosis of PrP^C in a similar way as for $CuSO_4$[66].

The OR region seems to play a crucial role in PrP^C endocytosis, and when deleted or when histidine residues were substituted to glycine residues, the endocytosis was abolished[66,67]. The first studies on Zn(II) binding to the isolated OR region yielded K_d values ~ 0.4 μM[53]. Later studies with EPR and MS performed by Walter et al.[98] suggest a weaker binding. Walter et al.[98] measured PrP^C-Zn(II) affinity using Cu(II) as a competitor, and obtained a binding curve with a K_d of 200 μM. The same group in a set of NMR experiments used Cd(II) as a Zn(II) surrogate, and obtained K_d of ~ 1 mM[99]. However, direct titrations of PrP^C with Zn(II) using Isothermal Titration Calorimetry (ICT) suggest much stronger Zn(II) binding, with a K_d ~16 μM[99]. Therefore, the use of metal ions mimicking the behavior of Zn(II), or competition studies between two metal ions, can possibly underestimate the PrP^C-Zn(II) affinity.

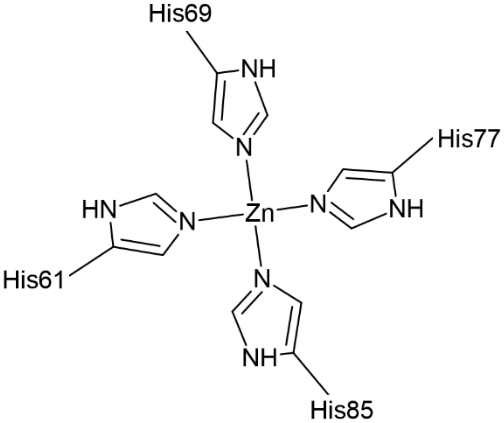

Figure 4. PrP^C binds a single Zn(II) ion by the four His residues from the OR region[100]. The figure was made in ACD/ChemSketch.

Full-length PrP^C binds a single Zn(II) ion by three to four His residues from the OR region (Fig. 4)[99,101]. Spevacek et al.[100] titrated full-length mouse PrP^C with Zn(II) ions using NMR spectroscopy, and observed disappearance or shifts of amide backbone cross peaks assigned to the C-terminal domain. The loss of signal involved residues located in the β1-α1 loop, the N-terminal part of α-helix 2, and the N-terminal part of α-helix 3, and was attributed to changes in the chemical environment. The authors hypothesized that the Zn(II)-bound OR region can interact with the C-terminal domain. In order to verify this hypothesis, they performed additional NMR titrations on mouse PrP^C(91-230), i.e. a truncated protein lacking the OR region. Most of the residues of the truncated PrP^C(91-230) were unaffected by the addition of Zn(II) ions. Therefore the authors concluded that the Zn(II)-bound OR region forms a tertiary contact with α-helices 2 and 3 located in the C-terminal domain of PrP^{C}[100].

From a physiological point of view, the biological function of PrP^{C} may be related to Zn(II) sensing[96]. PrP^{C} promotes Zn(II) uptake via the α-amino-3-hydroxy-5-methyl-4-isoxazolepropionate (AMPA) channels, and might therefore have an important role in neuronal zinc homeostasis[19].

1.3. Molecular basis of TSE

1.3.1. Misfolding of the prion protein

PrP^{C} can undergo a misfolding into a pathogenic form known as PrP^{Sc} [2]. Unlike PrP^{C}, PrP^{Sc} contains high amounts of β-sheet secondary structure, is highly insoluble and resistant to proteinase K digestion[102–104]. Accumulation of PrP^{Sc} form in the CNS results in neuropathological changes in the brain and development of fatal neurodegenerative diseases called Transmissible Spongiform Encephalopathies (TSEs)[2]. It is now widely accepted that PrP^{Sc} is a form of amyloid state[105,106] and consists of fibrils with a high degree of organization and a cross-β structure[107].

According to the protein-only hypothesis, the only substrate required for PrP^{Sc} formation is PrP^{C} itself[108]. Expression of PrP^{C} is necessary for PrP^{Sc} formation, as transgenic mice lacking the *PRNP* gene are resistant to TSEs[46,109]. Moreover, PrP^{Sc} is composed of PrP^{C}, and both conformers have the same posttranslational modifications[110]. PrP^{Sc} formation appears to occur at the cell surface in cholesterol-rich membranes[111]. Interestingly, mice models expressing PrP^{C} without the GPI anchor, formed PrP^{Sc} after inoculation with TSE, however with minimal clinical symptoms[112].

Neurotoxic PrP^{Sc} molecules can be reproduced *in vitro* from recombinant proteins expressed in *E. coli* and still maintain characteristic features of a prion strain[113–115]. A prion strain is an important concept connected with prion diseases. PrP^{C} can form distinct PrP^{Sc} states, each with different biochemical and biophysical properties. These distinct PrP^{Sc} forms are connected with different clinical outcomes and called strains. The same prion strain can be transmitted in one species with the same prion-disease phenotype[13,106,116]. Distinct prion strains can possess different secondary structures, even though they originate from the same form of PrP^{C}[117,118]. Some prion strains can be transmitted between different species with the same clinical symptoms. Nevertheless, interspecies inoculation is less efficient than intraspecies or even sometimes impossible. This phenomenon is called transmission barrier and originates from the difference in PrP^{C} sequence between the host and the donor[119].

1.3.2. Prion misfolding, propagation, and neurotoxicity

Studies on mice models suggest that prion diseases develop in two distinct phases. The first phase is responsible for propagation, and the second phase is responsible for neurotoxicity[120]. The propagation phase is characterized by exponential growth and saturation of prion infectivity in mouse bioassays (Fig. 5, solid lines). This phase probably involves formation of small proteinase K-resistant and proteinase K-sensitive oligomers[121], as the total PrP concentration remains constant and no PrP^{Sc} molecules are observed[122]. Interestingly, the PrP^{C} expression level is not a rate-limiting step of exponential growth. All mice lines expressing a different PrP^{C} concentrations reach the same level of infectivity, as this level seems to be independent of the PrP^{C} concentration[120].

When the propagation phase saturates, the neurotoxicity phase starts (Fig. 5, dashed lines). Despite the constant level of prion infectivity in mouse bioassays, the clinical symptoms of prion disease begin to manifest themselves over time. The more PrP^{C} the mice models express, the faster the TSE onset is[120]. In this phase the levels of PrP^{Sc} and proteinase K-sensitive PrP oligomers increase over time, with rates of production proportional to the PrP^{C} expression. However, the oligomers produced in the toxicity phase are probably the main disease-associated forms, and they differ from the oligomers formed in the propagation phase[106,122], as highly purified prion fibrils are not directly neurotoxic[123]. Moreover, the neurotoxic oligomers must reach the same threshold concentration, independent of the PrP^C expression level, for the manifestation of clinical symptoms[106,122]. It is therefore possible that prion diseases are mediated by a soluble, oligomeric species, similar to the case of the Aβ peptide oligomers responsible for Alzheimer’s disease[106,124,125].

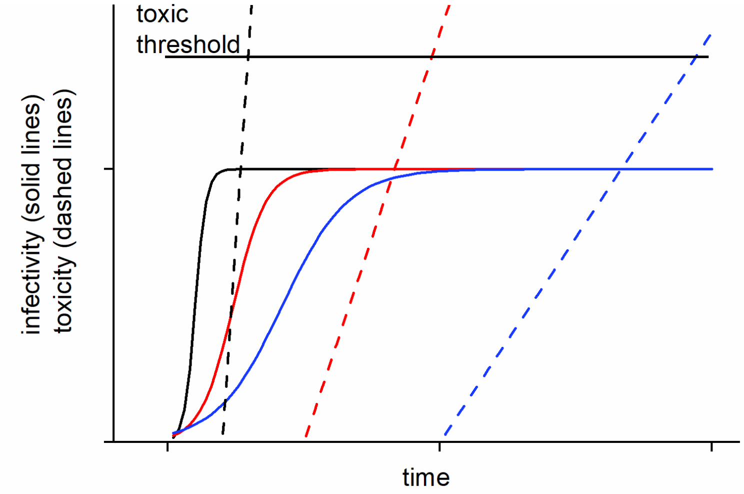

Figure 5. Propagation and neurotoxicity of TSE in mice models: expressing PrP^C eight times more than wild type (black), with normal PrP^C expression (red) and with 50% of PrP^C expression (blue). In the propagation phase (solid lines) all mice lines reach the same infectivity. The neurotoxicity phase (dashed lines) starts when the propagation phase reaches a plateau. Clinical symptoms of TSE appear when the toxicity phase reaches the toxic threshold. Adopted from Collinge[106]. The figure was made in OriginPro, Version 2019b, OriginLab Corporation, Northampton, USA.

1.3.3. Structure of prion protein fibrils

Even though the prion fibrils may not be directly neurotoxic, the structural models of PrP^{Sc} molecules are important for TSE research. Understanding the atomic structures of PrP^{Sc} gives invaluable clues about the conversion from soluble PrP^C into insoluble fibrils[126]. Determined structures give clues about the protein refolding processes required for fibril formation and elongation[127]. Recent progress in cryo-electron microscopy (cryo-EM) has allowed to determine the structures of many amyloid fibrils, including those of Aβ(1-42), involved in Alzheimer’s disease, and those of α-synuclein, involved in Parkinson’s disease[128–130].

Glynn et al.[131] used cryo-EM to determine the three-dimensional (3D) structure of fibrils of recombinant human PrP(94-178) (Fig. 6, A). Those fibrils contained a fragment of PrP^{Sc} core, and have similar biophysical properties to brain-derived PrP^{Sc} molecules[132,133].

A rPrP(94-178) sample incubated with 4 M urea formed long fibrils, shorter rods, and amorphous aggregates. Incubation with proteinase-K reduced the number of visible amorphous aggregates, and shifted the equilibrium towards fibrillar structures that were further analyzed. For rPrP(94-178), 40 out of 85 residues were modeled with cryo-EM data to yield a structural model. The fibril core consisted of two symmetric building blocks protofilaments - each of which comprised four β-strands: β1 (Lys106-Met109), β2 (Ala115-Leu125), β3 (Ala133-Ser135) and β4 (Ile138-His140). The two protofilaments formed a large interface between each other, stabilizing the fibrillar structure. Strands in each protofilament formed a parallel, in-register structure with a spacing of 4.8 Å, which is characteristic for amyloids.

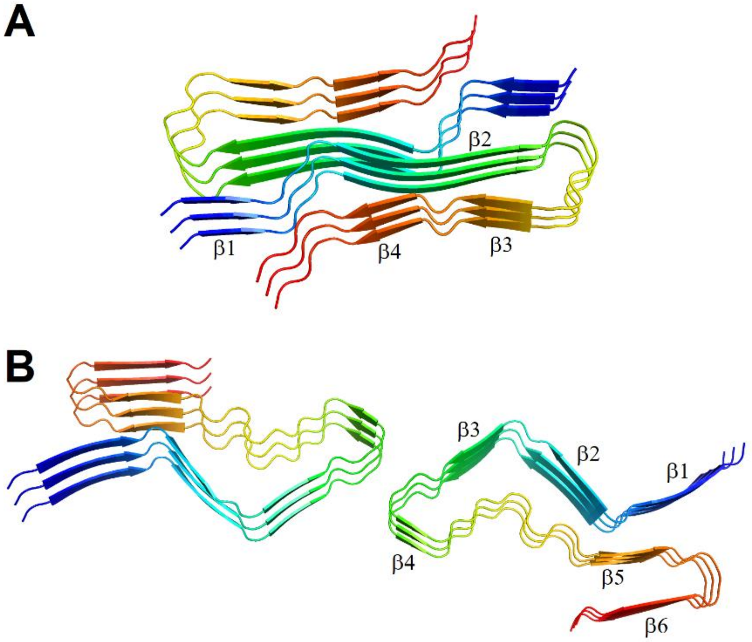

Figure 6. Cryo-EM structure of (A) human PrP(94-178) fibrils (PDB 6UUR) and (B) full length recombinant human PrP fibrils (PDB 6LNI). The N-terminus is shown in blue, and the C-terminus is shown in red.

Wang et al.[134] determined the atomic structure of full-length recombinant human PrP fibrils using cryo-EM (Fig. 6, B). The fibril structure consisted of two intertwined protofilaments that formed a dimer. Each protofilament also formed a parallel, in-register structure with 4.8 Å spacing, characteristic for amyloids. In the final model, each protofilament comprised residues 170-229 and contained six β-strands: β1 (Gln172-Asp178), β2 (Val180-Gln186), β3 (Thr188-Thr192), β4 (Asn197-Thr199), β5 (Gln212-Thr216) and β6 (Ser222-Gln227). The results suggest immense rearrangements in the C-terminal domain of PrP^C, as during refolding of PrP^C to a PrP fibril, α-helix 2 is converted to β-strands 1, 2, and 3, α-helix 3 is converted to β-strands 5 and 6, and the α2-α3 loop is converted to β-strand 4.

1.3.4. Metal ions and prion protein misfolding

Binding of metal ions to the OR region of PrP^C seems to have an important role on PrP^C misfolding. PrP^{Sc} molecules isolated from human brains are bound to Cu(II) and Zn(II) ions[117], and inoculation of cell cultures with PrP^{Sc} reduces the Cu(II) uptake[135]. Expansion in the number of octarepeats from four up to sixteen results in the human TSE called familial Creutzfeldt-Jakob Disease[136]. Interestingly, peptides with eight or nine ORs show ten times higher affinity to Cu(II) ions[137]. On the other hand, supplementation of cell cultures with Cu(II) protects them from PrP^{Sc} accumulation after inoculation with prions[138].

Biophysical studies of *de novo* full-length PrP^C fibrillization suggest that Cu(II) and Zn(II) ions can sequester amyloid fibril formation *in vitro*[139,140]. Thakur et al.[91] observed aggregation of Cu(II)-bound full length mouse PrP^C at pH 7.4. Aggregation occurred at 15 °C and was reversible at the physiological temperature of 37 °C. Interestingly, the N-terminally truncated mouse PrP^C(90-231) protein did not show any aggregation after addition of Cu(II) ions. The authors concluded that the Cu(II)-bound OR region is responsible for temperature-reversible PrP^C aggregation. This lead to the suggestion that Cu(II) may not be responsible for PrP^C aggregation at physiological temperatures. The authors also observed interactions between the Cu(II)-bound N-terminal domain and α-helices 1 and 2. This lead to the proposition that Cu(II)-driven interactions between the N-terminal and C-terminal domains may restrict interaction between PrP^C monomers and inhibit amyloid formation[91].

There is also the other side of the coin. Sigurdsson et al.[141] conducted studies on a mouse line supplemented with D-penicillamine, a copper chelator used to treat heavy metal poisoning. After inoculation with a prion strain, the mice received an injection with D-penicillamine, which delayed the prion disease onset by 11 days[141]. Thus, the metal ion context in TSE is a rather complex problem.

1.3.5. Interaction of cell penetrating peptides with prion protein and implications for amyloid formation

Cell-penetrating peptides (CPPs) are a group of peptides, generally shorter than forty residues, which can easily enter cells e.g. via endocytosis. CPPs have a low toxicity, can enter a variety of cell types, and conjugated with a cargo can deliver various molecules across the cell membrane, like nucleic acids, nanoparticles or drugs. The characteristic feature of CPPs, is that most of them have positively charged amino acids, and α-helical secondary structure[142–144]. Interestingly, the PrP N-terminal secretion signal fragment, constituting residues 1-22, is also a CPP[145–147].

As the PrP(19-30) peptide can bind to PrP^{Sc} fibrils[148], and the residues 23-30 of PrP^C are responsible for the conformational stability of the C-terminal domain[149], Löfgren et al.[22,23] investigated potentially beneficial properties of the PrP(1-28) peptides. Studies on GT1-1 neuronal cell lines, inoculated with RML, or 22L prion strains, showed an elevated levels of proteinase K-resistant form of PrP (PrP^{Res}). Treatment the inoculated cell lines with mouse PrP(1-28) (mPrP) peptide reduced the amount of PrP^{Res} in cultured cells, where a scrambled version of this peptide had no effect on the PrP^{Res} levels. Similar inhibitory effects were also observed for the bovine PrP(1-30) peptide. Shortening the N-terminus of mouse PrP of peptides to mPrP(6-29), mPrP(12-28), mPrP(19-30), and mPrP(23-28) abolished the anti-prion effect, and the authors suggested that the peptide requires an additional signal peptide motif for a sufficient anti-prion effect[22,23]. Other CPPs, including penetratin, transportan-10, transactivator of transcription (TAT) protein fragment, TAT(48-60), and their conjugates with mPrP(23-28) had no influence on the PrP^{Res} levels in the GT1-1 cells infected with RML and 22L prion strains. Nevertheless conjugation of other CPP, the secretion signal peptide from neural cell adhesion molecule-1 (NCAM1), harboring residues 1-19 with mPrP(23-28) restored the anti-prion properties, even with higher efficiency than mPrP(1-28) peptide[22]. The increased anti-prion efficiency of NCAM1 construct is probably due to the natural interaction between NCAM1 and PrP^C at the neuronal cell surface[150,151].

NCAM1(1-19) conjugates are promising CPPs, and can potentially inhibit amyloid-related diseases[152]. NCAM1(1-19)-mPrP(23-28) and NCAM1(1-19)-K-Aβ(16-20) are amyloidogenic themselves, as they can form amyloid structures[153,154]. However they can inhibit fibril formation by Aβ(1-40) and Aβ(1-42), a different amyloid peptides, shifting the equilibrium from amyloids towards nontoxic amorphous aggregates[152,155]. On the other hand the same peptide conjugates promote *in vitro* aggregation of S100A9, a protein involved in amyloid-related and inflammatory processes[154,156,157].

1.4. Overview of TSEs

1.4.1. Human TSEs

Human TSEs can be grouped into three main categories: genetic, sporadic, and acquired[105]. Genetic TSEs are caused by mutations in the *PRNP* gene and include familial Creutzfeldt-Jakob Disease (fCJD), Fatal Familial Insomnia (FFI), and Gerstmann-Sträussler-Scheinker syndrome (GSS). Diagnosis with a mutation within the *PRNP* gene is an inevitable sentence of being a TSE victim, as most of the individuals will develop disease[105]. However, some genetic variants seem to protect against TSEs, such as the Gly127Val substitution. Mice expressing this variant were resistant to all out of 18 isolated human prion strains[158].

The most common mutation resulting in GSS is the Pro102Leu point mutation[159], which is autosomal and dominant[159]. Patients clinically diagnosed with GSS manifest early cognitive impairment and ataxia, i.e. difficulties with balance, speaking, and walking[160]. The average onset for GSS is around 45 years, with an average 44 month duration[161]. FFI is caused by the Asp178Asn mutation[162]. This dominant mutation is connected with the presence of methionine residue at position 129. The average onset of this disease is 49 years, with an average duration of ~18 months[7,163,164]. Clinical symptoms of FFI include insomnia, dysautonomia, i.e. dysfunction of the autonomic nervous system (ANS), and ataxia[165,166]. The Asp178Asn mutation, also present in GSS, but conjugated with valine residue at position 129, induces fCJD. Other point mutations responsible for fCJD include Glu200Lys and Val210Ile as well as expansion or partial deletion of the OR region. Expansion of the OR region includes insertion of additional octapeptide repeats, from the natural four tandem octapeptide repeats up to sixteen repeats[7,136]. The clinical features of fCJD are similar to GSS and include cognitive impairment, dementia, and behavioral changes[136]. Together, the genetic TSE forms account for up to 15% of all human prion disease cases[167].

Sporadic TSEs include sporadic CJD (sCJD) and sporadic Fatal Insomnia (sFI). sCJD, which accounts for ~85% of all human TSE cases, has an unknown etiology[105]. Even though sCJD is the most common human TSE, it is a relatively rare disease that affects approximately one person in a million per annum[168,169]. The clinical symptoms of sCJD include progressive dementia, ataxia, and vision problems[12]. Most of the patients diagnosed with sCJD die within the first year after onset[170,171]. sFI has no established genetic background, but in all cases the patients were homozygotes with the 129 MetMet genotype. Clinical symptoms for sFI share similarities with FFI and include insomnia, ataxia, and cognitive impairment[172]. The average onset for sFI is 43 years, with a mean duration of 30 months[173].

Acquired TSEs are caused by transmission of a tissue material contaminated with TSE to a healthy individual. These include iatrogenic CJD (iCJD), variant CJD (vCJD), and kuru[167]. Kuru was the first human TSE to be discovered, by Daniel Gajdusek, who showed that kuru can be transmitted to other species[174]. This finding gave him a Nobel Prize in Physiology or Medicine in 1976[175]. Kuru was found in the Fore linguistic group of Papua New Guinea Eastern Highlands. The cause of kuru were cannibalistic rituals, involving consumption of deceased relatives[174]. With a prohibition of cannibalistic rituals introduced in the 1950's by the Australian government, the number of kuru cases began to decline over time[176]. Kuru has three clinical stages: ambulant, sedentary, and terminal. In the early ambulant phase, the patient has problems with gait, which in a month advances to astasia (inability to stand without assistance) and ataxia. The sedentary phase begins when the patient is unable to walk without assistance. The terminal phase begins when the patient is unable to sit without support and becomes bedridden. At this stage patients show signs of dementia and are unable to speak. The mean duration of kuru is 12 months[7,174].

vCJD was linked to consumption of beef contaminated with Bowine Spongiform Encephalopathy, an animal TSE disease[177]. Patients infected with vCJD show psychiatric or behavioral symptoms like apathy, depression, insomnia, and/or aggression. Neurological symptoms appear 6 months after the psychiatric symptoms and include ataxia, cognitive impairment, and involuntary movements. The average duration of vCJD is 14 months[7,176].

iCJD is the result of medical procedures[178], mainly treatment with cadaveric human growth hormone[179], dura mater grafts[180], cornea transplants[181], or improperly sterilized medical instruments[182]. With the introduction of recombinantly produced human growth hormone, expressed in *E. Coli*[183], treatment of dura mater before transplantation in 0.1 M sodium hydroxide, and new recommendations for medical instrument sterilization, the number of iCJD cases is decreasing[178]. Clinicopathological features of iCJD depend on the type of infection: patients infected with cadaveric human growth hormone show symptoms similar to kuru, while patients after dura mater graft or infected by insufficiently sterilized medical instruments show symptoms similar to sCJD[7].

1.4.2. Animal TSEs

Scrapie, the oldest animal TSE known to man-kind, was identified almost 300 years ago in Spain[184]. Scrapie affects sheep and goats, with similar clinical symptoms including pruritus, ataxia and tremor[6,185]. Two factors are connected with the spread of scrapie: tissue distribution of PrP^{Sc}, and the sequence of the *PRNP* gene. The main factor responsible for scrapie transmission is ingestion of PrP^{Sc} from contaminated materials in the environment. In the early phase, PrP^{Sc} replicates in guts, resulting in environmental contamination via saliva and feces. The disease can be transmitted also to the offspring through milk, the placenta, or placental fluids[1]. Ovine *PRNP* shows natural polymorphisms at codons 136, 154, and 171, where Val136 together with the Arg154 and Gln171 genotypes show the highest susceptibility to scrapie, and the Ala136, Arg154, and Arg171 genotypes show the highest resistance to scrapie[1,6]. Interestingly, scrapie can be detected in living sheep by a third-eyelid biopsy[186]. Up to date, there has not been any evidence that scrapie can be transmitted to humans[1].

Bovine Spongiform Encephalopathy (BSE), also known as “Mad Cow Disease”, is a fatal neurodegenerative TSE in cattle. Clinical symptoms of BSE are similar to CJD and include ataxia, tremor, aggression, and apathy[6]. BSE was first identified in the UK in 1986[187], and affected nearly 200,000 cattle worldwide[6]. The most likely cause of the BSE epidemic was usage of meat and bone meal (MBM). MBM, most likely prepared from infected cattle, was served as a high protein product to calfs[188], which amplified the number of BSE cases from 446 in 1987 to over 37,000 in 1992[11,189]. As the usage of MBM was prohibited in the UK in 1996, and in the EU in 2001, the number of BSE cases declined to a few cases per year[11]. BSE is a public health risk factor, as it can be transmitted to humans resulting in vCJD. Therefore, in order to prevent the entrance of contaminated meat products into the human food chain, it is still important to test cattle for BSE[177].

Transmissible mink encephalopathy (TME) is a neurodegenerative disease of mink. It was first discovered in the 1950's in mink farms in Wisconsin, USA[190]. The most like cause of TME was mink food preparation from bovine meat contaminated with BSE[191]. On the other hand, healthy minks can become infected by biting individuals with TME or by Kuru-like cannibalism[6]. Clinical symptoms are similar to BSE and include aggression, depression and anxiety. At the later stages of the disease the animals suffer from tremors, ataxia, and problems with gait[191,192].

Feline spongiform encephalopathy (FSE) is a TSE that affects domesticated cats and captive big cats. FSE was discovered in 1990[193], and its origin was connected with consumption of meat contaminated with BSE[194]. The majority of FSE cases among captive big cats were diagnosed in UK zoos, or in individuals originating from the UK, during the BSE epidemic. The clinical symptoms of FSE are similar to those of BSE[195].

Exotic Ungulate Encephalopathy (EUE) is a TSE that was diagnosed among members of the Bovidae family kept in UK zoos during the BSE epidemic. All infected animals were fed with MBM possibly contaminated with BSE. The last animal diagnosed with EUE died in 1998[195].

Chronic wasting disease (CWD) is a neurodegenerative disease of cervids, discovered in the 1960's in Colorado, USA. This disease mainly affected animals in North America[11], but has been found recently among reindeer and moose in Norway[196]. One possible cause of the CWD outbreak in Norway is "antler cannibalism". All reindeer infected with CWD showed signs of antler gnawing, and this phenomenon was especially visible among young females[197]. The antler velvet contains PrP^{Sc} molecules[198], and the origin of CWD in Norway may therefore be connected with a sort of cannibalism, similar to kuru[197]. The clinical symptoms of CWD include weight loss, fixed gaze, ataxia, head tremors, teeth grinding, and loss of fear of humans[6]. CWD prion strains are potentially harmful to humans as they can convert human PrP^{C} molecules into PrP^{Sc} *in vitro*[199]. As the CWD prions are present in muscles, human consumption of venison is a potential risk factor[200].

Camel prion disease (CPD) is the most recently discovered animal TSE[201]. It was discovered in 2018 among the dromedary camels in the southeastern region of Algeria. It is estimated that CPD occurs in 3% of the dromedary camels brought to the slaughterhouse. Brains of dromedaries diagnosed with CPD showed signs of spongiform degeneration with the presence of PrP^{Sc} deposits. Even though CPD has an unknown origin, two possible ways of transmission have been proposed. After the ban of MBM usage in the UK, MBM was exported to third world countries including Algeria. Thus, dromedary camels could have been infected by consumption of BSE-infected MBM. Another possibility is that camels grazing on garbage dumps near oil fields across the desert could have consumed prion-contaminated waste[201].

2. Aims of the thesis

Description of the molecular processes underlying PrP^C folding and misfolding is crucial for the understanding of the mechanisms responsible for amyloid formation and TSEs development. **Therefore, the main research aim of my thesis was to characterize the interactions between human prion protein, or its octarepeat (OR) fragment, and metal ions (Cu(II), Zn(II)), or NCAM1(1-19)-K-Aβ(16-20) peptide construct using complementary biophysical techniques, with the respect to PrP^C folding and amyloid formation.** The research objectives were as follows:

1. Determine the dissociation constant for the OR-Cu(II) and OR-Zn(II) complex.
2. Identify the structural consequences of Cu(II) and Zn(II) binding to OR peptide.
3. Determine the dissociation constant for the PrP^C-Zn(II) complex.
4. Identify the structural changes induced by the Zn(II) binding to the PrP^C.
5. Determine experimental conditions sufficient for PrP^C to form fibrils *in vitro*.
6. Verify the anti-prion effect of NCAM1(1-19)-K-Aβ(16-20) peptide *in vitro*.

3. Physicochemical principles of experimental methods

3.1. Ultraviolet-visible spectroscopy

Let us consider light traveling through a cuvette containing a buffer in a spectrometer. For each wavelength we can measure I_0 as the light intensity passing through a reference cell. If we now place the test sample solution in a cuvette and illuminate light through it, the measured intensity of light passing through the sample (i.e., I) will be smaller than I_0, therefore light was absorbed by the sample. We can define this absorbance, A, as:

$$A = \log\left(\frac{I_0}{I}\right) \tag{2}$$

According to the empirical Beer-Lambert law:

$$A = \varepsilon c l \tag{3}$$

The absorbance depends on the molar absorption coefficient, ε, the molar concentration of the sample, c, and the pathlength of the sample, l.

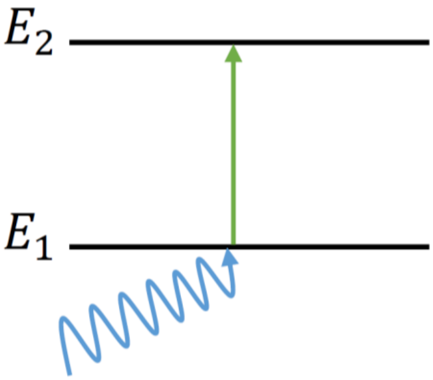

Figure 7. Absorption of the light corresponds to the electron transition between the initial state E_1 and final state E_2.

The sample absorbs light when an electron undergoes a transition between two states. As the electron energy levels are quantized, the sample absorbs only defined wavelengths of the light (Fig. 7):

$$E_2 - E_1 = h\nu \tag{4}$$

where E_2 is the electron energy in state 2, E_1 is the electron energy in state 1, h is the Planck constant, and ν is the light frequency.

Chemical groups with characteristic frequencies of light absorption are called chromophores. In peptides and proteins there are two main chromophores responsible for light absorption. The first is the carbonyl group present in the polypeptide main chain. One electron from the lone pair of oxygen nonbonding electrons can be excited into an antibonding orbital of the carbonyl group, resulting in a $\pi^* \leftarrow n$ transition. The $\pi^* \leftarrow n$ transitions in peptides are forbidden by symmetry, and they absorb light weakly. The second group responsible for light absorption is the C=C double bond, where a π electron can be excited into a π* antibonding orbital, resulting in a $\pi^* \leftarrow \pi$ transition. The C=C double bonds, present in the aromatic rings of tryptophan and tyrosine residues, form a conjugated system, and are responsible for light absorption around 280 nm[202,203]. Therefore, ultraviolet-visible (UV-Vis) spectroscopy allows the determination of polypeptide concentration, where molar absorption coefficient can be calculated from the polypeptide sequence[204].

UV-Vis spectroscopy can be also used to detect the presence of amyloid structures by the Congo Red (CR, full chemical name: disodium 4-amino-3-[4-[4-(1-amino-4-sulfonatonaphthalen-2-yl)diazenylphenyl]phenyl]diazenyl-naphthalene-1-sulfonate) assay. CR is a diazo dye with 38 conjugated π electrons (Fig. 8), and it absorbs light at 338 nm and at 486 nm. CR binds to β-sheets of amyloid fibrils via hydrogen bonds. Stacking of CR molecules perpendicular to the fibril axis causes a spectral shift of absorption from 486 nm to 542 nm, which can be used to identify amyloid structures *in vitro*[205–207].

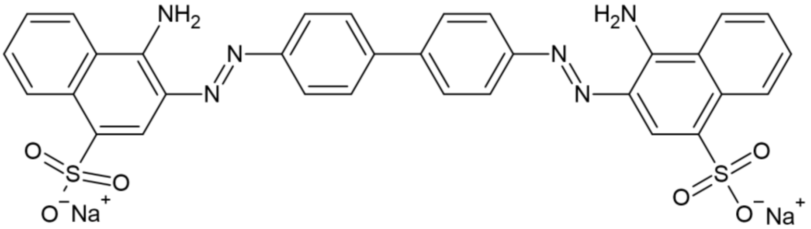

Figure 8. Chemical structure of Congo Red. The figure was made in ACD/ChemSketch.

3.2. Fluorescence spectroscopy

The processes associated with light absorption and emission can be described by a Jabłoński diagram (Fig. 9). Electrons in the ground singlet electronic state (S_0) have vibrational energy levels (0, 1, 2, …), where at room temperature the ground vibrational energy level is predominantly occupied. After light absorption, an electron can be excited to a higher singlet electronic state, and to a higher vibrational energy level. Excited electrons undergo internal conversion, that is, relaxation to the lowest vibrational state of the first singlet state. From the lowest vibrational energy level of S_1 electrons can return to S_0 by emitting the extra energy as a photon, in a process called fluorescence. S_1 electrons can also be converted to the first triplet state, T_1, by a process called intersystem crossing. T_1 electrons can return to the S_0 state via relaxation connected with light emission in a process called phosphorescence[208].

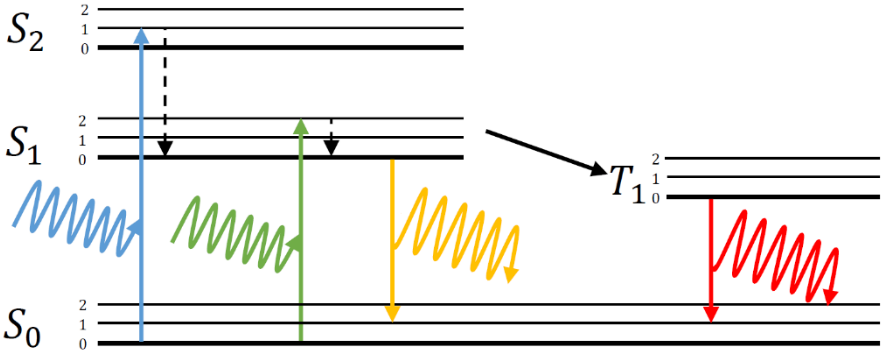

Figure 9. Schematic representation of a Jabłoński diagram. Adopted from *Principles of Fluorescence Spectroscopy* by J. R. Lakowicz[208].

Proteins have three fluorescent amino acids: tryptophan, tyrosine, and phenylalanine. Tryptophan residues, which are present in the metal-binding OR region of the PrP^C protein, can be used to study structural changes in the protein or peptide molecules. According to Burstein[209], tryptophan fluorescence spectra can be divided into five classes, each with different emission maxima (λ_m) due to differences in the local environment of tryptophan residues:

- class A (λ_m = 308 nm), where tryptophan residues are located in a structured fragment of a protein and do not form complexes with other residues or solvent molecules,
- class S (λ_m = 316 nm), where tryptophan residues are buried and in excited states can form hydrogen bonds with a single molecule,
- class I (λ_m = 330-332 nm), where tryptophan residues are buried and in excited states can form hydrogen bonds with two different molecules,
- class II (λ_m = 340-342 nm), where tryptophan residues are exposed to bound water molecules,
- class III (λ_m = 350-353 nm), where tryptophan residues are fully exposed to unbound water molecules.

Therefore, binding of metal ions to the flexible OR region by histidine residues should induce structural changes, and thereby shift the maximum of tryptophan fluorescence towards shorter wavelengths.

The tryptophan fluorescence can decrease due to either structural rearrangements in the peptide backbone, complex formation, or collisions with molecules in solution. A process resulting in a large decrease in fluorescence intensity is called quenching. The first trivial mechanism of fluorescence quenching is an inner filter effect, where the solute added to the protein absorbs light at wavelengths, corresponding to the excitation and/or fluorescence emission spectrum[210,211]. Two other non-trivial mechanisms of fluorescence intensity decrease are dynamic and static quenching. Dynamic quenching occurs when a quenching atom/molecule collides with a fluorophore (fluorescent compound) in its excited state. The fluorophore then returns to its ground state by transferring energy to the colliding unit without light emission. Static quenching can results from: (i) structural changes around the fluorophore, (ii) complex formation between a fluorophore in a ground-state and a quenching atom/molecule, and (iii) complex formation in an excited-state, called Förster resonance energy transfer (FRET). In FRET, energy is transferred from the fluorophore to the acceptor, therefore the fluorescence emission spectrum must overlap with the acceptor absorption spectrum, and the magnitude of this process depends on the distance between fluorophore and acceptor[208,210,211]. In PrP^C saturated with Cu(II) ions, each octapeptide repeat binds one Cu(II) ion, which is indirectly coordinated by the tryptophan residues via axially bound water molecules[82]. Cu(II) complexes with nitrogen and oxygen ligands absorb visible light with $\lambda_{max} \sim 540$ nm[212], which overlaps with the tryptophan emission spectrum[208]. Thus, the Cu(II) ions strongly quench the tryptophan fluorescence upon binding due to both structural changes around the tryptophan residues and FRET. Consequently, measurements of tryptophan fluorescence can be used to monitor Cu(II) binding to the OR domain. The Zn(II) ions are spectroscopically silent, therefore Zn(II) complexes does not absorb the light for wavelengths corresponding to tryptophan fluorescence, and the weak quenching effect of these complexes is caused only by structural changes around the tryptophan residues.

Fluorescence spectroscopy can also be used to monitor amyloid formation. Thioflavin T (ThT, 2-[4-(dimethylamino)phenyl]-3,6-dimethyl-1,3-benzothiazol-3-ium chloride, Fig. 10) is a benzothiazole dye that binds to the cross β-structure present in amyloids. Upon binding to amyloid material, the ThT excitation maximum shifts from 385 nm to 450 nm, and the emission maximum shifts from 445 nm to 482 nm, together with a significant increase in the fluorescence intensity. In solution, the ThT benzylamine and benzathiole rings can rotate around the central C-C bond, and this motion quenches the fluorescence signal. When bound to amyloid material, the aromatic rings can no longer rotate, resulting in increased fluorescence emission[213,214].

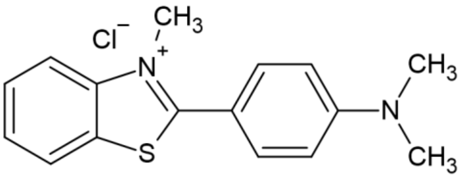

Figure 10. Chemical structure of Thioflavin T. The figure was made in ACD/ChemSketch.

3.3. Circular dichroism spectroscopy

Circular dichroism (CD) spectroscopy measures the difference between absorption of respectively left- and right-circularly polarized light. Only chiral molecules, i.e. those with a structure that cannot be superimposed on its mirror image, show different absorption of left and right circularly polarized light. By convention, molecules able to rotate polarized light counterclockwise are called levorotatory, and denoted with a minus (-) sign, while molecules able to rotate polarized light clockwise are called dextrorotatory, and denoted with a plus sign (+). Typical examples of chiral molecules are (R)-(-)-lactic acid and (S)-(+)-lactic acid (Fig. 11)[215].

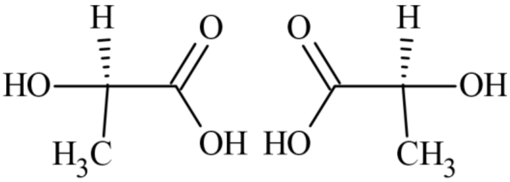

Figure 11. Chemical structures of (R)-(-)-lactic acid (on the left side) and (S)-(+)-lactic acid (on the right side). The figure was made in ACD/ChemSketch.

We can define the difference in absorbance as ΔA:

$$\Delta A = A_L - A_R \tag{5}$$

where A_L is the absorbance of left circularly polarized light, and A_R is absorbance of right circularly polarized light[216]. When $\Delta A \neq 0$, then light passing through the sample becomes elliptically polarized and can be detected in terms of ellipticity (θ) in millidegrees[217]:

$$\theta = \frac{32.98\,\Delta A}{1000} \qquad (6)$$

According to the Beer-Lambert law ΔA depends on the molar concentration, c, the pathlength of the sample, l, and molar CD, Δε:

$$\Delta A = \Delta\varepsilon c l \qquad (7)$$

Molar CD, Δε, is the difference between the molar extinction coefficients for left-, ε_L, and right-, ε_R, circularly polarized light[216]:

$$\Delta\varepsilon = \varepsilon_L - \varepsilon_R \qquad (8)$$

Therefore, ΔA can be expressed in units independent of concentration and pathlength. For proteins, ΔA is often expressed as Δε or mean residue ellipticity [θ]:

$$[\theta] = \frac{\theta \cdot MRW}{10 \cdot l \cdot c_p} \qquad (9)$$

where θ is the signal measured in millidegrees, MRW is mean residue weight of peptide or protein, l is the sample pathlength in centimeters, and c_p is the polypeptide concentration in milligrams per milliliter[218].

The amide group is the most abundant chiral chromophore in peptides and proteins. It absorbs light in the far ultraviolet at ~220 nm and at ~190 nm, which corresponds to $\pi^* \leftarrow$ n and $\pi^* \leftarrow \pi$ transitions respectively. As distinct protein secondary structures display different backbone conformations, which can be described by the polypeptide main chain dihedral angles ψ (between the N and C_α bonds) and φ (between the C_α and C bonds), they absorb circularly polarized light to a different extent. Each secondary structure absorbs circularly polarized light uniquely, resulting in a CD spectrum with a characteristic shape involving characteristic maxima and minima (Fig. 12). The CD spectrum of an entire protein can therefore be treated as a sum of the CD spectra of the elementary secondary structures present in the protein, and CD spectroscopy can be used to investigate a protein secondary structure[219,220].

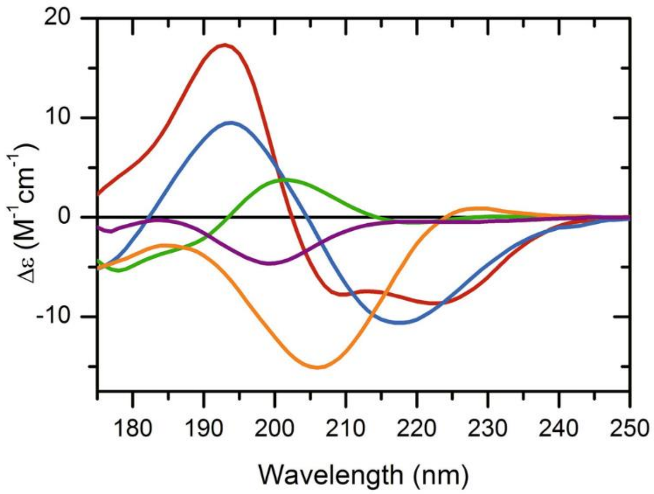

Figure 12. Far UV CD spectra for distinct protein secondary structures: α-helix (red), parallel β-sheet (blue), antiparallel β-sheet (green), polyproline-helix (orange), and disordered chain (purple). Figure comes from Micsonai et al.[221] under the terms of the Creative Commons Attribution 4.0 International License (http://creativecommons.org/licenses/by/4.0/).

3.4. Fourier-transformed infrared spectroscopy

Molecules are in constant motion, and vibrate in stretching, bending, rocking, wagging, and twisting modes. The frequency range for molecular vibrations is located in the infrared region (IR) of the electromagnetic radiation spectrum. The molecular bonds can absorb infrared light when the frequency of vibration and light is the same, and when bonds change dipole moment during vibration. The vibrational energy states are discrete, and can only have the permitted levels. For a harmonic oscillator:

$$E = \left(v + \frac{1}{2}\right)\hbar\sqrt{\frac{k}{m_{eff}}} \qquad v = 0, 1, 2, \dots \tag{10}$$

where ħ is the Planck constant divided by 2π, k is the force constant of the bond, and m_{eff} is the effective mass of atoms[202,203].

In Fourier-transformed infrared (FTIR) spectroscopy, the IR light is focused on a beam splitter. Half of the light beam is transmitted to a moving mirror, and the rest is reflected to a fixed mirror. Mirrors reflect the beams back to the beam splitter, where half of each beam travels to the detector. As two beams travel to the detector, they can interfere constructively or destructively, depending on the position of the moving mirror. The recorded spectrum as a function of the moving mirror distance is a Fourier transform of the IR spectrum. Calculating the inverse Fourier transform of this spectrum creates the standard IR absorption spectrum[222,223].

In a protein or peptide backbone, the peptide bond absorbs nine characteristic IR frequencies, called amide bands. Amide I extends from 1600 cm^{-1} to 1700 cm^{-1}, and it is a major band in the polypeptide IR spectrum. Amide I corresponds to C=O stretching vibrations, and it is sensitive to the secondary structure composition. Each type of secondary structure corresponds to different C=O stretching frequencies. Therefore, the amide I band is a convolution of IR spectra from different secondary structure motifs. Deconvolution of the amide I band by second-derivative analysis can be used to determine the secondary structure of a polypeptide[224].

3.5. Atomic force microscopy

Atomic force microscopy (AFM) is an experimental imaging technique used to record the topography of a sample deposited on a flat surface e.g. on a mica surface, ideally with sub-nanometer resolution. The previously described methods, i.e. UV-Vis, fluorescence, CD, and IR spectroscopy, are bulk techniques. Thus, when the sample is heterogeneous, as usually is the case with amyloid aggregates, they give only the average information on the sample. AFM is a single molecule technique, which allows individual molecules to be characterized in a heterogeneous sample. In amyloid research, AFM allows for visualization and characterization of the morphology of species present in the fibrillization process, such as monomers, dimers, oligomers, protofibrils, and mature fibrils. In case of early multimeric species, AFM is generally used to determine height and width, but for protofibrils it can also be used to analyze flexibility, and for mature fibrils it can be used to determine periodicity, packing of single protofilaments, and mechanical properties[225–228]. Modern high speed AFM units can even be used to study growth kinetics of the amyloid fibrils in a real time[229].

In AFM, a micrometer-sized cantilever scans the sample line by line. A small, sharp tip with a radius ideally smaller than 50 nm is placed at the end of a cantilever. When this tip interacts with the sample, a deflection is created in the cantilever. This deflection can be measured as a change in the reflection angle of a laser beam, focused on the cantilever, and this angle change can be converted to sample hight[222].

There are two main AFM operation modes: static and dynamic. In static mode, the tip is in close contact with the sample, and the cantilever bends due to repulsive interactions between the tip and the sample. During the scan, the tip force is kept constant by adjusting the distance between the tip and the sample. In dynamic mode, the tip oscillates a few nanometers over the sample surface, and is attracted to the sample by electrostatic and van der Waals forces. The dynamic mode can be divided into a tapping and a non-contact mode. In tapping mode, the oscillating tip is periodically in and out of contact with the sample, while in non-contact mode, the oscillating tip is attracted to the sample completely without physical contact[225,226].

3.6. Transmission electron microscopy

Transmission electron microscopy (TEM) is a robust experimental technique which is used in the entire field of science[230,231]. In the studies of amyloid deposits, TEM is frequently used to characterize the structure of amyloid fibrils. TEM can be used as a complementary method to AFM, and allows to resolve structural features of early aggregates, protofibrils, and mature fibrils, including width, length, or fibril twist[232].

In a traditional light microscope, the image resolution δ is proportional to the light wavelength, λ:

$$\delta \sim \lambda \tag{11}$$

and it is limited to ~200 nm. TEM overcomes this problem, by instead of a light beam using a beam of electrons. According to the de Broglie relation any particle traveling with a momentum, p, has a wavelength, λ:

$$\lambda = \frac{h}{p} \tag{12}$$

where h is the Planck constant. Thus, electrons accelerated with an electric potential difference, V, have a wavelength:

$$\lambda = \frac{h}{\sqrt{2m_e eV}} \tag{13}$$

where m_e is the electron mass, and e is the electron charge. For a potential difference of 40 kV, λ = 6.1 pm, which eliminates the problem of resolution[202].

A conventional TEM microscope uses thermionic emission of electrons, or field emission in an electron gun, and the electrons are accelerated in a vacuum by a high voltage. The electron beam is formed and focused on a sample by condenser electromagnets. Electrons can pass through the sample, or interact with it by elastic or inelastic scattering. The transmitted electron beam is focused by electromagnetic lenses on a CCD camera, and a digital image of the sample is generated[231]. Amyloid fibrils are hardly visible in standard TEM imaging, therefore the contrast has to be improved. Incoming electrons are scattered by the Coulomb potential of a nucleus, and therefore atoms with higher atomic numbers, like uranium or tungsten, scatter more electrons than e.g. carbon atoms. In the negative staining technique, a contrasting agent containing e.g. uranium or tungsten is deposited as a coating around the investigated structures in the sample, which a generates a good contrast to the background and also protects the sample from radiation damage[232,233]. With the recent advances in direct detection devices and sample cryo-fixation, cryo-electron microscopy (cryo-EM) has become the main imaging technique in structural biology, and it can be used to determine atomic structures of fibrils without negative staining[127,128].

3.7. Molecular dynamics simulations

To fully understand the function of a protein, knowledge of the 3D structure and dynamics is required. The atomic structures of proteins solved by X-ray crystallography give good, but static pictures of the protein structures, whereas NMR and to some extent also cryo-EM can provide information about both structures and the dynamic processes taking place in proteins[234,235]. When the protein is intrinsically disordered, or when it has intrinsically disordered regions, it is usually impossible to propose a single structural model due to the high mobility of the protein backbone[236,237]. Molecular dynamics (MD) simulations are a powerful method used in biophysics to predict how atoms constituting a protein will move as a function of time[234]. MD simulations can be used to investigate the protein folding, or conformational changes occurring in the protein during ligand binding, interactions with a lipid membrane, change of protonation state, and/or incorporations of specific mutations[234,238–240]. For example, understanding how a metal-bound PrP^C protein or OR peptide folds or misfolds, can give valuable insights in the molecular mechanisms causing TSE diseases.

During MD simulations, Newton's laws of motion are used to predict the positions of atoms as a function of time. In the first step, the initial model of a studied protein obtained from experimental studies, like X-ray crystallography or NMR, is solvated with explicit or implicit water molecules. Then the force vectors, $\mathbf{F}_i$ acting on the i^{th} atom are calculated as the negative derivative of the potential energy, V, with respect to i^{th} atom position vector, $\mathbf{r}_i$:

$$\boldsymbol{F}_i = -\frac{\partial V}{\partial \boldsymbol{r}_i} \tag{14}$$

The calculated force is used to update the position and velocity of the i^{th} atom, the force vectors are calculated from Eq. 14, and the whole process repeats. The potential energy is calculated using a molecular mechanics force-field, derived from a combination of quantum mechanical calculations and experimental studies[239,241,242]. The force-field potential V($\mathbf{r}$, s) can be split into two main parts: a potential of bonded interactions, V_{bon}($\mathbf{r}$, s), and a potential of nonbonded interactions, V_{nbon}($\mathbf{r}$, s):

$$V(\boldsymbol{r},s) = V_{bon}(\boldsymbol{r},s) + V_{nbon}(\boldsymbol{r},s) \qquad (15)$$

where s is the force field parameter. The potential of bonded interactions, V_{bon}($\mathbf{r}$, s) is a sum of the covalent bond stretching potential, V_{bond}($\mathbf{r}$, s), the potential of improper dihedral angles, V_{angle}($\mathbf{r}$, s), and the potential of torsion angles, $V_{torsion}$($\mathbf{r}$, s):

$$V_{bon}(\boldsymbol{r},s) = V_{bond}(\boldsymbol{r},s) + V_{angle}(\boldsymbol{r},s) + V_{torsion}(\boldsymbol{r},s) \qquad (16)$$

The potential of nonbonded interactions, V_{nbon}($\mathbf{r}$, s) is a sum of the Lennard-Jones potential, V_{LJ}($\mathbf{r}$, s), and the Coulomb potential, V_C($\mathbf{r}$, s)[242–245]:

$$V_{nbon}(\boldsymbol{r},s) = V_{LJ}(\boldsymbol{r},s) + V_C(\boldsymbol{r},s) \qquad (17)$$

3.8. Small angle X-ray scattering

Small angle X-ray scattering (SAXS) is a powerful technique, where the sample is illuminated with a monochromatic X-ray beam, usually from a high-brilliance laboratory source or a synchrotron, and scattered X-ray photons are collected at scattering angles (2θ) generally smaller than 5° (Fig. 13). In biological SAXS experiments, the scattering patterns for a protein in a buffer solution and for the pure buffer are collected separately, and the latter is subtracted from the former as a background signal. SAXS analysis of proteins and peptides allows to: (i) determine structural parameters, i.e. the radius of gyration (R_g), maximum particle dimension (D_{max}), (ii) reconstruct low resolution *ab initio* 3D shape, (iii) model missing fragments in protein crystal structures, (iv) determine oligomeric, and (v) conformational states[246].

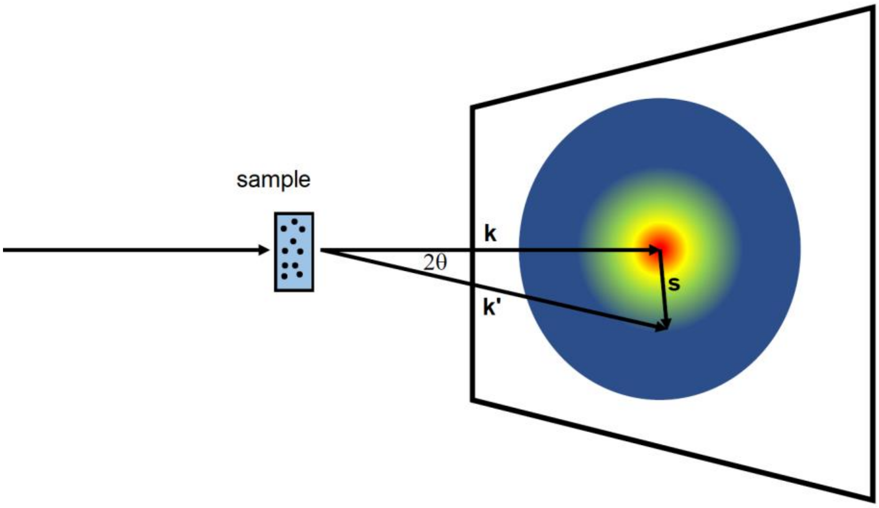

Figure 13. Schematic representation of a small angle X-ray scattering experiment. Adopted from Svergun et al.[246].

Let us consider a case of elastic scattering, where the wavelength of the scattered and the incident wave is the same. In SAXS a plane, monochromatic wave of X-ray radiation, **k**, incidents at a molecule. Electrons within the molecule become sources of spherical waves, **k’**. The scattering vector **s** is defined as (Fig. 13):

$$\boldsymbol{s} = \boldsymbol{k}' - \boldsymbol{k} \tag{18}$$

For molecules in a diluted solution the scattering is isotropic, i.e. the same in each direction:

$$|\boldsymbol{s}| = \frac{4\pi \, sin\theta}{\lambda} \tag{19}$$

where λ is wavelength of the incident X-ray beam, and θ is half of the scattering angle. For monodisperse, noninteracting molecules the scattering intensity, I(s), is an integral:

$$I(s) = 4\pi \int_0^{D_{max}} p(r) \frac{\sin{(sr)}}{sr} dr \tag{20}$$

where D_{max} is the maximum particle dimension, and p(r) is the intramolecular pair distance distribution function – a probability function of finding two scatterers at a distance r within a molecule. Therefore, the scattering data can be used to determine D_{max} of a molecule[246,247].

For compact, noninteracting particles the initial slope of the scattering curve can be approximated by a Guinier equation:

$$I(s) = I(0)e^{\frac{-s^2R_g^2}{3}} \tag{21}$$

where R_g is the radius of gyration. The Guinier approximation holds only for $s < 1/R_g$. Nevertheless, it allows calculation of scattering intensity at zero angle, I(0), and R_g from linear regression[246,247].

Scattering data contains low resolution (~2 nm) information, and can be used to determine the overall shape of a molecule *ab initio*. It can also be used to compare experimental SAXS curves with theoretical scattering profiles of atomic models (eg. From Protein Data Bank). For intrinsically disordered proteins, and proteins with intrinsically disordered regions, the sample is a polydisperse mixture of different conformers[246–248]. For a polydisperse sample consisting of a mixture of K different non-interacting molecules, the scattering curve is a linear sum of scattering intensities from each type of scatterer, i_k:

$$I(s) = \sum_{k=1}^{K} a_k i_k(s) \tag{22}$$

where a_k is the fraction of scatterer in solution. This equation can be used also in the case of shape polydispersity, where the sample contains particles with different shapes and sizes[246,247].

3.9. Fiber X-ray diffraction

Amyloid fibrils form one-dimensional structures with a crystal-like translational/rotational symmetry element parallel to the fibril axis[249]. In fiber X-ray diffraction, X-ray photons incident on a fiber, perpendicular to the fibril axis. The one-dimensional lattice of the amyloid fibrils reflects X-rays. When the reflected X-rays travel a distance of an integer number of wavelengths, they interfere constructively, resulting in a reflection on a detector. When the reflected X-rays travel a distance other than an integer number of wavelengths, they interfere destructively i.e. without reflection. Reflections are then observed at glancing angles, θ, that satisfy Bragg's law:

$$n\lambda = 2d\ sin(\theta) \tag{23}$$

where λ is the wavelength, d is the lattice spacing, and n is the order of reflection[202].

X-ray diffraction of aligned amyloid fibrils results in a specific X-ray diffraction pattern, called the cross-β pattern, which arises from β-strands ordered perpendicular to the fibril axis. This pattern contains two sets of characteristic reflexes: meridional and equatorial. The meridional reflexes are present at ~ 4.7 Å – 8 Å, and they correspond to the distances between the β-strands ordered parallel to the fibril axis. The equatorial reflexes are present at ~10 Å – 12 Å, and they correspond to distances between repeating elements in the fibril structure, organized perpendicular to the fibril axis[250–253].

Fiber X-ray diffraction patterns with both meridional and equatorial diffraction rings can confirm the presence of amyloid fibrils with a cross-β structure. Moreover, high quality diffraction patterns of ordered amyloid fibrils can be used to propose an atomic-level structural model[127,250,251].

4. Cu(II) and Zn(II) binding to the octarepeat fragment of PrP^{C}

4.1. The octarepeat fragment of PrP^{C} forms amyloid structures in the presence of Zn(II) ions (Paper I)

In order to investigate the structural changes induced by the Zn(II) binding to the PrP(58-93) peptide (Fig. 14, from here onwards: OR) I started with CD spectroscopy. The CD spectrum of OR peptide is well documented in the literature and shows a strong negative band at 200 nm, and a weak positive band at 225 nm[36,38,61,74,75]. This spectrum is interpreted as a mixture of random coil and polyproline II (PPII) helix secondary structure[36,38]. The direct addition of Zn(II) ions to the OR peptide resulted in a loss of the CD signal, which was attributed to peptide precipitation or aggregation.

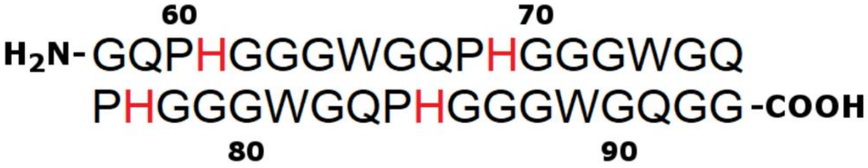

Figure 14. Sequence of the PrP$^{58\text{-}93}$ (OR) peptide. Possible metal-binding histidine residues are shown in red.

The ThT and CR assays confirmed that OR peptide does not form β-strand structures on its own over time. However, addition of Zn(II) ions resulted in a rapid increase of ThT fluorescence, and CR absorbance. This result is typical for formation of amyloid β-strand structures. The amide I band, monitored by ATR-FTIR spectroscopy, showed a shift toward shorter wavelengths after addition of Zn(II) ions. Second-derivative analysis of FTIR spectra suggested a reduction in the amount of PPII helix and formation of β-sheet secondary structure. AFM imaging of OR peptide incubated with Zn(II) ions for 24 h revealed the presence of single fibrils, as well as spherical oligomers. The fibrils height ranged from 1.5 to 1.8 nm, and they were directly connected to spherical oligomers, a possible centers for nucleation. Fibrils had lateral branches, which is indicative for a secondary nucleation. The presence of fibrillar structures was also confirmed by TEM images. X-ray diffraction on fibrillar structures confirmed the presence of the cross-β structure, characteristic for amyloid fibrils. The SAXS analysis of *apo* OR peptide suggested a presence of two predominant conformers: compact with multiple loops, and extended with properties of PPII helix. Addition of Zn(II) ions to the OR peptide resulted in sample aggregation. In order to analyze the SAXS curves for aggregated, polydisperse samples, the shape of *apo* OR peptide was approximated as a spheroid, and the shape of fibrils was approximated as a cylinder. Treating the sample as a mixture of two components suggested that Zn(II) binding to OR peptide decreases the fraction of monomers and increases the fraction of fibrils. Therefore metal ion binding is a primary event responsible for fibril formation.

4.2. The octarepeat fragment of PrP^C forms β-hairpin structures upon metal ion binding (Paper II)

The previous studies on OR peptide suggested that it possesses a random coil secondary structure together with PPII helix and/or β-turns[36,38,40,41,74,75]. To investigate the inner secondary structure of the OR peptide, CD thermal unfolding experiments were performed. An isodichroic point at 204 nm, present at 20 - 65 °C range, suggested a PPII helix to random coil transition, and it was estimated that ~45% of OR peptide adopts a PPII helix at 37 °C temperature.

Earlier CD studies on Cu(II) binding to OR peptide in water suggested formation of β-turns or structured loops[74,75]. I was able to recreate those experiments, however in our interpretation Cu(II) binding to OR peptide results in the formation of an antiparallel β-sheet secondary structure. CD titrations of OR peptide with Cu(II) in a phosphate buffer, pH 7.5 also suggested formation of β-sheet secondary structure. In our interpretation up to 1:1 OR peptide:Cu(II) molar ratio β-turns are being formed, where above 1:1 molar ratio relaxed antiparallel β-sheet structures are being formed. The changes in the secondary structure saturated at 1:4 OR:Cu(II) ratio, suggesting binding of four Cu(II) ions by one OR peptide, which is consistent with previous studies. The changes in secondary structure were used to determine the apparent dissociation constants for Cu(II) binding. For the first Cu(II) ion K_{d1} was ~0.5 μM, for the second Cu(II) ion K_{d2} ~7 μM, where for third and fourth Cu(II) ions K_{d3} was ~20 μM. Zn(II) ions induced changes in OR peptide CD spectrum, similar to those observed for Cu(II) ions, and were interpreted as formation of an antiparallel β-sheet secondary structure, however, possibly with a different geometry. Partial saturation of CD signal at 1:2 OR:Zn(II) molar ratio was interpreted as binding of two Zn(II) ions to a OR peptide. The calculated apparent K_d values were slightly lower for Zn(II), than for Cu(II) ions.

Copper ions were able to quench the OR peptide intrinsic tryptophan fluorescence at pH 7.5, with the apparent K_d of ~4.5 μM, probably corresponding to the average K_d value of three different Cu(II) binding modes. Under acidic conditions, pH 5.5, the apparent K_d was ~7.5 μM, and suggested weaker binding due to protonation of histidine residues. Zn(II) ions also quenched tryptophan fluorescence at pH 7.5, however the low signal to noise ratio did not allow us to calculate the K_d. On the other hand, Zn(II) ions were unable to quench the tryptophan fluorescence at pH 5.5, which implies no Zn(II) binding to OR peptide at acidic conditions.

During molecular dynamics simulations of OR peptide with a single metal ion, the OR peptide mainchain formed a β-hairpin structure, located in the N-terminal, or C-terminal region for Cu(II) and Zn(II) ion respectively. When simulated with two Cu(II) and two Zn(II) ions the OR polypeptide mainchain formed multiple β-hairpin structures enclosed by histidine bound metal ion. Interestingly in simulations with two metal ions OR peptide main chain frequently formed β-structures, which is consistent with CD studies. The residues Gln67-Gly70 and Gly74-Pro76 showed the highest propensity towards formation of β-structures and were proposed as a core of OR amyloid fibrils. On the other hand, simulation of two OR molecules with a single Cu(II) ion revealed a stable intermolecular conformation over time, which may be a first step towards aggregation and fibril formation.

In summary, the secondary structure of OR peptide is a combination of random coil and PPII helix. OR peptide binds up to four Cu(II) ions or two Zn(II) ions. The first metal ion binds with apparent K_d of ~500 nM, and next ions bind with low micromolar K_d. Metal ion binding to OR peptide up to 1:1 molar ratio results in formation of β-turn secondary structure, where above 1:1 molar ratio results in formation of antiparallel β-sheet secondary structure, beneficial for amyloid formation. A single metal cation can be coordinated by histidine residues from two different OR molecules, what might be a first step toward aggregation and fibril formation.

5. Zn(II) binding to the human prion protein

5.1. Zn(II) binding causes interdomain changes in the structure and flexibility of the human prion protein (Paper III)

In **Paper III** we studied interaction between full length human prion protein and Zn(II) ions. CD titrations revealed an isodichroic point at 242 nm, interpreted as a distortion of α-helices 2 and 3 with simultaneous formation of β-like motifs around the Zn(II)-bound octarepeat region. The distortion of α-helices suggested interdomain interactions between Zn(II)-bound octarepeat region and the C-terminal domain. The structural transition was used to determine the apparent dissociation constant for PrP^C-Zn(II) complex, which in phosphate buffer, pH 7.4 was ~12 μM.

Zn(II) ions were able to quench PrP^C intrinsic tryptophan fluorescence, with apparent K_d of ~17 μM and a blue shift in fluorescence emission maximum. The shift in fluorescence maximum was interpreted as change in tryptophan environment, from fully exposed to the solvent, to buried, and exposed to bound water molecules.

The two dimensional ^{1}H-^{15}N HSQC NMR solution spectra and ^{15}N spin-spin relaxation rates for PrP^C-Zn(II) complex showed reduced values for residues corresponding to α-helices 2 and 3, interpreted as increased local dynamics of the protein mainchain. NMR diffusion data showed increased value of the translational diffusion coefficient for PrP^C, when bound to Zn(II). Increased value of translational diffusion coefficient was interpreted as a more compact PrP^C structure, due to interdomain interaction between Zn(II)-bound octarepeat region and C-terminal domain.

Molecular dynamics simulations suggested a different folding path for *apo* and Zn(II)-bound PrP^C, where in the latter Zn(II) ions indirectly stabilized C-terminal fragment of α-helix 3. Analysis of our SAXS data with the ensemble approach, commonly used for proteins with intrinsically disordered domains[248,254], together with changes in the maximum particle diameter suggested a more compact PrP^C fold, when bound to Zn(II) ions.

In previous studies Zn(II) ions at concentration around or below 100 μM resulted in endocytosis of PrP^C from the cell surface[66,255] and increased Zn(II) uptake into neuronal cells[96], what was in line with our calculated K_d values. As Zn(II) ions seem to inhibit PrP^C conversion to amyloid fibrils[139], it may be a consequence of observed interdomain interactions between Zn(II)-bound octarepeat domain and a C-terminal domain.

6. Interaction between human PrP^C and designed cell penetrating peptide

6.1. The engineered NCAM1-Aβ peptide construct inhibits fibril formation by the human prion protein (Paper IV)

So far no therapeutic agents for TSEs are available[256]. In **Paper IV** I have investigated a possible effect of NCAM1(1-19)-KKLVFF as a modulator of PrP^C aggregation, and fibrillization. The bioengineered

NCAM1(1-19)-KKLVFF (from here onwards: NCAM1-Aβ) peptide contains the N-terminal secretion signal fragment of mouse NCAM1 protein (residues 1-19), the KLVFF fragment of the Aβ peptide (residues 16-20) and an additional lysine residue to increase solubility. NCAM1 is a plasma membrane-anchored glycoprotein and it interacts with PrP at the neuronal cell surface[150,151]. The KLVFF sequence was chosen as it inhibits aggregation of the full-length Aβ peptide[257]. AFM images of PrP^C incubated with 2 M urea at 50 °C for 8 hours showed the presence of long fibrils, with heights between 3 and 4 nm, and large aggregate clumps. NCAM1-Aβ incubated for 8 hours formed small aggregate clumps and mature fibrils with heights between 2 and 3 nm. PrP^C incubated together with NCAM1-Aβ for up to 72 hours formed only small aggregate clumps with heights around 3 to 4 nm. **The results were interpreted as a direct interaction between PrP^C and the NCAM1-Aβ peptide, interfering with PrP^C aggregation, probably involving hydrophobic forces.** Therefore NCAM1-Aβ constructs can be potentially used as a TSE drugs.

7. Conclusions

Using multiple, complementary biophysical methods, ranging from experimental techniques, including spectroscopy, microscopy, and scattering to theoretical computations, it was shown that metal ion binding and interactions with bioengineered NCAM1-Aβ peptide alters PrP^C folding and aggregation. Based on our findings, I conclude that:

- The isolated OR fragment of PrP^C binds up to four Cu(II) and two Zn(II) ions.
- The first metal ion binds with a nanomolar apparent dissociation constant, and the next metal ions bind with micromolar apparent dissociation constants.
- Binding of the first metal ion by the OR peptide results in formation of β-turn secondary structure, and binding of subsequent metal ions results in formation of antiparallel β-sheet secondary structure.
- Excess of metal ion to OR peptide ratio results in amyloid fibril formation.
- β-hairpin structures formed in the presence of metal ions may be the intermediates in amyloid formation.
- Full length PrP^C binds Zn(II) ions with a low micromolar dissociation constant.
- Zn(II)-bound PrP^C follows a different folding path compared to PrP^C alone.
- Intramolecular interactions between Zn(II)-bound OR region and C-terminal domain of PrP^C appears to inhibit fibril formation.
- The designed cell penetrating NCAM1-Aβ peptide construct interacts with PrP^C and interferes with fibril formation.

8. References

1. Greenlee, J. J. Review: Update on Classical and Atypical Scrapie in Sheep and Goats. *Vet Pathol* **56**, 6–16 (2019).
2. Prusiner, S. B. Nobel Lecture: Prions. *Proceedings of the National Academy of Sciences* **95**, 13363–13383 (1998).
3. Prusiner, S. Novel proteinaceous infectious particles cause scrapie. *Science* **216**, 136–144 (1982).
4. Cobb, M. 60 years ago, Francis Crick changed the logic of biology. *PLoS Biol* **15**, e2003243 (2017).
5. Salès, N. *et al.* Cellular prion protein localization in rodent and primate brain: PrP ^{c} brain localization. *European Journal of Neuroscience* **10**, 2464–2471 (1998).
6. Imran, M. & Mahmood, S. An overview of animal prion diseases. *Virol J* **8**, 493 (2011).
7. Imran, M. & Mahmood, S. An overview of human prion diseases. *Virol J* **8**, 559 (2011).
8. Wang, H., Rhoads, D. D. & Appleby, B. S. Human prion diseases: *Current Opinion in Infectious Diseases* **32**, 272–276 (2019).
9. Soto, C. Prion hypothesis: the end of the controversy? *Trends in Biochemical Sciences* **36**, 151–158 (2011).
10. Castilla, J. *et al.* Crossing the Species Barrier by PrPSc Replication In Vitro Generates Unique Infectious Prions. *Cell* **134**, 757–768 (2008).
11. Houston, F. & Andréoletti, O. Animal prion diseases: the risks to human health: Animal prion diseases. *Brain Pathol* **29**, 248–262 (2019).
12. Chen, C. & Dong, X.-P. Epidemiological characteristics of human prion diseases. *Infect Dis Poverty* **5**, 47 (2016).
13. Scialò, C., De Cecco, E., Manganotti, P. & Legname, G. Prion and Prion-Like Protein Strains: Deciphering the Molecular Basis of Heterogeneity in Neurodegeneration. *Viruses* **11**, 261 (2019).
14. Ma, J., Gao, J., Wang, J. & Xie, A. Prion-Like Mechanisms in Parkinson's Disease. *Front. Neurosci.* **13**, 552 (2019).
15. Walker, L. C. Prion-like mechanisms in Alzheimer disease. in *Handbook of Clinical Neurology* vol. 153 303–319 (Elsevier, 2018).
16. Mukherjee, A. & Soto, C. Prion-Like Protein Aggregates and Type 2 Diabetes. *Cold Spring Harb Perspect Med* **7**, a024315 (2017).
17. Salzano, G., Giachin, G. & Legname, G. Structural Consequences of Copper Binding to the Prion Protein. *Cells* **8**, 770 (2019).
18. Millhauser, G. L. Copper and the Prion Protein: Methods, Structures, Function, and Disease. *Annu. Rev. Phys. Chem.* **58**, 299–320 (2007).
19. Watt, N. T., Griffiths, H. H. & Hooper, N. M. Neuronal zinc regulation and the prion protein. *Prion* **7**, 203–208 (2013).
20. Toni, M., Massimino, M. L., De Mario, A., Angiulli, E. & Spisni, E. Metal Dyshomeostasis and Their Pathological Role in Prion and Prion-Like Diseases: The Basis for a Nutritional Approach. *Front. Neurosci.* **11**, (2017).
21. Kawahara, M., Tanaka, K. & Mizuno, D. Disruption of Metal Homeostasis and the Pathogenesis of Prion Diseases. in *Prion - An Overview* (ed. Tutar, Y.) (InTech, 2017). doi:10.5772/67327.
22. Söderberg, K. L., Guterstam, P., Langel, Ü. & Gräslund, A. Targeting prion propagation using peptide constructs with signal sequence motifs. *Archives of Biochemistry and Biophysics* **564**, 254–261 (2014).

23. Löfgren, K. *et al.* Antiprion properties of prion protein-derived cell-penetrating peptides. *FASEB j.* **22**, 2177–2184 (2008).
24. Eliezer, D. Biophysical characterization of intrinsically disordered proteins. *Current Opinion in Structural Biology* **19**, 23–30 (2009).
25. Basler, K. *et al.* Scrapie and cellular PrP isoforms are encoded by the same chromosomal gene. *Cell* **46**, 417–428 (1986).
26. Oesch, B. *et al.* A cellular gene encodes scrapie PrP 27-30 protein. *Cell* **40**, 735–746 (1985).
27. Sparkes, R. S. *et al.* Assignment of the human and mouse prion protein genes to homologous chromosomes. *Proceedings of the National Academy of Sciences* **83**, 7358–7362 (1986).
28. Zahn, R. *et al.* NMR solution structure of the human prion protein. *Proceedings of the National Academy of Sciences* **97**, 145–150 (2000).
29. Puig, B., Altmeppen, H. & Glatzel, M. The GPI-anchoring of PrP: Implications in sorting and pathogenesis. *Prion* **8**, 11–18 (2014).
30. Stahl, N. Scrapie prion protein contains a phosphatidylinositol glycolipid. *Cell* **51**, 229–240 (1987).
31. Rudd, P. Glycosylation and prion protein. *Current Opinion in Structural Biology* **12**, 578–586 (2002).
32. Rudd, P. M., Wormald, M. R., Wing, D. R., Prusiner, S. B. & Dwek, R. A. Prion Glycoprotein: Structure, Dynamics, and Roles for the Sugars. *Biochemistry* **40**, 3759–3766 (2001).
33. Mangé, A. *et al.* Alpha- and beta- cleavages of the amino-terminus of the cellular prion protein. *Biology of the Cell* **96**, 125–132 (2004).
34. Liang, J. & Kong, Q. α-Cleavage of cellular prion protein. *Prion* **6**, 453–460 (2012).
35. Gill, A. C. Post-translational hydroxylation at the N-terminus of the prion protein reveals presence of PPII structure in vivo. *The EMBO Journal* **19**, 5324–5331 (2000).
36. Smith, C. J. *et al.* Conformational properties of the prion octa-repeat and hydrophobic sequences. *FEBS Letters* **405**, 378–384 (1997).
37. Whittal, R. M. *et al.* Copper binding to octarepeat peptides of the prion protein monitored by mass spectrometry. *Protein Science* **9**, 332–343 (2000).
38. Di Natale, G. *et al.* Membrane Interactions and Conformational Preferences of Human and Avian Prion N-Terminal Tandem Repeats: The Role of Copper(II) Ions, pH, and Membrane Mimicking Environments. *J. Phys. Chem. B* **114**, 13830–13838 (2010).
39. Chebrek, R., Leonard, S., de Brevern, A. G. & Gelly, J.-C. PolyprOnline: polyproline helix II and secondary structure assignment database. *Database* **2014**, bau102–bau102 (2014).
40. Zahn, R. The Octapeptide Repeats in Mammalian Prion Protein Constitute a pH-dependent Folding and Aggregation Site. *Journal of Molecular Biology* **334**, 477–488 (2003).
41. Taubner, L. M., Bienkiewicz, E. A., Copié, V. & Caughey, B. Structure of the Flexible Amino-Terminal Domain of Prion Protein Bound to a Sulfated Glycan. *Journal of Molecular Biology* **395**, 475–490 (2010).
42. Lee, S. *et al.* Conformational diversity in prion protein variants influences intermolecular β-sheet formation. *EMBO J* **29**, 251–262 (2010).
43. Donne, D. G. *et al.* Structure of the recombinant full-length hamster prion protein PrP(29-231): The N terminus is highly flexible. *Proceedings of the National Academy of Sciences* **94**, 13452–13457 (1997).

44. Castle, A. R. & Gill, A. C. Physiological Functions of the Cellular Prion Protein. *Front. Mol. Biosci.* **4**, (2017).
45. Šišková, Z., Reynolds, R. A., O'Connor, V. & Perry, V. H. Brain Region Specific Pre-Synaptic and Post-Synaptic Degeneration Are Early Components of Neuropathology in Prion Disease. *PLoS ONE* **8**, e55004 (2013).
46. Prusiner, S. B. *et al.* Ablation of the prion protein (PrP) gene in mice prevents scrapie and facilitates production of anti-PrP antibodies. *Proceedings of the National Academy of Sciences* **90**, 10608–10612 (1993).
47. Manson, J. C. *et al.* 129/Ola mice carrying a null mutation in PrP that abolishes mRNA production are developmentally normal. *Mol Neurobiol* **8**, 121–127 (1994).
48. Büeler, H. *et al.* Normal development and behaviour of mice lacking the neuronal cell-surface PrP protein. *Nature* **356**, 577–582 (1992).
49. Tobler, I. *et al.* Altered circadian activity rhythms and sleep in mice devoid of prion protein. *Nature* **380**, 639–642 (1996).
50. Wulf, M.-A., Senatore, A. & Aguzzi, A. The biological function of the cellular prion protein: an update. *BMC Biol* **15**, 34 (2017).
51. Bremer, J. *et al.* Axonal prion protein is required for peripheral myelin maintenance. *Nat Neurosci* **13**, 310–318 (2010).
52. Schmitt-Ulms, G., Ehsani, S., Watts, J. C., Westaway, D. & Wille, H. Evolutionary Descent of Prion Genes from the ZIP Family of Metal Ion Transporters. *PLoS ONE* **4**, e7208 (2009).
53. Jackson, G. S. *et al.* Location and properties of metal-binding sites on the human prion protein. *Proceedings of the National Academy of Sciences* **98**, 8531–8535 (2001).
54. Roucou, X., Gains, M. & LeBlanc, A. C. Neuroprotective functions of prion protein. *J Neurosci Res* **75**, 153–161 (2004).
55. Kardos, J. *et al.* Copper signalling: causes and consequences. *Cell Commun Signal* **16**, 71 (2018).
56. D'Ambrosi, N. & Rossi, L. Copper at synapse: Release, binding and modulation of neurotransmission. *Neurochemistry International* **90**, 36–45 (2015).
57. Hopt, A. *et al.* Methods for studying synaptosomal copper release. *Journal of Neuroscience Methods* **128**, 159–172 (2003).
58. Kardos, J., Kovács, I., Hajós, F., Kálmán, M. & Simonyi, M. Nerve endings from rat brain tissue release copper upon depolarization. A possible role in regulating neuronal excitability. *Neuroscience Letters* **103**, 139–144 (1989).
59. Palumaa, P. Copper chaperones. The concept of conformational control in the metabolism of copper. *FEBS Letters* **587**, 1902–1910 (2013).
60. Brown, D. R. *et al.* The cellular prion protein binds copper in vivo. *Nature* **390**, 684–687 (1997).
61. Younan, N. D. *et al.* Copper(II)-Induced Secondary Structure Changes and Reduced Folding Stability of the Prion Protein. *Journal of Molecular Biology* **410**, 369–382 (2011).
62. Burns, C. S. *et al.* Copper coordination in the full-length, recombinant prion protein. *Biochemistry* **42**, 6794–6803 (2003).
63. Kramer, M. L. *et al.* Prion Protein Binds Copper within the Physiological Concentration Range. *J. Biol. Chem.* **276**, 16711–16719 (2001).
64. Herms, J. *et al.* Evidence of Presynaptic Location and Function of the Prion Protein. *J. Neurosci.* **19**, 8866–8875 (1999).

65. Lee, K. S. *et al.* Internalization of mammalian fluorescent cellular prion protein and N-terminal deletion mutants in living cells: GFP-PrPc internalization in living cells. *Journal of Neurochemistry* **79**, 79–87 (2008).
66. Pauly, P. C. & Harris, D. A. Copper Stimulates Endocytosis of the Prion Protein. *J. Biol. Chem.* **273**, 33107–33110 (1998).
67. Perera, W. S. S. & Hooper, N. M. Ablation of the metal ion-induced endocytosis of the prion protein by disease-associated mutation of the octarepeat region. *Current Biology* **11**, 519–523 (2001).
68. Varela-Nallar, L. *et al.* Induction of cellular prion protein gene expression by copper in neurons. *American Journal of Physiology-Cell Physiology* **290**, C271–C281 (2006).
69. Millhauser, G. L. Copper Binding in the Prion Protein †. *Acc. Chem. Res.* **37**, 79–85 (2004).
70. Rachidi, W. *et al.* Expression of Prion Protein Increases Cellular Copper Binding and Antioxidant Enzyme Activities but Not Copper Delivery. *Journal of Biological Chemistry* **278**, 9064–9072 (2003).
71. Brown, D. R., Schmidt, B. & Kretzschmar, H. A. Effects of Copper on Survival of Prion Protein Knockout Neurons and Glia. *Journal of Neurochemistry* **70**, 1686–1693 (2002).
72. Viles, J. H., Klewpatinond, M. & Nadal, R. C. Copper and the structural biology of the prion protein. *Biochemical Society Transactions* **36**, 1288–1292 (2008).
73. Klewpatinond, M., Davies, P., Bowen, S., Brown, D. R. & Viles, J. H. Deconvoluting the Cu2+ Binding Modes of Full-length Prion Protein*. *Journal of Biological Chemistry* **283**, 1870–1881 (2008).
74. Garnett, A. P. & Viles, J. H. Copper Binding to the Octarepeats of the Prion Protein: AFFINITY, SPECIFICITY, FOLDING, AND COOPERATIVITY: INSIGHTS FROM CIRCULAR DICHROISM. *J. Biol. Chem.* **278**, 6795–6802 (2003).
75. Viles, J. H. *et al.* Copper binding to the prion protein: Structural implications of four identical cooperative binding sites. *Proceedings of the National Academy of Sciences* **96**, 2042–2047 (1999).
76. Chattopadhyay, M. *et al.* The Octarepeat Domain of the Prion Protein Binds Cu(II) with Three Distinct Coordination Modes at pH 7.4. *J. Am. Chem. Soc.* **127**, 12647–12656 (2005).
77. Pushie, M. J., Rauk, A., Jirik, F. R. & Vogel, H. J. Can copper binding to the prion protein generate a misfolded form of the protein? *Biometals* **22**, 159–175 (2009).
78. Wells, M. A. *et al.* Multiple forms of copper (II) co-ordination occur throughout the disordered N-terminal region of the prion protein at pH 7.4. *Biochemical Journal* **400**, 501–510 (2006).
79. Walter, E. D., Chattopadhyay, M. & Millhauser, G. L. The Affinity of Copper Binding to the Prion Protein Octarepeat Domain: Evidence for Negative Cooperativity †. *Biochemistry* **45**, 13083–13092 (2006).
80. del Pino, P. *et al.* The configuration of the Cu2+ binding region in full-length human prion protein. *Eur Biophys J* **36**, 239–252 (2007).
81. Morante, S. *et al.* Inter- and Intra-octarepeat Cu(II) Site Geometries in the Prion Protein. *Journal of Biological Chemistry* **279**, 11753–11759 (2004).
82. Burns, C. S. *et al.* Molecular Features of the Copper Binding Sites in the Octarepeat Domain of the Prion Protein †. *Biochemistry* **41**, 3991–4001 (2002).

83. Pushie, M. J. & Vogel, H. J. Molecular Dynamics Simulations of Two Tandem Octarepeats from the Mammalian Prion Protein: Fully Cu2+-bound and Metal-Free Forms. *Biophysical Journal* **93**, 3762–3774 (2007).
84. Jones, C. E., Klewpatinond, M., Abdelraheim, S. R., Brown, D. R. & Viles, J. H. Probing Copper2+ Binding to the Prion Protein Using Diamagnetic Nickel2+ and 1H NMR: The Unstructured N terminus Facilitates the Coordination of Six Copper2+ Ions at Physiological Concentrations. *Journal of Molecular Biology* **346**, 1393–1407 (2005).
85. Gralka, E. *et al.* CuII binding sites located at His-96 and His-111 of the human prion protein: thermodynamic and spectroscopic studies on model peptides. *Dalton Trans.* 5207 (2008) doi:10.1039/b806192k.
86. Remelli, M. *et al.* Thermodynamic and spectroscopic investigation on the role of Met residues in CuII binding to the non-octarepeat site of the human prion protein. *Metallomics* **4**, 794 (2012).
87. Jones, C. E., Abdelraheim, S. R., Brown, D. R. & Viles, J. H. Preferential Cu2+ Coordination by His96 and His111 Induces β-Sheet Formation in the Unstructured Amyloidogenic Region of the Prion Protein. *Journal of Biological Chemistry* **279**, 32018–32027 (2004).
88. Klewpatinond, M. & Viles, J. H. Fragment length influences affinity for Cu2+ and Ni2+ binding to His96 or His111 of the prion protein and spectroscopic evidence for a multiple histidine binding only at low pH. *Biochemical Journal* **404**, 393–402 (2007).
89. Evans, E. G. B., Pushie, M. J., Markham, K. A., Lee, H.-W. & Millhauser, G. L. Interaction between Prion Protein's Copper-Bound Octarepeat Domain and a Charged C-Terminal Pocket Suggests a Mechanism for N-Terminal Regulation. *Structure* **24**, 1057–1067 (2016).
90. McDonald, A. J. *et al.* Altered Domain Structure of the Prion Protein Caused by Cu2+ Binding and Functionally Relevant Mutations: Analysis by Cross-Linking, MS/MS, and NMR. *Structure* **27**, 907-922.e5 (2019).
91. Thakur, A. K., Srivastava, A. K., Srinivas, V., Chary, K. V. R. & Rao, C. M. Copper Alters Aggregation Behavior of Prion Protein and Induces Novel Interactions between Its N- and C-terminal Regions. *J. Biol. Chem.* **286**, 38533–38545 (2011).
92. Kambe, T., Tsuji, T., Hashimoto, A. & Itsumura, N. The Physiological, Biochemical, and Molecular Roles of Zinc Transporters in Zinc Homeostasis and Metabolism. *Physiological Reviews* **95**, 749–784 (2015).
93. Mocchegiani, E., Bertoni-Freddari, C., Marcellini, F. & Malavolta, M. Brain, aging and neurodegeneration: Role of zinc ion availability. *Progress in Neurobiology* **75**, 367–390 (2005).
94. Vogt, K., Mellor, J., Tong, G. & Nicoll, R. The Actions of Synaptically Released Zinc at Hippocampal Mossy Fiber Synapses. *Neuron* **26**, 187–196 (2000).
95. Assaf, S. Y. & Chung, S.-H. Release of endogenous Zn2+ from brain tissue during activity. *Nature* **308**, 734–736 (1984).
96. Watt, N. T. *et al.* Prion protein facilitates uptake of zinc into neuronal cells. *Nat Commun* **3**, 1134 (2012).
97. Pushie, M. J. *et al.* Prion protein expression level alters regional copper, iron and zinc content in the mouse brain. *Metallomics* **3**, 206 (2011).
98. Walter, E. D., Stevens, D. J., Visconte, M. P. & Millhauser, G. L. The Prion Protein is a Combined Zinc and Copper Binding Protein: Zn $^{2+}$ Alters the Distribution of Cu $^{2+}$ Coordination Modes. *J. Am. Chem. Soc.* **129**, 15440–15441 (2007).

99. Markham, K. A., Roseman, G. P., Linsley, R. B., Lee, H.-W. & Millhauser, G. L. Molecular Features of the Zn2+ Binding Site in the Prion Protein Probed by 113Cd NMR. *Biophysical Journal* **116**, 610–620 (2019).
100. Spevacek, A. R. *et al.* Zinc Drives a Tertiary Fold in the Prion Protein with Familial Disease Mutation Sites at the Interface. *Structure* **21**, 236–246 (2013).
101. Pushie, M. J., Nienaber, K. H., McDonald, A., Millhauser, G. L. & George, G. N. Combined EXAFS and DFT Structure Calculations Provide Structural Insights into the 1:1 Multi-Histidine Complexes of Cu ^{II} , Cu ^{I} , and Zn ^{II} with the Tandem Octarepeats of the Mammalian Prion Protein. *Chem. Eur. J.* **20**, 9770–9783 (2014).
102. Pan, K. M. *et al.* Conversion of alpha-helices into beta-sheets features in the formation of the scrapie prion proteins. *PNAS* **90**, 10962–10966 (1993).
103. Safar, J., Roller, P. P., Gajdusek, D. C. & Gibbs, C. J. Thermal stability and conformational transitions of scrapie amyloid (prion) protein correlate with infectivity. *Protein Sci.* **2**, 2206–2216 (1993).
104. Bolton, D., McKinley, M. & Prusiner, S. Identification of a protein that purifies with the scrapie prion. *Science* **218**, 1309–1311 (1982).
105. Scheckel, C. & Aguzzi, A. Prions, prionoids and protein misfolding disorders. *Nat Rev Genet* **19**, 405–418 (2018).
106. Collinge, J. Mammalian prions and their wider relevance in neurodegenerative diseases. *Nature* **539**, 217–226 (2016).
107. Chiti, F. & Dobson, C. M. Protein Misfolding, Amyloid Formation, and Human Disease: A Summary of Progress Over the Last Decade. *Annu. Rev. Biochem.* **86**, 27–68 (2017).
108. Griffith, J. S. Nature of the Scrapie Agent: Self-replication and Scrapie. *Nature* **215**, 1043–1044 (1967).
109. Büeler, H. *et al.* Mice devoid of PrP are resistant to scrapie. *Cell* **73**, 1339–1347 (1993).
110. Stahl, N. *et al.* Structural studies of the scrapie prion protein using mass spectrometry and amino acid sequencing. *Biochemistry* **32**, 1991–2002 (1993).
111. Taraboulos, A. Cholesterol depletion and modification of COOH-terminal targeting sequence of the prion protein inhibit formation of the scrapie isoform [published erratum appears in J Cell Biol 1995 Jul;130(2):501]. *The Journal of Cell Biology* **129**, 121–132 (1995).
112. Chesebro, B. Anchorless Prion Protein Results in Infectious Amyloid Disease Without Clinical Scrapie. *Science* **308**, 1435–1439 (2005).
113. Saborio, G. P., Permanne, B. & Soto, C. Sensitive detection of pathological prion protein by cyclic amplification of protein misfolding. *Nature* **411**, 810–813 (2001).
114. Castilla, J., Saá, P., Hetz, C. & Soto, C. In Vitro Generation of Infectious Scrapie Prions. *Cell* **121**, 195–206 (2005).
115. Wang, F., Wang, X., Yuan, C.-G. & Ma, J. Generating a Prion with Bacterially Expressed Recombinant Prion Protein. *Science* **327**, 1132–1135 (2010).
116. Aguzzi, A. & Calella, A. M. Prions: Protein Aggregation and Infectious Diseases. *Physiological Reviews* **89**, 1105–1152 (2009).
117. Wadsworth, J. D. F. *et al.* Strain-specific prion-protein conformation determined by metal ions. *Nat Cell Biol* **1**, 55–59 (1999).
118. Safar, J. *et al.* Eight prion strains have PrPSc molecules with different conformations. *Nat Med* **4**, 1157–1165 (1998).

119. Colby, D. W. & Prusiner, S. B. Prions. *Cold Spring Harbor Perspectives in Biology* **3**, a006833–a006833 (2011).
120. Sandberg, M. K., Al-Doujaily, H., Sharps, B., Clarke, A. R. & Collinge, J. Prion propagation and toxicity in vivo occur in two distinct mechanistic phases. *Nature* **470**, 540–542 (2011).
121. Sang, J. C. *et al.* Direct observation of prion protein oligomer formation reveals an aggregation mechanism with multiple conformationally distinct species. *Chem. Sci.* **10**, 4588–4597 (2019).
122. Sandberg, M. K. *et al.* Prion neuropathology follows the accumulation of alternate prion protein isoforms after infective titre has peaked. *Nat Commun* **5**, 4347 (2014).
123. Benilova, I. *et al.* Highly infectious prions are not directly neurotoxic. *Proc Natl Acad Sci USA* **117**, 23815–23822 (2020).
124. Benilova, I., Karran, E. & De Strooper, B. The toxic Aβ oligomer and Alzheimer’s disease: an emperor in need of clothes. *Nat Neurosci* **15**, 349–357 (2012).
125. Aguzzi, A. & Falsig, J. Prion propagation, toxicity and degradation. *Nat Neurosci* **15**, 936–939 (2012).
126. Nelson, R. & Eisenberg, D. Recent atomic models of amyloid fibril structure. *Current Opinion in Structural Biology* **16**, 260–265 (2006).
127. Eisenberg, D. S. & Sawaya, M. R. Structural Studies of Amyloid Proteins at the Molecular Level. *Annu. Rev. Biochem.* **86**, 69–95 (2017).
128. Bai, X., McMullan, G. & Scheres, S. H. W. How cryo-EM is revolutionizing structural biology. *Trends in Biochemical Sciences* **40**, 49–57 (2015).
129. Guerrero-Ferreira, R. *et al.* Cryo-EM structure of alpha-synuclein fibrils. *eLife* **7**, e36402 (2018).
130. Gremer, L. *et al.* Fibril structure of amyloid-β(1–42) by cryo–electron microscopy. *Science* **358**, 116–119 (2017).
131. Glynn, C. *et al.* Cryo-EM structure of a human prion fibril with a hydrophobic, protease-resistant core. *Nat Struct Mol Biol* **27**, 417–423 (2020).
132. Choi, J.-K. *et al.* Amyloid fibrils from the N-terminal prion protein fragment are infectious. *Proc Natl Acad Sci USA* **113**, 13851–13856 (2016).
133. Wan, W. *et al.* Structural Studies of Truncated Forms of the Prion Protein PrP. *Biophysical Journal* **108**, 1548–1554 (2015).
134. Wang, L.-Q. *et al.* Cryo-EM structure of an amyloid fibril formed by full-length human prion protein. *Nat Struct Mol Biol* **27**, 598–602 (2020).
135. Rachidi, W. *et al.* Prion Infection Impairs Copper Binding of Cultured Cells. *J. Biol. Chem.* **278**, 14595–14598 (2003).
136. Ladogana, A. & Kovacs, G. G. Genetic Creutzfeldt–Jakob disease. in *Handbook of Clinical Neurology* vol. 153 219–242 (Elsevier, 2018).
137. Stevens, D. J. *et al.* Early Onset Prion Disease from Octarepeat Expansion Correlates with Copper Binding Properties. *PLoS Pathog* **5**, e1000390 (2009).
138. Hijazi, N., Shaked, Y., Rosenmann, H., Ben-Hur, T. & Gabizon, R. Copper binding to PrPC may inhibit prion disease propagation. *Brain Research* **993**, 192–200 (2003).
139. Bocharova, O. V., Breydo, L., Salnikov, V. V. & Baskakov, I. V. Copper(II) Inhibits in Vitro Conversion of Prion Protein into Amyloid Fibrils †. *Biochemistry* **44**, 6776–6787 (2005).

140. Ricchelli, F. *et al.* Aggregation/Fibrillogenesis of Recombinant Human Prion Protein and Gerstmann−Sträussler−Scheinker Disease Peptides in the Presence of Metal Ions. *Biochemistry* **45**, 6724–6732 (2006).
141. Sigurdsson, E. M. *et al.* Copper Chelation Delays the Onset of Prion Disease. *Journal of Biological Chemistry* **278**, 46199–46202 (2003).
142. Magzoub, M. & Gräslund, A. Cell-penetrating peptides: small from inception to application. *Quart. Rev. Biophys.* **37**, 147–195 (2004).
143. Xie, J. *et al.* Cell-Penetrating Peptides in Diagnosis and Treatment of Human Diseases: From Preclinical Research to Clinical Application. *Front. Pharmacol.* **11**, 697 (2020).
144. Copolovici, D. M., Langel, K., Eriste, E. & Langel, Ü. Cell-Penetrating Peptides: Design, Synthesis, and Applications. *ACS Nano* **8**, 1972–1994 (2014).
145. Lundberg, P. *et al.* Cell membrane translocation of the N-terminal (1–28) part of the prion protein. *Biochemical and Biophysical Research Communications* **299**, 85–90 (2002).
146. Magzoub, M., Pramanik, A. & Gräslund, A. Modeling the Endosomal Escape of Cell-Penetrating Peptides: Transmembrane pH Gradient Driven Translocation across Phospholipid Bilayers. *Biochemistry* **44**, 14890–14897 (2005).
147. Magzoub, M. *et al.* N-terminal peptides from unprocessed prion proteins enter cells by macropinocytosis. *Biochemical and Biophysical Research Communications* **348**, 379–385 (2006).
148. Lau, A. L. *et al.* Characterization of prion protein (PrP)-derived peptides that discriminate full-length PrPSc from PrPC. *Proceedings of the National Academy of Sciences* **104**, 11551–11556 (2007).
149. Ostapchenko, V. G., Makarava, N., Savtchenko, R. & Baskakov, I. V. The Polybasic N-Terminal Region of the Prion Protein Controls the Physical Properties of Both the Cellular and Fibrillar Forms of PrP. *Journal of Molecular Biology* **383**, 1210–1224 (2008).
150. Schmitt-Ulms, G. *et al.* Binding of neural cell adhesion molecules (N-CAMs) to the cellular prion protein. *Journal of Molecular Biology* **314**, 1209–1225 (2001).
151. Santuccione, A., Sytnyk, V., Leshchyns'ka, I. & Schachner, M. Prion protein recruits its neuronal receptor NCAM to lipid rafts to activate p59fyn and to enhance neurite outgrowth. *Journal of Cell Biology* **169**, 341–354 (2005).
152. Henning-Knechtel, A. *et al.* Designed Cell-Penetrating Peptide Inhibitors of Amyloid-beta Aggregation and Cytotoxicity. *Cell Reports Physical Science* **1**, 100014 (2020).
153. Mukundan, V. *et al.* Cytotoxicity of prion protein-derived cell-penetrating peptides is modulated by pH but independent of amyloid formation. *Archives of Biochemistry and Biophysics* **613**, 31–42 (2017).
154. Pansieri, J. *et al.* Pro-Inflammatory S100A9 Protein Aggregation Promoted by NCAM1 Peptide Constructs. *ACS Chem. Biol.* **14**, 1410–1417 (2019).
155. Król, S. *et al.* The amyloid-inhibiting NCAM-PrP peptide targets Aβ peptide aggregation in membrane-mimetic environments. *iScience* **24**, 102852 (2021).
156. Horvath, I. *et al.* Co-aggregation of pro-inflammatory S100A9 with α-synuclein in Parkinson's disease: ex vivo and in vitro studies. *J Neuroinflammation* **15**, 172 (2018).

157. Wang, C. *et al.* The role of pro-inflammatory S100A9 in Alzheimer's disease amyloid-neuroinflammatory cascade. *Acta Neuropathol* **127**, 507–522 (2014).
158. Asante, E. A. *et al.* A naturally occurring variant of the human prion protein completely prevents prion disease. *Nature* **522**, 478–481 (2015).
159. Hsiao, K. *et al.* Linkage of a prion protein missense variant to Gerstmann–Sträussler syndrome. *Nature* **338**, 342–345 (1989).
160. Webb, T. E. F. *et al.* Phenotypic heterogeneity and genetic modification of P102L inherited prion disease in an international series. *Brain* **131**, 2632–2646 (2008).
161. Tesar, A. *et al.* Clinical Variability in P102L Gerstmann–Sträussler–Scheinker Syndrome. *Ann Neurol* **86**, 643–652 (2019).
162. Medori, R. *et al.* Fatal Familial Insomnia, a Prion Disease with a Mutation at Codon 178 of the Prion Protein Gene. *N Engl J Med* **326**, 444–449 (1992).
163. Montagna, P. *et al.* Clinical Features of Fatal Familial Insomnia: Phenotypic Variability in Relation to a Polymorphism at Codon 129 of the Prion Protein Gene. *Brain Pathology* **8**, 515–520 (2006).
164. Gambetti, P., Parchi, P., Petersen, R. B., Chen, S. G. & Lugaresi, E. Fatal Familial Insomnia and Familial Creutzfeldt-Jakob Disease: Clinical, Pathological and Molecular Features. *Brain Pathology* **5**, 43–51 (1995).
165. Lugaresi, E. *et al.* Fatal Familial Insomnia and Dysautonomia with Selective Degeneration of Thalamic Nuclei. *N Engl J Med* **315**, 997–1003 (1986).
166. Tabernero, C. Fatal familial insomnia: clinical, neuropathological, and genetic description of a Spanish family. *Journal of Neurology, Neurosurgery & Psychiatry* **68**, 774–777 (2000).
167. Uttley, L., Carroll, C., Wong, R., Hilton, D. A. & Stevenson, M. Creutzfeldt-Jakob disease: a systematic review of global incidence, prevalence, infectivity, and incubation. *The Lancet Infectious Diseases* **20**, e2–e10 (2020).
168. Mead, S. Balancing Selection at the Prion Protein Gene Consistent with Prehistoric Kurulike Epidemics. *Science* **300**, 640–643 (2003).
169. Ladogana, A. *et al.* Mortality from Creutzfeldt-Jakob disease and related disorders in Europe, Australia, and Canada. *Neurology* **64**, 1586–1591 (2005).
170. Chen, C. *et al.* Analyses of the Survival Time and the Influencing Factors of Chinese Patients with Prion Diseases Based on the Surveillance Data from 2008–2011. *PLoS ONE* **8**, e62553 (2013).
171. Collins, S. J. Determinants of diagnostic investigation sensitivities across the clinical spectrum of sporadic Creutzfeldt-Jakob disease. *Brain* **129**, 2278–2287 (2006).
172. Cracco, L., Appleby, B. S. & Gambetti, P. Fatal familial insomnia and sporadic fatal insomnia. in *Handbook of Clinical Neurology* vol. 153 271–299 (Elsevier, 2018).
173. Abu-Rumeileh, S. *et al.* Sporadic Fatal Insomnia in Europe: Phenotypic Features and Diagnostic Challenges: sFI in Europe. *Ann Neurol.* **84**, 347–360 (2018).
174. Liberski, P., Gajos, A., Sikorska, B. & Lindenbaum, S. Kuru, the First Human Prion Disease. *Viruses* **11**, 232 (2019).
175. Gajdusek, D. Unconventional viruses and the origin and disappearance of kuru. *Science* **197**, 943–960 (1977).

176. Watson, N. *et al.* The importance of ongoing international surveillance for Creutzfeldt–Jakob disease. *Nat Rev Neurol* **17**, 362–379 (2021).
177. Diack, A. B. *et al.* Variant CJD: 18 years of research and surveillance. *Prion* **8**, 286–295 (2014).
178. Brown, P. *et al.* Iatrogenic Creutzfeldt-Jakob Disease, Final Assessment. *Emerg. Infect. Dis.* **18**, 901–907 (2012).
179. Appleby, B. S. *et al.* Iatrogenic Creutzfeldt-Jakob Disease from Commercial Cadaveric Human Growth Hormone. *Emerg. Infect. Dis.* **19**, 682–684 (2013).
180. Kobayashi, A., Matsuura, Y., Mohri, S. & Kitamoto, T. Distinct origins of dura mater graft-associated Creutzfeldt-Jakob disease: past and future problems. *acta neuropathol commun* **2**, 32 (2014).
181. Maddox, R. A. *et al.* Creutzfeldt-Jakob Disease in Recipients of Corneal Transplants. *Cornea* **27**, 851–854 (2008).
182. Rutala, W. A. & Weber, D. J. Guideline for Disinfection and Sterilization of Prion-Contaminated Medical Instruments. *Infect. Control Hosp. Epidemiol.* **31**, 107–117 (2010).
183. Olson, K. C. *et al.* Purified human growth hormone from E. coli is biologically active. *Nature* **293**, 408–411 (1981).
184. Liberski, P. P. Historical overview of prion diseases: a view from afar. *Folia Neuropathol* **50**, 1–12 (2012).
185. Acín, C. *et al.* Classical and Atypical Scrapie in Sheep and Goats. Review on the Etiology, Genetic Factors, Pathogenesis, Diagnosis, and Control Measures of Both Diseases. *Animals* **11**, 691 (2021).
186. O'Rourke, K. I. *et al.* Active Surveillance for Scrapie by Third Eyelid Biopsy and Genetic Susceptibility Testing of Flocks of Sheep in Wyoming. *Clin Vaccine Immunol* **9**, 966–971 (2002).
187. Wells, G. *et al.* A novel progressive spongiform encephalopathy in cattle. *Veterinary Record* **121**, 419–420 (1987).
188. Wilesmith, J. W., Wells, G. A., Cranwell, M. P. & Ryan, J. B. Bovine spongiform encephalopathy: epidemiological studies. *Vet Rec* **123**, 638–644 (1988).
189. Kumagai, S., Daikai, T. & Onodera, T. Bovine Spongiform Encephalopathy – A Review from the Perspective of Food Safety. *Food Safety* **7**, 21–47 (2019).
190. Hartsough, G. R. & Burger, D. Encephalopathy of mink: I. Epizootiologic and clinical observations. *Journal of Infectious Diseases* **115**, 387–392 (1965).
191. Mathiason, C. K. Scrapie, CWD, and Transmissible Mink Encephalopathy. in *Progress in Molecular Biology and Translational Science* vol. 150 267–292 (Elsevier, 2017).
192. Sigurdson, C. J. & Miller, M. W. Other animal prion diseases. *British Medical Bulletin* **66**, 199–212 (2003).
193. Aldhous, P. Spongiform encephalopathy found in cat. *Nature* **345**, 194–194 (1990).
194. Bruce, M. E. *et al.* Transmissions to mice indicate that 'new variant' CJD is caused by the BSE agent. *Nature* **389**, 498–501 (1997).
195. Dudhatra, G. B. *et al.* Prion diseases: A challenge to animal health. *Journal of Applied Pharmaceutical Science* **1**, 215–221 (2011).
196. Benestad, S. L., Mitchell, G., Simmons, M., Ytrehus, B. & Vikøren, T. First case of chronic wasting disease in Europe in a Norwegian free-ranging reindeer. *Vet Res* **47**, 88 (2016).

197. Mysterud, A. *et al.* Antler cannibalism in reindeer. *Sci Rep* **10**, 22168 (2020).
198. Angers, R. C. *et al.* Chronic Wasting Disease Prions in Elk Antler Velvet. *Emerg. Infect. Dis.* **15**, 696–703 (2009).
199. Barria, M. A., Libori, A., Mitchell, G. & Head, M. W. Susceptibility of Human Prion Protein to Conversion by Chronic Wasting Disease Prions. *Emerg. Infect. Dis.* **24**, 1482–1489 (2018).
200. Nemani, S. K., Myskiw, J. L., Lamoureux, L., Booth, S. A. & Sim, V. L. Exposure Risk of Chronic Wasting Disease in Humans. *Viruses* **12**, 1454 (2020).
201. Babelhadj, B. *et al.* Prion Disease in Dromedary Camels, Algeria. *Emerg. Infect. Dis.* **24**, 1029–1036 (2018).
202. Atkins, P. W. & Paula, J. de. *Physical chemistry*. (Oxford University Press, 2006).
203. Allen, J. P. *Biophysical chemistry*. (Wiley-Blackwell Pub, 2008).
204. Wilkins, M. R. *et al.* Protein identification and analysis tools in the ExPASy server. in *(2-D Proteome Analysis Protocols)* vol. 112 531–552 (Humana Press Inc., 1999).
205. Dapson, R. W. Amyloid from a histochemical perspective. A review of the structure, properties and types of amyloid, and a proposed staining mechanism for Congo red staining. *Biotechnic & Histochemistry* **93**, 543–556 (2018).
206. Yakupova, E. I., Bobyleva, L. G., Vikhlyantsev, I. M. & Bobylev, A. G. Congo Red and amyloids: history and relationship. *Bioscience Reports* **39**, BSR20181415 (2019).
207. Klunk, W. E., Jacob, R. F. & Mason, R. P. [19] Quantifying amyloid by congo red spectral shift assay. in *Methods in Enzymology* vol. 309 285–305 (Elsevier, 1999).
208. Lakowicz, J. R. *Principles of fluorescence spectroscopy*. (Springer, 2010).
209. Reshetnyak, Y. K. & Burstein, E. A. Decomposition of Protein Tryptophan Fluorescence Spectra into Log-Normal Components. II. The Statistical Proof of Discreteness of Tryptophan Classes in Proteins. *Biophysical Journal* **81**, 1710–1734 (2001).
210. Alarcón, E., Aspée, A., Abuin, E. B. & Lissi, E. A. Evaluation of solute binding to proteins and intra-protein distances from steady state fluorescence measurements. *Journal of Photochemistry and Photobiology B: Biology* **106**, 1–17 (2012).
211. van de Weert, M. Fluorescence Quenching to Study Protein-ligand Binding: Common Errors. *J Fluoresc* **20**, 625–629 (2010).
212. Housecroft, C. E. & Sharpe, A. G. *Inorganic chemistry*. (Pearson, 2012).
213. Biancalana, M. & Koide, S. Molecular mechanism of Thioflavin-T binding to amyloid fibrils. *Biochimica et Biophysica Acta (BBA) - Proteins and Proteomics* **1804**, 1405–1412 (2010).
214. Khurana, R. *et al.* Mechanism of thioflavin T binding to amyloid fibrils. *Journal of Structural Biology* **151**, 229–238 (2005).
215. McMurry, J. *Organic chemistry*. (Brooks/Cole, Cengage Learning, 2012).
216. Fasman, G. D. *Circular dichroism and the conformational analysis of biomolecules*. (Springer, 2011).
217. Kelly, S. M. & Price, N. C. The application of circular dichroism to studies of protein folding and unfolding. *Biochimica et Biophysica Acta (BBA) - Protein Structure and Molecular Enzymology* **1338**, 161–185 (1997).

218. Kelly, S. M., Jess, T. J. & Price, N. C. How to study proteins by circular dichroism. *Biochimica et Biophysica Acta (BBA) - Proteins and Proteomics* **1751**, 119–139 (2005).
219. Greenfield, N. J. Using circular dichroism spectra to estimate protein secondary structure. *Nat Protoc* **1**, 2876–2890 (2006).
220. Micsonai, A. *et al.* Accurate secondary structure prediction and fold recognition for circular dichroism spectroscopy. *Proc Natl Acad Sci USA* **112**, E3095–E3103 (2015).
221. Micsonai, A., Bulyáki, É. & Kardos, J. BeStSel: From Secondary Structure Analysis to Protein Fold Prediction by Circular Dichroism Spectroscopy. in *Structural Genomics* (eds. Chen, Y. W. & Yiu, C.-P. B.) vol. 2199 175–189 (Springer US, 2021).
222. Nölting, B. *Methods in modern biophysics*. (Springer, 2009).
223. Barth, A. Infrared spectroscopy of proteins. *Biochimica et Biophysica Acta (BBA) - Bioenergetics* **1767**, 1073–1101 (2007).
224. Yang, H., Yang, S., Kong, J., Dong, A. & Yu, S. Obtaining information about protein secondary structures in aqueous solution using Fourier transform IR spectroscopy. *Nat Protoc* **10**, 382–396 (2015).
225. Ruggeri, F. S., Šneideris, T., Vendruscolo, M. & Knowles, T. P. J. Atomic force microscopy for single molecule characterisation of protein aggregation. *Archives of Biochemistry and Biophysics* **664**, 134–148 (2019).
226. Simone Ruggeri, F., Habchi, J., Cerreta, A. & Dietler, G. AFM-Based Single Molecule Techniques: Unraveling the Amyloid Pathogenic Species. *CPD* **22**, 3950–3970 (2016).
227. Adamcik, J. & Mezzenga, R. Study of amyloid fibrils via atomic force microscopy. *Current Opinion in Colloid & Interface Science* **17**, 369–376 (2012).
228. Aubrey, L. D. *et al.* Quantification of amyloid fibril polymorphism by nano-morphometry reveals the individuality of filament assembly. *Commun Chem* **3**, 125 (2020).
229. Watanabe-Nakayama, T. *et al.* High-speed atomic force microscopy reveals structural dynamics of amyloid $\beta_{1–42}$ aggregates. *Proc Natl Acad Sci USA* **113**, 5835–5840 (2016).
230. Franken, L. E., Grünewald, K., Boekema, E. J. & Stuart, M. C. A. A Technical Introduction to Transmission Electron Microscopy for Soft-Matter: Imaging, Possibilities, Choices, and Technical Developments. *Small* **16**, 1906198 (2020).
231. *Transmission Electron Microscopy*. vol. 36 (Springer New York, 2008).
232. Gras, S. L., Waddington, L. J. & Goldie, K. N. Transmission Electron Microscopy of Amyloid Fibrils. in *Protein Folding, Misfolding, and Disease* (eds. Hill, A. F., Barnham, K. J., Bottomley, S. P. & Cappai, R.) vol. 752 197–214 (Humana Press, 2011).
233. Barreto-Vieira, D. F. & Barth, O. M. Negative and Positive Staining in Transmission Electron Microscopy for Virus Diagnosis. in *Microbiology in Agriculture and Human Health* (ed. Shah, M. M.) (InTech, 2015). doi:10.5772/60511.
234. Karplus, M. & Kuriyan, J. Molecular dynamics and protein function. *Proceedings of the National Academy of Sciences* **102**, 6679–6685 (2005).
235. Matsumoto, S. *et al.* Extraction of protein dynamics information from cryo-EM maps using deep learning. *Nat Mach Intell* **3**, 153–160 (2021).
236. Uversky, V. N. Intrinsically Disordered Proteins and Their “Mysterious” (Meta)Physics. *Front. Phys.* **7**, 10 (2019).

237. Bondos, S. E., Dunker, A. K. & Uversky, V. N. On the roles of intrinsically disordered proteins and regions in cell communication and signaling. *Cell Commun Signal* **19**, 88, s12964-021-00774–3 (2021).
238. Lindorff-Larsen, K., Piana, S., Dror, R. O. & Shaw, D. E. How Fast-Folding Proteins Fold. *Science* **334**, 517–520 (2011).
239. Hollingsworth, S. A. & Dror, R. O. Molecular Dynamics Simulation for All. *Neuron* **99**, 1129–1143 (2018).
240. Scheraga, H. A., Khalili, M. & Liwo, A. Protein-Folding Dynamics: Overview of Molecular Simulation Techniques. *Annu. Rev. Phys. Chem.* **58**, 57–83 (2007).
241. Gelpi, J., Hospital, A., Goñi, R. & Orozco, M. Molecular dynamics simulations: advances and applications. *AABC* 37 (2015) doi:10.2147/AABC.S70333.
242. Oostenbrink, C., Villa, A., Mark, A. E. & Van Gunsteren, W. F. A biomolecular force field based on the free enthalpy of hydration and solvation: The GROMOS force-field parameter sets 53A5 and 53A6. *J. Comput. Chem.* **25**, 1656–1676 (2004).
243. Lindahl, Abraham, Hess & Spoel, V. D. GROMACS 2021.3 Manual. (2021) doi:10.5281/ZENODO.5053220.
244. Jorgensen, W. L., Maxwell, D. S. & Tirado-Rives, J. Development and Testing of the OPLS All-Atom Force Field on Conformational Energetics and Properties of Organic Liquids. *J. Am. Chem. Soc.* **118**, 11225–11236 (1996).
245. Robertson, M. J., Tirado-Rives, J. & Jorgensen, W. L. Improved Peptide and Protein Torsional Energetics with the OPLS-AA Force Field. *J. Chem. Theory Comput.* **11**, 3499–3509 (2015).
246. Svergun, D. I., Koch, M. H. J., Timmins, P. A. & May, R. P. *Small Angle X-Ray and Neutron Scattering from Solutions of Biological Macromolecules*. (Oxford University Press, 2013). doi:10.1093/acprof:oso/9780199639533.001.0001.
247. Feigin, L. A. & Svergun, D. I. *Structure Analysis by Small-Angle X-Ray and Neutron Scattering*. (Springer US, 1987). doi:10.1007/978-1-4757-6624-0.
248. Kikhney, A. G. & Svergun, D. I. A practical guide to small angle X-ray scattering (SAXS) of flexible and intrinsically disordered proteins. *FEBS Letters* **589**, 2570–2577 (2015).
249. Greenwald, J. & Riek, R. Biology of Amyloid: Structure, Function, and Regulation. *Structure* **18**, 1244–1260 (2010).
250. Morris, K. L. & Serpell, L. C. X-Ray Fibre Diffraction Studies of Amyloid Fibrils. in *Amyloid Proteins* (eds. Sigurdsson, E. M., Calero, M. & Gasset, M.) vol. 849 121–135 (Humana Press, 2012).
251. Makin, O. S. & Serpell, L. C. Structures for amyloid fibrils: Structures for amyloid fibrils. *FEBS Journal* **272**, 5950–5961 (2005).
252. Sunde, M. *et al.* Common core structure of amyloid fibrils by synchrotron X-ray diffraction 1 1Edited by F. E. Cohen. *Journal of Molecular Biology* **273**, 729–739 (1997).
253. Serpell, L. C. Alzheimer's amyloid fibrils: structure and assembly. *Biochimica et Biophysica Acta (BBA) - Molecular Basis of Disease* **1502**, 16–30 (2000).
254. Tria, G., Mertens, H. D. T., Kachala, M. & Svergun, D. I. Advanced ensemble modelling of flexible macromolecules using X-ray solution scattering. *IUCrJ* **2**, 207–217 (2015).

255. Brown, L. R. & Harris, D. A. Copper and zinc cause delivery of the prion protein from the plasma membrane to a subset of early endosomes and the Golgi: Copper and zinc effect on prion protein localization. *Journal of Neurochemistry* **87**, 353–363 (2003).
256. Aguzzi, A., Lakkaraju, A. K. K. & Frontzek, K. Toward Therapy of Human Prion Diseases. *Annu. Rev. Pharmacol. Toxicol.* **58**, 331–351 (2018).
257. Tjernberg, L. O. *et al.* Arrest of -Amyloid Fibril Formation by a Pentapeptide Ligand. *Journal of Biological Chemistry* **271**, 8545–8548 (1996).

9. Full text of publications constituting the thesis

RSC Advances

PAPER

View Article Online
View Journal | View Issue

Check for updates

Cite this: RSC Adv., 2019, 9, 22211

PrP (58–93) peptide from unstructured N-terminal domain of human prion protein forms amyloid-like fibrillar structures in the presence of Zn^{2+} ions†

Maciej Gielnik, [a] Zuzanna Pietralik, [a] Igor Zhukov, [bc] Aneta Szymańska, [d] Wojciech M. Kwiatek [e] and Maciej Kozak *[afg]

Many transition metal ions modulate the aggregation of different amyloid peptides. Substoichiometric zinc concentrations can inhibit aggregation, while an excess of zinc can accelerate the formation of cytotoxic fibrils. In this study, we report the fibrillization of the octarepeat domain to amyloid-like structures. Interestingly, this self-assembling process occurred only in the presence of Zn(II) ions. The formed peptide aggregates are able to bind amyloid specific dyes thioflavin T and Congo red. Atomic force microscopy and transmission electron microscopy revealed the formation of long, fibrillar structures. X-ray diffraction and Fourier transform infrared spectroscopy studies of the formed assemblies confirmed the presence of cross-β structure. Two-component analysis of synchrotron radiation SAXS data provided the evidence for a direct decrease in monomeric peptide species content and an increase in the fraction of aggregates as a function of Zn(II) concentration. These results could shed light on Zn(II) as a toxic agent and on the metal ion induced protein misfolding in prion diseases.

Received 27th February 2019
Accepted 7th July 2019

DOI: 10.1039/c9ra01510h

rsc.li/rsc-advances

Introduction

Insoluble fibrillar polypeptide structures appear as a result of a misfolding process in numerous proteins or peptides and accompany the amyloid aggregation process.[1–6] The most spectacular structures of this type are linked to the development of fatal neurodegenerative disorders such as Alzheimer's disease,[7,8] Icelandic type amyloidosis[9,10] or Creutzfeldt–Jakob disease.[11,12] The latter belongs to the group of diseases called transmissible spongiform encephalopathies (TSE) in which a misfolding of human prion protein (PrP) is responsible for the formation of fibrillar aggregates in the brain.[11–15]

Mature form of cellular human prion protein (PrP^C) is 208 residues long glycosylphosphatidylinositol-anchored to outer membrane protein,[16] located in the synaptic cleft and expressed at high levels in striatum, hippocampus, cortex and olfactory bulb.[17] As shown by NMR studies, human PrP^C protein is composed of two structurally different domains: unstructured N-terminal part of polypeptide chain containing residues 23–120 and structured, globular C-terminal domain composed of residues 121–231.[18] For the development of TSE, a conformational transformation of the cellular form of the prion protein into the pathogenic and insoluble PrP^{Sc} is necessary. This transformation involves the formation of the intermolecular cross-β structure at the sacrifice of the helical structure of the PrP C-terminal domain.[13,14] The molecular function of PrP^C is not known, however, it has been suggested that it might be responsible for the upkeep of divalent transition metal ions and disruption of such homeostasis may facilitate the formation of PrP^{Sc}.[19–21] Prion protein contains also two high-affinity metal binding sites: the octarepeat region (residues 60–91) and non-octarepeat region (residues 92–111), both located in unstructured N-terminal domain.[22] Octarepeat region contains four tandem octapeptide repeats characterized by PHGGGWGQ sequence, which exhibits high binding affinity towards Cu(II)[22–29] and also binds Zn(II) with lower affinity.[22,30,31]

Zinc is the second most abundant transition metal in living organisms and it is responsible for many important biological functions, including structure stabilization, catalysis of biochemical reactions and regulation of enzymatic activity.[32] In the highest concentrations Zn(II) occurs in the brains, it is on average equal to 150 μM.[33] Zinc plays a key role in synaptic transmission and during the synaptic excitation the local

---

[a] Department of Macromolecular Physics, Faculty of Physics, Adam Mickiewicz University, Uniwersytetu Poznańskiego 2, PL 61-614 Poznań, Poland. E-mail: mkozak@amu.edu.pl
[b] Institute of Biochemistry and Biophysics, Polish Academy of Sciences, PL 02-106 Warszawa, Poland
[c] NanoBioMedical Centre, Adam Mickiewicz University, PL 61-614 Poznań, Poland
[d] Department of Biomedical Chemistry, Faculty of Chemistry, Gdańsk University, PL 80-308 Gdańsk, Poland
[e] Institute of Nuclear Physics Polish Academy of Sciences, PL 31-342 Krakow, Poland
[f] Joint Laboratory for SAXS Studies, Faculty of Physics, Adam Mickiewicz University, PL 61-614 Poznań, Poland
[g] National Synchrotron Radiation Centre SOLARIS, Jagiellonian University, PL 30-392 Kraków, Poland

† Electronic supplementary information (ESI) available. See DOI: 10.1039/c9ra01510h

transient concentration of Zn(II) can reach values up to 300 μM.[33,34] Assuming that the cellular function of PrP^C is most likely connected with metal binding, it was proposed that PrP^C is responsible for zinc homeostasis in the brain.[21] Three main functions are attributed to PrP^C: zinc sensor, transporter or sequester.[21,35,36] PrP^C enhances the rate of zinc uptake in neurons and neuronal cell lines.[37] Zinc at concentration 100 μM also stimulates endocytosis of PrP^C from the cell surface into endosomes and Golgi apparatus.[38,39] At the molecular level, coordination of Zn(II) by octarepeat region of PrP^C causes a tertiary contact between Zn(II) saturated octarepeat region and surface of helices 2 and 3 in C-terminal domain.[40] Zinc may also play an important role during TSE. In prion diseases, zinc concentration in the brain decreases to 20%[41] and inoculation of neuronal cell lines with scrapie disrupts zinc uptake.[37] Also tertiary contacts between Zn(II) coordinated octarepeat domain and helices 2 and 3 in pathogenic mutants of PrP^C are altered.[40]

Here we studied the aggregation of isolated metal binding PrP^{58-93} domain, naturally located in the unstructured N-terminal domain of PrP^C in the presence of Zn(II).

We report for the very first time the fibrillization of the octarepeat domain to amyloid-like structures. This self-assembling process occurred in the presence of Zn^{2+} ions. The assemblies obtained were analyzed by various spectroscopic, microscopic and scattering techniques. The formed PrP^{58-93} fibrillar structures were characterized by the amyloid-specific assays (thioflavin T, Congo red) and were visualized using atomic force microscopy (AFM) and transmission electron microscopy (TEM). The presence of the cross-β-structure in the formed fibrils was verified by the X-ray diffraction pattern combined with Fourier transform infrared (FTIR) spectroscopy. SAXS experiments suggested that Zn(II) had a direct impact on PrP^{58-93} monomeric state. The presented studies may be crucial for better comprehension of the molecular etiology of TSE and other amyloid diseases.

Materials and methods

Peptide synthesis and purification

PrP^{58-93} was synthesized by standard Fmoc/*t*Bu amino acid chemistry and purified to at least 98% purity by means of reversed-phase high-performance liquid chromatography. The molecular weight of the peptide was confirmed by the mass spectrometry method using an ESI-IT-TOF-LC-MS system (Shimadzu) with a C12 Jupiter Proteo column (150 × 2 mm, 4 μm, 90 Å; Phenomenex). The exact procedure of peptide synthesis and purification is described in ESI.† For determination of PrP^{58-93} concentration, we used extinction coefficient calculated in protparam[42] equal 22 000 M^{-1} cm^{-1}.

Thioflavin T assay

Spectrofluorometric measurements of PrP^{58-93} were performed in a 1 cm cuvette using an FP-8300 spectrofluorimeter (Jasco, Tokyo, Japan). Excitation and emission wavelengths were 440 and 480 nm, respectively. 2 mM stock solution of Thioflavin T (ThT) was prepared in 10 mM NaH_2PO_4/Na_2HPO_4 buffer, pH 7.4 and filtered through 0.22 μm syringe filter. Samples for thioflavin T assay contained 40 μM of ThT and 10 μM of PrP^{58-93} peptide in 10 mM NaH_2PO_4/Na_2HPO_4, pH 7.4. Zinc(II) ions were added as $ZnCl_2$ solution directly into the cuvette after recording the fluorescence intensity for 40 μM ThT with 10 μM peptide for a few minutes. All ThT experiments were performed in triplicate at room temperature and in quiescent conditions.

Congo red binding assay

Congo red (CR) stock solution was prepared in 10 mM NaH_2PO_4/Na_2HPO_4 buffer, pH 7.4 with 10% (v/v) ethanol and filtered through an 0.22 μm syringe filter. Concentration of CR stock solution was determined in 1 mM NaH_2PO_4/Na_2HPO_4 buffer, pH 7.0 with 40% ethanol at 505 nm using the molar extinction coefficient $\varepsilon = 59\ 300\ M^{-1}\ cm^{-1}$.[43]

Congo red binding assays were performed in a 1 cm cuvette (2500 μl volume). CR at concentration of 2 μM with 10 μM PrP^{58-93} peptide samples were incubated with or without 40 μM $ZnCl_2$ for 12 hours in 10 mM NaH_2PO_4/Na_2HPO_4 buffer, pH 7.4. Spectra were recorded every 15 minutes over the spectral range from 300 to 800 nm on a V-650 UV-Vis spectrometer (Jasco, Tokyo, Japan), with bandwidth 1 nm, scan speed 200 nm min^{-1}. All CR experiments were performed in room temperature and in quiescent conditions.

Fourier transform infrared spectroscopy

The absorption spectra within the Amide I bands region for PrP^{58-93} peptide solution (600 μM PrP^{58-93} dissolved in 10 mM NaH_2PO_4/Na_2HPO_4, pH 7.4) were collected with a resolution of 6 cm^{-1} at room temperature. A small drop of PrP^{58-93} peptide solution (20 μl) was placed on a horizontal single-reflection diamond crystal of PLATINUM ATR (Bruker, Billerica, USA) unit and then FTIR spectra (128 scans) were collected using TENSOR 27 (Bruker, Billerica, USA) equipped with MCT detector. After addition of 25 mM of $ZnCl_2$ solution (2 μl), the FTIR spectra were collected every 5 or 10 minutes for up to 2 hours. The recorded FTIR spectra were corrected for buffer absorption and smoothed with 10 point Savitzky–Golay filter. Second-derivative analysis was performed as described by Yang *et al.*[44]

Atomic force microscopy

The topographic images of peptide fibrils were collected using JPK Nanowizard 4 atomic microscope (JPK, Berlin, Germany) operated in air contact mode. The imaging was conducted using Tap150AL AFM cantilevers (Ted Pella, Inc., Redding, USA). Sample preparation procedure for AFM imaging of 10 μM PrP^{58-93} peptide (apo) and 10 μM peptide incubated for 24 h with 40 μM of $ZnCl_2$ was identical: 10 μl of solution was placed on a freshly cleaved mica surface, adsorbed for 3 min, rinsed with a small amount of distilled water and dried at room temperature. The AFM images were analyzed using the Gwyddion 2.49 software.[45]

Transmission electron microscopy

The PrP^{58-93} peptide solution at concentration of 10 μM was incubated with 40 μM of $ZnCl_2$ in 10 mM NaH_2PO_4/Na_2HPO_4

buffer, pH 7.4 for 24 h at room temperature. After incubation, 5 μl of samples were placed on PELCO® 300 mesh copper grid (Ted Pella, Inc., Redding, USA) and adsorbed within 60 seconds on the grid. Then the sample was removed from the grid using filter paper strips. The peptide fibrils adsorbed on the grid were contrasted by the use of 0.5% uranyl formate solution for 60 seconds. TEM images were recorded using JEM-1400 transmission electron microscope (JEOL, Tokyo, Japan) operated at 120 kV.

Synchrotron radiation small angle X-ray scattering (SR-SAXS)

SR-SAXS data were collected at P12 beamline, PETRA III storage ring (DESY, Hamburg), using a Pilatus 3X 6M pixel detector (DECTRIS Ltd. Baden-Daettwil, Switzerland) and synchrotron radiation ($\lambda = 0.124$ nm).[46] The sample-to-detector distance was 3.0 m and the scattering vector (s) range was: $0.026 < s < 7.288$ nm^{-1}. In SR-SAXS experiments 0.8 mM PrP$^{58-93}$ peptide was dissolved in 50 mM HEPES, pH 7.4, 100 mM NaCl and ZnCl$_2$ (concentration from 0 to 0.8 mM). For each sample, thirty subsequent frames, 50 ms each, were recorded and radiation damage was inspected. Due to radiation damage only the first three frames were analyzed.

Buffer subtraction and Guinier analysis were performed in PRIMUS[47] from ATSAS 2.8 package.[48] The pair distribution function ($P(r)$) was calculated using GNOM.[49]

Due to the polydispersity of sample after addition of ZnCl$_2$, we performed two component analysis of SR-SAXS data in SASfit.[50] The shape of apo PrP$^{58-93}$ peptide can be reduced into a spheroid and the form factor can be calculated analytically:[50]

$$P_{\text{spheroid}}(s) = \int_0^{\pi/2} \left[\frac{3[\sin(sr) - sr\cos(sr)]}{(sr)^3}\right]^2 [sr]^2 \sin\alpha \, \mathrm{d}\alpha \quad (1)$$

$$r = s[{R_\mathrm{p}}^2 \sin^2(\alpha) + {R_\mathrm{e}}^2 \cos^2(\alpha)]^{1/2} \quad (2)$$

where R_p is the principal semi-axis and R_e is the equatorial semi-axis of spheroid. Moreover, the shape of PrP$^{58-93}$ peptide fibrils can be simplified as cylinders of the following form factor:

$$P_{\text{cylinder}}(s) = \int_0^{\pi/2} \left[\frac{2J_1(sR\sin\alpha)}{sR\sin\alpha}\frac{\sin((sL\cos\alpha)/2)}{(sL\cos\alpha)/2}\right]^2 \sin\alpha \, \mathrm{d}\alpha \quad (3)$$

where J_1 is the regular cylindrical Bessel function of the first order, R is the radius of the cylinder and L is its length.

X-ray diffraction

X-ray fiber diffraction experiment of PrP$^{58-93}$ fibrils was conducted on XEUSS 2.0 SAXS/WAXS system (XENOCS, Sassenage, France), using Ga Kα radiation from a MetalJet microfocus generator with a liquid-metal jet anode (Excillum AB, Kista, Sweden) and a Pilatus 3R 1M detector (DECTRIS Ltd. Baden-Daettwil, Switzerland). The sample-to-detector distance was calibrated by the use of silver behenate (reference $q_{001} = 1.070$ nm^{-1}). 500 μl of 0.4 mM PrP$^{58-93}$ peptide prepared in 50 mM HEPES, pH 7.4, 100 mM NaCl with 1.6 mM ZnCl$_2$ was incubated at room temperature for 24 h. After incubation time, the aggregated deposits, visible on the walls of the Eppendorf test tube, were transferred into thin-walled borosilicate glass and the data were collected.

Results and discussion

PrP$^{58-93}$ peptide binds amyloid specific dyes only in the presence of Zn(II)

For the initial characterization of PrP$^{58-93}$ peptide, we performed circular dichroism spectroscopy experiments (Fig. S1, ESI†). The CD spectrum of this peptide is well-documented in literature:[23,26,27,51,52] and it shows a weak positive band at 225 nm, a strong negative band at 200 nm, which are interpreted to correspond to a mixture of random coil and polyproline-II helix – extended left-handed helix.[51,52] Surprisingly, we found that the investigated peptide was very stable – 1 mM stock solution incubated over six months at room temperature and diluted into 5 μM concentration did not show any significant changes in the secondary structure (Fig. S1, ESI†). However, the addition of 20 μM ZnCl$_2$ into the cuvette with 5 μM PrP$^{58-93}$ peptide resulted in a rapid loss of the CD signal, which suggests precipitation or aggregation of the peptide (data not shown). In order to check the possible aggregation of PrP$^{58-93}$ peptide in the presence of Zn(II) we performed ThT and CR assays.

ThT is an amyloid-specific dye whose fluorescence increases upon binding *via* hydrophobic interaction with β sheets to amyloid fibrils, therefore it is commonly used to monitor the fibrillization kinetics.[53,54] The fluorescence of 40 μM of ThT with 10 μM of apo PrP$^{58-93}$ peptide showed a slight increase in intensity over time (Fig. 1a, black line), which can be attributed to rather slow fibril formation and subsequent ThT binding. To rule out a possible aggregation of apo PrP$^{58-93}$ peptide, we conducted additional dynamic Congo red (CR) binding assay. Congo red is a diazo dye highly specific for binding a cross-β structure present in amyloid fibrils. When it binds to fibrils, CR absorption increases and shows a red shift from 490 to 540 nm.[43] Time-resolved spectra obtained for PrP$^{58-93}$ peptide revealed low and constant CR absorbance at 541 nm over time (Fig. 1b, black squares). This result, together with the ThT and CD data, strongly indicate that the PrP$^{58-93}$ alone does not aggregate and its structure is stable in solution.

Upon addition of ZnCl$_2$ (40 μM) to the 10 μM peptide sample, ThT fluorescence increased rapidly and PrP$^{58-93}$ acquired the ability to bind ThT (Fig. 1a, red line). This observation suggests that upon interaction with Zn(II) PrP$^{58-93}$ peptide forms amyloid-like structures. The kinetic ThT curve showed no lag phase, what suggests that the induced fibrillization is a very rapid process which quickly exhausts most of the monomeric peptide form. Indeed, the fluorescence intensity reached a plateau after ~1 h of incubation. Longer incubation resulted in a decrease in the ThT fluorescence intensity and a final stabilization of the signal at a constant level after ~11 h. The loss of ThT signal was most probably caused by sedimentation of the formed fibrils, visible as a yellowish precipitate at the bottom of the cuvette after 12 h.

For the cross-validation of the possible fibrillization of PrP$^{58-93}$ in the presence of Zn(II), we applied the Congo red (CR) binding

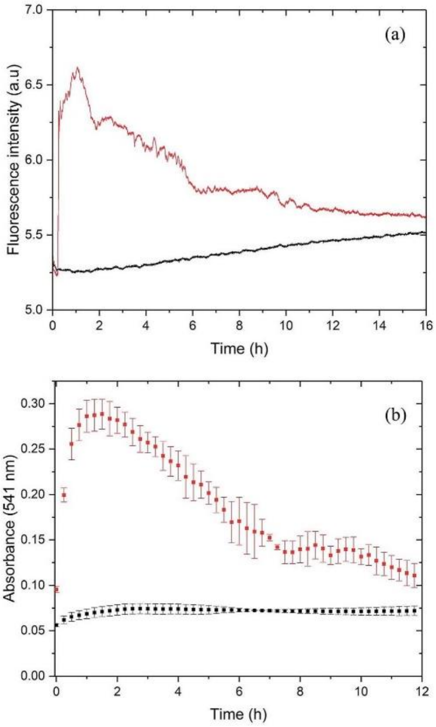

Fig. 1 (a) ThT binding assay for 10 μM PrP^{58-93} peptide (black line) and for 10 μM PrP^{58-93} peptide with 40 μM of $ZnCl_2$ (red line). (b) CR binding assay for 10 μM PrP^{58-93} peptide (black squares) and for 10 μM PrP^{58-93} peptide with 40 μM of $ZnCl_2$ (red squares). Both experiments were performed in 10 mM NaH_2PO_4/Na_2HPO_4 buffer, pH 7.4.

assay (Fig. 1b, red squares). In the presence of Zn(II), the absorbance of CR at 541 nm increased significantly from 0.07 to 0.27 very quickly after metal ion addition. This elevation in the absorbance is an evidence for the binding of CR to the β-sheets and suggests fibril formation by PrP^{58-93} peptide in the presence of Zn(II). The shape of the kinetic curve in the CR assay resembles the ThT curve (Fig. 1a red line). CR absorbance reached a plateau very fast, in about 1 h after addition of $ZnCl_2$, which confirms a rapid fibril formation. Further incubation resulted in a decrease in CR absorbance in a fashion similar to the ThT fluorescence intensity for PrP^{58-93} peptide with Zn(II). At the end of CR assay, a reddish precipitate was visible at the bottom of the cuvette, therefore reduction of CR absorbance was probably caused by direct binding of CR to the formed fibrils and sedimentation of the aggregates. In conclusion, both ThT and CR assays indicated that PrP^{58-93} peptide might form amyloid-like structures in the presence of Zn(II) in contrast to the apo peptide that seemed to be stable over time.

Zn(II) induces β-sheet formation in PrP^{58-93}

CD spectroscopy failed to monitor β-sheet formation, probably due to sedimentation of formed fibrillar structures. Therefore, in order to observe a transition in the secondary structure of PrP^{58-93} peptide after addition of Zn(II), we subjected the samples to ATR-FTIR spectroscopy. Amide I band for PrP^{58-93} peptide was broad and had a maximum of absorption at 1661 cm^{-1} (Fig. 2, dark green line). Second-derivative analysis suggested, that apart from the predominant absorption maximum at 1645 cm^{-1}, corresponding to the random coil structure, the bands assigned to 3_{10}-helix, β-turns and β-sheets were also present (Fig. S2, ESI†).[44] These bands, other than assigned to random coil, seemed to be a consequence of the inherence of PPII helix secondary structure in the PrP^{58-93} peptide.[51,52] Theoretical and experimental amide I FTIR spectra of $(PPG)_{10}$ collagen peptides, forming triple PPII helix suggest that the C═O stretching vibration of PPII amide group gives rise to frequencies described in a standard secondary structure analysis as 3_{10}-helix, β-turns and β-sheets[55] and match well with our data. As a consequence, the secondary structure of apo PrP^{58-93} peptide is a mixture of a random coil and PPII helix, as postulated in literature.[51,52]

Addition of Zn(II) cations to the PrP^{58-93} sample resulted in a gradual shift of the absorption maximum up to 1645 cm^{-1} after 30 minutes (Fig. 2, red line). The accompanying decrease in amide I band intensity at 1675 cm^{-1} and the concurrent increase at 1622 cm^{-1} (Fig. 2, blue line) corresponded to a structural transition in a PrP^{58-93} peptide induced by Zn(II). These changes in FTIR spectrum indicated a reduction of β-turn content and formation of β-sheets, respectively.[44] Further second-derivative analysis confirmed the formation of β-sheets, the disappearance of peaks that might be assigned to PPII helix,

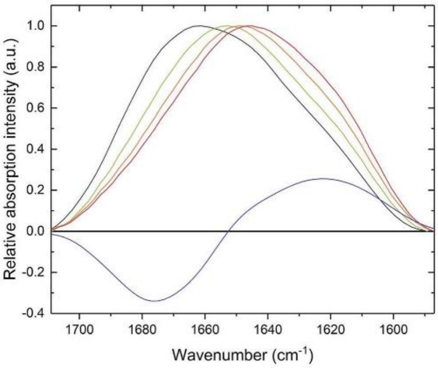

Fig. 2 FTIR spectra of 600 μM PrP^{58-93} peptide (olive), 600 μM PrP^{58-93} peptide with 2.3 mM $ZnCl_2$ (lime), 600 μM PrP^{58-93} peptide with 2.3 mM $ZnCl_2$ after 15 minutes (orange), 600 μM PrP^{58-93} peptide with 2.3 mM $ZnCl_2$ after 30 minutes (red), differential spectrum between 600 μM PrP^{58-93} peptide with 2.3 mM $ZnCl_2$ after 30 minutes and 600 μM PrP^{58-93} peptide (blue).

and an increase in random coil content (Fig. S3, ESI†). Zn(II) binding with PrP$^{58-93}$ may cause the unfolding of the PPII helix what, accompanied by the lowering of the energetic barrier for nucleation and aggregation, might result in a conformational transition unavailable for apo PrP$^{58-93}$. The FTIR data are consistent with the results from ThT and CR assays and provide further evidence for β-sheet formation in PrP$^{58-93}$ peptide upon interaction with Zn(II).

PrP$^{58-93}$ upon interaction with Zn(II) forms structured fibrils with cross-β structure

To further investigate the effect of Zn(II) on PrP$^{58-93}$ peptide aggregation and possible fibril formation, we performed also microscopic studies. Fig. 3a presents the AFM image of monomeric 10 μM PrP$^{58-93}$ peptide adsorbed on the mica surface and dried at room temperature. The measured height of dried peptide monomers varies from 1.5 to 2.5 nm. After 24 h incubation of 10 μM PrP$^{58-93}$ peptide with 40 μM $ZnCl_2$, some spherical oligomers, as well as single peptide fibrils were visible (Fig. 3b). PrP$^{58-93}$ fibrils had a well-defined shape and quite uniform height in the range 1.5 to 1.8 nm. Moreover, the AFM images suggested that the formed fibrils had lateral branches, directed at right angles from the main fibril axis. The shape of the spherical oligomers was not well defined and their height ranged from 5 to 16 nm. Interestingly, the spherical oligomers were connected with the ends of the fibrils and therefore, the observed spherical oligomers might be centers of fibril nucleation.

The microstructure of PrP$^{58-93}$ peptide fibrils with $ZnCl_2$ was also verified by the transmission electron microscopy (TEM). The formed structures show a high tendency to cluster and form

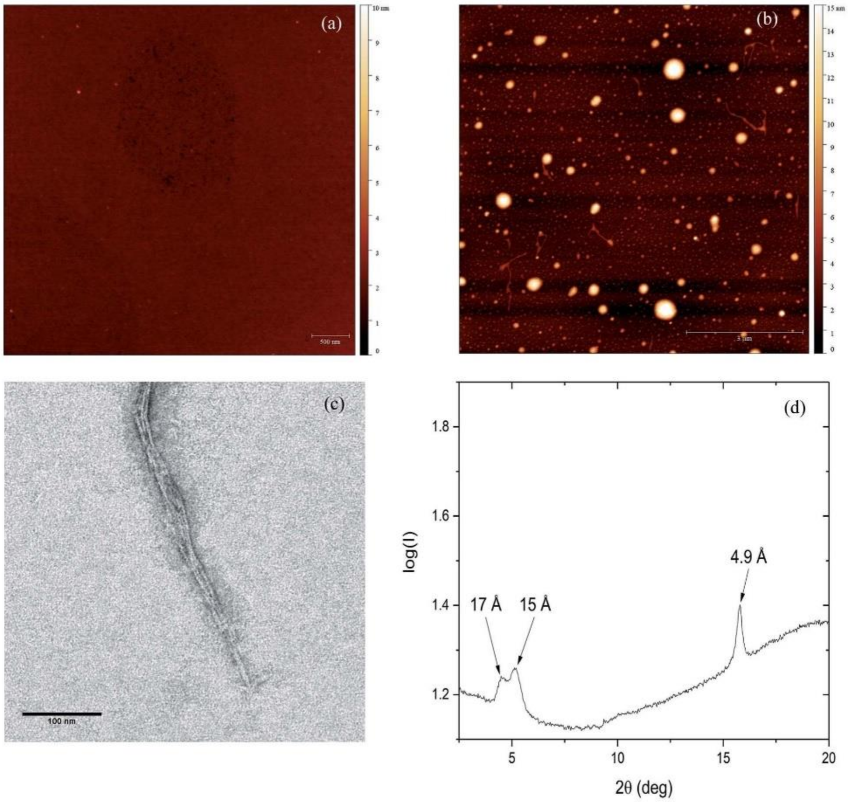

Fig. 3 (a) AFM micrograph of monomeric PrP$^{58-93}$ peptide. (b) AFM micrograph of formed PrP$^{58-93}$ fibrils and oligomers in presence of $ZnCl_2$. (c) TEM image of PrP$^{58-93}$ fibrils formed in presence of $ZnCl_2$. (d) X-ray diffraction pattern for PrP$^{58-93}$ fibrils formed in presence of $ZnCl_2$. Three reflections are visible: one meridional at 4.9 Å and two equatorial at ~15 Å and ~17 Å.

well-defined parallel bundles (Fig. 3c), nevertheless the diameters of individual fibrils could be assessed and ranged from 2.6 to 3 nm. Taking into account the grain size of uranyl formate (~0.4 nm)[56] the diameter of fibrils measured in TEM images is in good agreement with the height of single fibrils measured by AFM. Spherical oligomers were not visible in TEM micrographs probably because they could not be well stained with uranyl formate. One possible reason for that is a high content of random coil. Our FTIR spectra suggest that, upon the interaction between Zn(II) and PrP$^{58-93}$, the content of random coil in peptide increases. Therefore, the spherical oligomers might be unstructured intermediates in fibril formation.

The cross-β structure of the formed peptide fibrils was confirmed by X-ray diffraction (Fig. 4d). The diffraction pattern shows an intense and sharp meridional reflection at 4.9 Å, that indicates a structural spacing of β-sheets along the fibril axis.[8,57] Two weak and broad equatorial reflections at ~15 Å and ~17 Å are also visible (Fig. S4, ESI†). This result together with our previously presented spectroscopic and microscopic studies, indicates the existence of cross-β-structure for PrP$^{58-93}$ fibrils formed in the presence of Zn(II).

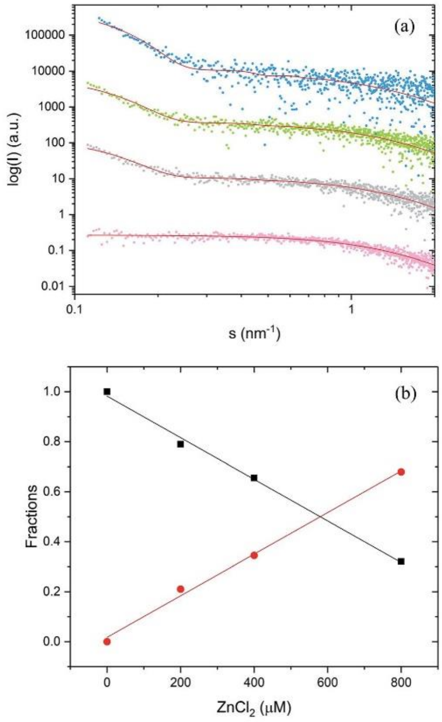

Fig. 4 SAXS analysis of PrP$^{58-93}$ peptide in solution. (a) SAXS data fitted in SASfit as a spheroid for 0.8 mM apo peptide (pink, MSWD 1.06) and as a mixture of spheroids and cylinders for 0.8 mM peptide with: 0.2 mM ZnCl$_2$ (gray MSWD 1.14), 0.4 mM ZnCl$_2$ (green, MSWD 1.09) and 0.8 mM ZnCl$_2$ (blue, MSWD 1.16). SAXS curves were displaced along the vertical axis for clarity. (b) Fractions of monomeric PrP$^{58-93}$ peptide (black squares) and fibrils (red dots) as a function of ZnCl$_2$ concentration.

Effect of Zn(II) on PrP$^{58-93}$ peptide monomeric state

To gain structural information on the peptide structure in solution we subjected it to synchrotron radiation small angle X-ray scattering study. The initial apo PrP$^{58-93}$ sample was monodisperse (DLS – Fig S5 and S6, ESI†). For PrP$^{58-93}$ at a concentration of 0.8 mM, the peptide molecules were characterized by the radius of gyration (R_g) equal to 1.31 ± 0.03 nm ($s_{\max}R_g < 1.3$, fidelity 0.74; Fig. S7, ESI†). This value is significantly smaller than the theoretical $R_g = 1.65$ nm calculated for an intrinsically disordered protein of the same length,[58] which suggests compactness and nonlinear shape of the peptide molecule. The shape of the calculated pair-distance distribution function suggests that the peptide molecule adopts a spherical shape with an elastic tail, characterized by $D_{\max} = 4.3$ nm (Fig. S8, ESI†).

On the basis of our initial SAXS analysis, the behavior of PrP$^{58-93}$ peptide seemed to be different than expected for an unstructured peptide. SAXS data alone can be used for a construction of a low-resolution model of a peptide structure[59] therefore we performed molecular modeling with two different approaches. In the first approach, commonly used for structured proteins, molecular envelope of a peptide was reconstructed by *ab initio* bead-modeling in DAMMIN,[60] and in the second, commonly used in the analysis of intrinsically disordered proteins,[61] a large pool of random PrP$^{58-93}$ peptide conformations was created and a final ensemble of models best matching the experimental data was chosen.[62] Models generated by both approaches fitted well our data (Fig. S9, ESI,† $\chi^2 = 1.013$ and $\chi^2 = 1.011$ respectively). From the pool of random conformations, PrP$^{58-93}$ peptide apparently adopted two equally distributed states: compact and extended. Even though each of the two states is highly dynamic the compact state seemed to form a loop and was similar to the NMR structure of PrP$^{61-84}$ published by Zahn (PDB: 1OEI),[63] where the extended conformation resembled the features of PPII helix (Fig. S10, ESI†).[64] Both conformations could be superimposed with the calculated *ab initio* bead-model (Fig. S10, ESI†), which suggested that the molecular envelope may correspond to a volume available for all conformational states of PrP$^{58-93}$.

Subsequent addition of ZnCl$_2$ up to the equimolar concentration of the prion peptide (0.8 mM), resulted in an increase in the scattering intensity at the scattering vectors $s < 0.3$ nm^{-1}, which can be attributed to peptide aggregation[65] caused by zinc (Fig. 4a, gray, green and blue circles Fig. 4a). Because of the appearance of sample polydispersity after addition of ZnCl$_2$, further analysis was performed in SASfit[46] upon three assumptions: (1) the molecular shape of apo peptide can be simplified to a spheroid with the polar semi-axis = 2.86 nm, equatorial semi-axis = 0.98 nm and scattering length density = 0.33, (2) addition of Zn^{2+} results in the appearance of the second scattering component in SAXS curve and (3) only the number of scatters can change. The fitting procedure of the polydisperse SAXS curve is complex because both, the particle shape, as well as the particle size distribution of the second component can vary. The second scattering component was chosen arbitrarily as a cylinder of a radius 14.1 nm, length 36.7 nm, and scattering length density = 0.33, because the cylinder shape corresponds to the shape of fibrillar structures, observed by us in the TEM and AFM images. After careful model selection, scattering intensity weighted models were fitted well to experimental data (red lines Fig. 4a).

The proposed models fitted well our SAXS data with the highest MSWD = 1.16 for 0.8 mM PrP^{58-93} with 0.8 mM $ZnCl_2$. Two-component analysis of SAXS data revealed that the addition of zinc into PrP^{58-93} sample causes a gradual decrease in the content of the monomer (spheroid) fraction in favor of the oligomer (cylinder) fraction (Fig. 4b). The reported dissociation constant for Zn(II)-octarepeat peptide complex differs from ~0.4 μM to ~200 μM,[22,30] however in the experiment with 800 μM PrP^{58-93} concentration, the direct binding should give a linear response up to the stoichiometric point. In our SAXS experiments, the content of the monomer fraction changed linearly as a function of zinc ions concentration, which can be interpreted as a result of direct metal binding to the octarepeat peptide.

Many different metal ions modulate aggregation of amyloid peptides or proteins.[66] Here we reported the discovery of amyloid-like structures formed by an isolated prion protein octarepeat domain PrP^{58-93}. The fibrils formed from the unstructured PrP^{58-93} peptide in the presence of Zn^{2+} ions fulfill the fundamental criteria to be classified as amyloid structures: they form cross-β structure, bind two amyloid-specific dyes and form elongated structures, observed by AFM and TEM.[5] Even though the outcome of our research is a model, we hypothesize, that such a phenomenon might occur in the synaptic cleft, where transient zinc concentration can reach millimolar values.[36]

The results of ThT, CR assays and SAXS experiments suggest heterogeneous primary nucleation of PrP^{58-93} peptide in the presence of Zn(II) cations.[54] PrP^{58-93} starts to aggregate after the addition of zinc cations and the relative content of monomeric peptide drops gradually only in the presence of the metal ion. Nevertheless, branched fibrils visible in AFM micrographs indicate the existence of secondary nucleation.[68] Spherical oligomers seem to be the centers of fibril nucleation, as fibrils appear to grow directly from them, nevertheless, they could be observed only in AFM images. The reason for the inability to observe these oligomers in TEM images is the apparent lack of structure, which can hamper staining with uranyl formate. Oligomers were also not visible on the SAXS curves, probably due to a concentration dependent shift of equilibrium towards fibrils rather than to oligomers.

On the basis of our data we propose a hypothetical scenario of PrP^{58-93} aggregation that requires several steps: (i) Zn^{2+} cation is bound by four deprotonated histidine residues of a single peptide molecule; (ii) direct binding induces structural rearrangements that are not available for peptide in the apo state; (iii) two newly formed Zn(II)-PrP^{58-93} species have low energetic barrier for nucleation and can form a dimer; (iv) elongation occurs by addition of other Zn(II)-PrP^{58-93} molecules as building bricks (but not apo PrP^{58-93} segments), (v) fibril termini contain solvent-exposed hydrophobic residues, therefore, in order to minimize energy, they can connect to already existing fibrils, forming perpendicular branches.

A similar heterogeneous primary nucleation has been observed for the four-repeat domain of Tau protein in the presence of heparin. In this case, two Tau protein molecules bound to the same heparin molecule can form aggregation-prone dimer and further fibril elongation occurs by the addition of monomers to the ends of the formed nucleation center.[69] Our results are in contrast to the studies performed on the full-length mouse and human PrP^C, in which the presence of Zn(II) cations inhibited the formation of amyloid fibrils.[70,71] Nevertheless, these studies were performed under denaturing conditions, where different conformational states of the Zn(II)-occupied octarepeat domain are favored. Denaturing conditions may disrupt the coordination of Zn(II) by the octarepeat domain and therefore change the aggregation path. Other possible explanation of the formation of PrP^{58-93} fibrils in the presence of Zn^{2+} ions might be the lack of tertiary contact between the Zn(II)-occupied octarepeat domain and helices 2 and 3.[40] Such a tertiary fold is altered in the E199K point mutant of mouse PrP^C, which is responsible for familial Creutzfeldt–Jakob disease, and a lack of such interaction might be responsible for PrP^C misfolding and formation of PrP^{Sc}.[40]

Similar studies have been also performed for amyloid β (Aβ), the peptide involved in the formation of amyloid aggregates in Alzheimer's disease. Dissociation constant reported for Zn(II)-$A\beta_{40}$ is in low micromolar range,[72,73] which is to some degree similar to the reported K_D for PrP^C,[22,30,31] nevertheless, zinc seems to have a protective influence on Aβ aggregation. Stoichiometric concentrations of Zn(II) induced precipitation of Aβ oligomers,[74,75] the form more cytotoxic than fibrillar structures.[76] At sub-stoichiometric concentrations Zn(II) inhibited fibril formation[77] and reduced toxicity in cultured primary hippocampal neurons.[78] Prion protein was shown to interact with Aβ oligomers and fibrils,[79–81] therefore it would be interesting to investigate Aβ fibrillization with PrP^{58-93} at different Zn(II) concentration.

The formation of fibrillar structures by various proteins or peptides accompanies the protein misfolding processes. Some of these proteins are characterized by the intrinsic flexibility of their three-dimensional structure. A good example of such flexible protein structure is human cystatin C (HCC) for which, in the native state, the domain swapping phenomenon, the formation of polymorphic structures, oligomers, fibrils, and aggregates have been observed.[82–87]

Conclusions

In our study we investigated the effect of Zn(II) on the aggregation of prion octarepeat peptide. Our results show that this monomeric peptide upon interaction with Zn(II) forms ThT and CR-specific fibrillar aggregates with cross-β structure. The formed fibrils fulfill the main criteria of classifications as amyloid fibrils. Moreover, we proposed a hypothetical model of Zn(II)-induced PrP$^{58-93}$ aggregation, that might be verified by future kinetic or structural studies. Our results provide important clues on protein misfolding and Zn(II) homeostasis that are associated with prion diseases.

PrP$^{58-93}$ peptide fibrils formed are also a potential functional material.[88] Therefore, from the bionanotechnological point of view, we can expect that this system could be very useful in the design of nanofibrils formed in the presence of divalent cations (*e.g.* Zn^{2+}).

Conflicts of interest

There are no conflicts to declare.

Acknowledgements

This research was supported by a research grant (2014/15/B/ST4/04839) from the National Science Centre (Poland). The synchrotron SAXS data were collected at beamline P12 operated by EMBL Hamburg at the PETRA III storage ring (DESY, Hamburg, Germany). We would like to thank the beamline staff for kind assistance in using the beamline. Authors thank Dr Barbara Peplinska from NanoBioMedical Centre (A. Mickiewicz University) for support in collection of TEM images.

References

1 N. Gour, P. C. Kanth, B. Koshti, V. Kshtriya, D. Shah, S. Patel, R. Agrawal-Rajput and M. K. Pandey, *ACS Chem. Neurosci.*, 2019, **10**, 1230–1239.

2 S. Shaham-Niv, P. Rehak, D. Zaguri, A. Levin, L. Adler-Abramovich, L. Vuković, P. Král and E. Gazit, *Commun. Chem.*, 2018, **1**, 25.

3 W. Gospodarczyk and M. Kozak, *RSC Adv.*, 2017, **7**, 10973–10984.

4 R. N. Rambaran and L. C. Serpell, *Prion*, 2008, **2**, 112–117.

5 F. Chiti and C. M. Dobson, *Annu. Rev. Biochem.*, 2017, **86**, 27–68.

6 G. Wei, Z. Su, N. P. Reynolds, P. Arosio, I. W. Hamley, E. Gazit and R. Mezzenga, *Chem. Soc. Rev.*, 2017, **46**, 4661–4708.

7 T. Lührs, C. Ritter, M. Adrian, D. Riek-Loher, B. Bohrmann, H. Döbeli, D. Schubert and R. Riek, *Proc. Natl. Acad. Sci. U. S. A.*, 2005, **102**, 17342–17347.

8 T. Stromer and L. C. Serpell, *Microsc. Res. Tech.*, 2005, **67**, 210–217.

9 M. Wahlbom, X. Wang, V. Lindström, E. Carlemalm, M. Jaskolski and A. Grubb, *J. Biol. Chem.*, 2007, **282**, 18318–18326.

10 A. Szymańska, E. Jankowska, M. Orlikowska, I. Behrendt, P. Czaplewska and S. Rodziewicz-Motowidło, *Front. Mol. Neurosci.*, 2012, **5**, 82.

11 P. Saá, D. A. Harris and L. Cervenakova, *Expert Rev. Mol. Med.*, 2016, **18**, e5.

12 N. J. Cobb and W. K. Surewicz, *Biochemistry*, 2009, **48**, 2574–2585.

13 D. W. Colby and S. B. Prusiner, *Cold Spring Harbor Perspect. Biol.*, 2011, **3**, a006833.

14 S. B. Prusiner, *Proc. Natl. Acad. Sci. U. S. A.*, 1998, **95**, 13363–13383.

15 N. Mabbott, *Pathogens*, 2017, **6**, 60.

16 N. Stahl, D. R. Borchelt, K. Hsiao and S. B. Prusiner, *Cell*, 1987, **51**, 229–240.

17 N. Salès, K. Rodolfo, R. Hässig, B. Faucheux, L. Di Giamberardino and K. L. Moya, *Eur. J. Neurosci.*, 1998, **10**, 2464–2471.

18 R. Zahn, A. Liu, T. Lührs, R. Riek, C. von Schroetter, F. López García, M. Billeter, L. Calzolai, G. Wider and K. Wüthrich, *Proc. Natl. Acad. Sci. U. S. A.*, 2000, **97**, 145–150.

19 M.-A. Wulf, A. Senatore and A. Aguzzi, *BMC Biol.*, 2017, **15**, 34.

20 A. R. Castle and A. C. Gill, *Front. Mol. Biosci.*, 2017, **4**, 19.

21 N. T. Watt and N. M. Hooper, *Trends Biochem. Sci.*, 2003, **28**, 406–410.

22 G. S. Jackson, I. Murray, L. L. Hosszu, N. Gibbs, J. P. Waltho, A. R. Clarke and J. Collinge, *Proc. Natl. Acad. Sci. U. S. A.*, 2001, **98**, 8531–8535.

23 J. H. Viles, F. E. Cohen, S. B. Prusiner, D. B. Goodin, P. E. Wright and H. J. Dyson, *Proc. Natl. Acad. Sci. U. S. A.*, 1999, **96**, 2042–2047.

24 C. S. Burns, E. Aronoff-Spencer, C. M. Dunham, P. Lario, N. I. Avdievich, W. E. Antholine, M. M. Olmstead, A. Vrielink, G. J. Gerfen, J. Peisach, W. G. Scott and G. L. Millhauser, *Biochemistry*, 2002, **41**, 3991–4001.

25 M. Chattopadhyay, E. D. Walter, D. J. Newell, P. J. Jackson, E. Aronoff-Spencer, J. Peisach, G. J. Gerfen, B. Bennett, W. E. Antholine and G. L. Millhauser, *J. Am. Chem. Soc.*, 2005, **127**, 12647–12656.

26 N. D. Younan, M. Klewpatinond, P. Davies, A. V. Ruban, D. R. Brown and J. H. Viles, *J. Mol. Biol.*, 2011, **410**, 369–382.

27 A. P. Garnett and J. H. Viles, *J. Biol. Chem.*, 2003, **278**, 6795–6802.

28 M. L. Kramer, H. D. Kratzin, B. Schmidt, A. Römer, O. Windl, S. Liemann, S. Hornemann and H. Kretzschmar, *J. Biol. Chem.*, 2001, **276**, 16711–16719.

29 M. A. Wells, C. Jelinska, L. L. P. Hosszu, C. J. Craven, A. R. Clarke, J. Collinge, J. P. Waltho and G. S. Jackson, *Biochem. J.*, 2006, **400**, 501–510.

30 E. D. Walter, D. J. Stevens, M. P. Visconte and G. L. Millhauser, *J. Am. Chem. Soc.*, 2007, **129**, 15440–15441.

31 P. Davies, F. Marken, S. Salter and D. R. Brown, *Biochemistry*, 2009, **48**, 2610–2619.

32 B. L. Vallee and D. S. Auld, *Biochemistry*, 1990, **29**, 5647–5659.

33 J. H. Weiss, S. L. Sensi and J. Y. Koh, *Trends Pharmacol. Sci.*, 2000, **21**, 395–401.

34 S. Y. Assaf and S. H. Chung, *Nature*, 1984, **308**, 734–736.

35 S. Lehmann, *Curr. Opin. Chem. Biol.*, 2002, **6**, 187–192.

36 N. T. Watt, H. H. Griffiths and N. M. Hooper, *Prion*, 2013, **7**, 203–208.

37 N. T. Watt, D. R. Taylor, T. L. Kerrigan, H. H. Griffiths, J. V. Rushworth, I. J. Whitehouse and N. M. Hooper, *Nat. Commun.*, 2012, **3**, 1134.

38 L. R. Brown and D. A. Harris, *J. Neurochem.*, 2003, **87**, 353–363.

39 P. C. Pauly and D. A. Harris, *J. Biol. Chem.*, 1998, **273**, 33107–33110.

40 A. R. Spevacek, E. G. B. Evans, J. L. Miller, H. C. Meyer, J. G. Pelton and G. L. Millhauser, *Structure*, 2013, **21**, 236–246.

41 B. S. Wong, D. R. Brown, T. Pan, M. Whiteman, T. Liu, X. Bu, R. Li, P. Gambetti, J. Olesik, R. Rubenstein and M. S. Sy, *J. Neurochem.*, 2001, **79**, 689–698.

42 M. R. Wilkins, E. Gasteiger, A. Bairoch, J. C. Sanchez, K. L. Williams, R. D. Appel and D. F. Hochstrasser, *Methods Mol. Biol.*, 1999, **112**, 531–552.

43 W. E. Klunk, R. F. Jacob and R. P. Mason, *Methods Enzymol.*, 1999, **309**, 285–305.

44 H. Yang, S. Yang, J. Kong, A. Dong and S. Yu, *Nat. Protoc.*, 2015, **10**, 382–396.

45 D. Nečas and P. Klapetek, *Cent. Eur. J. Phys.*, 2012, **10**, 181–188.

46 C. E. Blanchet, A. Spilotros, F. Schwemmer, M. A. Graewert, A. Kikhney, C. M. Jeffries, D. Franke, D. Mark, R. Zengerle, F. Cipriani, S. Fiedler, M. Roessle and D. I. Svergun, *J. Appl. Crystallogr.*, 2015, **48**, 431–443.

47 P. V. Konarev, V. V. Volkov, A. V. Sokolova, M. H. J. Koch and D. I. Svergun, *J. Appl. Crystallogr.*, 2003, **36**, 1277–1282.

48 D. Franke, M. V. Petoukhov, P. V. Konarev, A. Panjkovich, A. Tuukkanen, H. D. T. Mertens, A. G. Kikhney, N. R. Hajizadeh, J. M. Franklin, C. M. Jeffries and D. I. Svergun, *J. Appl. Crystallogr.*, 2017, **50**, 1212–1225.

49 D. I. Svergun, *J. Appl. Crystallogr.*, 1992, **25**, 495–503.

50 I. Breßler, J. Kohlbrecher and A. F. Thünemann, *J. Appl. Crystallogr.*, 2015, **48**, 1587–1598.

51 C. J. Smith, A. F. Drake, B. A. Banfield, G. B. Bloomberg, M. S. Palmer, A. R. Clarke and J. Collinge, *FEBS Lett.*, 1997, **405**, 378–384.

52 G. Di Natale, G. Pappalardo, D. Milardi, M. F. M. Sciacca, F. Attanasio, D. La Mendola and E. Rizzarelli, *J. Phys. Chem. B*, 2010, **114**, 13830–13838.

53 R. Khurana, C. Coleman, C. Ionescu-Zanetti, S. A. Carter, V. Krishna, R. K. Grover, R. Roy and S. Singh, *J. Struct. Biol.*, 2005, **151**, 229–238.

54 M. Biancalana and S. Koide, *Biochim. Biophys. Acta, Proteins Proteomics*, 2010, **1804**, 1405–1412.

55 M. A. Bryan, J. W. Brauner, G. Anderle, C. R. Flach, B. Brodsky and R. Mendelsohn, *J. Am. Chem. Soc.*, 2007, **129**, 7877–7884.

56 C. A. Scarff, M. J. G. Fuller, R. F. Thompson and M. G. Iadaza, *J. Visualized Exp.*, 2018, **132**, 57199.

57 K. L. Morris and L. C. Serpell, *Methods Mol. Biol.*, 2012, **849**, 121–135.

58 P. Bernadó and D. I. Svergun, *Mol. BioSyst.*, 2012, **8**, 151–167.

59 H. D. T. Mertens and D. I. Svergun, *J. Struct. Biol.*, 2010, **172**, 128–141.

60 D. I. Svergun, *Biophys. J.*, 1999, **76**, 2879–2886.

61 A. G. Kikhney and D. I. Svergun, *FEBS Lett.*, 2015, **589**, 2570–2577.

62 G. Tria, H. D. T. Mertens, M. Kachala and D. I. Svergun, *IUCrJ*, 2015, **2**, 207–217.

63 R. Zahn, *J. Mol. Biol.*, 2003, **334**, 477–488.

64 A. A. Adzhubei, M. J. E. Sternberg and A. A. Makarov, *J. Mol. Biol.*, 2013, **425**, 2100–2132.

65 S. Skou, R. E. Gillilan and N. Ando, *Nat. Protoc.*, 2014, **9**, 1727–1739.

66 L. Breydo, J. M. Redington and V. N. Uversky, *Int. Rev. Cell Mol. Biol.*, 2017, **329**, 145–185.

67 A. K. Buell, *Int. Rev. Cell Mol. Biol.*, 2017, **329**, 187–226.

68 S. Linse, *Pure Appl. Chem.*, 2019, **91**, 211–229.

69 G. Ramachandran and J. B. Udgaonkar, *J. Biol. Chem.*, 2011, **286**, 38948–38959.

70 O. V. Bocharova, L. Breydo, V. V. Salnikov and I. V. Baskakov, *Biochemistry*, 2005, **44**, 6776–6787.

71 K. Pan, C.-W. Yi, J. Chen and Y. Liang, *Biochim. Biophys. Acta, Proteins Proteomics*, 2015, **1854**, 907–918.

72 A. Clements, D. Allsop, D. M. Walsh and C. H. Williams, *J. Neurochem.*, 1996, **66**, 740–747.

73 J. Danielsson, R. Pierattelli, L. Banci and A. Gräslund, *FEBS J.*, 2007, **274**, 46–59.

74 K. Garai, B. Sahoo, S. K. Kaushalya, R. Desai and S. Maiti, *Biochemistry*, 2007, **46**, 10655–10663.

75 K. Garai, P. Sengupta, B. Sahoo and S. Maiti, *Biochem. Biophys. Res. Commun.*, 2006, **345**, 210–215.

76 M. Sakono and T. Zako, *FEBS J.*, 2010, **277**, 1348–1358.

77 A. Abelein, A. Gräslund and J. Danielsson, *Proc. Natl. Acad. Sci. U. S. A.*, 2015, **112**, 5407–5412.

78 M. A. Lovell, C. Xie and W. R. Markesbery, *Brain Res.*, 1999, **823**, 88–95.

79 K. Nieznanski, K. Surewicz, S. Chen, H. Nieznanska and W. K. Surewicz, *ACS Chem. Neurosci.*, 2014, **5**, 340–345.

80 J. Laurén, D. A. Gimbel, H. B. Nygaard, J. W. Gilbert and S. M. Strittmatter, *Nature*, 2009, **457**, 1128–1132.

81 D. A. Gimbel, H. B. Nygaard, E. E. Coffey, E. C. Gunther, J. Lauren, Z. A. Gimbel and S. M. Strittmatter, *J. Neurosci.*, 2010, **30**, 6367–6374.

82 R. Janowski, M. Kozak, E. Jankowska, Z. Grzonka, A. Grubb, M. Abrahamson and M. Jaskolski, *Nat. Struct. Biol.*, 2001, **8**, 316–320.

83 M. Kozak, E. Jankowska, R. Janowski, Z. Grzonka, A. Grubb, M. Alvarez Fernandez, M. Abrahamson and M. Jaskolski, *Acta Crystallogr., Sect. D: Biol. Crystallogr.*, 1999, **55**, 1939–1942.

84 R. Janowski, M. Kozak, M. Abrahamson, A. Grubb and M. Jaskolski, *Proteins: Struct., Funct., Bioinf.*, 2005, **61**, 570–578.

85 G. Östner, V. Lindström, P. Hjort Christensen, M. Kozak, M. Abrahamson and A. Grubb, *J. Biol. Chem.*, 2013, **288**, 16438–16450.

86 M. Chrabąszczewska, M. Maszota-Zieleniak, Z. Pietralik, M. Taube, S. Rodziewicz-Motowidło, A. Szymańska, K. Szutkowski, D. Clemens, A. Grubb and M. Kozak, *J. Appl. Phys.*, 2018, **123**, 174701.

87 M. Taube, Z. Pietralik, A. Szymanska, K. Szutkowski, D. Clemens, A. Grubb and M. Kozak, *Sci. Rep.*, 2019, **9**, 8548.

88 C. Li, R. Qin, R. Liu, S. Miao and P. Yang, *Biomater. Sci.*, 2018, **6**, 462–472.

Electronic Supplementary Material (ESI) for RSC Advances.
This journal is © The Royal Society of Chemistry 2019

Electronic Supplementary Information

PrP (58-93) peptide from unstructured N-terminal domain of prion protein forms amyloid-like fibrillar structures in the presence of Zn2+ ions

*Maciej Gielnik[1], Zuzanna Pietralik[1], Igor Zhukov[2], Aneta Szymańska[3], Wojciech M. Kwiatek[4], Maciej Kozak[1,5,6]**

[1]Department of Macromolecular Physics, Faculty of Physics, Adam Mickiewicz University, PL 61-614 Poznań, Poland

[2]Institute of Biochemistry and Biophysics, Polish Academy of Sciences, PL 02-106 Warszawa, Poland

[3]Department of Biomedical Chemistry, Faculty of Chemistry, Gdańsk University, PL 80-308 Gdańsk, Poland

[4]Institute of Nuclear Physics Polish Academy of Sciences, PL 31-342 Krakow, Poland.

[5]Joint Laboratory for SAXS Studies, Faculty of Physics, Adam Mickiewicz University, PL 61-614 Poznań, Poland

[6]National Synchrotron Radiation Centre SOLARIS, Jagiellonian University, PL 30-392 Kraków, Poland

Corresponding Author

* e-mail: mkozak@amu.edu.pl

Peptide synthesis

The peptide NH$_2$-GQ(PHGGGWGQ)$_4$GG-COOH was synthesized on TentaGel R RAM resin (loading capacity of 0.2 mmol/g; Rapp Polymere, Germany) using a Microwave Liberty Blue (CEM) peptide synthesizer. The peptide standard Fmoc/tBu amino acid chemistry was used. The cleavage of the peptide from the resin with the simultaneous deprotection of the amino acids side chains was accomplished using a cleavage cocktail consisting of 88% trifluoroacetic acid (TFA), 5% water, 5% phenol and 2% triethylsilane (v/v/m/v) under neutral (argon) atmosphere and in the dark. Crude peptide was precipitated using cold diethyl ether, centrifuged and lyophilized. The compound was next purified to at least 98% purity by means of reversed-phase high-performance liquid chromatography (RP-HPLC) using a Luna C8(2) AXIA Pack column (250 x 21.2 mm, 5 µm, 100 Å; Phenomenex). A linear gradient of acetonitrile in 0.1% aqueous trifluoroacetic acid (TFA) was applied as a mobile phase. The purity of the synthesized compound was evaluated by analytical UHPLC method using a Kinetex C8 column (100 x 2.1 mm, 2.6 µm, 100 Å; Phenomenex) operated by the NEXERA X2 chromatography system (Shimadzu) in a 15 min linear gradient of 4–80% acetonitrile in 0.1% aqueous TFA. UV absorption was monitored at $\lambda = 223$ nm and 254 nm. The molecular weight of the peptide was confirmed by the mass spectrometry method using an ESI-IT-TOF-LC-MS system (Shimadzu) with a C12 Jupiter Proteo column (150 × 2 mm, 4µm, 90 Å; Phenomenex).

Circular dichroism

CD spectra were measured on Jasco J-815 spectropolarimeter over the spectral range 260 - 200 nm with data pitch 0.5 nm, bandwidth 2 nm in a step scan mode with digital integration time of 4 s.

SAXS modeling of apo PrP$^{58\text{-}93}$ peptide

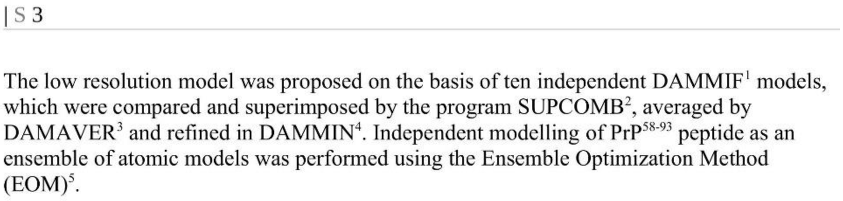

The low resolution model was proposed on the basis of ten independent DAMMIF[1] models, which were compared and superimposed by the program SUPCOMB[2], averaged by DAMAVER[3] and refined in DAMMIN[4]. Independent modelling of PrP$^{58\text{-}93}$ peptide as an ensemble of atomic models was performed using the Ensemble Optimization Method (EOM)[5].

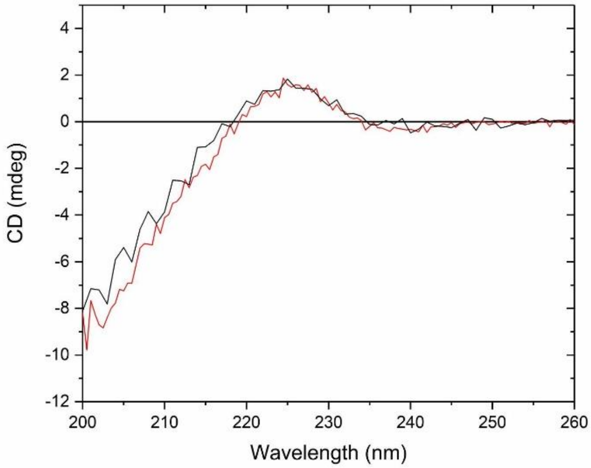

Figure S1. Far UV CD spectra for 5µM PrP$_{58\text{-}93}$ peptide prepared from fresh 1mM stock solution (red line) and after incubation of stock solution for seven months in room temperature (black line). Stock solution and measurements were performed in 10 mM NaH_2PO_4/Na_2HPO_4 buffer, pH 7.4

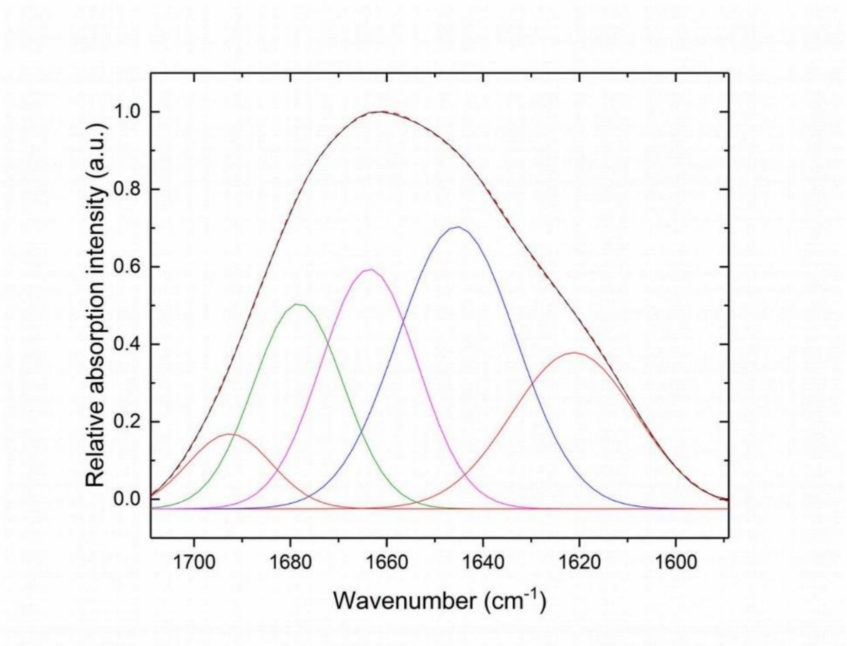

Figure S2. FTIR spectrum for 600 μM *apo*-PrP$_{58-93}$ peptide (black solid line), and curve fitted spectrum (red dashed line). Blue, magenta, green and red curves correspond to random coil, 3_{10}-helix, β-turns, β-sheets respectively.

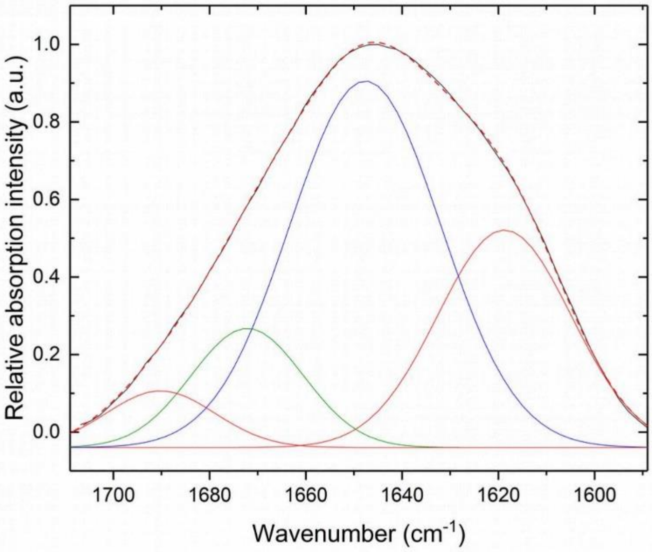

Figure S3. FTIR spectrum for 600 µM *apo*-PrP$_{58-93}$ peptide incubated with 2.4 mM of ZnCl$_2$ for 30 minutes (black solid line), and curve fitted spectrum (red dashed line). Blue, green and red curves correspond to random coil, β-turns, β-sheets respectively.

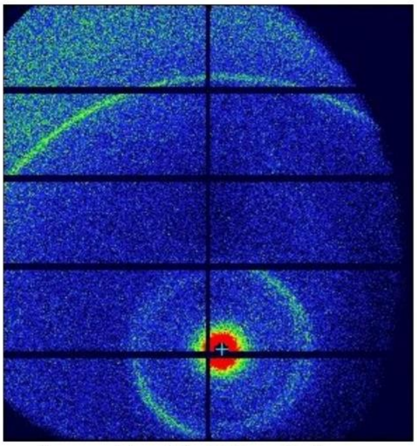

Figure S4. 2D diffraction pattern registered for PrP$_{58\text{-}93}$ fibrils.

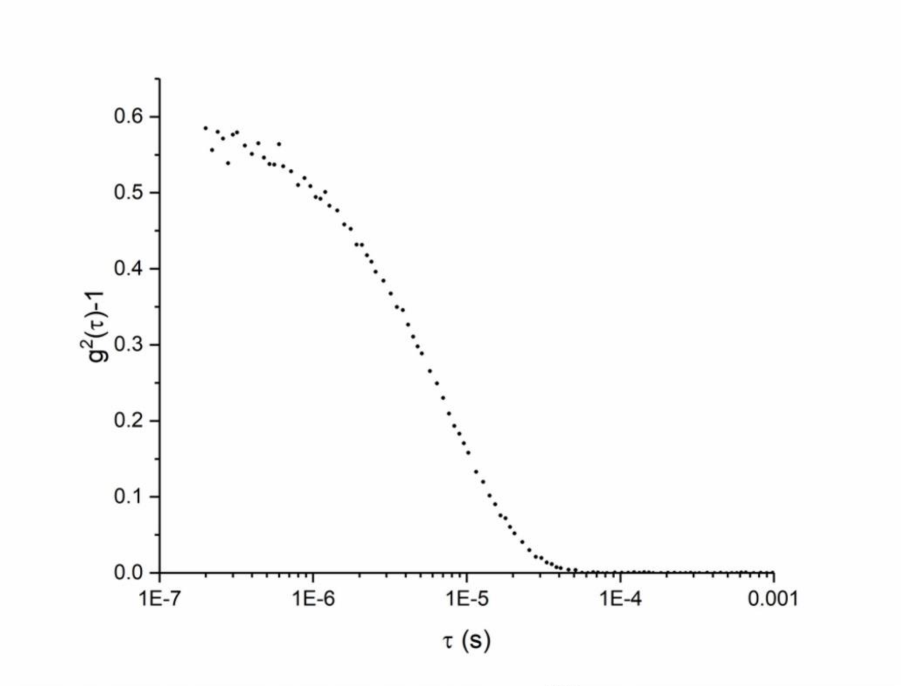

Figure S5. Second-order correlation function for 0.6 mM PrP$^{58-93}$ peptide.

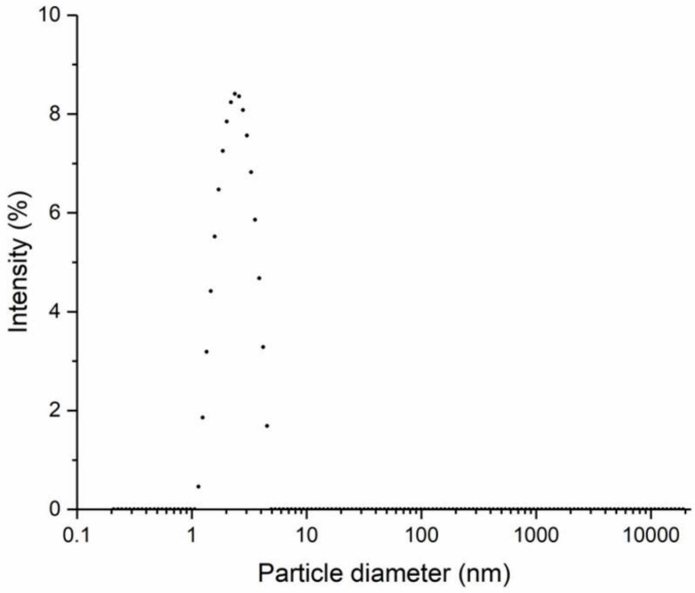

Figure S6. Intensity-weighted size distribution for for 0.6 mM PrP$^{58\text{-}93}$ peptide.

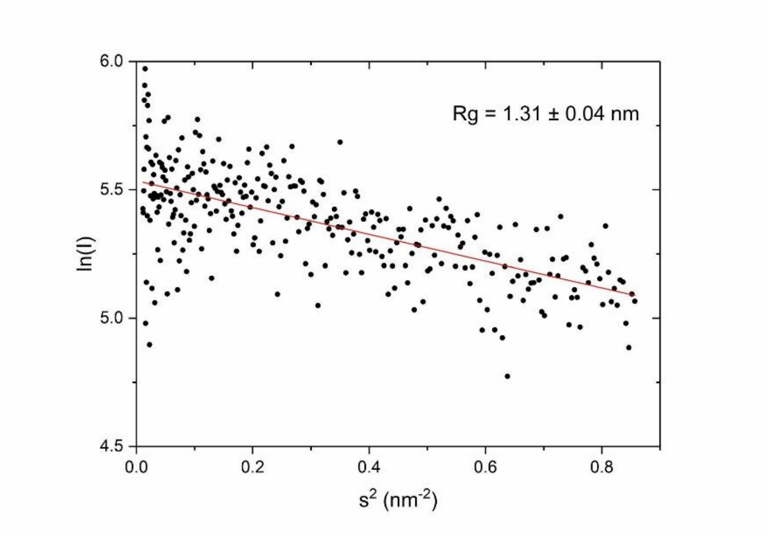

Figure S7. Guinier plot for *apo* PrP$_{58\text{-}93}$ peptide. Straight red line represents the fit to Guinier equation and corresponds to Rg = 1.31 ± 0.04 nm (fidelity 0.74).

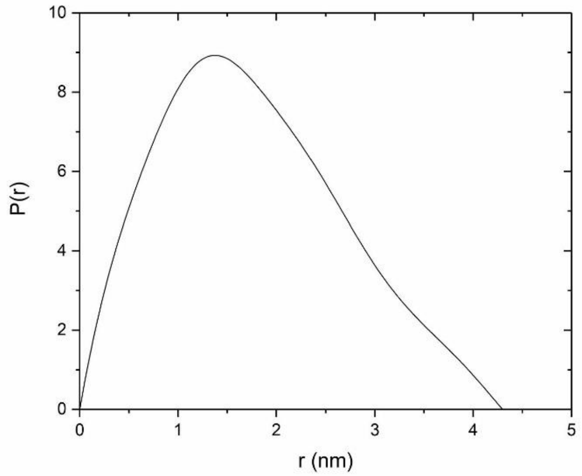

Figure S8. Pair-distance distribution function [P(r)] calculated on the basis of experimental SAXS data. The shape of P(r) function suggests that *apo* PrP_{58-93} peptide has spherical shape with elastic tail.

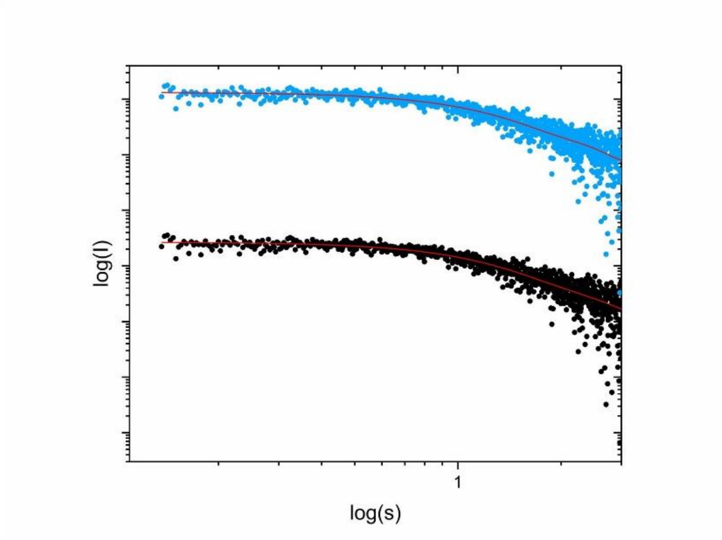

Figure S9. Quality of SAXS modeling for *apo* peptide. *Ab initio* model fitted into SAXS data (red line and black dots) and ensemble model fitted into SAXS data (red line and blue dots).

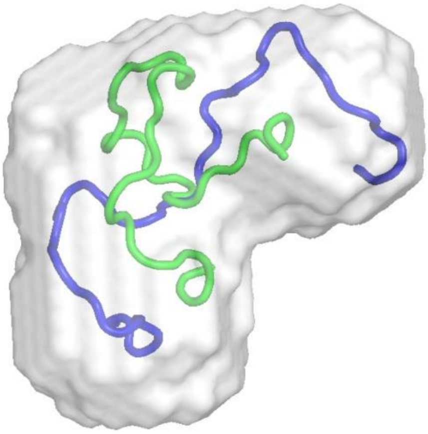

Figure S10. Superposition of total space molecular envelope calculated in DAMAVER and models generated in EOM for PrP (58-93) peptide. Green and blue ribbons corresponds to a compact and extended extended conformation respectively.

References

1 D. Franke and D. I. Svergun, *J. Appl. Crystallogr.*, 2009, **42**, 342–346.
2 M. B. Kozin and D. I. Svergun, *J. Appl. Crystallogr.*, 2001, **34**, 33–41.
3 V. V. Volkov and D. I. Svergun, *J. Appl. Crystallogr.*, 2003, **36**, 860–864.
4 D. I. Svergun, *Biophys. J.*, 1999, **76**, 2879–2886.
5 G. Tria, H. D. T. Mertens, M. Kachala and D. I. Svergun, *IUCrJ*, 2015, **2**, 207–217.

The Prion Protein Octarepeat Domain Forms Transient β-sheet Structures Upon Residue-Specific Cu(II) and Zn(II) Binding

Maciej Gielnik [1], Aneta Szymańska [2], Xiaolin Dong[3], Jüri Jarvet [3,4], Željko M. Svedružić [5], Astrid Gräslund [3], Maciej Kozak [1,6], and Sebastian K. T. S. Wärmländer [3,*]

1 Department of Macromolecular Physics, Faculty of Physics, Adam Mickiewicz University, PL 61-614 Poznań, Poland; maciejgielnik@amu.edu.pl (M.G.); mkozak@amu.edu.pl (M.K)

2 Department of Biomedical Chemistry, Faculty of Chemistry, Gdańsk University, PL 80-308 Gdańsk, Poland; aneta.szymanska@ug.edu.pl (A.S.)

3 Department of Biochemistry and Biophysics, Stockholm University, 10691 Stockholm, Sweden; seb@student.su.se (S.K.T.S.W.); jyri.jarvet@dbb.su.se (J.J.); astrid@dbb.su.se (A.G.)

4 The National Institute of Chemical Physics and Biophysics, 12618 Tallinn, Estonia

5 Department of Biotechnology, University of Rijeka, HR 51000, Rijeka, Croatia; zeljko.svedruzic@biotech.uniri.hr (Ž.S.)

6 National Synchrotron Radiation Centre SOLARIS, Jagiellonian University, PL 30-392 Kraków, Poland

* Corresponding author.

Keywords: copper; zinc; prion protein; prion disease; β-sheet formation; spectroscopy

Acknowledgments: This study was supported by a research grant (2014/15/B/ST4/04839) from the National Science Centre in Poland to MK, by a grant from the Magnus Bergvall foundation in Sweden to SKTSW, and from grants from the Swedish Research Council and the Brain Foundation in Sweden to AG. High-performance computing at the University of Rijeka was supported by grants to ŽS from the European Fund for Regional Development (ERDF) and from the Ministry of Science, Education and Sports of the Republic of Croatia under project number RC.2.2.06-0001.

Abstract

Misfolding of the cellular prion protein (PrP^{C}) is associated with the development of fatal neurodegenerative diseases called transmissible spongiform encephalopathies (TSEs). Metal ions appear to play a crucial role in the protein misfolding, and metal imbalance may be part of TSE pathologies. PrP^{C} is a combined Cu(II) and Zn(II) metal binding protein, where the main metal binding site is located in the octarepeat (OR) region. Here, we used biophysical methods to characterize Cu(II) and Zn(II) binding to the isolated OR region. Circular dichroism (CD) spectroscopy data suggest that the OR domain binds up to four Cu(II) ions or two Zn(II) ions. Upon metal binding, the OR region seems to adopt a transient antiparallel β-sheet hairpin structure. Fluorescence spectroscopy data indicates that under neutral conditions, the OR region can bind both Cu(II) and Zn(II) ions, whereas under acidic conditions it binds only Cu(II) ions. Molecular dynamics simulations suggest that binding of both metal ions to the OR region results in formation of β-hairpin structures. As formation of β-sheet structures is a first step towards amyloid formation, we propose that high concentrations of either Cu(II) or Zn(II) ions may have a pro-amyloid effect in TSEs.

1. Introduction

Transmissible spongiform encephalopathies (TSEs) are a group of neurodegenerative disorders initiated by misfolding of the cellular prion protein (PrP^C)[1,2]. The human PrP^C is a 208 residues long protein expressed at high level in the central nervous system. It is composed of two structurally different regions: an unstructured N-terminal domain, and a globular and mostly α-helical C-terminal domain[3] that attaches to the pre- and post-synaptic membranes via a GPI anchor[4,5]. For unknown reasons, and in a process similar to those for amyloid-forming peptides and proteins[6,7], PrP^C can undergo a structural transition into an insoluble, aggregated form with high β-sheet content called PrP^{Sc}. It has been suggested that PrP is most toxic when forming soluble oligomers, i.e. intermediate species during PrP^{Sc} formation, which can accumulate in brain tissue and cause neurodegeneration[8]. Even though human TSEs are very rare and only affect one person per million[9], they share many similarities with the pathologies characterized by proteins aggregating into amyloid states, and multiple evidence indicates that the prion and amyloid diseases all belong to a large family of protein aggregation diseases[10–13]. Examples include tauopathies (tau protein)[14], Alzheimer's disease (Aβ peptide)[15], Parkinson's disease (α-synuclein protein)[16], and amyotrophic lateral sclerosis/ALS (TDP-43 protein)[17,18]. Thus, it has recently been proposed that beside TSEs, PrP can be involved also in the development of other neurodegenerative diseases, such as Alzheimer's disease[19].

The native function of PrP^C is still elusive. The PrP^C protein is encoded by the *PRNP* gene, and most *PRNP* knockout animals (i.e., without the *PRNP* gene) show normal development and behavior, although some individuals show deviation in neuronal signal transduction and locomotion[20]. Interestingly, all *PRNP* knockout mice are immune to PrP^{Sc} inoculation, which supports the theory of template-driven autocatalytic conversion of PrP^C to PrP^{Sc}[2,11]. Among the many functions attributed to PrP^C, i.e. cell signaling, antioxidation, and myelination[8], phylogenetic analysis indicates that PrP^C is evolutionary linked to the Zrt- and Irt-like Protein (ZIP) family of divalent metal transporters[21]. This suggests that one role for PrP^C might be in metal ion homeostasis, and metal imbalance has been suggested to be part of the pathology of prion diseases[22–24].

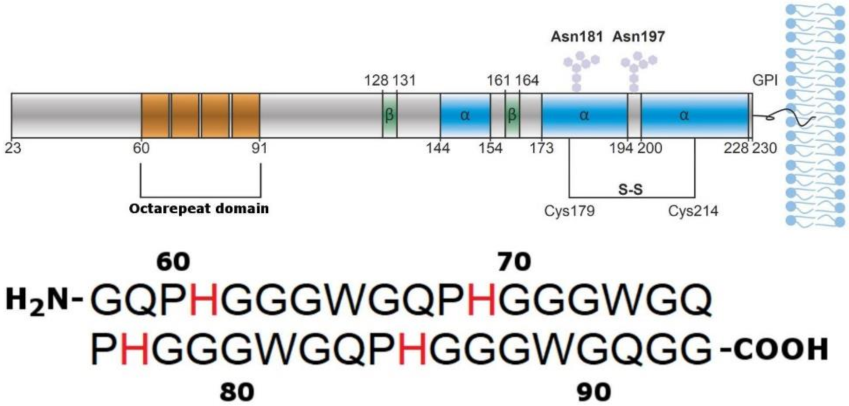

Figure 1. Top: Sequence of the human prion protein, with the octarepeat region marked as orange, β-sheets marked as green, and α-helices marked as blue. Image is from Gielnik et al.[25] under CC BY 4.0. Bottom: The octarepeat (OR) region studied in this paper comprises residues 58 – 93 of the prion protein, i.e. PrP^C(58-93). At neutral pH it has no charged residues. Possible metal-binding aromatic histidine residues are shown in red.

The PrP^C protein binds up to six different types of divalent metal ions, including Cu(II), Zn(II), Ni(II), and Mn(II), by two distinct domains with different metal ion affinities[26–28]. The octarepeat (OR) region is located in the N-terminal domain where it spans residues 60-91 (Fig. 1). It contains four tandem PHGGGWGQ repeats, and binds Cu(II), Zn(II) and Ni(II) ions with strong affinity[29]. The so-called "non-octarepeat region" spans residues 92-111, and binds Cu(II) ions with weaker affinity, where H96 and H111 are likely binding ligands[30,31]. The capacity of the OR region to bind Cu(II) ions has been intensively studied during the last twenty years. Cu(II) is an important neurotransmitter and the third most common transition metal in the brain[32]. The reported Cu(II) concentration in the synaptic cleft during neuron depolarization ranges from 3 μM[33] to 250 μM[34], which suggests that the dissociation constant (K_d) for the OR·Cu(II) complex is at least of this order of magnitude. The OR region has been reported to bind up to four Cu(II) ions[35–37], where the first ion is bound with the highest affinity (around 0.1 nM), and the three other display intermediate affinities around 10 µM[38]. Many possible biological functions have been attributed to the Cu(II)-binding capacity of PrP^C, including superoxide dismutase activity, transmembrane copper transport, copper buffering, and neuronal protection [39–42].

Another important metal ion for PrP^C neurobiology is Zn(II). Zinc is the second-most (after iron) abundant metal ion in the human body[43]. Upon neuronal stimulation, the transient concentration of Zn(II) ions in the synaptic vesicle can reach values around 300 µM[44]. Such Zn(II) concentrations stimulate PrP^C endocytosis into human neuroblastoma cells [45], and PrP^C has been shown to enhance Zn(II) transport[46]. An early study reported a K_d of 200 µM for the $PrP^C \cdot Zn(II)$ complex[47], but more recent ITC studies by the same researchers suggest a K_d of 17 µM, together with NMR experiments implying 1:1 stoichiometry[48]. The proposed PrP^C functions related to Zn(II) binding are similar to those proposed for Cu(II) binding, e.g. metal ion buffering and transport[24,49].

We have recently shown that the isolated OR region (i.e., an OR peptide) upon interaction with Zn(II) ions forms fibrillar cross-β structures that bind thioflavin T and Congo Red, and which possess all the characteristic features of amyloid material[50]. This indicates that metal ions can directly induce a transition of PrP^C into the amyloid state.

Here, we use circular dichroism (CD) and fluorescence spectroscopy, combined with molecular dynamics simulations, to estimate apparent K_d values for the $OR \cdot Cu(II)$ and $OR \cdot Zn(II)$ complexes, and to characterize the initial structural changes of the isolated OR region, i.e. PrP^C(58-93) (Fig. 1), after exposure to Cu(II) and Zn(II) ions.

2. Materials and Methods

2.1. Peptide synthesis and purification

The OR peptide, PrP(58-93), was obtained using solid peptide synthesis methodology. TentaGel R RAM resin (loading capacity of 0.18 mmol/g; Rapp Polymere, Germany) was used as a matrix. The synthesis was performed using a standard Fmoc/tBu amino acid chemistry on Microwave Liberty Blue synthesizer (CEM) peptide synthesizer. The crude peptide was cleaved from the solid support using a cleavage cocktail consisting of 88% trifluoroacetic acid (TFA), 5% water, 5% phenol and 2% triisopropylsilane (v/v/m/v) under neutral (argon) atmosphere, and protected from direct exposure to light. After precipitation with diethyl ether, the crude product was dissolved in water and lyophilized.

Peptide purification was carried out by reversed-phase high-performance liquid chromatography (RP-HPLC), using a Luna C8(2) AXIA Pack column (250 x 21.2 mm, 5 µm, 100 Å; Phenomenex, USA). A linear gradient of acetonitrile in 0.1% aqueous TFA was applied as a mobile phase. The purity of the obtained fractions was evaluated by analytical UHPLC, using a Kinetex C8 column (100 x 2.1 mm, 2.6 µm, 100 Å; Phenomenex, USA) operated by the NEXERA-i chromatography system (Shimadzu, Japan) in a 15 min linear gradient of 5-100% B (where B is 80% acetonitrile in 0.1% aqueous TFA). UV absorption was monitored at $\lambda = 223$ nm. Fractions with a purity higher than 99 % were pooled together for further analyses. The molecular weight of the final peptide sample was confirmed by mass spectrometry, using an ESI-IT-TOF-LC-MS system (Shimadzu, Japan) with a C12 Jupiter Proteo column (150 × 2 mm, 4µm, 90 Å; Phenomenex, USA).

2.2. Circular dichroism spectroscopy

Circular dichroism (CD) spectra of the OR peptide were recorded on a Chirascan CD (Applied Photophysics, UK) spectropolarimeter. Thermal unfolding experiments were performed for 20 µM OR peptide in 10 mM sodium phosphate buffer, pH 7.0, in a cuvette with 4 mm pathlength, in the range from 5 °C to 65 °C with 5 °C intervals. Spectra were recorded from 190 nm to 250 nm, with 0.5 nm steps and a time-per-point of 4 s. The content of PPII helix was estimated from the CD intensity expressed in mean residue ellipticity (a concentration-independent unit) at the local maximum at 225 nm of the CD spectra, i.e. θ_{max}, using the equation published by Kelly et al.[51], i.e., eq. 1:

$$\%PPII = \frac{[\theta]_{\max} + 6100}{13700} \times 100 \qquad (1)$$

Titrations with metal ions were conducted for 5 µM OR peptide dissolved either in pure MilliQ water or in 10 mM sodium phosphate buffer, pH 7.5. Using 1 cm path-length quartz cuvettes with gentle magnetic stirring at 25°C, the OR peptide (volume 2.5 ml) was titrated with small amounts of stock solutions of $CuCl_2$ or $ZnCl_2$ (100 µM, 500 µM, 1.25 µM or 5 µM stock concentrations) directly in the cuvette. All spectra were collected from 200 to 260 nm with sampling points every 0.5 nm, a time-per-point of 4 s, and 2 nm bandwidth. The final spectra were baseline-corrected and smoothed with a Savitzky-Golay filter. Data with single visible transitions were fitted to the transformed Hill equation, i.e., eq. 2:

$$[\theta] = [\theta]_0 + \frac{[\theta]_\infty - [\theta]_0}{1 + 10^{n_H(\log[K_d^{app}] - \log[Me])}} \tag{2}$$

Here, $[\theta]_0$ is the signal intensity before the transition, $[\theta]_\infty$ is the signal intensity at the end of the transition, n_H is the Hill coefficient, $[K_d^{app}]$ is the apparent dissociation constant, and [Me] is the metal ion concentration. When two transitions were observed, and the signal was monotonically increasing or decreasing, the data was fitted as a sum of two transformed Hill equations, i.e., eq. 3:

$$\begin{aligned} [\theta] = [\theta]_0 + ([\theta]_\infty - [\theta]_0)\Bigg[&\frac{p}{1 + 10^{n_{H1}(\log[K_{d1}^{app}] - \log[Me])}} \\ &+ \frac{1-p}{1 + 10^{n_{H2}(\log[K_{d2}^{app}] - \log[Me])}}\Bigg] \end{aligned} \tag{3}$$

Here, $[\theta]_0$ is the signal intensity before the transition, $[\theta]_\infty$ is the signal intensity at saturation, $[K_{d1}^{app}]$ and $[K_{d2}^{app}]$ are the apparent dissociation constants for the first and second binding sites, n_{H1} and n_{H2} are the Hill coefficients for the first and second binding sites, [Me] is the metal ion concentration, and p and 1-p are the relative signal intensities for the first and second binding sites. When the two transitions were observed with a local maximum or minimum in the signal, data was fitted as the sum of one transformed and one reverse-transformed Hill equation, i.e., eq. 4:

$$[\theta] = [\theta]_{max} + \frac{[\theta]_1 - [\theta]_{max}}{1 + 10^{n_{H1}(\log[Me] - \log[K_{d1}^{app}])}} + \frac{[\theta]_2 - [\theta]_{max}}{1 + 10^{n_{H2}(\log[K_{d2}^{app}] - \log[Me])}} \tag{4}$$

Here, $[\theta]_{max}$ is the signal intensity at the extreme point, $[\theta]_1$ is the signal intensity before the transition, $[\theta]_2$ is the signal intensity after the transition, and n_{H1}, n_{H2}, $[K_{d1}^{app}]$, $[K_{d2}^{app}]$, and [Me] have the same meaning as in eq. (3).

2.3. Fluorescence Spectroscopy

Fluorescence spectra of the OR peptide were recorded with a Cary Eclipse (Varian, USA) fluorometer equipped with a Peltier multicell holder, using quartz cuvettes with 1 cm path length. 5 μM of OR peptide was titrated with stock solutions of $CuCl_2$ and $ZnCl_2$, similar to the CD titrations (above), and using the following different buffers: (i)10 mM sodium phosphate buffer, pH 7.5, (ii) 10 mM MES (2-morpholinoethanesulfonic acid) buffer, pH 5.5, (iii) 10 mM MES buffer, pH 7.5. Some titrations with $CuCl_2$ were conducted in the presence of 1 mM of the reducing agent TCEP (tris(2-carboxyethyl)phosphine), to investigate the effect of reduced Cu(I) ions. The samples were excited at 285 nm, and emission spectra were recorded in the 300 - 500 nm range, with a 1 nm data interval and a scan speed of 600 nm/min. The excitation and emission bandwidths were respectively 10 nm and 5 nm, and the experiments were performed at 25 °C under quiescent conditions (i.e., no stirring). The fluorescence intensity at 255 nm was plotted versus metal ion concentration, and the resulting data curves were fitted with the same equations as those used for CD data (i.e., eq. 2).

2.4. Molecular dynamics simulations

Molecular dynamics simulations were performed in GROMACS 2019.2[52] using the OPLS-AA[53] force field. The systems were solvated with the TIP4P[54] water model and restrained using Van der Waals radii[55]. The LINCS algorithm[56] was used to restrain all covalent bonds in the peptide, and the SETTLE algorithm[57] was used to restrain all water molecules. In the initial model one or two nonbonded dummy Cu(II) or Zn(II) ion models[58] were placed in close proximity to $N^{\varepsilon 2}$ atoms of histidine side chains. The $N^{\varepsilon 2}$ atoms of the four histidine residues were either protonated or uncharged, to study the interactions under different pH conditions (for short peptides histidine protonation/deprotonation correspond to $pH < 6.8$ or $pH > 6.8$, respectively)[59]. The systems were neutralized with Cl^- ions, and the energy was minimized using steepest-descent energy minimization over 5000 steps. The temperature was equilibrated at 300 K, in an NVT ensemble over 0.5 ns with 1 fs time steps, using the modified Berendsen[60] thermostat. The pressure was equilibrated at 1 bar, in NPT ensemble over 0.5 ns with 1 fs time steps, using the Parrinello-Rahman[61] barostat. For long-range electrostatic interactions we applied PME[62] with 1.2 nm cutoff, and the same cutoff was used for Van der Waal forces. The MD production runs were performed in an NVT ensemble with 2 fs time step. The trajectories for the peptide with uncharged histidine residues were produced over 100 ns, while trajectories for the peptide with protonated histidine residues were produced over 10 ns. The results were analyzed in VMD[63] and visualized in the PyMOL Molecular Graphics System, Version 2.3.4 (Schrödinger, LLC). The secondary structure was assigned using the PROSS software[64], which estimates secondary structures as α-helix, β-strand, β-turn, and PPII, and classifies all other structures as "coil". The principal component analysis was performed in the Bio3D R package[65].

2.5 Calculation of pKa values

Final peptide conformations were extracted as frames from MD simulations by storing the structures as PDB files, which then were used as input for the two best known protocols for pKa calculations for protein structures. Thus, pKa values for the OR peptide were calculated using both the PropKa 2.0 software[66] with the PARSE[67] force field, and the DelPhiPKa software[68] with the AMBER force field[69]. The pKa values were calculated at physiological pH and ionic strength at 37 °C, following the instructions for each program. Two independent protocols were used for evaluation of calculation accuracy.

3. Results

3.1. The octarepeat (OR) region exhibits a mixture of random coil and PPII helix

The initial low-temperature (5 °C) CD spectrum of 20 µM *apo*-OR peptide showed one positive band at 225 nm, together with two negative bands: a weak one at 238 nm, and a strong one at 199 nm (Fig. 2A, dark green spectrum). The minimum around 199 nm is consistent with a random coil structure, but this conformation should not give rise to positive CD bands, such as the one at 225 nm. Other researchers have previously suggested that the OR peptide in aqueous solution adopts a PPII left-handed extended helix[70,71,72], or exhibits a mixture of random-coil and β-turn structures[35,73,74]. To clarify the secondary structure of the OR peptide, we recorded CD spectra at different temperatures to monitor the thermal unfolding of the peptide (Figs. 2A and 2B).

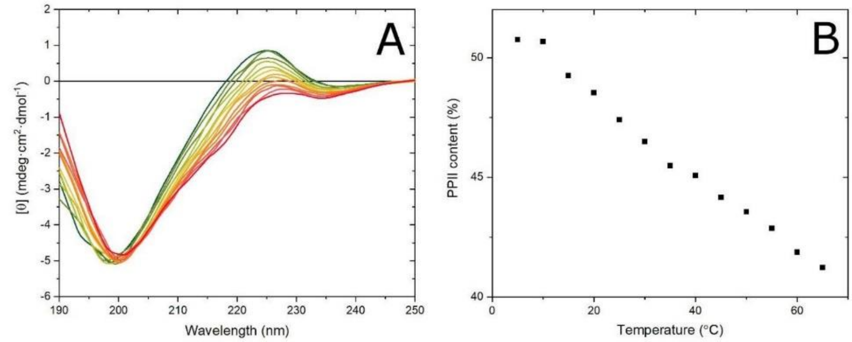

Figure 2. (**A**) CD spectra for thermal unfolding of 20 μM OR peptide from 5 °C (dark green line) to 65 °C (red bottom line) at 5 °C intervals. The isodichroic point at 204 nm, for spectra from 20 °C to 65 °C, suggests a PPII helix to random coil transition. All CD spectra were recorded in 10 mM phosphate buffer, pH 7.0. (**B**) Estimated content of PPII helix for all recorded temperatures, calculated from eq. 1 and CD intensities at 225 nm.

The intensity of the CD spectra at 225 nm gradually decreased when the temperature increased from 5 °C to 20 °C, but the spectral quality did not allow for any detailed interpretation of the spectral shape (Fig. 2A). For the spectra between 20 °C and 65 °C, however, an isodichroic point appeared at 204 nm (Fig. 2A). Together with the gradual decrease of the 225 nm band, this indicates a structural transition from PPII helix to random coil conformation[75]. We therefore calculated the PPII content in the OR peptide as a function of temperature (Fig. 2B), using the CD signal intensity at 225 nm and eq. 1.[51] The PPII content was highest at 5 °C, i.e. around 51%, and then gradually decreased to around 41% at 65 °C (Fig. 2B). Interestingly, in the temperature range of the isodichroic point, i.e. 20 °C to 65 °C, the amount of PPII helix decreased linearly as a function of temperature. Overall, these CD results indicate that the secondary structure of the OR peptide at physiological temperature is a mixture of random coil and PPII helix, with a significant amount - more than 45% - of PPII structure.

3.2. Cu(II) and Zn(II) binding to the OR peptide both induce formation of antiparallel β-sheet structure

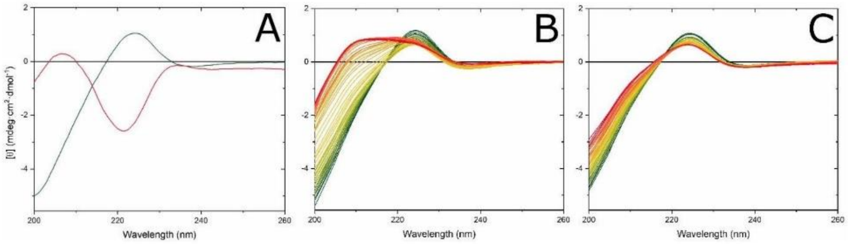

Figure 3. CD spectra for Cu(II) and Zn(II) binding to the OR peptide at 25 °C. (**A**) 5 μM OR peptide in water at pH 7.5 (no buffer) before (green line) and after (red line) addition of 20 μM $CuCl_2$. $CuCl_2$ was added at a pH of 4.0, and then the pH was adjusted to 7.5 with small amounts of NaOH. The shape of the red CD spectrum shows features reported in the literature as typical for a Cu(II)-OR complex. (**B**) Titration of 5 μM OR peptide in 10 mM phosphate buffer, pH 7.5, with $CuCl_2$ from 0 μM (green) to 40 μM (red). (**C**) Titration of 5 μM OR peptide in 10 mM phosphate buffer, pH 7.5, with $ZnCl_2$ from 0 μM (green) to 40 μM (red).

Previous studies suggest that Cu(II) binding to the OR peptide in pure water induces certain changes in the peptide's secondary structure, involving formation of β-turns or structured loops around the metal ions[35]. Our initial titrations of 5 μM OR peptide with $CuCl_2$ in water (pH adjusted to ~7.5 with NaOH and controlled by a pH meter) showed a gradual decrease in the CD signal that can be associated with peptide precipitation (Figure S1A). The final spectrum had a weak single minimum at 220 nm and a maximum at 208 nm, which may suggest formation of β-sheets. As the direct titrations with $CuCl_2$ in water appeared to induce severe aggregation, a different approach was tried. The 5 μM peptide solution was acidified with small amounts of acetic acid to pH ~4.0, then 20 μM of $CuCl_2$ was added, and the pH of the solution was slowly increased to ~7.5

with NaOH. This approach allowed us to acquire a CD spectrum with a shape that previously has been described in the literature as typical for the OR:Cu(II) complex, and interpreted as formation of β-turns or structured loops[35,72,73] (Fig. 3A, red spectrum).

To investigate the binding of Cu(II) ions to the OR peptide in a more controlled environment, we titrated $CuCl_2$ to 5 µM OR peptide in 10 mM phosphate buffer, pH 7.5 at 25 °C (Fig. 3B). The initial CD spectrum then began to lose intensity as 224 nm, and a new band appeared at 208 nm. Careful analysis of these CD spectra revealed three distinct spectral transitions, likely corresponding to transitions in the peptide's secondary structure. The first transition was present from 0 µM up to 5 µM of $CuCl_2$, corresponding to 1:1 Cu(II):OR peptide ratio. During this process the CD intensity at 224 nm decreased, and a new weak band appeared at 208 nm (Fig. 3B, green to yellow spectra). The isodichroic point at 217 nm was clearly visible, which could suggest a PPII to β-turn structural transition[76].

The second spectral transition appeared at $CuCl_2$ concentrations from 5 µM to 10 µM, corresponding to 2:1 Cu(II):OR peptide ratio. During this process the CD intensity at 208 nm strongly increased, while the CD band at 224 nm showed a small intensity increase (Fig. 3B, yellow to orange spectra). The absence of an observed isodichroic point excluded the possibility of a two-state transition and suggests formation of a new CD band. The difference spectrum for this transition (Fig. S2B, red line) resembled the CD spectrum for relaxed antiparallel β-sheets[77]. On the other hand, the difference spectrum could also be an inverted CD spectrum of a random coil[76], which would imply a loss in random coil secondary structure. However, the CD spectrum of a random coil secondary structure should have a minimum below 200 nm, but in our case the extremum is at 205 nm (Fig. S2B, red line). We therefore suggest that the second spectral transition involves formation of a relaxed antiparallel β-sheet secondary structure.

The third transition appeared for $CuCl_2$ concentrations from 10 µM to 40 µM (Fig. 3B, orange to red spectra). During this process, the newly formed band at 208 nm reached a maximum and maintained constant intensity, where the band at 224 nm began to lose intensity. No isodichroic point was observed, similarly to the second transition, which again suggests formation of a new spectral band. The difference spectrum (Fig. S2B, blue line) showed features similar to those observed in the second spectral transition, again suggesting formation of relaxed antiparallel β-sheets[77]. However, as the changes in the CD spectral intensity were smaller for the third transition then for the second transition, less of the new structure appears to have formed.

The final CD spectrum for the OR·Cu(II) complex in the phosphate buffer has two maxima at 224 nm and 208 nm (Fig. 3B, red spectrum), whereas the CD spectrum for the OR·Cu(II) complex in pure water has a maximum at 208 nm and a minimum at 220 nm (Fig. 3A, red spectrum). Thus, the presence of the buffer may influence the structural transitions in the OR peptide during Cu(II) binding. The difference spectrum for the OR·Cu(II) complex in water has a maximum at 202 nm and a minimum at 222 nm (Fig. S2A), and thus resembles the CD spectrum of a left-hand twisted antiparallel β-sheet, which is supposed to have a maximum at ~203 nm and a minimum at ~226 nm[77]. This suggests that both in water and phosphate buffer, Cu(II) binding to the OR peptide results in formation of antiparallel β-sheet structures, however possibly with different geometries, i.e., relaxed antiparallel β-sheets vs. left-hand twisted antiparallel β-sheets.

Interestingly, titrating 5 µM OR peptide in the phosphate buffer with $CuCl_2$ up to 40 µM, in 5 µM intervals, produced different CD spectra (Fig. S1B), than the $CuCl_2$ titrations with very small steps (Fig. 3B). The final CD spectrum in the small-step titration had a maximum at 224 nm, and formation of a new band at 208 nm was visible (Fig. 3B, red spectrum). For the titrations with larger steps, i.e. 5 µM intervals, the isodichroic point at 217 nm was absent, the new band formed at 208 nm had lower intensity, and the band at 224 nm was not affected by the Cu(II) ions at all. The difference spectrum between these two titrations (Fig. S1B, blue line) shares similarities with the difference spectra for titrations in the phosphate buffer with small steps (Fig. S2B, red line, blue line), thus suggesting formation of antiparallel relaxed β-sheets. We therefore suggest that during the large-step titrations, Cu(II) ions may have been bound in a rather chaotic way, possibly favoring intermolecular binding conformations that would induce peptide aggregation.

The titrations of the OR peptide with Cu(II) ions using small steps (Fig. 3B) resembled a steady-state approximation, wherefore we analyzed these data in a more quantitative manner. Plotting the mean residue ellipticity at 208 nm and 224 nm versus $CuCl_2$ concentration shows all three spectral transitions in the OR peptide (Figs. 4A and

4B). The data at 208 nm fitted with eq. 3 yields apparent dissociation constants of 0.52 μM for the first transition, and 5.57 μM for the second transition. The change in CD intensity at 224 nm for the first transition fitted with eq. 2 produced an K_{d1}^{app} of 0.24 μM. The second and third transitions, visible at 224 nm and fitted to eq. 4, produced the values $K_{d2}^{app} = 7.84$ μM and $K_{d3}^{app} = 18.0$ μM (Table 1). Thus, both the 208 nm and 224 nm CD data produced affinity values that were in the sub-micromolar range for the first transition and in the low micromolar range for the second transition. Moreover, the 208 nm and 224 nm CD data produced also similar Hill coefficients. The Hill coefficient for the first transition (PPII helix to β-turn) oscillates around 1, suggesting a single binding site. For the second and third transitions, the Hill coefficients are larger than 1, suggesting multiple binding sites (Table 1).

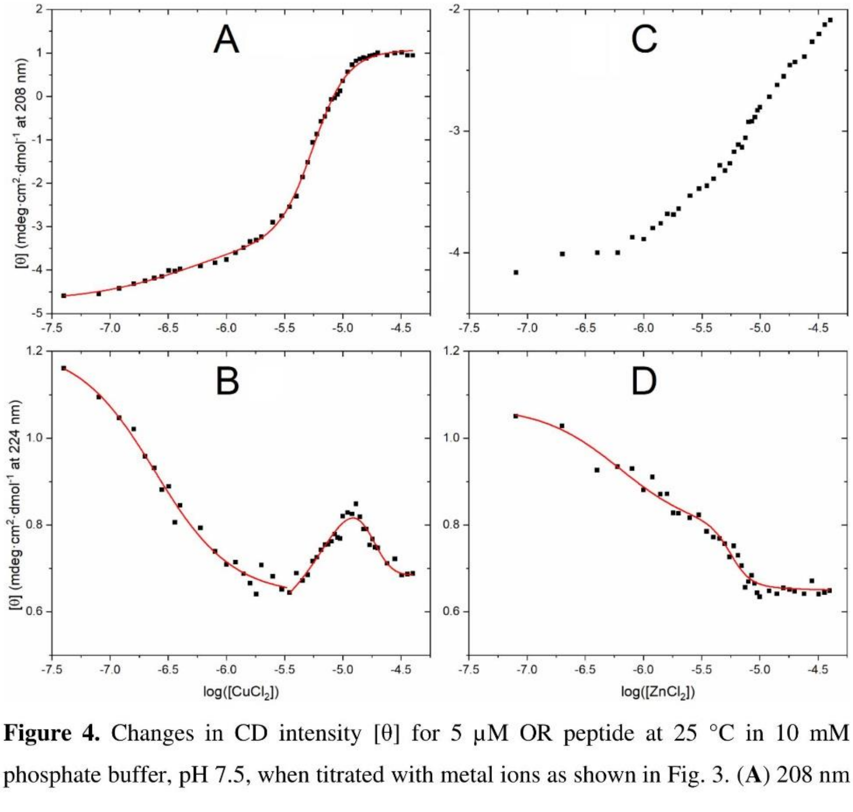

Figure 4. Changes in CD intensity [θ] for 5 μM OR peptide at 25 °C in 10 mM phosphate buffer, pH 7.5, when titrated with metal ions as shown in Fig. 3. (**A**) 208 nm

for Cu(II) ions (Fig. 3B); (**B**) 224 nm for Cu(II) ions (Fig. 3B); (**C**) 208 nm for Zn(II) ions (Fig. 3C); (**D**) 224 nm for Zn(II) ions (Fig. 3C).

To investigate the Zn(II) binding to the OR peptide we titrated 5 μM OR peptide with $ZnCl_2$ in the phosphate buffer, pH 7.5, at 25 °C (Fig. 3C). During the titrations with Zn(II) ions, the CD spectra of the OR peptide gradually lost intensity at 224 nm, and a weak new band appeared at 208 nm. Plotting the CD signal intensities at 208 nm and 224 nm versus the $ZnCl_2$ concentration clearly showed three spectral transitions (Figs. 4C and 4D). The data at 224 nm showed two transitions, and fitting to eq. 3 produced apparent dissociation constants of 0.64 μM and 5.61 μM for the first and second transitions (Table 1). The CD intensity at 208 nm did not show a saturation or inflection point in the studied concentration range of $ZnCl_2$, and was therefore not used for calculating binding affinity values. We may however speculate that this signal could have an inflection point above 40 μM, corresponding to rather weak binding.

The first transition appeared from 0 μM to 5 μM of $ZnCl_2$, (Fig. 3C, green to yellow spectra). During this process the CD intensity at 224 nm decreased, and a new weak band at 208 nm appeared. A clear isodichroic point at 217 nm was visible, suggesting a PPII to β-turn structural transition[76].

The second transition was visible from 5 μM to 10 μM of $ZnCl_2$ (Fig. 3C, yellow to orange). During this process the CD signal intensity at 224 nm and 208 nm decreased (Fig. 4C and 4D), while the isodichroic point gradually shifted from 217 nm to 218.5 nm. The new isodichroic point suggests a two-state structural transition, different from the PPII to β-turn transition. The difference spectrum for this transition had one minimum at 226 nm, and at least two maxima, one at 208 nm and a second below 200 nm (Fig. S2C, red line). The maximum at 208 nm and the minimum at 226 nm might correspond to a left-handed twisted antiparallel β-sheet, suggesting that such a structure could be induced by higher concentrations of Zn(II) ions.

The third transition was observed for $ZnCl_2$ concentrations above 10 μM (Fig. 3C, orange to red). In this spectral transition no clear isodichroic point was present, and the band at 208 nm gradually lost intensity, while the signal at 224 nm remained constant (Figs. 4C and 4D). The difference CD spectrum between the start and end points of this transition (Fig. S2C, blue line) was similar to the difference spectrum for the OR peptide titrated with Cu(II) ions (Fig. S2B, blue line), suggesting that this transition also involves formation of antiparallel β-sheets.

Interestingly, the final CD spectrum for the Zn(II) titration, i.e. the OR peptide with 40 µM $ZnCl_2$, is nearly identical to the CD spectrum for the OR peptide with 4 µM $CuCl_2$ (Figs. 3B and 3C). Characteristic features are here decreased signal intensity at 224 nm and formation of a new band at 208 nm. But for the Cu(II) titration, this is just an intermediate step – the final step with 40 µM $CuCl_2$ shows a very strong increase of the 208 nm band, which is something that Zn(II) ions apparently are not able to induce.

Table 1. Apparent dissociation constants (K_d^{app}) and Hill coefficients (n_H) for the OR-metal ion complex, based on fluorescence quenching and circular dichroism (CD) experiments.

Metal ion	Method	Buffer	K_{d1}^{app} [µM]	n_{H1}	K_{d2}^{app} [µM]	n_{H2}	K_{d3}^{app} [µM]	n_{H3}
Cu(II)	CD at 208 nm	10 mM NaH_2PO_4, pH 7.5	0.52 ± 0.31	0.97 ± 0.48	5.57 ± 0.11	2.97 ± 0.25		
Cu(II)	CD at 224 nm	10 mM NaH_2PO_4, pH 7.5	0.24 ± 0.03	1.31 ± 0.20	7.84 ± 0.25	1.81 ± 0.14	18.0 ± 0.7	4.50 ± 0.41
Zn(II)	CD at 224 nm	10 mM NaH_2PO_4, pH 7.5	0.64 ± 0.17	1.28 ± 0.26	5.61 ± 0.37	5.11 ± 2.02		
Cu(II)	Fluorescence at 355 nm	10 mM NaH_2PO_4, pH 7.5	4.29 ± 0.06	1.5 ± 0.03				
Cu(II)	Fluorescence at 355 nm	10 mM MES, pH 7.5	4.5 ± 0.1	1.61 ± 0.05				
Cu(II)	Fluorescence at 355 nm	10 mM MES, pH 5.5	7.4 ± 0.1	1.21 ± 0.02				
Cu(II)	Fluorescence at 355 nm	10 mM MES, pH 7.5	81 ± 31	0.61 ± 0.03				

3.3. Protonation of His residues decreases the OR affinity for Cu(II) and Zn(II) ions

Tryptophan residues have previously been shown to indirectly coordinate Cu(II) ions in a HGGGW sequence, corresponding to the core of a single isolated octarepeat sequence[36], and quenching of tryptophan fluorescence has been successfully applied to calculate the affinity between the octarepeat region and metal ions[29,38,78,79]. Thus, we here used fluorescence spectroscopy measurements of the intrinsic tryptophan fluorescence to further investigate binding of Cu(II) and Zn(II) ions to the OR peptide. Cu(II) is a paramagnetic ion, and can therefore strongly quench nearby fluorophores. Zn(II) is not paramagnetic, and any changes in tryptophan fluorescence should therefore originate only from zinc-induced changes in the peptide structure.

Cu(II) ions were titrated to 5 μM OR peptide at 25 °C in three sets of buffers: 10 mM phosphate buffer, pH 7.5; 10 mM MES buffer, pH 7.5 and 10 mM MES buffer, pH 5.5. As we believe that the OR peptide coordinates Cu(II) ions via histidine sidechains[36,37,80], we expect the binding to be weaker at pH 5.5, where the His residues will become protonated[59]. In all three buffers Cu(II) ions were found to quench the intrinsic tryptophan fluorescence, clearly demonstrating that Cu(II) ions bind to the OR peptide in all the studied conditions. In all cases the maximum fluorescence intensity was at 355 nm, and this maximum did not change its position during the titrations. In buffers at pH 7.5, the Cu(II) ions quenched the tryptophan fluorescence to 30% of the initial intensity (Figs. 5A and 5B), while in 10 mM MES buffer at pH 5.5, the tryptophan quenching was reduced to 50% of the initial fluorescence intensity (Fig. 5C). To derive apparent K_d values, we plotted the fluorescence intensity at 355 nm as a function of the $CuCl_2$ concentration and fitted the data to eq. 2 (Figs. 5A, 5B, and 5C: insets). The calculated K_d^{App} values were similar in the phosphate buffer and in the MES buffer at neutral pH, i.e. respectively 4.3 μM and 4.5 μM (Table 1). At acidic conditions the calculated K_d^{App} was somewhat higher, i.e. 7.5 μM, suggesting a slightly weaker binding. The K_d^{App} values derived with fluorescence spectroscopy are roughly one order of magnitude higher than those derived with CD spectroscopy, which is something that we attribute to differences in the two methods, although it should be pointed out that different buffers were used (Table 1). MES is a "Good" buffer with minimal metal binding[81], but it is not suitable for CD measurements. Phosphate buffer is compatible with most spectroscopic techniques, and biologically relevant, but the phosphate ions may have some interactions with metal ions.

To investigate if the OR peptide also binds Cu(I) ions, we performed tryptophan fluorescence titrations with $CuCl_2$ under reducing conditions obtained with 1 mM TCEP. Our results showed that titrating Cu(I) ions to 5 μM OR peptide in 10 mM MES buffer, pH 7.5, and 1 mM TCEP, clearly quenched the tryptophan fluorescence (Fig. 5G), demonstrating binding also of Cu(I) to the OR peptide. Fitting the fluorescence data at 355 nm to eq. 2 yielded an apparent K_d of ~81 µM. As no inflection point was observed for the binding curve, this value should be considered a rough estimation. But even so, it appears that the OR peptide has weaker affinity for Cu(I) ions than for Cu(II) ions.

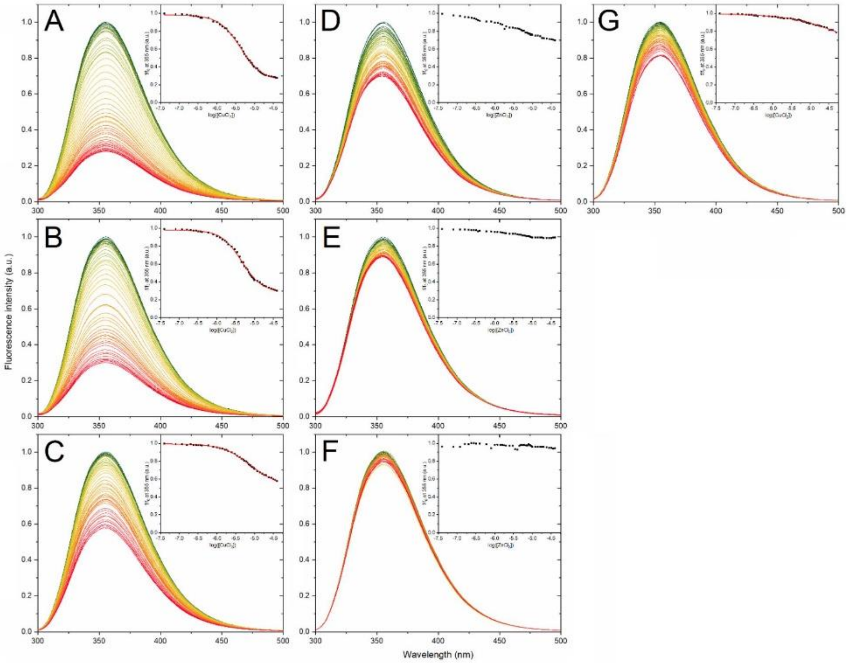

Figure 5. Fluorescence spectra for 5 µM OR peptide at 25 °C quenched with: (**A**) $CuCl_2$ in 10 mM phosphate buffer, pH 7.5; (**B**) $CuCl_2$ in 10 mM MES buffer, pH 7.5; (**C**) $CuCl_2$ in 10 mM MES buffer, pH 5.5; (**D**) $ZnCl_2$ in 10 mM phosphate buffer, pH 7.5; (**E**) $ZnCl_2$ in 10 mM MES buffer, pH 7.5; (**F**) $ZnCl_2$ in 10 mM MES buffer, pH 5.5; (**G**) $CuCl_2$ in 1 mM TCEP, 10 mM MES buffer, pH 7.5.

Titrations with Zn(II) ions to 5 µM OR peptide at 25 °C were performed in the same three buffers as the titrations with $CuCl_2$, i.e. 10 mM phosphate buffer, pH 7.5; 10 mM

MES buffer, pH 7.5 and 10 mM MES buffer, pH 5.5. The changes in the OR tryptophan fluorescence at pH 7.5 were stronger in the phosphate buffer than in the MES buffer, indicating a buffer effect on the zinc binding (Figs. 5D and 5E). At pH 5.5 no significant changes in fluorescence were observed (Fig. 5F), indicating that the OR peptide does not bind Zn(II) ions at acidic conditions. In all titrations the fluorescence maximum was at 355 nm and did not change its position. The weaker fluorescence quenching by Zn(II) ions compared to Cu(II) ions is to be expected, as Zn(II) ions are not paramagnetic. However, the observed quenching effect does show that also Zn(II) ions bind to the peptide at neutral pH, even though the signal-to-noise ratio is too low to quantitatively evaluate the binding curves.

3.4. Cu(II) and Zn(II) ions bound to the OR peptide both induce formation of hairpin structures

Molecular dynamics (MD) simulations were carried out to characterize the structural transitions in the OR peptide, i.e. PrP^C(58-93), when bound to Cu(II) and Zn(II) ions. Final models from the MD simulations are shown in Figs. 6, 7, and 8, and visualizations of the first principal components of the simulations are shown in Fig. S3.

To study interactions corresponding to acidic pH, a single Cu(II) ion was positioned next to four protonated histidine $N^{\varepsilon 2}$ atoms. As expected, the Cu(II) ion rapidly moved away from the protonated His residues during the MD equilibration phase. The simulations quickly converged, as shown by the RMSD values (Figure S4A). During the whole simulation time, the Cu(II) ion remained bound to the Cβ main chain carbonyl groups of residues His85, Gly87, Gly88, and Trp89, suggesting non-specific electrostatic binding (Fig. 6A). The OR peptide in this protonation state adopted an extended and flexible conformation with an RMSF around 0.5 nm (Figure S5A), where the secondary structure mainly was coil with some regions showing propensities for β-turn and PPII helix conformations (Fig. 6D). Principal component analysis (PCA) suggested that the main conformational changes involved motions in the N- and C-termini (Figure S3A).

Next, we simulated the OR peptide with either one or two Cu(II) ions located next to the neutral $N^{\varepsilon 2}$ atoms of the four OR histidine residues, corresponding to the OR peptide at neutral pH. Both simulations quickly converged (Fig. S4A), and the single Cu(II) ion remained bound by all four histidine residues and two axially-bound water molecules over the whole simulation time (Fig. S6A). In this binding mode the peptide backbone formed multiple loops around the Cu(II) ion, while residues His61-Gly71 formed a hairpin-like structure stabilized by Cu(II)-bound His61 and His69 (Fig. 6B). This model had smaller RMSF values than the OR peptide model with protonated histidine residues (Fig. S5A), indicating a more rigid structure. Indeed, the main PCA component showed smaller backbone displacements near the Cu(II) ion than at the N- and C-termini (Figure S3B). Moreover, in this binding mode more OR residues adopted PPII helix and transient β-strand secondary structures, compared to the OR peptide with protonated histidine residues (Fig. 6E). For the simulations with two Cu(II) ions, each copper ion remained bound by two histidine residues and four water molecules (Fig. 6C) over the whole simulation time (Fig. S6B). In this binding mode, the peptide backbone formed a structure with three hairpins. The first hairpin was stabilized by one of the Cu(II) ions, and was located near the N-terminus, involving residues Gly62-His69. The second hairpin, which was stabilized by the other Cu(II) ion, involved residues Gly74-His85 and was thus located near the C-terminus. The third hairpin involved residues His69-Pro76 and formed a bridge between the two Cu(II)-bound segments (Fig. 6C). The RMSF data showed intermediate values, with minima corresponding to the histidine residues involved in Cu(II)-binding (Fig. S5A). The primary PCA component suggests that the two Cu(II)-stabilized hairpin structures were rigid in themselves, but could move relative to each other, resulting in formation of the middle bridging hairpin (Fig. S3C). Secondary structure analysis indicated a reduction of PPII structure and formation of antiparallel β-strands around residues Gln67-Gly70 and Gly74-Pro76, i.e. roughly the region of the middle bridging hairpin (Fig. 6F).

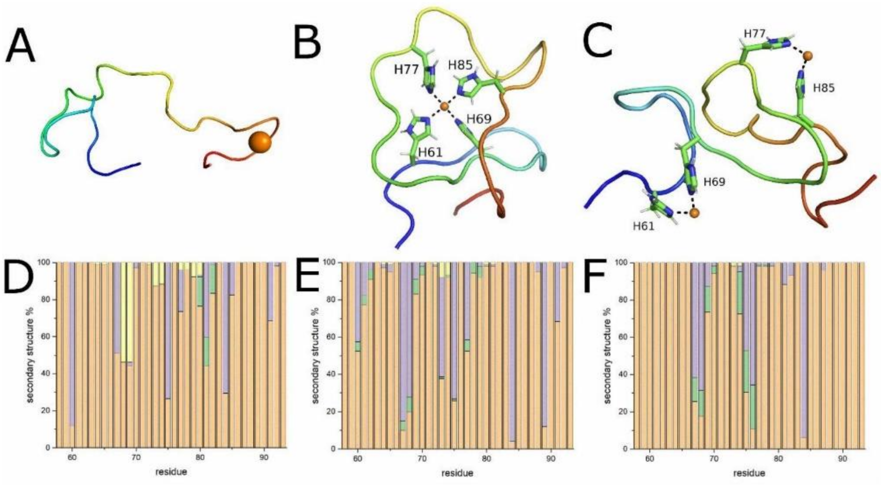

Figure 6. Final snapshots and secondary structure distributions of the OR peptide simulated with: (**A, D**): a single Cu(II) ion and protonated histidine $N^{\varepsilon 2}$ atoms; (**B, E**): a single Cu(II) ion and neutral histidine $N^{\varepsilon 2}$ atoms; (**C, F**): two Cu(II) ions and neutral histidine $N^{\varepsilon 2}$ atoms. The secondary structures were determined for each generated model using the PROSS[64] algorithm: β-turns are shown in yellow, polyproline II helices in violet, β-strands in green, and coils in orange.

Similar simulations were performed also for the OR peptide with Zn(II) ions. For the OR peptide with fully protonated histidine residues and simulated with a single Zn(II) ion, the metal ion moved away from the peptide in the MD equilibration phase and remained unbound for the whole simulation time. The peptide adopted an elongated (Fig. 7A) and flexible conformation with an average RMSF of 0.6 nm (Fig. S5B). The first PCA component suggests that the main movement in the OR peptide involves motions in the N- and C-termini (Fig. S3D). During the simulation time the OR peptide here adopted mainly coil and PPII secondary structures (Fig. 7D).

In the next step we simulated the OR peptide with neutral $N^{\varepsilon 2}$ atoms, together with one or two Zn(II) ions. Both simulations converged (Fig. S4B). The single Zn(II) ion placed next to the four histidine residues remained bound over the whole simulation time (Fig. S6C) and was additionally coordinated by two axially bound water molecules. In this binding mode the peptide backbone again formed multiple loops around the Zn(II) ion, and residues Gly74-Gly86 formed a hairpin structure stabilized by the zinc ion bound to His77 and His85. The average value of the Cα RMSF was 0.3 nm, which is a much smaller value than for the OR peptide with protonated histidine residues (Fig. S4B). The first PCA component suggests that the main movement of the peptide backbone occurred in the hairpin loop (residues Gly78-Gly82) and the C-terminal loop (residues 86-91), while the backbone around the Zn(II) ion had smaller mobility (Fig. S3E). Analysis of the secondary structure showed that more residues formed a β-strand secondary structure than for the OR peptide with protonated histidine residues (Fig. 7E). However, the peptide mainly adopted coil and PPII helix secondary structures.

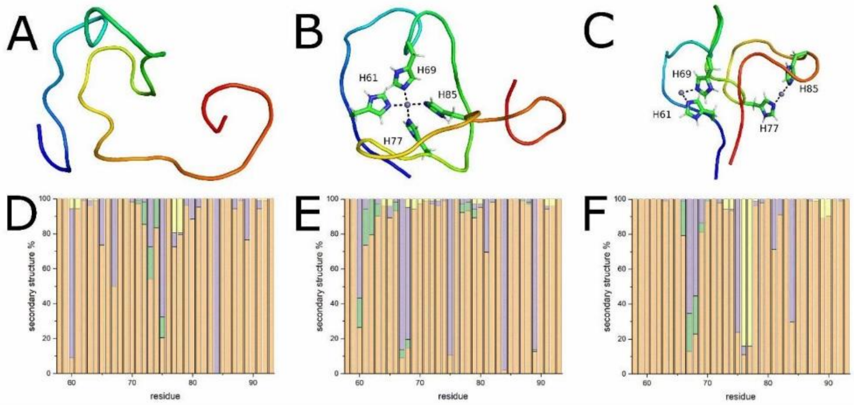

Figure 7. Final snapshots and secondary structure distributions of the OR peptide simulated with: (**A, D**): a single Zn(II) ion and protonated histidine $N^{\varepsilon2}$ atoms; (**B, E**): a single Zn(II) ion and neutral histidine $N^{\varepsilon2}$ atoms; (**C, F**): two Zn(II) ions and neutral histidine $N^{\varepsilon2}$ atoms. The secondary structure distributions were calculated using the PROSS method: β-turns are shown in yellow, polyproline II helices in violet, β-strands in green, and coils in orange.

When two Zn(II) ions were positioned close to the histidine residues, both ions again remained bound over the whole simulation time, and each was coordinated by two histidine residues and four water molecules (Fig. S6D). In this binding mode the peptide backbone formed four hairpin structures. Two hairpin structures, located at the N- and C-termini, involved respectively residues His61-His69 and His77-His85, and each of them was stabilized by a single Zn(II) ion. Then, two bridging hairpins involving respectively residues Gln67-Trp73 and Gln75-Gly78 were located between the two Zn(II)-stabilized hairpins (Fig. 7C). The peptide backbone had an average RMSF of 0.4 nm (Fig. S5B), indicating higher Cα fluctuations than when only one Zn(II) ion was bound to the OR peptide. The primary PCA component suggests that in this binding mode, the main motion of peptide backbone corresponds to formation of the two bridging hairpin structures (residues Gln67-Trp73 and Gln75-Gly78) and closing the whole model by terminal residues Gly58, Gln59 and Gly92, Gly93 (Fig. S3F). Analysis of the peptide's secondary structure showed a reduced PPII helix content, but an increase in the coil and β-turn secondary structures (Fig. 7F).

In the last step we simulated two OR peptide molecules with neutral $N^{\varepsilon 2}$ atoms, bound to a single Cu(II) ion. The initial model contained the Cu(II) ion bound to His77 and His 85 from the first OR molecule (OR-1), and to His61 and His69 from the second OR molecule (OR-2). The models of OR-1 and OR-2 were taken from the last MD step of our OR simulation together with two Cu(II) ions. The simulation converged and surprisingly showed a minimal RMSD over time (Fig. S4A). The average value of the Cα RMSF was below 0.05 nm (Fig. S5C), which is the smallest value from all simulations performed in this study, and the single Cu(II) ion placed next to the four histidine residues remained bound during the entire simulation time (Fig. S6E). The three hairpin structures, previously formed in the OR peptide simulated with two Cu(II) ions, were preserved in each OR molecule (Fig. 8A). Secondary structure analysis indicated similar structural compositions for the OR-1 and OR-2 molecules. The two peptide molecules predominantly adapted coil structures, with a PPII structure at residues Gln67, Pro68, Gln75, Pro76, Pro84 in OR-1 and OR-2, and β-strands at residues Gln67-His69, Gly74-Pro76 in OR-1, and Gly74-Pro76 in OR-2 (Fig. 8B, C).

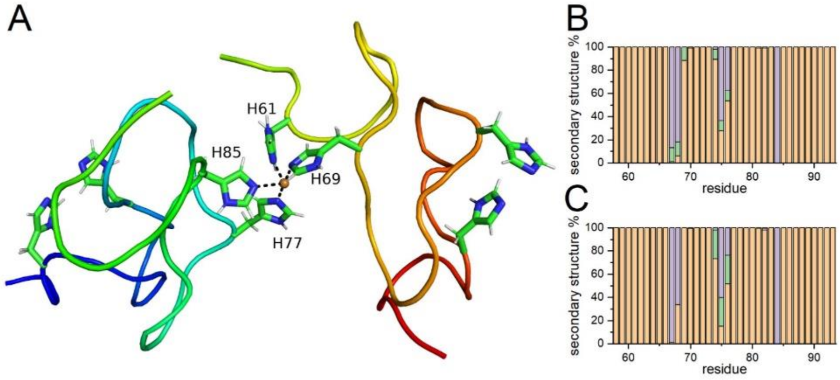

Figure 8. Final snapshot (**A**) of two OR peptide molecules simulated with a single Cu(II) ion. The N-terminus and C-terminus of the first OR peptide (OR-1) are marked in respectively blue and green, and the N-terminus and C-terminus of the second OR peptide (OR-2) are marked in respectively green and red. The secondary structure distributions for the two OR peptides are shown in (**B**) (OR-1) and (**C**) (OR-2), and were calculated using the PROSS method: β-turns are shown in yellow, polyproline II helices in violet, β-strands in green, and coils in orange.

3.5 Calculation of pKa values for the OR peptide histidines

Protein binding affinities for Cu(II) and Zn(II) ions can be affected by the pKa values of the His residue side chains, which are known to be close to the physiological pH[59,82]. Changes in pKa values can be observed in structural conformations that favor hydrogen bond interactions with the histidine side chains, and such pKa changes can affect the binding affinity for metal ions.

We therefore calculated pKa values for His residue side chains for different MD conformations (Table 2). To increase the accuracy of the calculations, two independent protocols were used, namely PropKa 2.0 and DelPhiPKa[66,68]. The two protocols gave pKa values for all four His residues that are maximally within ± 6% of the average calculated values (Table 2).

The two protocols consistently show that both the position of the His residue and the protein conformation have noticeable effects on the pKa values (Table 2). For the final models from the MD simulations, both protocols produce slightly higher pKa values for His 85 than for the other three residues. His 85 is the histidine most exposed to the solvent, and ionic interactions with water molecules are energetically more favorable than hydrogen bonds. For the same reasons, both protocols consistently show slightly higher pKa values for the final models from simulations with charged His residues, than for models from simulations with neutral His residues.

Table 2. pKa values for the four histidine residues in the OR peptide, calculated for both neutral and protonated histidine, and with either the PropKa 2.0 or the DelPhiPKa 2.3 protocol.

	Cu(II)	**Zn(II)**	**Cu(II)**	**Zn(II)**
PropKa 2.0	**Neutral histidines**		**Protonated histidines**	
His 61	5.87	6.88	6.50	6.43
His 69	6.41	6.01	6.50	6.43
His 77	6.20	6.11	6.43	6.29
His 85	6.48	7.15	6.47	6.50
DelPhiPKa 2.3				
His 61	5.64	5.88	6.43	6.43
His 69	6.11	6.06	6.45	6.43
His 77	6.10	6.12	6.49	6.29
His 85	6.16	6.18	6.46	6.50

4. Discussion

4.1 Solution structure of the OR peptide

Previous studies have suggested that the OR peptide in aqueous solution adopts a combination of random coil structure together with either PPII left-handed extended helix[70–72] or β-turn structures[35,73,74]. Our CD results for the apo-OR peptide, i.e. PrP^{C}(58-93), show unfolding at elevated temperatures (Fig. 2), thus demonstrating the existence of secondary structures different from random coil at low temperatures. In the 20-65 °C temperature range an isodichroic point at 204 nm indicates a PPII-helix to random coil transition[76]. This is consistent with previous studies of the OR peptide [70–72], and also similar to our earlier results on the structure of the Aβ peptides involved in Alzheimer's disease[75]. Temperature studies of the Aβ(1-40) peptide and its shorter N-terminal fragments generally show an isodichroic point around 208 nm, a weak positive band at ~222 nm that becomes negative at high temperatures, and a strong negative band at ~200 nm whose intensity is reduced at high temperatures. The similar results obtained here for the OR peptide suggest similar structures and temperature-induced structural transitions in the two peptides. Our results suggest that ~45% of the OR peptide is in PPII conformation at 37°C, with the remaining structure being random coils. For the Aβ(1-40) peptide, the corresponding numbers are ~30% PPII helix and ~70% random coil structure[75]. The lack of a well-defined isodichroic point below 20 °C (Fig. 2) indicates that the OR peptide can form various secondary structures at low temperatures. This is consistent with NMR studies of the OR sequence at 20 °C, which suggest the presence of structured loops and β-turns[83].

4.2 Metal binding to the OR peptide induce β-sheet formation

Earlier studies have shown that the OR domain can bind up to four Cu(II) ions, but no detailed structural model for the OR peptide backbone during Cu(II) binding has been proposed. More than twenty years ago Viles et al. performed far-UV CD titrations with Cu(II) ions to the OR peptide in water at pH 7.4[35]. Addition of Cu(II) ions was found to decrease the intensity of both a negative band at 200 nm and a positive band at 225 nm, and to induce a new negative band at 222 nm together with a new positive band at 204 nm. This was interpreted as a structural alteration corresponding to formation of β-turns or structured loops[35]. Later studies have suggested that the negative band at 222 nm might reflect the structures of tryptophan side chains[27]. In this study we were able to largely recreate the results of Viles et al., but we present a different interpretation. The difference spectrum for the Cu(II)-OR complex in water (Fig. S2A) has a strong negative band at 222 nm and a strong positive band at 202 nm. It thereby resembles the CD spectrum for left-handed twisted antiparallel β-sheets[77], as well as the CD spectrum for a hydrophobic fragment of the Aβ peptide, i.e. Aβ(25-35), to which we previously have attributed an antiparallel β-sheet secondary structure[75]. We therefore argue that binding of Cu(II) ions to the OR peptide in water results in formation of antiparallel β-sheet structures.

We further propose that antiparallel β-sheets are formed also when Cu(II) ions bind to 5 µM OR peptide in the phosphate buffer, pH 7.5, but these β-sheets then appear to have a different geometry. Addition of up to 5 µM $CuCl_2$, corresponding to a 1:1 OR:Cu(II) molar ratio, produces an isodichroic point at 217 nm, which suggests a two-state PPII-helix to β-turn transition. Above 5 µM of $CuCl_2$, the new CD band at 208 might be caused by formation of a relaxed antiparallel β-sheet secondary structure[77]. The intensity increase for the new 208 nm band was higher for Cu(II) concentrations in the 5 µM to 10 µM than for the 10 µM to 40 µM interval, suggesting that binding of two Cu(II) ions to the OR peptide is a primary event. Further binding up to four Cu(II) ions increases the formation of antiparallel β-sheet structure, however to a lesser amount.

In an earlier study, a CD spectrum for 50 µM of Syrian hamster OR peptide together with 250 µM of Cu(II) ions in 20 mM ammonium acetate at pH 6.0[84], is almost identical to our CD spectrum for 5 µM OR peptide with 10 µM of Cu(II) ions in 10 mM phosphate buffer, pH 7.5 (Fig. 3B). The CD spectrum of the Syrian hamster OR peptide in the ammonium acetate buffer was interpreted as representing a Cu(II)-OR complex[84]. The CD spectrum of this proposed Cu(II)-OR complex was different than for the previously reported complex in water at pH 7.4[35], which is consistent with our current observations (Figs. 3A and 3B). In another study, no changes in the CD spectrum were reported when Cu(II) ions were titrated to the OR peptide in 10 mM phosphate buffer, pH 7.0[72]. Although the OR peptide concentration was not specified and CD data were shown only for one $CuCl_2$ concentration, the reported CD spectra look like they might have an isodichroic point around ~220 nm, which is close to our observed isodichroic point at 217 nm (Fig. 3B). The authors explained the lack of a clear effect when adding copper ions by phosphate ions being able to compete for Cu(II) binding[72]. In living organisms Cu(II) ions never exist in free form[32], and phosphate ions may indeed form complexes with Cu(II) ions[85]. If binding of Cu(II) ions to phosphate was so much stronger than binding to the OR peptide, then Cu(II) binding to the OR peptide would be physiologically irrelevant, given the high concentration of free phosphate ions in the extracellular fluid[86]. But our current data clearly show that the OR peptide binds both Cu(II) and Zn(II) ions, also in the phosphate buffer.

As the OR domain is known to bind multiple - up to four - Cu(II) ions, the binding modes depend on the Cu(II) concentration[37,73,78,80]. The first Cu(II) ion is coordinated by four $N^{\varepsilon 2}$ atoms from the four histidine residues[37,80]. This binding mode has the highest affinity, with a K_d below 3 nM[38,80]. With two Cu(II) ions, each one is coordinated by two histidine sidechain $N^{\varepsilon 2}$ atoms[37], possibly together with negatively charged atoms, and the K_d is ~200 nM[80]. Further addition up to four Cu(II) ions rearranges the binding configuration, so that each Cu(II) ion is coordinated by one histidine sidechain $N^{\delta 1}$ atom and three negatively charged atoms, such as two deprotonated amide nitrogens and one carbonyl oxygen from the preceding glycine residues[36,37,80]. In this binding mode the OR peptide has the weakest affinity for Cu(II) ions, with a K_d in the 1 – 10 µM range[38,80].

The OR peptide backbone is expected to adopt different conformations for each binding configuration. Our CD titrations confirm this notion (Fig. 3B), and the transitions are particularly clear at 224 nm (Fig. 4B). Up to 5 µM $CuCl_2$, i.e. 1:1 Cu(II):OR ratio, the intensity at 224 nm monotonically decreased. From 5 µM to 10 µM $CuCl_2$, i.e. 1:1 to 2:1 Cu(II):OR ratio, the intensity at 224 nm monotonically increased. From 10 µM to 40 µM $CuCl_2$, i.e. 2:1 to 8:1 Cu(II):OR ratio, the intensity at 224 nm decreased and reached a plateau around ~20 µM $CuCl_2$, i.e. around 4:1 Cu(II):OR ratio. These observations are clearly consistent with binding of one, two, and up to four Cu(II) ions to the OR peptide in the three intervals of $CuCl_2$ concentration (Fig. 4B).

Binding of Zn(II) ions to the OR peptide in 10 mM phosphate buffer, pH 7.5, seems to induce similar structures in the OR peptide as Cu(II) ions. However, while binding of Zn(II) ions also appears to induce formation of an antiparallel β-sheet secondary structure, the geometry of this β-sheet could be different[77]. Again, the changes in CD intensity at 224 nm seem to reflect distinct structural transitions (Fig. 3C). For additions of up to 5 µM of $ZnCl_2$, i.e. 1:1 Zn(II):OR ratio, the 224 nm intensity monotonically decreased, suggesting binding of a single Zn(II) in this interval (Fig. 4D). From 5 µM to 10 µM of $ZnCl_2$, i.e. from 1:1 to 2:1 Zn(II):OR ratios, the 224 nm intensity decreased even more steeply, suggesting binding of two Zn(II) ions in this interval. Above 10 µM $ZnCl_2$ no further changes appear in the CD spectrum at 224 nm, indicating that binding of two Zn(II) ions saturates the OR peptide. Other researchers have suggested that all four OR histidine residues are involved in binding a single Zn(II) ion[47,48,87]. This might be true when the OR peptide binds Zn(II) ions in a 1:1 molar ratio, but at higher Zn(II) concentration we suggest that two Zn(II) ions are bound by two histidine residues each, in a similar fashion as for Cu(II) ions (above).

4.3 Histidine protonation and metal ion binding to OR peptide

Our fluorescence measurements of the OR peptide titrated with Cu(II) ions at pH 7.5 suggest an apparent K_d ~4.5 μM (Table 1). This value is close to the mean apparent dissociation constant of 7.2 μM reported for an isolated HGGGW repeat[38]. Calculating real K_d values requires competition experiments with e.g. glycine[38]. As our main objective was to show changes in metal ion binding affinity under different conditions, no competition experiments were performed in this study. Our CD experiments for the OR peptide titrated with Cu(II) ions clearly shows three spectral transitions, that we attribute to binding of four Cu(II) ions. The single apparent K_d value from our fluorescence experiments therefore seems to represent the averaged K_d from all three possible Cu(II) binding modes[80]. In our fluorescence experiments under acidic conditions at pH 5.5 (Fig. 5C), the K_d value (~7.4 μM) suggested slightly weaker binding than at pH 7.5 (~4.5 μM) (Table 1). Despite this small difference in binding affinity, this result clearly shows that the OR peptide can bind Cu(II) ions also under acidic conditions where the histidines are protonated[59] as their pKa values are between 6 and 7, depending on the degree of solvent exposure and hydrogen bonds created (Table 2). Earlier studies with mass spectrometry indicate that the OR peptide can bind only up to two Cu(II) ions at pH 6.0, i.e. less than the four Cu(II) ions that can be bound at pH 7.4[84]. Thus, our fluorescence quenching measurements at pH 5.5 (Fig. 5C) may reflect the average affinity for binding two Cu(II) ions to OR peptide. Tryptophan fluorescence measurements of the OR peptide with $ZnCl_2$ at pH 7.5 showed reduced fluorescence intensity indicative of binding, but the poor signal-to-noise ratio of the data did not allow the binding affinity to be calculated (Figs 5D and 5E). At pH 5.5 addition of $ZnCl_2$ did not affect the intrinsic OR peptide fluorescence at all (Fig. 5F), indicating that the OR peptide does not bind Zn(II) ions under acidic conditions.

4.4 Models for β-sheet formation

Molecular dynamics simulations of the OR peptide with metal ions generally support our CD results. The secondary structure of the OR peptide with protonated histidine residues, in the presence of a single Cu(II) or Zn(II) ion, mainly consists of coil structure, although some PPII-helix structure (12% overall) is present around residues Pro60, Gln67, Gln75 and Pro84 (Fig. 6D, Fig. 7D). When the OR peptide with neutral histidine residues is modeled together with a single bound metal ion, the peptide again mainly formed a coil structure, although together with four transient β-strands. For a bound Cu(II) ion, the transient β-strands were Pro60-Gly62, Gln67-Gly70, Trp73-Gln75, and His77-Gly79. For a bound Zn(II) ion, the transient β-strands were Pro60-Gly63, Gly66-Pro68, His77-Gln79, and Gly87-Trp89. Thus, most of the β-strands appeared in close proximity to the histidine residues involved in metal ion binding, i.e. His61, His69, His77, and His85. The overall amount of PPII-helix structure was around 15% in these simulations, with the main contributions coming from Pro60, Gln67, Pro68, Gln75, Pro84 and Trp89.

Although the OR peptide simulated with neutral histidine residues and two bound metal ions mainly adopted a coil structure, we observed significant reduction in the PPII-helix structure (9% overall), which is in line with our CD analysis. The PPII-helix content was here distributed in a more uniform way, mainly around the Pro68, Pro76, and Pro84 residues. Furthermore, modeling with two bound Cu(II) ions (Fig. 6C) induced formation of two β-strands consisting of residues Gln67-Gly70 and Gly74-Pro76, i.e. mainly in the middle of the bridging hairpin structure (residues His69-Pro76). For two bound Zn(II) ions, a similar β-strand was formed at Gly66-Gly70, together with two accompanying short β-turns at Trp73-Gly74 and Pro76-His77. In this case the formed β-structures were located around the first (residues Gln67-Trp73) and second (residues Gln75-Gly78) bridging hairpins, which connect the N-terminal and C-terminal hairpin structures stabilized by the two metal ions (Fig. 7C). These observations are consistent with our CD results, where formation of antiparallel β-sheets was observed for the second spectral transition (i.e., for binding of the second Zn(II) ion (Fig. 4D).

Structural models with a single bound metal ion from our MD simulations agree with previously published results for a single Cu(II) ion bound to the OR peptide, where the metal binding site remained exposed to the solvent and the peptide backbone formed multiple loops around the Cu(II) ion[88,89]. Interestingly, Pushie et al. performed molecular dynamics simulations for two octapeptide repeats, each bound with a single Cu(II) ion[90]. The authors observed stacking of the two HGG metal binding regions on each other, where the GWGQ linker region formed a bend or a turn structure. Those models resemble our hairpin structures from the simulation of the OR peptide with two Cu(II) ions. In the "stacked" models two copper binding sites were located in close proximity, with a copper-copper distance of ~5 Å. With two neighboring histidine imidazole moieties, it is possible that the 2:1 binding mode (two Cu(II) ions/one OR peptide) under higher Cu(II) occupancy undergoes rearrangement to a 4:1 binding mode, with the hairpin properties being preserved, which would agree with our CD results. Future modeling with multiple OR peptides (or full-length PrP^C) and multiple metal ions may shed more light on the structural effects of metal binding to aggregated peptides/proteins.

4.5 OR peptide metal ion binding and amyloid formation

The OR domain is an important part of PrP^C, being involved in the protein's neuroprotective effect[91]. Previous studies have suggested that Cu(II) and Zn(II) ions may inhibit in vitro conversion of PrP^C to PrP^{Sc} by formation of nonamyloid aggregates[92]. However, we have previously reported that after addition of four molar equivalents of Zn(II) ions, the OR peptide forms structured fibrils that bind the amyloid-specific dyes Thioflavin T and Congo Red, and which display the cross-β structure typical for amyloid material [50]. Thus, the OR peptide incubated with an excess of Cu(II) ions may also form amyloid aggregates. Our CD titrations and MD simulations of the OR peptide bound with two metal ions (i.e., Cu(II) or Zn(II)) showed formation of β-structures, which is consistent with our previous results. In our MD simulations the OR peptide formed β-structures in the Gln67-Gly70 and Gly74-Pro76 regions, and as β-structures – especially hairpins – are favorable for amyloid formation[6], we speculate that these regions may form a core for amyloid aggregation of the OR peptide or full-length PrP^{Sc}. However, our CD and MD results indicate that binding of a single metal ion to the OR peptide induces only minor changes in the peptide's secondary structure. Thus, it is possible that only high concentrations of metal ions – more than 1:1 ratio – would induce secondary structures suitable for amyloid formation. On the other hand, binding of divalent metal ions to full-length PrP^C is known to induce interactions between the metal-bound OR domain and the C-terminal helical domain[25,87,93]. Such interactions likely help to hold the protein structure together, and it is generally known that structured proteins first must become unstructured before they can "misfold" into β-sheets (or β-sheet hairpins) and begin to assemble into amyloid forms. In a PrP^C variant with point mutations, corresponding to genetic Creutzfeldt-Jakob disease, fatal familial insomnia, and the Gerstmann-Straussler-Scheinker disease, addition of Zn(II) ions induced broadening of NMR peaks indicative of weaker interactions between the Zn(II)-bound OR region and the C-terminal domain[87] than in the native protein. Thus, the metal-induced interactions between the OR region and the C-terminal domain likely counteracts amyloid formation, by stabilizing the protein fold, and these stabilizing interactions may be weaker in some disease-related PrP^C mutants. Finally, metal ions may promote aggregation by binding to the OR region of two or more PrP^C proteins, thereby bringing the two proteins together (a first step towards aggregation). Our MD simulations (Fig. 8) showed that such intermolecular Cu(II) coordination was very stable over time, indicating that complexes with Cu(II) ions and two or more PrP^C molecules are likely to form *in vivo*.

The relation between metal binding and PrP^C aggregation is clearly complex, with two effects that likely promote aggregation (one metal ion binding multiple PrP^C molecules, and metal ions inducing β-sheet structures suitable for amyloid formation), and one effect that likely counteracts amyloid formation (stabilizing the protein fold by interactions between the C-terminal domain and the metal-bound OR region). Our tentative understanding is that the effects that promote aggregation will dominate at high concentrations of metal ions, i.e. at metal:protein ratios higher than 1:1. As four Cu(II) ions but only two Zn(II) ions could bind to one OR peptide, and as Cu(II) ions had a larger effect on the peptide structure than the Zn(II) ions, amyloid formation is probably more efficiently induced by Cu(II) than Zn(II) ions.

5. Conclusions

In summary, our results show that the OR region in the PrP^C protein can bind up to four Cu(II) ions or two Zn(II) ions. The average apparent binding affinities are in the low micromolar range for both metal ions (Table 1). The OR histidine residues are important binding ligands, where Zn(II) binding is more sensitive to histidine protonation than Cu(II) binding, and the metal ions can be coordinated by histidines from different PrP^{C} molecules – such intermolecular complexes appear to be stable first steps towards protein aggregation. Without bound metal ions, the secondary structure of the OR peptide is a combination of random coil and PPII helix. Addition of metal ions induces structural changes into β-sheet conformations, which generally are beneficial for amyloid aggregation. The structural conversions are most prominent for large concentrations (i.e. above 1:1 ratio) of Cu(II) ions, suggesting that especially Cu(II) ions could be an important factor in converting the PrP^{C} protein into amyloids of the neurotoxic PrP^{Sc} form.

References

1. Prusiner, S. B. Nobel Lecture: Prions. *Proceedings of the National Academy of Sciences* **95**, 13363–13383 (1998).
2. Colby, D. W. & Prusiner, S. B. Prions. *Cold Spring Harbor Perspectives in Biology* **3**, a006833–a006833 (2011).
3. Zahn, R. *et al.* NMR solution structure of the human prion protein. *Proceedings of the National Academy of Sciences* **97**, 145–150 (2000).
4. Stahl, N. Scrapie prion protein contains a phosphatidylinositol glycolipid. *Cell* **51**, 229–240 (1987).
5. Herms, J. *et al.* Evidence of Presynaptic Location and Function of the Prion Protein. *J. Neurosci.* **19**, 8866–8875 (1999).
6. Abelein, A. *et al.* The hairpin conformation of the amyloid β peptide is an important structural motif along the aggregation pathway. *J Biol Inorg Chem* **19**, 623–634 (2014).
7. Selkoe, D. J. & Hardy, J. The amyloid hypothesis of Alzheimer's disease at 25 years. *EMBO Mol Med* **8**, 595–608 (2016).
8. Saá, P., Harris, D. A. & Cervenakova, L. Mechanisms of prion-induced neurodegeneration. *Expert Rev. Mol. Med.* **18**, e5 (2016).
9. Chen, C. & Dong, X.-P. Epidemiological characteristics of human prion diseases. *Infect Dis Poverty* **5**, 47 (2016).
10. Prusiner, S. B. A Unifying Role for Prions in Neurodegenerative Diseases. *Science* **336**, 1511–1513 (2012).
11. Collinge, J. Mammalian prions and their wider relevance in neurodegenerative diseases. *Nature* **539**, 217–226 (2016).
12. Miller, G. Could They All Be Prion Diseases? *Science* **326**, 1337–1339 (2009).
13. Sabate, R. When amyloids become prions. *Prion* **8**, 233–239 (2014).

14. Walker, L. C. Prion-like mechanisms in Alzheimer disease. in *Handbook of Clinical Neurology* vol. 153 303–319 (Elsevier, 2018).
15. Luo, J., Wärmländer, S. K. T. S., Gräslund, A. & Abrahams, J. P. Cross-interactions between the Alzheimer Disease Amyloid-β Peptide and Other Amyloid Proteins: A Further Aspect of the Amyloid Cascade Hypothesis. *Journal of Biological Chemistry* **291**, 16485–16493 (2016).
16. Ma, J., Gao, J., Wang, J. & Xie, A. Prion-Like Mechanisms in Parkinson's Disease. *Front. Neurosci.* **13**, 552 (2019).
17. Nonaka, T. & Hasegawa, M. TDP-43 Prions. *Cold Spring Harb Perspect Med* **8**, a024463 (2018).
18. Koski, L., Ronnevi, C., Berntsson, E., Wärmländer, S. K. T. S. & Roos, P. M. Metals in ALS TDP-43 Pathology. *IJMS* **22**, 12193 (2021).
19. Corbett, G. T. *et al.* PrP is a central player in toxicity mediated by soluble aggregates of neurodegeneration-causing proteins. *Acta Neuropathol* **139**, 503–526 (2020).
20. Linden, R. *et al.* Physiology of the Prion Protein. *Physiological Reviews* **88**, 673–728 (2008).
21. Schmitt-Ulms, G., Ehsani, S., Watts, J. C., Westaway, D. & Wille, H. Evolutionary Descent of Prion Genes from the ZIP Family of Metal Ion Transporters. *PLoS ONE* **4**, e7208 (2009).
22. Toni, M., Massimino, M. L., De Mario, A., Angiulli, E. & Spisni, E. Metal Dyshomeostasis and Their Pathological Role in Prion and Prion-Like Diseases: The Basis for a Nutritional Approach. *Front. Neurosci.* **11**, (2017).
23. Kawahara, M., Tanaka, K. & Mizuno, D. Disruption of Metal Homeostasis and the Pathogenesis of Prion Diseases. in *Prion - An Overview* (ed. Tutar, Y.) (InTech, 2017). doi:10.5772/67327.
24. Watt, N. T., Griffiths, H. H. & Hooper, N. M. Neuronal zinc regulation and the prion protein. *Prion* **7**, 203–208 (2013).
25. Gielnik, M. *et al.* Zn(II) binding causes interdomain changes in the structure and flexibility of the human prion protein. *Sci Rep* **11**, 21703 (2021).
26. Brown, D. R. *et al.* The cellular prion protein binds copper in vivo. *Nature* **390**, 684–687 (1997).

27. Younan, N. D. *et al.* Copper(II)-Induced Secondary Structure Changes and Reduced Folding Stability of the Prion Protein. *Journal of Molecular Biology* **410**, 369–382 (2011).
28. Nowakowski, M. *et al.* Electronic properties of a PrP ^{C} –Cu(II) complex as a marker of 5-fold Cu(II) coordination. *Metallomics* **11**, 632–642 (2019).
29. Jackson, G. S. *et al.* Location and properties of metal-binding sites on the human prion protein. *Proceedings of the National Academy of Sciences* **98**, 8531–8535 (2001).
30. Remelli, M. *et al.* Thermodynamic and spectroscopic investigation on the role of Met residues in CuII binding to the non-octarepeat site of the human prion protein. *Metallomics* **4**, 794 (2012).
31. Jones, C. E., Abdelraheim, S. R., Brown, D. R. & Viles, J. H. Preferential Cu2+ Coordination by His96 and His111 Induces β-Sheet Formation in the Unstructured Amyloidogenic Region of the Prion Protein. *Journal of Biological Chemistry* **279**, 32018–32027 (2004).
32. Kardos, J. *et al.* Copper signalling: causes and consequences. *Cell Commun Signal* **16**, 71 (2018).
33. Hopt, A. *et al.* Methods for studying synaptosomal copper release. *Journal of Neuroscience Methods* **128**, 159–172 (2003).
34. Kardos, J., Kovács, I., Hajós, F., Kálmán, M. & Simonyi, M. Nerve endings from rat brain tissue release copper upon depolarization. A possible role in regulating neuronal excitability. *Neuroscience Letters* **103**, 139–144 (1989).
35. Viles, J. H. *et al.* Copper binding to the prion protein: Structural implications of four identical cooperative binding sites. *Proceedings of the National Academy of Sciences* **96**, 2042–2047 (1999).
36. Burns, C. S. *et al.* Molecular Features of the Copper Binding Sites in the Octarepeat Domain of the Prion Protein †. *Biochemistry* **41**, 3991–4001 (2002).
37. Chattopadhyay, M. *et al.* The Octarepeat Domain of the Prion Protein Binds Cu(II) with Three Distinct Coordination Modes at pH 7.4. *J. Am. Chem. Soc.* **127**, 12647–12656 (2005).

38. Walter, E. D., Chattopadhyay, M. & Millhauser, G. L. The Affinity of Copper Binding to the Prion Protein Octarepeat Domain: Evidence for Negative Cooperativity [†]. *Biochemistry* **45**, 13083–13092 (2006).
39. Millhauser, G. L. Copper Binding in the Prion Protein [†]. *Acc. Chem. Res.* **37**, 79–85 (2004).
40. Millhauser, G. L. Chapter 12. Copper and Prion Protein Function: A Brief Review of Emerging Theories of Neuroprotection. in *Drug Discovery* (eds. Milardi, D. & Rizzarelli, E.) 249–258 (Royal Society of Chemistry, 2011). doi:10.1039/9781849733014-00249.
41. Millhauser, G. L. Copper and the Prion Protein: Methods, Structures, Function, and Disease. *Annu. Rev. Phys. Chem.* **58**, 299–320 (2007).
42. Salzano, G., Giachin, G. & Legname, G. Structural Consequences of Copper Binding to the Prion Protein. *Cells* **8**, 770 (2019).
43. Kambe, T., Tsuji, T., Hashimoto, A. & Itsumura, N. The Physiological, Biochemical, and Molecular Roles of Zinc Transporters in Zinc Homeostasis and Metabolism. *Physiological Reviews* **95**, 749–784 (2015).
44. Assaf, S. Y. & Chung, S.-H. Release of endogenous Zn2+ from brain tissue during activity. *Nature* **308**, 734–736 (1984).
45. Perera, W. S. S. & Hooper, N. M. Ablation of the metal ion-induced endocytosis of the prion protein by disease-associated mutation of the octarepeat region. *Current Biology* **11**, 519–523 (2001).
46. Watt, N. T. *et al.* Prion protein facilitates uptake of zinc into neuronal cells. *Nat Commun* **3**, 1134 (2012).
47. Walter, E. D., Stevens, D. J., Visconte, M. P. & Millhauser, G. L. The Prion Protein is a Combined Zinc and Copper Binding Protein: Zn $^{2+}$ Alters the Distribution of Cu $^{2+}$ Coordination Modes. *J. Am. Chem. Soc.* **129**, 15440–15441 (2007).

48. Markham, K. A., Roseman, G. P., Linsley, R. B., Lee, H.-W. & Millhauser, G. L. Molecular Features of the Zn2+ Binding Site in the Prion Protein Probed by 113Cd NMR. *Biophysical Journal* **116**, 610–620 (2019).

49. Watt, N. T. & Hooper, N. M. The prion protein and neuronal zinc homeostasis. *Trends in Biochemical Sciences* **28**, 406–410 (2003).

50. Gielnik, M. *et al.* PrP (58–93) peptide from unstructured N-terminal domain of human prion protein forms amyloid-like fibrillar structures in the presence of Zn $^{2+}$ ions. *RSC Adv.* **9**, 22211–22219 (2019).

51. Kelly, M. A. *et al.* Host−Guest Study of Left-Handed Polyproline II Helix Formation †. *Biochemistry* **40**, 14376–14383 (2001).

52. Abraham, M. J. *et al.* GROMACS: High performance molecular simulations through multi-level parallelism from laptops to supercomputers. *SoftwareX* **1–2**, 19–25 (2015).

53. Kaminski, G. A., Friesner, R. A., Tirado-Rives, J. & Jorgensen, W. L. Evaluation and Reparametrization of the OPLS-AA Force Field for Proteins via Comparison with Accurate Quantum Chemical Calculations on Peptides †. *J. Phys. Chem. B* **105**, 6474–6487 (2001).

54. Jorgensen, W. L., Chandrasekhar, J., Madura, J. D., Impey, R. W. & Klein, M. L. Comparison of simple potential functions for simulating liquid water. *The Journal of Chemical Physics* **79**, 926–935 (1983).

55. Bondi, A. van der Waals Volumes and Radii. *J. Phys. Chem.* **68**, 441–451 (1964).

56. Hess, B., Bekker, H., Berendsen, H. J. C. & Fraaije, J. G. E. M. LINCS: A linear constraint solver for molecular simulations. *Journal of Computational Chemistry* **18**, 1463–1472 (1997).

57. Miyamoto, S. & Kollman, P. A. Settle: An analytical version of the SHAKE and RATTLE algorithm for rigid water models. *J. Comput. Chem.* **13**, 952–962 (1992).

58. Liao, Q., Kamerlin, S. C. L. & Strodel, B. Development and Application of a Nonbonded Cu $^{2+}$ Model That Includes the Jahn–Teller Effect. *J. Phys. Chem. Lett.* **6**, 2657–2662 (2015).

59. Pogostin, B. H., Malmendal, A., Londergan, C. H. & Åkerfeldt, K. S. pKa Determination of a Histidine Residue in a Short Peptide Using Raman Spectroscopy. *Molecules* **24**, 405 (2019).
60. Bussi, G., Donadio, D. & Parrinello, M. Canonical sampling through velocity rescaling. *The Journal of Chemical Physics* **126**, 014101 (2007).
61. Parrinello, M. & Rahman, A. Polymorphic transitions in single crystals: A new molecular dynamics method. *Journal of Applied Physics* **52**, 7182–7190 (1981).
62. Essmann, U. *et al.* A smooth particle mesh Ewald method. *The Journal of Chemical Physics* **103**, 8577–8593 (1995).
63. Humphrey, W., Dalke, A. & Schulten, K. VMD: Visual molecular dynamics. *Journal of Molecular Graphics* **14**, 33–38 (1996).
64. Srinivasan, R. & Rose, G. D. A physical basis for protein secondary structure. *Proceedings of the National Academy of Sciences* **96**, 14258–14263 (1999).
65. Skjærven, L., Yao, X.-Q., Scarabelli, G. & Grant, B. J. Integrating protein structural dynamics and evolutionary analysis with Bio3D. *BMC Bioinformatics* **15**, 399 (2014).
66. Bas, D. C., Rogers, D. M. & Jensen, J. H. Very fast prediction and rationalization of pKa values for protein-ligand complexes. *Proteins* **73**, 765–783 (2008).
67. Sitkoff, D., Sharp, K. A. & Honig, B. Accurate Calculation of Hydration Free Energies Using Macroscopic Solvent Models. *J. Phys. Chem.* **98**, 1978–1988 (1994).
68. Pahari, S., Sun, L., Basu, S. & Alexov, E. DelPhiPKa: Including salt in the calculations and enabling polar residues to titrate. *Proteins* **86**, 1277–1283 (2018).
69. Case, D. A. *et al.* The Amber biomolecular simulation programs. *J. Comput. Chem.* **26**, 1668–1688 (2005).
70. Smith, C. J. *et al.* Conformational properties of the prion octa-repeat and hydrophobic sequences. *FEBS Letters* **405**, 378–384 (1997).
71. Jenness, D. D., Sprecher, C. & Johnson, W. C. Circular dichroism of collagen, gelatin, and poly(proline) II in the vacuum ultraviolet. *Biopolymers* **15**, 513–521 (1976).

72. Di Natale, G. *et al.* Membrane Interactions and Conformational Preferences of Human and Avian Prion N-Terminal Tandem Repeats: The Role of Copper(II) Ions, pH, and Membrane Mimicking Environments. *J. Phys. Chem. B* **114**, 13830–13838 (2010).
73. Garnett, A. P. & Viles, J. H. Copper Binding to the Octarepeats of the Prion Protein: AFFINITY, SPECIFICITY, FOLDING, AND COOPERATIVITY: INSIGHTS FROM CIRCULAR DICHROISM. *J. Biol. Chem.* **278**, 6795–6802 (2003).
74. Taubner, L. M., Bienkiewicz, E. A., Copié, V. & Caughey, B. Structure of the Flexible Amino-Terminal Domain of Prion Protein Bound to a Sulfated Glycan. *Journal of Molecular Biology* **395**, 475–490 (2010).
75. Danielsson, J., Jarvet, J., Damberg, P. & Gräslund, A. The Alzheimer β-peptide shows temperature-dependent transitions between left-handed 31-helix, β-strand and random coil secondary structures: Structural transitions of Alzheimer β-peptide. *FEBS Journal* **272**, 3938–3949 (2005).
76. Ranjbar, B. & Gill, P. Circular Dichroism Techniques: Biomolecular and Nanostructural Analyses- A Review. *Chemical Biology & Drug Design* **74**, 101–120 (2009).
77. Micsonai, A. *et al.* Accurate secondary structure prediction and fold recognition for circular dichroism spectroscopy. *Proc Natl Acad Sci USA* **112**, E3095–E3103 (2015).
78. Kramer, M. L. *et al.* Prion Protein Binds Copper within the Physiological Concentration Range. *J. Biol. Chem.* **276**, 16711–16719 (2001).
79. Stöckel, J., Safar, J., Wallace, A. C., Cohen, F. E. & Prusiner, S. B. Prion Protein Selectively Binds Copper(II) Ions [†]. *Biochemistry* **37**, 7185–7193 (1998).
80. Wells, M. A. *et al.* Multiple forms of copper (II) co-ordination occur throughout the disordered N-terminal region of the prion protein at pH 7.4. *Biochemical Journal* **400**, 501–510 (2006).
81. Good, N. E. *et al.* Hydrogen Ion Buffers for Biological Research [*]. *Biochemistry* **5**, 467–477 (1966).

82. Hansen, A. L. & Kay, L. E. Measurement of histidine pKa values and tautomer populations in invisible protein states. *Proceedings of the National Academy of Sciences* **111**, E1705–E1712 (2014).
83. Zahn, R. The Octapeptide Repeats in Mammalian Prion Protein Constitute a pH-dependent Folding and Aggregation Site. *Journal of Molecular Biology* **334**, 477–488 (2003).
84. Whittal, R. M. *et al.* Copper binding to octarepeat peptides of the prion protein monitored by mass spectrometry. *Protein Science* **9**, 332–343 (2000).
85. Moehl, W., Schweiger, A. & Motschi, H. Modes of phosphate binding to copper(II): investigations of the electron spin echo envelope modulation of complexes on surfaces and in solutions. *Inorg. Chem.* **29**, 1536–1543 (1990).
86. Penido, M. G. M. G. & Alon, U. S. Phosphate homeostasis and its role in bone health. *Pediatr Nephrol* **27**, 2039–2048 (2012).
87. Spevacek, A. R. *et al.* Zinc Drives a Tertiary Fold in the Prion Protein with Familial Disease Mutation Sites at the Interface. *Structure* **21**, 236–246 (2013).
88. Pushie, M. J., Rauk, A., Jirik, F. R. & Vogel, H. J. Can copper binding to the prion protein generate a misfolded form of the protein? *Biometals* **22**, 159–175 (2009).
89. Pushie, M. J. & Vogel, H. J. Modeling by Assembly and Molecular Dynamics Simulations of the Low Cu2+ Occupancy Form of the Mammalian Prion Protein Octarepeat Region: Gaining Insight into Cu2+-Mediated β-Cleavage. *Biophysical Journal* **95**, 5084–5091 (2008).
90. Pushie, M. J. & Vogel, H. J. Molecular Dynamics Simulations of Two Tandem Octarepeats from the Mammalian Prion Protein: Fully Cu2+-bound and Metal-Free Forms. *Biophysical Journal* **93**, 3762–3774 (2007).
91. Bounhar, Y., Zhang, Y., Goodyer, C. G. & LeBlanc, A. Prion Protein Protects Human Neurons against Bax-mediated Apoptosis. *J. Biol. Chem.* **276**, 39145–39149 (2001).
92. Bocharova, O. V., Breydo, L., Salnikov, V. V. & Baskakov, I. V. Copper(II) Inhibits in Vitro Conversion of Prion Protein into Amyloid Fibrils †. *Biochemistry* **44**, 6776–6787 (2005).

93. Evans, E. G. B., Pushie, M. J., Markham, K. A., Lee, H.-W. & Millhauser, G. L. Interaction between Prion Protein's Copper-Bound Octarepeat Domain and a Charged C-Terminal Pocket Suggests a Mechanism for N-Terminal Regulation. *Structure* **24**, 1057–1067 (2016).

The Prion Protein Octarepeat Domain Forms Transient β-sheet Structures Upon Residue-Specific Cu(II) and Zn(II) Binding

Maciej Gielnik [1], Aneta Szymańska [2], Xiaolin Dong[3], Jüri Jarvet [3,4], Željko M. Svedružić [5], Astrid Gräslund [3], Maciej Kozak [1,6], and Sebastian K. T. S. Wärmländer [3,*]

1 Department of Macromolecular Physics, Faculty of Physics, Adam Mickiewicz University, PL 61-614 Poznań, Poland; maciejgielnik@amu.edu.pl (M.G.); mkozak@amu.edu.pl (M.K)
2 Department of Biomedical Chemistry, Faculty of Chemistry, Gdańsk University, PL 80-308 Gdańsk, Poland; aneta.szymanska@ug.edu.pl (A.S.)
3 Department of Biochemistry and Biophysics, Stockholm University, 10691 Stockholm, Sweden; seb@student.su.se (S.K.T.S.W.); jyri.jarvet@dbb.su.se (J.J.); astrid@dbb.su.se (A.G.)
4 The National Institute of Chemical Physics and Biophysics, 12618 Tallinn, Estonia
5 Department of Biotechnology, University of Rijeka, HR 51000, Rijeka, Croatia; zeljko.svedruzic@biotech.uniri.hr (Ž.S.)
6 National Synchrotron Radiation Centre SOLARIS, Jagiellonian University, PL 30-392 Kraków, Poland

Supporting material

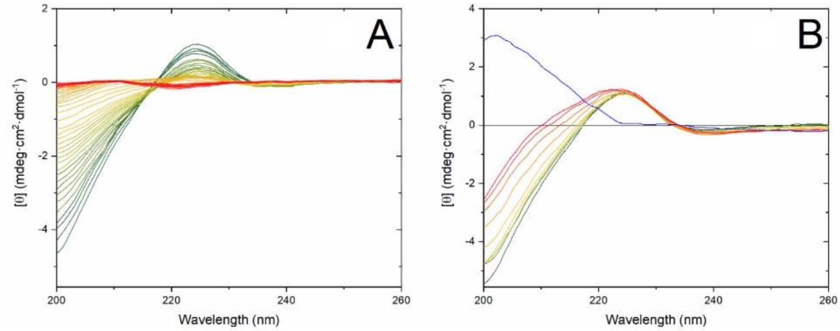

Figure S1. CD spectra of the OR peptide titrated with $CuCl_2$. (**a**) Titration of 5 µM OR peptide in pure water at 25 °C, with $CuCl_2$ in increasing (0.04 µM, 0.2 µM, 0.5 µM, 2 µM and 4 µM) intervals. The pH was adjusted to 7.5 with small amounts of NaOH. Initial spectrum: blue. Final spectrum (40 µM $CuCl_2$): red. (**b**) Titration of 5 µM OR peptide in 10 mM phosphate buffer, pH 7.5, with $CuCl_2$ in 5 µM intervals. Initial spectrum: green. Final spectrum (40 µM $CuCl_2$): red. Difference spectrum between the initial and final states: blue.

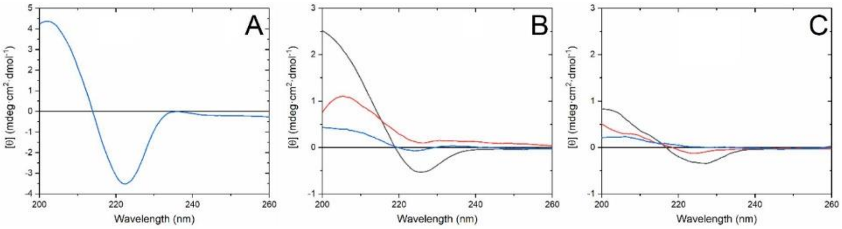

Figure S2. Difference spectra for CD curves in Figure 3. (**a**) Difference between the two spectra shown in Fig. 3a, i.e., 5 µM OR peptide in water at pH 7.5 before and addition of 20 µM $CuCl_2$. (**b**) Difference spectra between the first and last spectrum of the first (black - 5 µM OR peptide with 5 µM $CuCl_2$ minus 5 µM OR peptide), second (red - 5 µM OR peptide with 10 µM $CuCl_2$ minus 5 µM OR peptide with 5 µM $CuCl_2$), and third (blue - 5 µM OR peptide with 20 µM $CuCl_2$ minus 5 µM OR peptide with 10 µM $CuCl_2$) transitions shown in Figure 3b; (**c**) Difference spectra between the first and last spectrum of the first (black - 5 µM OR peptide with 5 µM $ZnCl_2$ minus 5 µM OR peptide), second (red - 5 µM OR peptide with 10 µM $ZnCl_2$ minus 5 µM OR peptide with 5 µM $ZnCl_2$), and third (blue - 5 µM OR peptide with 20 µM $ZnCl_2$ minus 5 µM OR peptide with 10 µM $ZnCl_2$) transitions shown in Figure 3c.

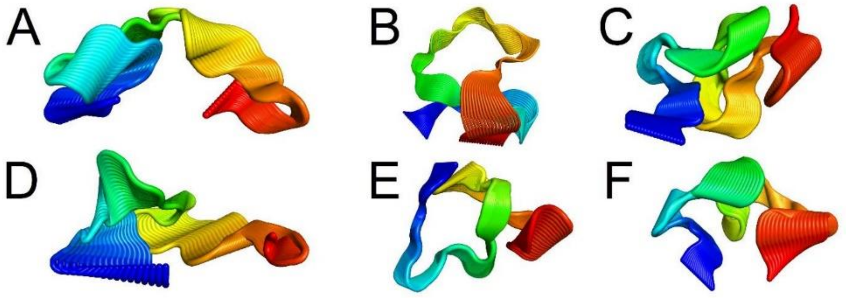

Figure S3. Visualization of the first principal component of the OR peptide simulated together with (**a**) a single Cu(II) ion and protonated histidine residues, (**b**) a single Cu(II) ion bound to four $N^{\varepsilon 2}$ atoms of neutral histidine residues, (**c**) two Cu(II) ions, each bound to two $N^{\varepsilon 2}$ atoms of neutral histidine residues, (**d**) a single Zn(II) ion and protonated histidine residues, (**e**) a single Zn(II) ion bound to four $N^{\varepsilon 2}$ atoms of neutral histidine residues and (**f**) two Zn(II) ions, each bound to two $N^{\varepsilon 2}$ atoms of neutral histidine residues.

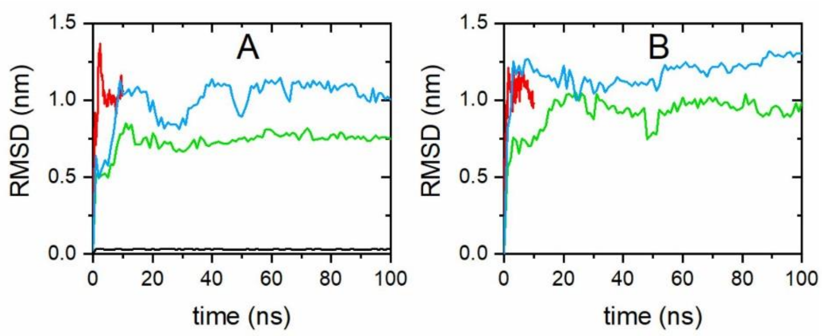

Figure S4. Root mean square deviation (RMSD) of atomic positions for simulations of the OR peptide together with: (**a**) Cu(II) ions, and (**b**) Zn(II) ions. The OR peptide with fully protonated histidine residues and a single metal ion (i.e., either Cu(II) or Zn(II)) is shown in red, while the OR peptide with neutral histidine residues simulated with a single metal ion is shown in green, the OR peptide with neutral histidine residues simulated with two metal ions is shown in blue, and the two OR peptides with neutral histidine residues simulated with a single metal ion are shown in black.

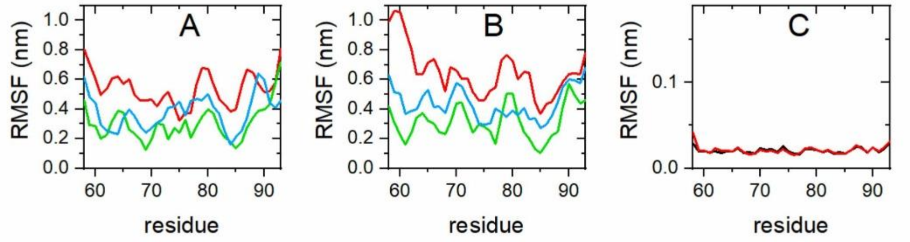

Figure S5. Root mean square fluctuations (RMSF) for simulations of the OR peptide Cα atoms together with: (**a**) Cu(II) ions, and (**b**) Zn(II) ions. Simulations of the OR peptide with fully protonated histidine residues and a single metal ion (i.e., either Cu(II) or Zn(II)) are shown in red, while the OR peptide with neutral histidine residues and a single metal ion are shown in green, and the OR peptide with neutral histidine residues and two metal ions are shown in blue. RMSF for (**c**) two OR peptide molecules simulated with neutral histidine residues and a single Cu(II) ion. OR-1 data is black and OR-2 data red.

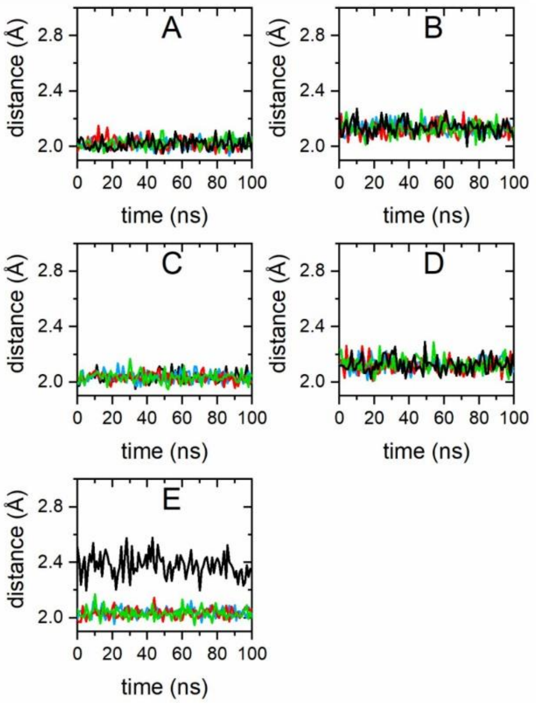

Figure S6. Distances between metal ions and histidine $N^{\varepsilon 2}$ atoms (H61: blue, H69: red, H77: green, H85: black) for simulations of the OR peptide together with: (**a**) a single Cu(II) ion; (**b**) two Cu(II) ions; (**c**) a single Zn(II) ion; (**d**) two Zn(II) ions, and (**e**) two OR peptide molecules with a single Cu(II) ion.

www.nature.com/scientificreports

scientific reports

Check for updates

OPEN

Zn(II) binding causes interdomain changes in the structure and flexibility of the human prion protein

Maciej Gielnik[1], Michał Taube[1], Lilia Zhukova[2], Igor Zhukov[2], Sebastian K. T. S. Wärmländer[3]✉, Željko Svedružić[4], Wojciech M. Kwiatek[5], Astrid Gräslund[3] & Maciej Kozak[1,6]✉

The cellular prion protein (PrP^{C}) is a mainly α-helical 208-residue protein located in the pre- and postsynaptic membranes. For unknown reasons, PrP^{C} can undergo a structural transition into a toxic, β-sheet rich scrapie isoform (PrP^{Sc}) that is responsible for transmissible spongiform encephalopathies (TSEs). Metal ions seem to play an important role in the structural conversion. PrP^{C} binds Zn(II) ions and may be involved in metal ion transport and zinc homeostasis. Here, we use multiple biophysical techniques including optical and NMR spectroscopy, molecular dynamics simulations, and small angle X-ray scattering to characterize interactions between human PrP^{C} and Zn(II) ions. Binding of a single Zn(II) ion to the PrP^{C} N-terminal domain via four His residues from the octarepeat region induces a structural transition in the C-terminal α-helices 2 and 3, promotes interaction between the N-terminal and C-terminal domains, reduces the folded protein size, and modifies the internal structural dynamics. As our results suggest that PrP^{C} can bind Zn(II) under physiological conditions, these effects could be important for the physiological function of PrP^{C}.

Misfolding and aggregation of the 208-residue prion protein (PrP) is the molecular event underlying the progressive and fatal neurodegenerative diseases collectively known as transmissible spongiform encephalopathies (TSEs)[1], or prion diseases. PrP is an outer membrane glycoprotein encoded by the PRNP gene, highly conserved within mammals[2], and expressed at high levels in the brain—especially in the striatum, hippocampus and cortex[3]. Single-nucleotide mutations or sequence expansions within the PRNP gene are the cause of genetic prion diseases such as familial Creutzfeldt-Jakob disease (fCJD), fatal familial insomnia (FFI), and Gerstmann-Sträussler-Scheinker (GSS) syndrome. Post-translational modifications of PrP produce the mature cellular form known as PrP^{C}[4–6], which can undergo a structural rearrangement into the aggregated, β-sheet-rich, and pathological (scrapie) isoform denoted as PrP^{Sc}. This form acts as a template for PrP^{C} to refold into toxic conformations[1,7]. The infectious prion diseases arise from contact with pathogenic PrP^{Sc} via events such as organ transplantation from people with CJD (iatrogenic CJD), consumption of beef contaminated with bovine spongiform encephalopathy (variant CJD)[1,7], or human cannibalistic rituals (Kuru)[8]. The most common prion disease in humans is however sporadic CJD, but its origins are unknown. Despite intense research, no drugs have so far been devised that can cure prion diseases[9–11].

The human PrP protein is expressed as a 253-residue long precursor polypeptide chain. The post-translational modifications include: removal of the N-terminal 22-residue signal sequence, removal of 23 C-terminal residues, formation of one disulfide bridge (Cys179-Cys214), glycosylation of two asparagine residues (Asn181, Asn197), as well as binding of a glycosylphosphatidylinositol (GPI) anchor[4–6] (Fig. 1). The N-terminal domain of PrP^{C} is intrinsically disordered[12], although it contains four octapeptide repeats with β-turn or polyproline II secondary structure[13–15]. The C-terminal domain, whose 3D-fold is well conserved within mammals, consists of three α-helices and two antiparallel β-sheets[12,16–18]. The first α-helix is formed by residues 144–154 and is flanked

[1]Department of Macromolecular Physics, Faculty of Physics, Adam Mickiewicz University, 61-614 Poznań, Poland. [2]Institute of Biochemistry and Biophysics, Polish Academy of Sciences, 02-106 Warszawa, Poland. [3]Department of Biochemistry and Biophysics, Stockholm University, 10691 Stockholm, Sweden. [4]Department of Biotechnology, University of Rijeka, 51000 Rijeka, Croatia. [5]Institute of Nuclear Physics Polish Academy of Sciences, 31-342 Kraków, Poland. [6]National Synchrotron Radiation Centre SOLARIS, Jagiellonian University, 30-392 Kraków, Poland. ✉email: seb@student.su.se; mkozak@amu.edu.pl

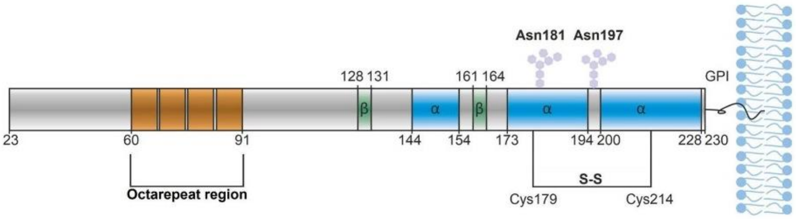

Figure 1. Schematic representation of the mature human PrP^C protein. PrP^C consists of an N-terminal intrinsically disordered domain and a C-terminal structured domain. The octarepeat (OR) region is marked in orange, α-helices are marked in blue, β-sheets are marked in green, hexagons represent the glycosylation sites, S–S is a disulfide bridge and GPI represents the glycosylphosphatidylinositol anchor.

by two short β-strands, i.e. residues 128–131 and 161–164. Helices α2 and α3 consist of residues 173–194 and 200–228, and are interconnected by a disulfide bond between Cys179 and Cys214[12,18,19]. In vitro studies suggest that conversion of the mainly α-helical PrP^C into the toxic and β-sheet-rich PrP^{Sc} isoform requires misfolding or unfolding of PrP^C as an intermediate step[1,7].

The biological function of PrP^C is not fully understood. The protein is involved in controlling synaptic transmission and neuronal plasticity. Studies on mouse models suggest that PrP^C may be crucial for the regulation of the circadian rhythm, and the development of the central nervous system[20,21]. Moreover, it has been proposed that PrP^C might have a significant role in the homeostasis of different metal ions[21,22], as the brain distribution of metal ions correlates with the PrP^C expression level[23]. It is still unclear if zinc dyshomeostasis, or metal imbalances in general, are part of the pathology in prion diseases, as appears to be the case in other neurodegenerative protein aggregation diseases such as Alzheimer's [24].

Human PrP^C has been tested for binding of various divalent metal ions including Cu(II), Ni(II), Zn(II), and Mn(II)[25–30]. Zinc is the second-most abundant (after iron) metal in living organisms. It is a co-factor of many enzymes[31], and plays an important role in cell signaling and proliferation[32]. Zn(II) ions are important neurotransmitters in the synaptic cleft where concentrations can reach up to 300 μM[33,34]. In PrP^C both Cu(II) and Zn(II) mainly binds to the octarepeat region (Fig. 1, orange)[25,29,35]. Upon binding of Zn(II) ions, the N-terminal domain forms a tertiary contact with the C-terminal domain via the octarepeats[36]. This interaction is disrupted in PrP^C mutants associated with TSE, suggesting that disruption of Zn(II)-mediated intramolecular interactions might cause TSE[36]. Even though the interaction between PrP^C and Zn(II) has been investigated for the last twenty years, the dissociation constant values reported in literature for the formed complex vary in almost three orders of magnitude, i.e. from ~0.5 μM to ~200 μM, even when measured in similar environments[25,37,38].

Here, we used multiple biophysical techniques, including spectroscopic, scattering, and theoretical methods, to study Zn(II) binding to the full-length human PrP^C protein.

Results

CD spectroscopy reveals α-helix to β-sheet transition in PrP^C upon Zn(II) binding.

Circular dichroism (CD) spectroscopy was used to monitor changes in protein secondary structure induced by Zn(II) ions. The CD spectrum of the pure protein in N-ethyl morpholine (NEM) buffer corresponds to a typical α-helix, with characteristic minima at 208 and 222 nm and a maximum at 193 nm (Fig. 2A). Addition of twenty molar equivalents of Zn(II) to PrP^C resulted in a general decrease in CD intensity over the whole wavelength range (Fig. 2A). The observed change corresponds to a decrease in the content of regular α-helices (helix 1, Table S1), and an increase in the content of distorted α-helices (helix 2, Table S1). Addition of Zn(II) also increased the content of antiparallel β-sheets and β-turns, and reduced the content of parallel β-sheets (Table S1). The changes in PrP^C secondary structure upon addition of Zn(II) were clearly visible in the far UV region; we therefore proceeded with careful Zn(II) titrations in this region.

$ZnCl_2$ was titrated to PrP^C, both in 10 mM NEM, pH 7.4 (Fig. 2B), and in 10 mM sodium phosphate buffer, pH 7.4 (Fig. 2C). The measurements in NEM buffer displayed an isodichroic point at ~ 242 nm (Fig. 2B). In phosphate buffer no isodichroic point was visible (Fig. 2C). The presence of this isodichroic point shows that the Zn(II)-induced general loss of CD signal intensity is caused by a two-phase structural transition, and not by a lowered protein concentration related to e.g. possible Zn-related aggregation and precipitation of the protein. Figure 2D,E show plots of the CD intensity at 217 nm vs Zn(II) concentration, derived from the spectra in Fig. 2B,C. Fitting binding Eq. (1) to the Zn(II) titration data in NEM buffer (Fig. 2B) produced a dissociation constant (K_d) of 28.8 ± 1.5 μM (Fig. 2D), while the titration data in sodium phosphate buffer (Fig. 2C) suggested stronger binding of Zn(II) to PrP^C. Fitting to Eq. (1) yielded the dissociation constant $K_d = 12.1 \pm 0.7$ μM (Fig. 2E). Clearly, the binding behavior of the Zn(II) ions is to some extent influenced by the environmental conditions, such as buffer composition. Because possible binding of Zn(II) ions to the buffer is not taken into account, the calculated K_d values should be considered to be apparent.

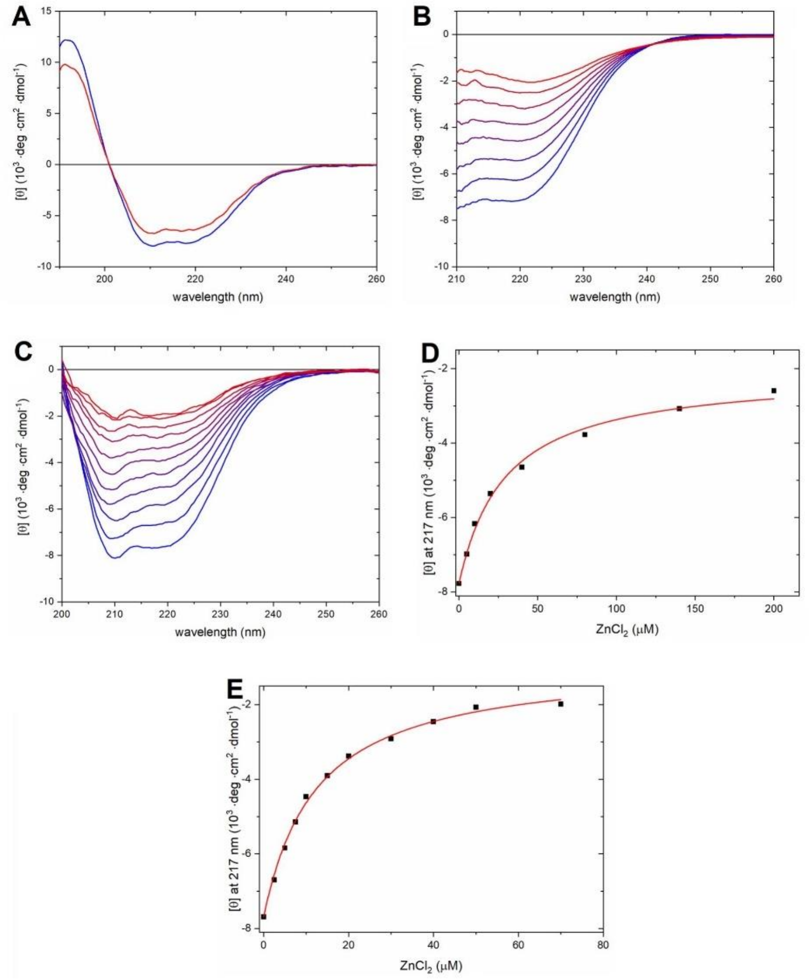

Figure 2. CD spectra of *hu*PrP^C(23–231) titrated with $ZnCl_2$. **(A)** 20 µM PrP^C (blue line) and 20 µM PrP^C with 400 µM $ZnCl_2$ (red line) in 10 mM NEM buffer, pH 7.4. **(B)** Titration of 1 µM PrP^C with $ZnCl_2$ in 10 mM NEM buffer, pH 7.4. The initial spectrum is in blue and the final one in red. **(C)** Titration of 0.5 µM PrP^C with $ZnCl_2$ in 10 mM sodium phosphate buffer, pH 7.4. The initial spectrum is in blue and the final spectrum is in red. **(D)** CD signal intensity at 217 nm derived from the spectra in Fig. 2B, plotted as a function of added $ZnCl_2$ and fitted to Eq. (1) ($K_d = 28.8 \pm 1.5$ µM). **(E)** CD signal intensity at 217 nm derived from the spectra in (C), plotted as a function of added $ZnCl_2$ and fitted to Eq. (1) ($K_d = 12.1 \pm 0.7$ µM).

Fluorescence spectroscopy shows that tryptophan residues are in close proximity to the PrP^C-Zn(II) binding site. The PrP^C protein has seven tryptophan residues located in the N-terminal unstructured domain. Four of these residues, i.e. Trp65, Trp73, Trp81 and Trp89, are located in the octarepeat region where they appear to be indirectly involved in copper binding[35]. Addition of Cu(II) ions quench the tryptophan fluorescence signal[25]. Here, a similar effect is observed upon addition of Zn(II) ions to 0.5 µM PrP^C

protein in 10 mM sodium phosphate buffer, pH 7.4 (Fig. 3A). The fluorescence spectrum of *apo*-PrP^{C} showed a single maximum at ~ 347 nm, indicating full exposure of the tryptophan residues to the solvent[39].

The titration with ZnCl$_2$ solution resulted in a reduced fluorescence intensity, a slight blue shift of the maximum to 343 nm, and revealed the presence of two additional peaks at 333 nm and 313 nm (Fig. 3A). The blue shift of tryptophan fluorescence to ~ 342 nm corresponds to a change in tryptophan environment and exposure to the bound water molecules, while the two new peaks at 333 nm and 313 nm may be attributed to buried and structured tryptophan residues, respectively[39]. In the last fluorescence spectrum of the titration, corresponding to a Zn(II) concentration of 70 μM, the maximum at 343 nm is still visible. Plotting the fluorescence intensity at 347 nm versus ZnCl$_2$ concentration and fitting the data to Eq. (2) suggested binding of Zn(II) ions to the PrP^{C} protein (Fig. 3B) with an apparent dissociation constant $K_d = 16.8 \pm 0.9$ μM.

NMR spectroscopy shows Zn(II) binding promotes interactions between the PrP^{C} N- and C-terminal domains. To investigate the structural alteration of PrP^{C} under Zn(II) saturation, high-resolution 2D heteronuclear ^{1}H-^{15}N HSQC NMR solution spectra of the protein were acquired in 50 mM deuterated HEPES buffer, 50 mM NaCl, pH 7.0, before and after addition of two molar equivalents of ZnCl$_2$ (Fig. 4A). Comparison of the spectra collected without and with Zn(II) ions revealed no differences in peak positions. Reduced cross-peak intensities for certain amino acids, however, indicate residue-specific binding interactions with Zn(II) ions (Fig. 4A). As Zn(II) ions are not paramagnetic, this loss of signal intensity is likely caused by chemical exchange on an intermediate NMR time scale. Substantial intensity changes were observed for cross-peaks corresponding to amino acids in the folded domain of the PrP^{C} 3D structure—in particular in the C-terminal region with α-helices 2 and 3. In α-helix 2, decreased cross-peak amplitudes were detected for residues in the last two turns of the helix, e.g. Thr183, His187, and Thr188 (Fig. 4A).

A more compact structure of the PrP^{C} protein in presence of Zn(II) ions was demonstrated by measurements of the translational diffusion coefficient (D_{tr}) by PGSE-NMR experiments. Addition of ZnCl$_2$ resulted in higher translational mobility of the protein compared to the *apo* form, with D_{tr} values increasing from $1.09 \pm 0.02\ 10^{-10}$ m^2/s up to $1.23 \pm 0.03\ 10^{-10}$ m^2/s (Fig. 4B).

To further explore molecular dynamic processes in the PrP^{C} sample, the ^{15}N spin–spin relaxation rates (R_2) were measured. The data acquired for the Zn-bound state were compared with previously collected R_2 values obtained for the *apo* form of PrP^{C} at the same conditions. For the 71 amide nitrogens assigned in the C-terminal domain, this comparison revealed decreased ^{15}N R_2 relaxation rates for the majority of the ^{15}N backbone resonances under Zn(II) saturation (Fig. 4C). Strong effects of Zn(II)-binding were seen in a number of C-terminal residues. For example, significantly decreased R_2 values for Gly126 and Tyr128 suggest changes towards more mobility for the short β–sheet fragment ^{128}YMLG^{131}. In addition, the significantly decreased R_2 values for the Cys214, Thr216, Ser222, and Gln223 residues in the third α-helix suggest increased local dynamics also in this region upon Zn(II) binding (Fig. 4C).

The changes in molecular dynamic processes, observed under saturation by Zn(II), are highlighted in the 3D structure of the C-terminal domain of the protein (Fig. 4D). Together with an overall lower structural stability deduced from the ^{15}N R_2 data for Zn(II)-bound PrP^{C}, we conclude that there are pronounced changes in the dynamics of the C-terminal region consisting of α–helices 2 and 3 joined with a β-strand motif (Fig. 4D). Our data suggest that even though local dynamics increase in the C-terminal domain by Zn(II) binding, the resulting effect is to promote interactions between the N-terminal and C-terminal domains, resulting in an overall more compact protein structure. Such an effect is in agreement with previous studies of Zn(II) binding to PrP^{C}[36,38].

Molecular dynamics simulations show the Zn(II) binding coordination, and consequent structural and dynamic changes in the PrP^{C} C-terminal domain. As reported previously, the Zn(II) ion can be coordinated in PrP^{C}(23–231) by four imidazole ring nitrogens from histidine His61, His69, His77, and His85 in the octarepeat fragment[36]. Our NMR data showed that addition of Zn(II) to PrP^{C} at pH 7.0 shifted only ^{13}Cε1-^{1}Hε1 resonances (Fig. S1). Despite lacking residue-specific assignments for the ^{13}C and ^{1}H histidine side-chain resonances, there are clear chemical shifts in four out of nine histidine ^{13}Cε1 signals (Fig. 5A). We speculate that these shifts are caused by Zn(II)-binding to the four histidine residues in the octarepeat region. Thus, molecular dynamic simulations were used to create the 3D structure of the Zn(II)-binding motif shown in Fig. 5. Due to the spherical geometry of Zn(II) coordination, it is difficult to predict the exact geometry of the Zn(II)-binding motif. Nevertheless, in the second coordination sphere we note the existence of two oxygens from the carbonyl groups of Gly71 and Trp89, which may compensate for the lack of negative charges in the histidine imidazole rings[40].

Molecular dynamics simulations were performed also to investigate changes in the C-terminal α-helices upon Zn(II) binding. In the first step, a 195 ns trajectory for *apo*-PrP^{C} with an extended N-terminal domain was performed. After ~ 25 ns of simulation the RMSD values converged (Fig. S2), and the N-terminal domain formed a compact structure with three antiparallel β-sheets (Pro51-Gly53, Gln67-His69, Gly72-Gly74) located around the C-terminal region of α-helix 3, which became partially unfolded (Fig. 6A, model marked in blue).

In the second step we generated a 100 ns trajectory for *holo*-PrP^{C} bound to a Zn(II) ion. Because our NMR experiments suggest an involvement of histidine Nε2 atoms in the Zn(II) coordination (Fig. S1), our initial model involved Zn(II) coordinated by the four deprotonated (i.e., neutral) Nε2 atoms from the His61, His69, His77, and His85 residues, located in the octarepeat region. The distances between the histidine ε2 nitrogen atoms and the Zn(II) ion were stable over the simulation time, with average values around ~ 2.15 Å (Fig. S3) and fluctuations in the range from 1.96 to 2.49 Å.

The simulation for *holo*-PrP^{C} also converged after ~ 25 ns (Fig. S2). During the simulation time the N-terminal domain moved closer to the C-terminal domain, in a similar way as for the *apo* form, although the resulting

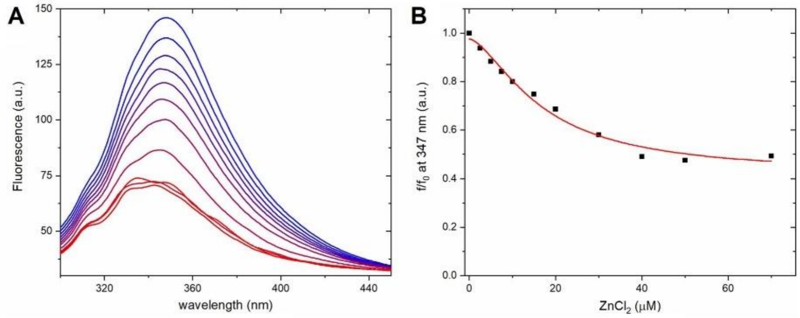

Figure 3. **(A)** Fluorescence spectra (excitation wavelength = 280 nm) of 0.5 μM *hu*PrP^{C} protein titrated with 0 to 70 μM ZnCl$_2$, see **(B)**, in 10 mM sodium phosphate buffer, pH 7.4 at 25 °C. The initial spectrum is in blue and the final in red. **(B)** Changes in the relative fluorescence intensity at 347 nm, fitted to Eq. (2) ($K_d = 16.8 \pm 0.9$ μM).

structure was less compact (Fig. 6A, model marked in red). The Zn(II)-bound octarepeat region moved to the C-terminus of α-helix 2 and unfolded this region (Fig. 6B).

Surprisingly, the main changes in PrP^{C} after Zn(II) binding involved stabilization of α-helix 3 (Fig. 6B). We therefore used MD simulations to investigate possible mechanisms for this stabilization. In *apo* form the C-terminal region of α-helix 3, involving Ser222-Arg228, becomes unfolded during a 195 ns simulation (Fig. 6B). This process may be mediated by Met166 from the β2-α2 loop. In the initial steps of the *apo*-PrP^{C} simulation, the C-terminal fragment of α-helix 3 forms hydrogen bonds with the β2-α2 loop, stabilizing α-helix 3 (Fig. 7A, Fig. S4). As the N-terminal domain can move freely, the Nδ1 atom of His111 forms a hydrogen bond with the Oε1 atom of Glu168, and disrupts the hydrogen bond between Oε2 of Glu168 and OH of Tyr226 (Fig. S5). The newly formed hydrogen bond allows Met166 to rotate (Fig. S4, Fig. S5), and then form a hydrogen bond between Sδ of Met166 and NH2 of Arg228 (Fig. S5). In the final step, Arg228 forms a hydrogen bond involving OH of Tyr163 (Fig. 7B, S6), resulting in unfolding of the C-terminal part of α-helix 3. In difference from the *apo*-PrP^{C} simulation, such unfolding of α-helix 3 was not observed in the simulation of the Zn(II)-PrP^{C} complex. In the *holo* form, α-helix 3 is initially stabilized by the β2-α2 loop in a similar manner as initially in the *apo* form (Fig. 7C, Fig. S7). In the next step, however, the three hydrophobic residues Ala120, Val121, and Val122 intercalate between the β2-α2 loop and α-helix 3, thereby separating Met166 and Arg228 (Fig. 7D, Fig. S8). Finally, α-helix 3 becomes stabilized by the N-terminal domain, where the interaction involves four possible hydrogen bonds (Fig. 7D, Fig. S9).

Our fluorescence experiments showed a blue shift for the PrP^{C} fluorescence maximum upon Zn(II) binding (Fig. 3), which suggests less exposure to the solvent and/or partial structure induction around the tryptophan residues. To investigate if such a phenomenon correlates with our MD simulations, we analyzed the χ1 and χ2 torsion angles for all tryptophan residues. The χ2- χ1 plots for the tryptophan residues located in the octarepeat region are presented in Fig. 6C,D, while χ2- χ1 plots for other tryptophan residues are presented in Figure S10. From the seven analyzed tryptophan residues two residues from the octarepeat region (i.e., Trp65 and Trp89) showed a decrease in mobility, defined as a narrower range of preferred χ2-χ1 angles, for Zn(II)-bound PrP^{C}. Interestingly, two tryptophan residues not located in the octarepeat region, i.e. Trp57 and Trp99, also showed a decrease in mobility upon Zn(II) binding. This suggests that Zn(II) binding slows down PrP^{C} dynamics not only in the octarepeat region itself, but also in the regions before and after it. In addition, χ1 for Trp81 and Trp89 from the octarepeat region more often adopted an unstable gauche^{-} conformation when Zn(II) was bound to PrP^{C}. Gauche^{-} conformations were also prominent for Trp31 and Trp57, which are located outside the octarepeat region, when Zn(II) was present. This observation suggests that Zn(II) binding can act as a driving force for PrP^{C} to access a different conformational pool, that rarely is available for *apo*-PrP^{C}.

Characterization of the PrP^{C}-Zn(II) complex using small angle X-ray scattering. Earlier results of Spevacek et al.[36] suggest that Zn(II) binding to the PrP^{C} protein induces a tertiary fold between the N-terminal and C-terminal domains. To investigate this hypothesis we performed small angle X-ray scattering (SAXS) experiments. In the initial SAXS analysis, we investigated scattering parameters that can be easily and directly obtained from the SAXS curve without any external structural models, namely the radius of gyration (R_g) and the pair distance distribution function P(r). The latter is a probability function for finding two particles at a given distance, and it allows us to easily calculate the maximum diameter of a protein. The Guinier plot (Fig. 8A, inset) for *apo*-PrP^{C} and Zn(II)-bound PrP^{C} was linear ($s \cdot R_g < 1.3$), indicating a monodisperse sample. This observation allowed us to calculate the radius of gyration (R_g) from the Guinier approximation. Our calculated R_g values for the *apo*-PrP^{C} (2.51 ± 0.11 nm) and Zn(II)-bound PrP^{C} (2.66 ± 0.07 nm) were the same within experimental error. Despite no clear differences in the R_g values, we proceeded with calculation of the P(r) function. This function, and also the determined maximum particle diameter (D_{max}), differed significantly between *apo*- and Zn(II)-

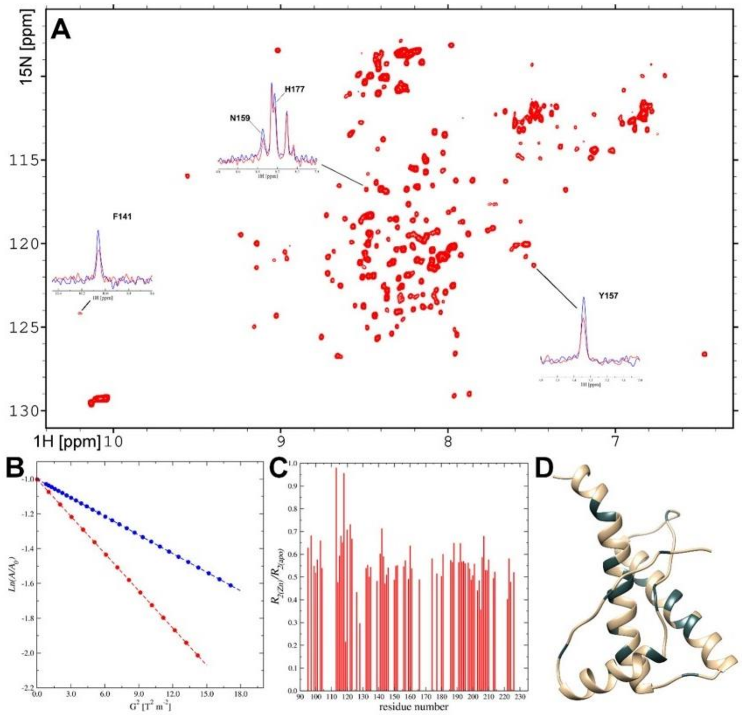

Figure 4. **(A)** 2D NMR ^{1}H-^{15}N-HSQC spectrum of 300 μM *hu*PrP^C protein in 50 mM HEPES, 50 mM NaCl, pH 7.0, under saturation with Zn(II) ions. The ^{1}H traces shown as insets reveal decreased peak amplitudes under Zn(II) saturation (red) compared to the spectra for the *apo* form (blue). **(B)** Relative amplitudes of the resonance peaks *versus* gradient strength, used to calculate translational diffusion coefficients for the *apo* (blue) and Zn(II)-saturated (red) forms of the PrP^C protein. **(C)** Relative ratios between ^{15}N R_2 relaxation rates obtained for the *apo* ($R_{2(\mathrm{apo})}$) and Zn-bound ($R_{2(\mathrm{Zn})}$) states of PrP^C residues. Data are presented only for residues in the C-terminal domain. **(D)** A ribbon presentation of the C-terminal fragment of the PrP^C protein. Residues exhibiting decreased R_2 relaxation rates under saturation with Zn(II) ions are shown in dark.

bound PrP^C. The D$_{max}$ values were ~ 11.6 nm for *apo*-PrP^C and ~ 10.2 nm for Zn(II)-bound PrP^C, suggesting a reduction in the maximum PrP^C diameter of ~ 1.4 nm (Fig. 8B).

At the next stage, the PrP^C conformation was studied by the ensemble optimization method (EOM)[41], which is commonly used for conformational analysis of intrinsically disordered proteins or proteins with intrinsically disordered domains[42]. In this approach, the sample is treated as a polydisperse mixture of different conformers, and the experimental SAXS curve is fitted as a sum of weighted calculated scattering intensities from all conformers. As initial conformers, we used the *apo* and Zn(II)-bound PrP^C models generated in our molecular dynamics simulations. Thus, the SAXS curve can be represented as a population of molecules with different R$_g$ or D$_{max}$ values. In the R$_g$ distribution, *apo*-PrP^C occupied three major and distinct conformations (Fig. 8C, blue line): compact (R$_g$ ~ 2.0 nm, ~ 71%), intermediate (R$_g$ ~ 4.0 nm, ~ 14%), and extended (R$_g$ ~ 5.2 nm, ~ 14%). Addition of Zn(II) (Fig. 8C, red line) resulted in the appearance of a predominant conformation with R$_g$ ~ 2.3 nm (~ 62%), reduction of the extended conformations to R$_g$ ~ 4.2 nm (cumulatively 24%) and a reduction of the intermediate conformations to R$_g$ ~ 3.4 (~ 12%). Similar features were observed in the D$_{max}$ distribution: *apo*-PrP^C coexisted in three main conformations (Fig. 8D, blue line, Fig. 8E) characterized by different D$_{max}$ values: compact (D$_{max}$ ~ 7.5 nm, ~ 71%), intermediate (D$_{max}$ ~ 12 nm, ~ 14%), and extended (D$_{max}$ ~ 16 nm, ~ 14%). For PrP^C bound to a Zn(II) ion, D$_{max}$ of the extended PrP^C conformers was shifted to ~ 12 nm (~ 24%) and ~ 11 nm (12%), with a reduction in the amount of the compact conformations to ~ 62% and an increase in D$_{max}$ to ~ 8.1 nm (Fig. 8D, red line, Fig. 8F). Overall, the SAXS results clearly show that binding of Zn(II) ions induces a more compact fold of the PrP^C protein.

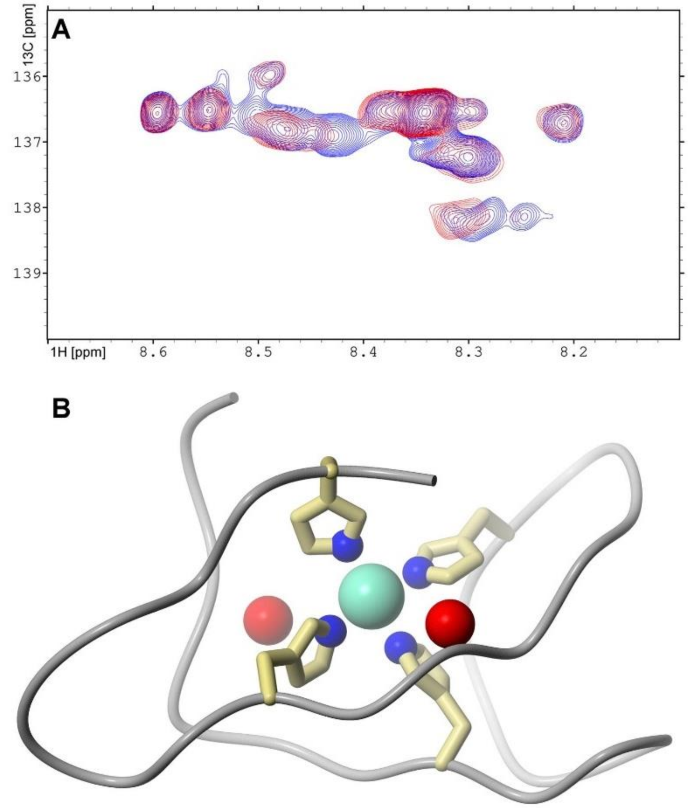

Figure 5. **(A)** Region of NMR cross-peaks for aromatic hydrogens, from 2D ^{1}H-^{13}C HSQC spectra acquired for ^{13}C,^{15}N-labeled *hu*PrP^{C}(23–231) protein in *apo* (blue) and Zn-saturated (red) form; **(B)** 3D model of the *hu*PrP^{C} Zn(II)-binding motif, obtained from MD simulations. The histidine nitrogen atoms coordinating the Zn(II) ion are shown in blue. The two additional carbonyl oxygens (Gly71 and Trp89) present in the second coordination shell are shown in red.

Discussion

Earlier studies performed on murine PrP^{C} have indicated that the N-terminal domain becomes more ordered and interacts with the C-terminal domain upon addition of Zn(II) ions[36]. To investigate such possible effects in human PrP^{C}, and if they might correspond to changes in the secondary structure of the protein, circular dichroism spectroscopy experiments were conducted. Estimation of the secondary structure from the CD spectrum of the *apo*-PrP^{C} by the BeStSel software[43] showed an α-helical content similar to that reported for the PrP^{C} NMR structure (PDB ID: 1QLX[12]) (Table S1). The observed small discrepancy between the amounts of other structural motifs in *apo*-PrP^{C}, observed by CD spectroscopy and reported in the 1QLX NMR model, are probably caused by multiple structural states of the flexible N-terminal domain[13–15]. Addition of twenty molar equivalents of Zn(II) to PrP^{C} immediately changed the CD spectrum (Fig. 2). The observed isodichroic point at ~ 242 nm suggests a decrease in the amount of regular α-helices and increase in the amount of parallel β-sheets[43]. This phenomenon probably corresponds to structural transitions within the N-terminal domain and α-helices 2 and 3, as α-helix 1 is flanked by two β-sheets (Fig. 1) and it is also more conformationally stable[12]. The proposed structural transitions would involve distortion of α-helices 2 and 3 together with structure induction in the octarepeat region with β-like motifs forming around the Zn(II) ion, rather than formation of parallel β-sheets. Such structural transitions suggest a tertiary contact between the Zn(II)-occupied octarepeat region and the

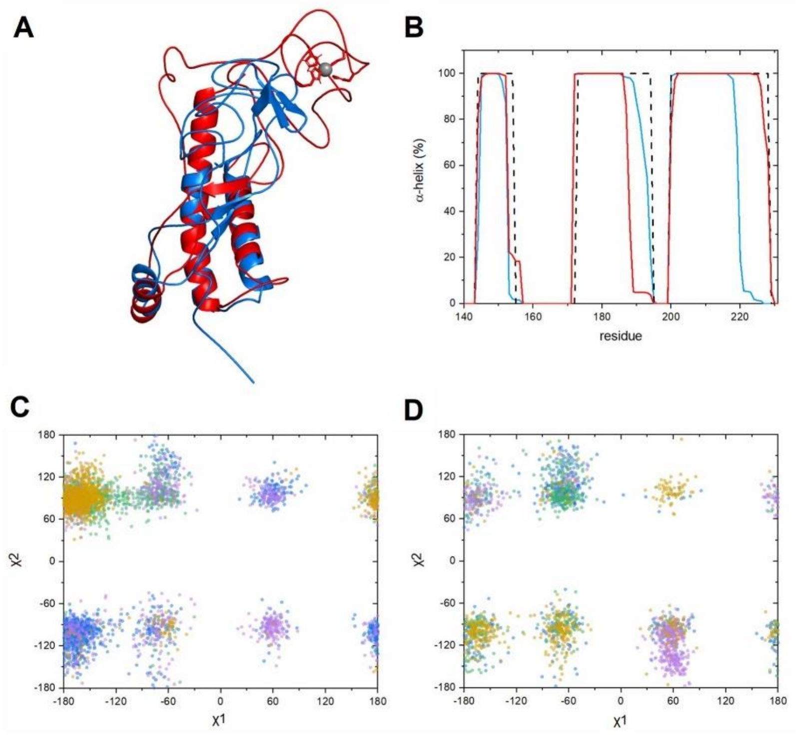

Figure 6. **(A)** Overlaid models of *apo*-PrP^C (blue) and Zn(II)-bound PrP^C (red), obtained at the end of the molecular dynamics simulations. The bound Zn(II) ion (gray) is coordinated by four histidine side chains from the PrP^C octarepeat region. **(B)** The changes in α-helicity of the PrP^C C-terminal domain during the whole time of the simulations for *apo*-PrPC (blue) and Zn(II)-bound PrP^C (red), compared to the 1QLX[13] NMR model of PrP^C (dashed black line). **(C,D)** Torsion angles χ2 versus χ1, characterizing the side chain conformations of tryptophan residues from the N-terminal domain of PrP^C in *apo* form **(C)** and with a bound Zn(II) ion **(D)**. Trp65 is blue, Trp73 is green, Trp81 is violet, and Trp89 is yellow.

C-terminal domain, in line with previous observations for mouse PrP^C(23–230) done by Spevacek et. al[36]. The increase in the amount of distorted α-helices probably originates from contacts between the Zn(II)-saturated octarepeat region and helices 2 and 3[36], leading to local secondary structure instabilities. According to our CD titrations the K_d for PrP^C-Zn(II) in phosphate buffer is 12.1 μM. This value is close to that reported in a recently published ITC study, i.e. 16.9 μM[38]. The K_d values for the PrP^C-Zn(II) complex that we here derive with different techniques (CD and fluorescence spectroscopy) and in different buffers (NEM and phosphate buffer) are slightly different, as is to be expected, but they all are in the range of 10–30 μM (Figs. 2 and 3). Thus, we conclude that the dissociation constant for the Zn(II)-PrP^C complex is in the low micromolar range.

Fluorescence spectroscopy also suggests structure induction in the N-terminal domain of PrP^C in the presence of Zn(II) ions. The fluorescence peak with a maximum at 313 nm most likely originates from tyrosine residues, as PrP^C does not contain any structured tryptophan residues[12,39,44]. Most tyrosine residues (nine out of twelve) are located in the C-terminal domain. Thus, minor changes in the tyrosine fluorescence signal likely correspond to changes in the local environment of C-terminal tyrosine residues. If such changes are induced by Zn(II) binding to the N-terminal region, they would arguably constitute evidence for interactions between the N-terminal and C-terminal domains.

During the titrations with $ZnCl_2$ the initial fluorescence peak at 347 nm, which corresponds to multiple exposed tryptophan residues, split into two well-resolved peaks of lower intensity and with maxima at 333 nm and 343 nm. These two peaks likely correspond to tryptophan residues buried and exposed to bound water molecules, respectively[39]. This observation, which is connected also to fluorescence quenching of some tryptophan residues, suggests structure induction in the PrP^C octarepeat region upon Zn(II) binding. As a comparison,

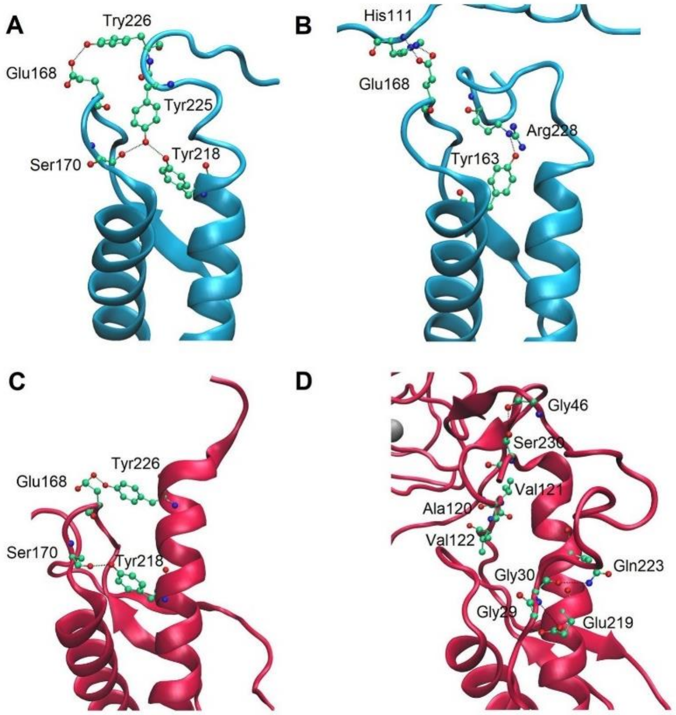

Figure 7. Different behavior of α-helix 3 in *apo* (blue) and *holo* (red) PrP^C. The C-terminal region of α-helix 3 is stabilized by the β2-α2 loop **(A,C)**. In the *apo* form formation of a His111-Glu168 hydrogen bond results in rotation of Met166, which then affects the hydrogen bond formation between Arg228 and Tyr163, resulting in partial α-helix 3 unfolding **(B)**. In the *holo* form the hydrophobic amino acids Ala120, Val121, Val122 separate the β2-α2 loop from α-helix 3, and the N-terminal domain stabilizes α-helix 3 **(D)**.

crystallographic studies of Cu(II) ions bound to the HGGGW fragment of the octarepeat region showed that tryptophan residues participate in Cu(II) coordination by forming a hydrogen bond with a water molecule axially bound to Cu(II)[35]. The octarepeat region appears to bind Cu(II) and Zn(II) ions via the same histidine residues, but in different binding conformations[25,29,35]. The K_d values calculated from our fluorescence experiments in phosphate buffer are in good agreement with our CD results, i.e. in the 10–30 μM range, which agrees with the results of previously published ICT experiments[38]. This suggests that tryptophan residues might be indirectly involved in Zn(II) binding to PrP^C.

Our NMR data suggest that binding of Zn(II) ions to PrP^C produces relatively small alterations in the 3D structure of the folded C-terminal domain, as the position of the backbone amide resonances did not show significant changes. Nevertheless, Zn(II) binding leads to increased linewidths for several backbone resonances, indicating changes in spin–spin relaxation. This was confirmed by measuring ^{15}N R_2 values. A comparison can be made with the Amyloid-*β* (Aβ) peptide related to Alzheimer´s disease, which is well known to bind metal ions[24,45]. In analogy with the interpretations proposed in a previous NMR study of Zn(II) binding to Aβ, binding of Zn(II) to the prion protein may give rise to folding of the peptide chain around the bound metal ion[46], which could explain the observed signal intensity changes in the HSQC spectrum. The NMR diffusion data furthermore suggest a more compact 3D structure of PrP^C in the presence of Zn(II), characterized by stronger interactions and an increased number of contacts between the N- and C-terminal domains, which is in agreement with the previously reported data for mouse PrP^C[36].

The prion protein structures deposited in PDB do not have fully defined N-terminal domain structures, as this domain is in a dynamic equilibrium between random coil, PPII helix, and β-turn secondary structures[13–15]. Two deposited structures of human PrP^C proteins, one for the G127V mutation and the other for wild-type PrP

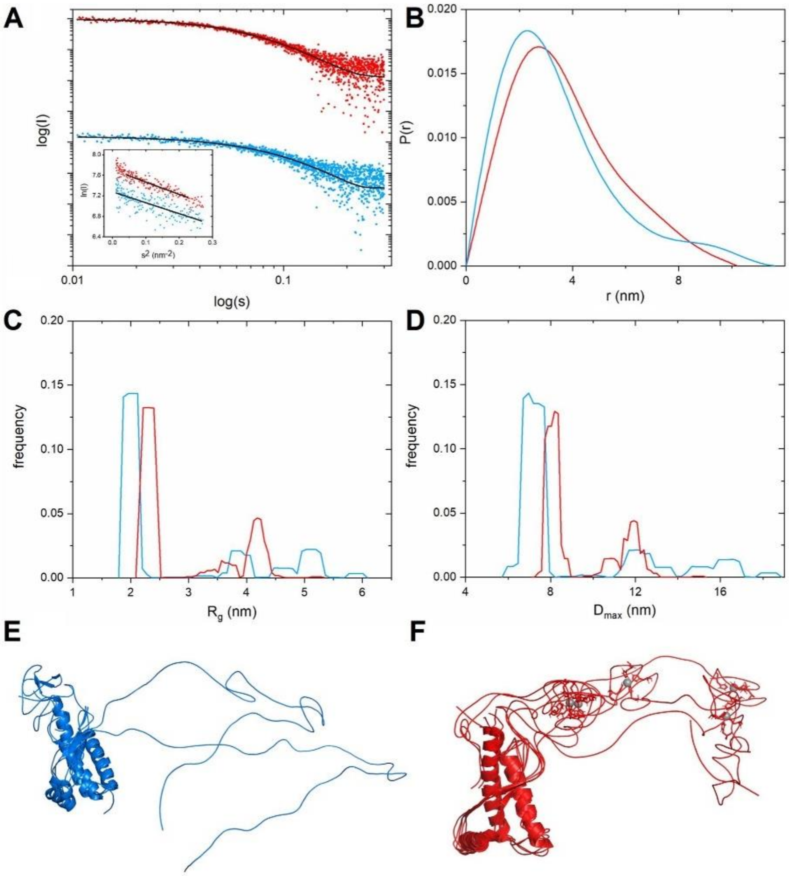

Figure 8. SAXS studies of PrP^C in *apo*- (blue) and Zn(II)-bound (red) forms. **(A)** Experimental SAXS data fitted with GAJOE (black line $\chi^2 = 1.03$ and 0.95, respectively). SAXS curves were displaced along the vertical axis for clarity. Left bottom inlet shows linear fits (black lines) in the Guinier regime. **(B)** P(r) functions for the two protein forms. **(C)** R_g distribution for the two protein forms. **(D)** D_{max} distribution for the two protein forms. **(E,F)** Pool of conformers representing *apo*-PrP^C **(E)** and Zn(II)-bound PrP^C **(F)**.

(5YJ4, 5YJ5), obtained from NMR and MD studies, contain in addition to the C-terminal domain also a collection of proposed models of the N-terminal domain[47]. However, such models do not answer what happens to PrP^C upon metal ion binding. Our MD simulations indicate that the N-terminal domain, upon Zn(II) binding, interacts with the C-terminal domain and destabilizes α-helix 2. Similar tertiary folds were previously observed for murine PrP^C interacting with Cu(II), Zn(II), and Cd(II) ions[36,38,48,49], and may therefore have similar functions in metal ion recognition.

The MD simulations suggest also that PrP^C upon Zn(II) binding might follow a different folding path, with altered interactions between the β2-α2 loop and α-helix 3. In our proposed model for Zn(II)-bound PrP^C, an interaction between His111 and Glu168 caused unfolding of the α-helix 3 C-terminal part. Such an interaction between His111 and the β2-α2 loop might be a first step in PrP^C unfolding and fibrillization. Introduction of different amino acids, in the form of glutamines in the β2-α2 loop, has previously been shown to shorten the lag phase for mouse PrP^C fibrillization[50]. As histidine residues at pH 7.4 can act both as donors and acceptors for hydrogen bonding, it is possible that His111 can form hydrogen bonds with glutamines from the β2-α2 loop, disturbing the α-helix 3 and resulting in faster PrP^C fibrillization. On the other hand, Zn(II) binding to PrP^C could disrupt such interactions by burying His111 in a different protein region. Previous in vitro studies on different forms of PrP^{C} seem to support this idea, as Zn(II) inhibits PrP aggregation[51,52].

The radius of gyration for *apo*-PrP^{C} and Zn(II)-bound PrP^{C}, determined by Guinier approximation, remained unchanged within experimental error, and were furthermore similar to those reported by Thakur et al. for *apo* and Cu(II)-bound PrP^{C}[48]. The decrease in D_{max} after addition of Zn(II) ions indicates that the N-terminal PrP^{C} domain adopts a more compact shape in the presence of Zn(II) ions. The distance distribution function moreover suggests a reduction in the maximum particle dimension by ~ 1 nm in the presence of Zn(II), similar to what was earlier observed for the Cu(II)-PrP^{C} complex[48]. Ensemble analysis performed by a genetic algorithm produced R_g and D_{max} distributions similar to those for the Cu(II)-PrP^{C} complex[48]. Our results suggest that Zn(II) binding to the PrP^{C} shows similar features to those observed for Cu(II) binding, resulting in decreased N-terminal conformational freedom and therefore partial folding of the octarepeat region around the bound metal ion.

Using crosslinking, mass spectrometry, and NMR, McDonald et al. suggested that the conformational states of Cu(II)-bound PrP^{C} are available for *apo* PrP^{C} *and* vice versa, with Cu(II) acting as a switch that shifts this equilibrium[53]. Our CD, NMR and MD results suggest that PrP^{C} upon Zn(II) binding adopts a distinct conformation, that might be unavailable for *apo* PrP^{C}. This distinct conformation is a result of the metal binding by the histidine residues that during coordination of a metal ion cannot form contacts with other parts of the protein. On the other hand our SAXS analysis shows the overlap between the R_g and D_{max} for *apo* and Zn(II)-bound PrP^{C}. This might suggest that even though major conformations of *apo* and Zn(II)-bound PrP^{C} differ, some conformations are similar, which is in line with previous studies[53].

While Zn(II) can promote dimerization of the lipid-anchored octarepeat region[54], we have recently shown that upon interaction with Zn(II) ions octarepeat peptides (consisting of PrP(58–93)) form fibrillar structures with features characteristic for amyloids: they form the characteristic cross-β structure and bind the thioflavin T and Congo Red dyes[55]. We proposed that the reason for fibril formation could be a lack of the previously reported tertiary contact between the metal ion-saturated octarepeat region and the C-terminal domain[36,49]. Indeed, the octarepeat region seems to have an important role in PrP^{Sc} formation. Studies of antibodies targeting the C-terminal domain suggest that the octarepeat region is required to maintain high PrP^{C} toxicity, while ligands targeting octarepeat region seem to reduce PrP^{C} toxicity[56].

Despite many years of research, the PrP^{C} function in terms of metal ion binding is still elusive, and it is still unclear if metal imbalance is part of the pathology in prion diseases. Out of three proposed functions for PrP^{C}, i.e. zinc sensor, transporter, or sequester[57–59], the first two seem to be the most tempting. With internalization of PrP^{C} into the Golgi apparatus and endosomes upon interaction with Zn(II)[60,61], or enhancement of zinc uptake by PrP^{C} in neurons[62] at Zn(II) concentrations around or below 100 μM, our calculated K_d values for the PrP^{C}-Zn(II) complex in the 10–30 μM range appear reasonable and physiologically important.

In summary, our results suggest that binding of Zn(II) ions to the PrP^{C} N-terminal domain via four His residues from the octarepeat region induces a structural transition in the C-terminal α-helices 2 and 3, promotes interaction between the N-terminal and C-terminal domains, reduces the folded protein size, and modifies the internal structural dynamics. The stabilization of α-helix 3 by Zn(II) binding to the N-terminal domain may explain why Zn(II) appears to inhibit PrP^{C} fibrillization.

Materials and methods

Materials. The human recombinant protein PrP^{C}(23–231) was expressed using previously published protocols[63,64]. The pRSETB vector (Invitrogen, USA) was used to clone plasmid containing a fusion of human PrP^{C} protein with a thrombin cleavage site and an N-terminal HisTag. The construct was expressed in *E. coli* (BL21-DE3) together with 100 μg/mL ampicillin antibiotic and induced by isopropyl *β*-D-galactopyranoside (IPTG) at $OD_{600} = 0.8$. A buffer containing 100 mM Tris at pH 8, 10 mM K_2HPO_4, 10 mM glutathione (GSH), 6 M GuHCl, and 0.5 mM phenylmethane sulfonyl fluoride (PMSF) was used during sonication of the lysates. Next, the supernatant was loaded to an Ni–NTA column (GE Healthcare) and eluted with buffer E (100 mM Tris at pH 5.8, 10 mM K_2HPO_4, and 500 mM imidazole). The imidazole was removed with two-step dialysis. After thrombin cleavage the *hu*PrP^{C}(23–231) was concentrated using an Amicon Ultra filter (cutoff: 3 kDa).

The ^{15}N-labeled and ^{13}C,^{15}N-double labeled forms form of *hu*PrP^{C}(23–231) were prepared by the same protocol, except that the M9 media was supplemented with 1 g of $^{15}NH_4Cl$ and 2 g of the ^{13}C-glucose (both CIL Inc, Cambridge, UK) for one liter of *E. coli* culture. Mass spectrometry was used for quality control of the samples. Protein concentrations were determined by spectrophotometry, using the extinction coefficient $\varepsilon_{280} = 57{,}995\ M^{-1}\ cm^{-1}$[65].

Circular dichroism (CD) spectroscopy. The initial potassium acetate buffer was exchanged to phosphate or N-ethylmorpholine (NEM) buffer using a Amicon® Ultra-0.5 centrifugal filter device (Merck) with an NMWL cutoff of 3 kDa. After the first round of concentration, 10 mM phosphate, pH 7.4 or 10 NEM, pH 7.4 buffer was added to increase the sample volume up to 500 μl. The sample was then centrifuged again, and the whole procedure was repeated three times. After buffer exchange the *hu*PrP^{C} sample was filtered using an Ultrafree®-MC centrifugal filter with 0.22 μm pore size.

Circular dichroism spectra were collected using a Jasco J-815 spectropolarimeter (Jasco, Tokyo, Japan). The data were collected in a step scan mode with 0.5 nm resolution, 2 nm bandwidth and digital integration time of 4 s. The spectra in a 190–260 nm and 200–260 nm range were recorded in 0.1 mm and 10 mm cells respectively. All experiments were performed in triplicate with buffer baseline correction at 25 °C. Experimental data were fitted to tight binding equation[66] (1):

$$[\theta] = [\theta]_0 - \frac{[\theta]_0 - [\theta]_\infty}{2 \cdot [PrP^C]}\left(\left(K_d^{app} + [Zn] + [PrP^C]\right) - \sqrt{\left(K_d^{app} + [Zn] + [PrP^C]\right)^2 - 4 \cdot [Zn] \cdot [PrP^C]}\right) \tag{1}$$

where $[\theta]_0$ and $[\theta]_\infty$ are the initial and saturated CD intensities, [Zn] is the Zn(II) concentration, $[PrP^C]$ is the PrP^C concentration and K_d^{app} is the dissociation constant of Zn(II)-PrP^C complex. Because possible binding of Zn(II) ions to the buffer is not taken into account, the calculated dissociation constants should be considered to be apparent.

Estimation of the secondary structure from the CD spectra was performed by the BeStSel software[43].

Fluorescence spectroscopy. Intrinsic tryptophan fluorescence was measured on a FP-8300 spectrofluorimeter (Jasco, Tokyo, Japan). Samples were excited with a wavelength of 280 nm and spectra were collected from 300 to 450 nm with 5 nm excitation and emission bandwidth. All titrations were acquired in triplicate at 25 °C. The fluorescence data were fitted with a modified Hill equation[67] (2):

$$f = f_\infty + \frac{(f_0 - f_\infty)}{1 + 10^{n_H\left(\log\left[K_d^{app}\right] - \log[Zn]\right)}} \tag{2}$$

where f_0 and f_∞ are the initial and saturated fluorescence intensities, [Zn] is the Zn(II) concentration, K_d^{app} is the apparent dissociation constant, n_H is the Hill coefficient. During the fitting procedure n_H was 1.58 ± 0.13.

Nuclear magnetic resonance (NMR) spectroscopy. NMR experiments were conducted at 298 K on an Agilent DDR2 800 MHz spectrometer operated at a magnetic field of 18.8 T (^{1}H resonance frequency 799.838 MHz). 2D ^{1}H-^{15}N-HSQC and diffusion experiments were recorded for a sample containing 300 µM uniformly ^{15}N-labeled human PrP^C(23–231) protein dissolved in 50 mM HEPES-d_{18} (CIL, Cambridge, UK) at pH 7.0 with 50 mM NaCl added.

Due to limited amount of the ^{13}C, ^{15}N-double labeled protein the aromatic ^{1}H-^{13}C HSQC was collected for the sample prepared in a 3 mm sample tube at a concentration of 100 µM also in 50 mM HEPES-d_{18}, 50 mM NaCl, pH 7.0. NMR spectra were recorded before and after addition of $ZnCl_2$ (in two steps of respectively 50 µM and 120 µM). The recorded spectra were referenced indirectly to DSS (sodium 2,2-dimethyl-2-silapentane-5-sulfonate) using a $\Xi = 0.251449530$ and 0.101329118 ratio for ^{13}C and ^{15}N resonances, respectively[68]. All NMR data were processed with NMRPipe[69] and analyzed with the Sparky[70] software.

The ^{15}N spin–spin relaxation rates (R_2) were determined at 18.8 T using a pulse sequence based on previously published experiments[71] and present in the BioPack library (Agilent Inc., PaloAlto, CA, USA). Due to fast relaxation of amide groups in human PrP^C(23–231), the ^{15}N R_2 values were calculated only with six delays—10, 30, 50, 70, 90, and 110 ms. The experimental errors were estimated as standard deviation from 500 Monte Carlo simulations with the Relax (version 4.0.3) software[72].

The diffusion data were collected using the DPFGDSTE (Double Polar Field Gradient Double Stimulated Echo) pulse sequence[73]. 28 and 15 data points were acquired to extract information about the translational diffusion coefficients (D_{tr}), respectively for the apo and the Zn(II)-bound forms of the *hu*PrP^C(23–231) protein. The DOSY data was processed using either VnmrJ v4.3 (Agilent Technologies Inc., USA) or MnovaNMR (Mestrelab Research SL. Santiago de Compostela, Spain) software. The D_{tr} experimental values were calculated according to the Stejskal-Tanner equation[74] (3):

$$I(G) = (G\gamma_H\delta)^2\left(\Delta - \frac{1}{3}G\right)D_{tr} \tag{3}$$

where γ_H is the ^{1}H gyromagnetic ratio, δ is gradient duration (2 ms), Δ is diffusion time (150 ms), and G is the gradient strength.

Molecular dynamics simulations. The initial model of full length human PrP^C was constructed by adding the missing N-terminal domain and three C-terminal residues to the 1QLX NMR structure [12]. The Zn(II) ion was placed near four histidine residues from the octarepeat domain using a sculpting tool implemented in pymol. Molecular dynamics simulations were performed in GROMACS 2019.2[75] using the GROMOS 53A6[76] force field, which contains nonbonded parameters for Zn(II). Both *apo* and Zn(II) bound PrP^C models were placed in a rectangular box with periodic boundary conditions (PBC) 5.0 nm from the box wall and solvated with a single point charge (SPC)[77] water model restrained by the SETTLE algorithm[78] using Van der Waals radii[79]. All systems were neutralized with Cl- ions and the energy was minimized with steepest descent minimization up to 5,000 steps. Temperature and pressure were equilibrated over 100 ps with a 1 fs time step using a modified Berendsen thermostat[80] and the Parrinello-Rahman barostat[81], respectively using the particle mesh Ewald (PME) method[82]. For both the *apo* and the Zn(II)-bound PrP^C molecule, the final trajectories were generated at 300 K over 195 ns with 2 fs time step or 100 ns with 1 fs time step, respectively. All covalent bonds were constrained using the LINCS[83] algorithm. The final trajectories were analyzed in the VMD software[84].

Small angle X-ray scattering. The small angle X-ray scattering (SAXS) data for human PrP^C(23–231) protein in solution were collected at the P12 beamline, operated by EMBL Hamburg at the PETRA III storage ring (DESY, Hamburg, Germany)[85] using synchrotron radiation with a wavelength of 1.24 nm. The range of the scattering vector was from 0.105 to 3.793 nm^{-1}.

For the SAXS experiments, the initial buffer was exchanged to MOPS buffer using an Amicon Ultra-0.5 centrifugal filter device (Merck) with an NMWL cutoff of 3 kDa, as described above. During the experiments the concentration of the *hu*PrP^C protein was 2 mg/ml. $ZnCl_2$ was added from a 50 mM stock solution to a final concentration of 88 μM, corresponding to a 1:1 Zn(II):*hu*PrP^C(23–231) molar ratio.

The SAXS data were processed and analyzed using the PRIMUS software[86] from the ATSAS 2.8 package[87]. The radius of gyration was obtained via the Guinier approximation for $s \cdot R_g < 1.3$. The pair distribution function, P(r), and the maximum intramolecular distance, D_{max}, were calculated using the GNOM software[88]. Because the N-terminal domain of *apo*-PrP^C is unstructured and forms multiple conformations, the SAXS data were fitted with 3D conformations from our molecular dynamics simulations using 100 cycles of GAJOE[41].

Received: 29 April 2021; Accepted: 5 October 2021

References

1. Prusiner, S. B. Nobel lecture: Prions. *Proc. Natl. Acad. Sci.* **95**, 13363–13383 (1998).
2. Harrison, P. M., Khachane, A. & Kumar, M. Genomic assessment of the evolution of the prion protein gene family in vertebrates. *Genomics* **95**, 268–277 (2010).
3. Salès, N. *et al.* Cellular prion protein localization in rodent and primate brain: PrP ^{c} brain localization. *Eur. J. Neurosci.* **10**, 2464–2471 (1998).
4. Stahl, N. Scrapie prion protein contains a phosphatidylinositol glycolipid. *Cell* **51**, 229–240 (1987).
5. Haraguchi, T. *et al.* Asparagine-linked glycosylation of the scrapie and cellular prion proteins. *Arch. Biochem. Biophys.* **274**, 1–13 (1989).
6. Heller, U., Winklhofer, K. F., Heske, J., Reintjes, A. & Tatzelt, J. Post-translational import of the prion protein into the endoplasmic reticulum interferes with cell viability: A critical role for the putative transmembrane domain. *J. Biol. Chem.* **278**, 36139–36147 (2003).
7. Colby, D. W. & Prusiner, S. B. Prions. *Cold Spring Harb. Perspect. Biol.* **3**, a006833–a006833 (2011).
8. Gajdusek, D. Unconventional viruses and the origin and disappearance of kuru. *Science* **197**, 943–960 (1977).
9. Aguzzi, A., Lakkaraju, A. K. K. & Frontzek, K. Toward therapy of human prion diseases. *Annu. Rev. Pharmacol. Toxicol.* **58**, 331–351 (2018).
10. Söderberg, K. L., Guterstam, P., Langel, Ü. & Gräslund, A. Targeting prion propagation using peptide constructs with signal sequence motifs. *Arch. Biochem. Biophys.* **564**, 254–261 (2014).
11. Gielnik, M. *et al. The Engineered Peptide Construct NCAM1-Aβ Inhibits Aggregation of the Human Prion Protein (PrP).* https://doi.org/10.1101/2021.01.04.425177 (2021).
12. Zahn, R. *et al.* NMR solution structure of the human prion protein. *Proc. Natl. Acad. Sci.* **97**, 145–150 (2000).
13. Gill, A. C. Post-translational hydroxylation at the N-terminus of the prion protein reveals presence of PPII structure in vivo. *EMBO J.* **19**, 5324–5331 (2000).
14. Zahn, R. The octapeptide repeats in mammalian prion protein constitute a pH-dependent folding and aggregation site. *J. Mol. Biol.* **334**, 477–488 (2003).
15. Smith, C. J. *et al.* Conformational properties of the prion octa-repeat and hydrophobic sequences. *FEBS Lett.* **405**, 378–384 (1997).
16. Riek, R., Hornemann, S., Wider, G., Glockshuber, R. & Wüthrich, K. NMR characterization of the full-length recombinant murine prion protein, *m* PrP(23–231). *FEBS Lett.* **413**, 282–288 (1997).
17. Pérez, D. R., Damberger, F. F. & Wüthrich, K. Horse prion protein NMR structure and comparisons with related variants of the mouse prion protein. *J. Mol. Biol.* **400**, 121–128 (2010).
18. Biljan, I. *et al.* Structural basis for the protective effect of the human prion protein carrying the dominant-negative E219K polymorphism. *Biochem. J.* **446**, 243–251 (2012).
19. Ciric, D. & Rezaei, H. Biochemical insight into the prion protein family. *Front. Cell Dev. Biol.* **3**, 15 (2015).
20. Wulf, M.-A., Senatore, A. & Aguzzi, A. The biological function of the cellular prion protein: An update. *BMC Biol.* **15**, 34 (2017).
21. Castle, A. R. & Gill, A. C. Physiological functions of the cellular prion protein. *Front. Mol. Biosci.* **4**, 633 (2017).
22. Kawahara, M., Kato-Negishi, M. & Tanaka, K. Neurometals in the pathogenesis of prion diseases. *Int. J. Mol. Sci.* **22**, 1267 (2021).
23. Pushie, M. J. *et al.* Prion protein expression level alters regional copper, iron and zinc content in the mouse brain. *Metallomics* **3**, 206 (2011).
24. Wärmländer, S. K. T. S. *et al.* Metal binding to the amyloid-β peptides in the presence of biomembranes: Potential mechanisms of cell toxicity. *JBIC J. Biol. Inorg. Chem.* **24**, 1189–1196 (2019).
25. Jackson, G. S. *et al.* Location and properties of metal-binding sites on the human prion protein. *Proc. Natl. Acad. Sci.* **98**, 8531–8535 (2001).
26. Giese, A., Levin, J., Bertsch, U. & Kretzschmar, H. Effect of metal ions on de novo aggregation of full-length prion protein. *Biochem. Biophys. Res. Commun.* **320**, 1240–1246 (2004).
27. Jószai, V. *et al.* Mixed metal copper(II)-nickel(II) and copper(II)-zinc(II) complexes of multihistidine peptide fragments of human prion protein. *J. Inorg. Biochem.* **112**, 17–24 (2012).
28. Treiber, C., Thompsett, A. R., Pipkorn, R., Brown, D. R. & Multhaup, G. Real-time kinetics of discontinuous and highly conformational metal-ion binding sites of prion protein. *JBIC J. Biol. Inorg. Chem.* **12**, 711–720 (2007).
29. Evans, E. G. B. & Millhauser, G. L. Copper- and zinc-promoted interdomain structure in the prion protein: A mechanism for autoinhibition of the neurotoxic N-terminus. in *Progress in Molecular Biology and Translational Science*, Vol. 150. 35–56 (Elsevier, 2017).
30. Millhauser, G. L. Chapter 12. Copper and prion protein function: A brief review of emerging theories of neuroprotection. in *Drug Discovery* (eds. Milardi, D. & Rizzarelli, E.). 249–258. https://doi.org/10.1039/9781849733014-00249 (Royal Society of Chemistry, 2011).
31. Vallee, B. L. & Auld, D. S. Zinc coordination, function, and structure of zinc enzymes and other proteins. *Biochemistry* **29**, 5647–5659 (1990).
32. MacDonald, R. S. The role of zinc in growth and cell proliferation. *J. Nutr.* **130**, 1500S-1508S (2000).
33. Weiss, J. H., Sensi, S. L. & Koh, J. Y. Zn2+: a novel ionic mediator of neural injury in brain disease. *Trends Pharmacol. Sci.* **21**, 395–401 (2000).
34. Assaf, S. Y. & Chung, S.-H. Release of endogenous Zn2+ from brain tissue during activity. *Nature* **308**, 734–736 (1984).
35. Burns, C. S. *et al.* Molecular features of the copper binding sites in the octarepeat domain of the prion protein †. *Biochemistry* **41**, 3991–4001 (2002).
36. Spevacek, A. R. *et al.* Zinc drives a tertiary fold in the prion protein with familial disease mutation sites at the interface. *Structure* **21**, 236–246 (2013).

37. Walter, E. D., Stevens, D. J., Visconte, M. P. & Millhauser, G. L. The prion protein is a combined zinc and copper binding protein: Zn $^{2+}$ alters the distribution of Cu $^{2+}$ coordination modes. *J. Am. Chem. Soc.* **129**, 15440–15441 (2007).
38. Markham, K. A., Roseman, G. P., Linsley, R. B., Lee, H.-W. & Millhauser, G. L. Molecular features of the Zn2+ binding site in the prion protein probed by 113Cd NMR. *Biophys. J.* **116**, 610–620 (2019).
39. Reshetnyak, Y. K. & Burstein, E. A. Decomposition of protein tryptophan fluorescence spectra into log-normal components. II. The statistical proof of discreteness of tryptophan classes in proteins. *Biophys. J.* **81**, 1710–1734 (2001).
40. Le Brun, N. *et al.* Charge compensated binding of divalent metals to bacterioferritin: H+ release associated with cobalt(II) and zinc(II) binding at dinuclear metal sites. *FEBS Lett.* **397**, 159–163 (1996).
41. Tria, G., Mertens, H. D. T., Kachala, M. & Svergun, D. I. Advanced ensemble modelling of flexible macromolecules using X-ray solution scattering. *IUCrJ* **2**, 207–217 (2015).
42. Kikhney, A. G. & Svergun, D. I. A practical guide to small angle X-ray scattering (SAXS) of flexible and intrinsically disordered proteins. *FEBS Lett.* **589**, 2570–2577 (2015).
43. Micsonai, A. *et al.* Accurate secondary structure prediction and fold recognition for circular dichroism spectroscopy. *Proc. Natl. Acad. Sci.* **112**, E3095–E3103 (2015).
44. Lakowicz, J. R. *Principles of Fluorescence Spectroscopy*. (Springer, 2010).
45. Wärmländer, S. *et al.* Biophysical studies of the amyloid β-peptide: Interactions with metal ions and small molecules. *ChemBioChem* **14**, 1692–1704 (2013).
46. Abelein, A., Gräslund, A. & Danielsson, J. Zinc as chaperone-mimicking agent for retardation of amyloid β peptide fibril formation. *Proc. Natl. Acad. Sci.* **112**, 5407–5412 (2015).
47. Zheng, Z. *et al.* Structural basis for the complete resistance of the human prion protein mutant G127V to prion disease. *Sci. Rep.* **8**, 13211 (2018).
48. Thakur, A. K., Srivastava, A. K., Srinivas, V., Chary, K. V. R. & Rao, C. M. Copper alters aggregation behavior of prion protein and induces novel interactions between Its N- and C-terminal regions. *J. Biol. Chem.* **286**, 38533–38545 (2011).
49. Evans, E. G. B., Pushie, M. J., Markham, K. A., Lee, H.-W. & Millhauser, G. L. Interaction between prion protein's copper-bound octarepeat domain and a charged C-terminal pocket suggests a mechanism for N-terminal regulation. *Structure* **24**, 1057–1067 (2016).
50. Avbelj, M., Hafner-Bratkovič, I. & Jerala, R. Introduction of glutamines into the B2–H2 loop promotes prion protein conversion. *Biochem. Biophys. Res. Commun.* **413**, 521–526 (2011).
51. Bocharova, O. V., Breydo, L., Salnikov, V. V. & Baskakov, I. V. Copper(II) inhibits in vitro conversion of prion protein into amyloid fibrils †. *Biochemistry* **44**, 6776–6787 (2005).
52. Pan, K., Yi, C.-W., Chen, J. & Liang, Y. Zinc significantly changes the aggregation pathway and the conformation of aggregates of human prion protein. *Biochim. Biophys. Acta BBA Proteins Proteom.* **1854**, 907–918 (2015).
53. McDonald, A. J. *et al.* Altered domain structure of the prion protein caused by Cu2+ binding and functionally relevant mutations: Analysis by cross-linking, MS/MS, and NMR. *Structure* **27**, 907-922.e5 (2019).
54. Kenward, A. G., Bartolotti, L. J. & Burns, C. S. Copper and zinc promote interactions between membrane-anchored peptides of the metal binding domain of the prion protein †. *Biochemistry* **46**, 4261–4271 (2007).
55. Gielnik, M. *et al.* PrP (58–93) peptide from unstructured N-terminal domain of human prion protein forms amyloid-like fibrillar structures in the presence of Zn $^{2+}$ ions. *RSC Adv.* **9**, 22211–22219 (2019).
56. Sonati, T. *et al.* The toxicity of antiprion antibodies is mediated by the flexible tail of the prion protein. *Nature* **501**, 102–106 (2013).
57. Watt, N. T. & Hooper, N. M. The prion protein and neuronal zinc homeostasis. *Trends Biochem. Sci.* **28**, 406–410 (2003).
58. Lehmann, S. Metal ions and prion diseases. *Curr. Opin. Chem. Biol.* **6**, 187–192 (2002).
59. Watt, N. T., Griffiths, H. H. & Hooper, N. M. Neuronal zinc regulation and the prion protein. *Prion* **7**, 203–208 (2013).
60. Pauly, P. C. & Harris, D. A. Copper stimulates endocytosis of the prion protein. *J. Biol. Chem.* **273**, 33107–33110 (1998).
61. Brown, L. R. & Harris, D. A. Copper and zinc cause delivery of the prion protein from the plasma membrane to a subset of early endosomes and the Golgi: Copper and zinc effect on prion protein localization. *J. Neurochem.* **87**, 353–363 (2003).
62. Watt, N. T. *et al.* Prion protein facilitates uptake of zinc into neuronal cells. *Nat. Commun.* **3**, 1134 (2012).
63. Morillas, M., Swietnicki, W., Gambetti, P. & Surewicz, W. K. Membrane environment alters the conformational structure of the recombinant human prion protein. *J. Biol. Chem.* **274**, 36859–36865 (1999).
64. Zahn, R., von Schroetter, C. & Wüthrich, K. Human prion proteins expressed in *Escherichia coli* and purified by high-affinity column refolding. *FEBS Lett.* **417**, 400–404 (1997).
65. Wilkins, M. R. *et al.* Protein identification and analysis tools in the ExPASy server. in *2-D Proteome Analysis Protocols*, Vol. 112. 531–552 (Humana Press Inc., 1999).
66. Williams, M. A. Protein–ligand interactions: Fundamentals. in *Protein-Ligand Interactions* (eds. Williams, M. A. & Daviter, T.) Vol. 1008. 3–34 (Humana Press, 2013).
67. Bindslev, N. Hill in hell. in *Drug-Acceptor Interactions*. 257–282. https://doi.org/10.3402/bindslev.2008.14 (Co-Action Publishing, 2008).
68. Wishart, D. S. *et al.* 1H, 13C and 15N chemical shift referencing in biomolecular NMR. *J. Biomol. NMR* **6**, 135–140 (1995).
69. Delaglio, F. *et al.* NMRPipe: A multidimensional spectral processing system based on UNIX pipes. *J. Biomol. NMR* **6**, 313 (1995).
70. Lee, W., Tonelli, M. & Markley, J. L. NMRFAM-SPARKY: Enhanced software for biomolecular NMR spectroscopy. *Bioinformatics* **31**, 1325–1327 (2015).
71. Farrow, N. A. *et al.* Backbone dynamics of a free and a phosphopeptide-complexed Src homology 2 domain studied by ^{15}N NMR relaxation. *Biochemistry* **33**, 5984–6003 (1994).
72. d'Auvergne, E. J. & Gooley, P. R. Optimisation of NMR dynamic models I. Minimisation algorithms and their performance within the model-free and Brownian rotational diffusion spaces. *J. Biomol. NMR* **40**, 107–119 (2008).
73. Wu, D. H., Chen, A. D. & Johnson, C. S. An improved diffusion-ordered spectroscopy experiment incorporating bipolar-gradient pulses. *J. Magn. Reson. A* **115**, 260–264 (1995).
74. Stejskal, E. O. & Tanner, J. E. Spin diffusion measurements: Spin echoes in the presence of a time-dependent field gradient. *J. Chem. Phys.* **42**, 288–292 (1965).
75. Abraham, M. J. *et al.* GROMACS: High performance molecular simulations through multi-level parallelism from laptops to supercomputers. *SoftwareX* **1–2**, 19–25 (2015).
76. Oostenbrink, C., Villa, A., Mark, A. E. & Van Gunsteren, W. F. A biomolecular force field based on the free enthalpy of hydration and solvation: The GROMOS force-field parameter sets 53A5 and 53A6. *J. Comput. Chem.* **25**, 1656–1676 (2004).
77. Berendsen, H. J. C., Postma, J. P. M., van Gunsteren, W. F. & Hermans, J. Interaction models for water in relation to protein hydration. in *Intermolecular Forces* (ed. Pullman, B.), Vol. 14. 331–342 (Springer Netherlands, 1981).
78. Miyamoto, S. & Kollman, P. A. Settle: An analytical version of the SHAKE and RATTLE algorithm for rigid water models. *J. Comput. Chem.* **13**, 952–962 (1992).
79. van der Bondi, A. Waals volumes and radii. *J. Phys. Chem.* **68**, 441–451 (1964).
80. Bussi, G., Donadio, D. & Parrinello, M. Canonical sampling through velocity rescaling. *J. Chem. Phys.* **126**, 014101 (2007).
81. Parrinello, M. & Rahman, A. Polymorphic transitions in single crystals: A new molecular dynamics method. *J. Appl. Phys.* **52**, 7182–7190 (1981).
82. Essmann, U. *et al.* A smooth particle mesh Ewald method. *J. Chem. Phys.* **103**, 8577–8593 (1995).

83. Hess, B., Bekker, H., Berendsen, H. J. C. & Fraaije, J. G. E. M. LINCS: A linear constraint solver for molecular simulations. *J. Comput. Chem.* **18**, 1463–1472 (1997).
84. Humphrey, W., Dalke, A. & Schulten, K. V. M. D. Visual molecular dynamics. *J. Mol. Graph.* **14**, 33–38 (1996).
85. Blanchet, C. E. *et al.* Versatile sample environments and automation for biological solution X-ray scattering experiments at the P12 beamline (PETRA III, DESY). *J. Appl. Crystallogr.* **48**, 431–443 (2015).
86. Konarev, P. V., Volkov, V. V., Sokolova, A. V., Koch, M. H. J. & Svergun, D. I. PRIMUS : A Windows PC-based system for small-angle scattering data analysis. *J. Appl. Crystallogr.* **36**, 1277–1282 (2003).
87. Franke, D. *et al.* ATSAS 2.8: A comprehensive data analysis suite for small-angle scattering from macromolecular solutions. *J. Appl. Crystallogr.* **50**, 1212–1225 (2017).
88. Svergun, D. I. Determination of the regularization parameter in indirect-transform methods using perceptual criteria. *J. Appl. Crystallogr.* **25**, 495–503 (1992).

Acknowledgements

This research was supported by a research grant (2014/15/B/ST4/04839) from National Science Centre (Poland). The synchrotron SAXS data were collected at beamline P12 operated by EMBL Hamburg at the PETRA III storage ring (DESY, Hamburg, Germany). We would like to thank the beamline staff for kind assistance. S.K.T.S.W. was supported by a grant from the Magnus Bergvall foundation, and A.G. by grants from the Swedish Research Council and the Brain Foundation in Sweden. High-performance computing at University of Rijeka is supported by European Fund for Regional Development (ERDF) and by the Ministry of Science, Education and Sports of the Republic of Croatia under the project number RC.2.2.06-0001.

Author contributions

L.Z. expressed the PrP^C protein. M.G. performed CD, fluorescence, MD and SAXS experiments. I.Z. performed NMR experiments. M.G., S.K.T.S.W., Ž.S., A.G. and M.K. analysed the CD and fluorescence data. I.Z., S.K.T.S.W. and A.G. analysed the NMR data. M.G., Ž.S. and I.Z. analysed the MD data. M.G., M.T. and M.K. analysed the SAXS data. M.K., W.M.K. and I.Z. conceptualized the study. M.G., I.Z., Ž.S. and M.K. designed the study. M.G. prepared the initial draft. M.G., S.K.T.S.W., I.Z., A.G. and M.K. reviewed and edited the manuscript. All authors have read and agreed to the published version of the manuscript.

Competing interests

The authors declare no competing interests.

Additional information

Supplementary Information The online version contains supplementary material available at https://doi.org/10.1038/s41598-021-00495-0.

Correspondence and requests for materials should be addressed to S.K.T.S.W. or M.K.

Reprints and permissions information is available at www.nature.com/reprints.

Supplementary information

Zn(II) binding causes interdomain changes in the structure and flexibility of the human prion protein

Maciej Gielnik[1], Michał Taube[1], Lilia Zhukova[2], Igor Zhukov[2], Sebastian K.T.S. Wärmländer[3]*, Željko Svedružić[4], Wojciech M. Kwiatek[5], Astrid Gräslund[3], Maciej Kozak[1,6]*

1 Department of Macromolecular Physics, Faculty of Physics, Adam Mickiewicz University, PL 61-614 Poznań, Poland; maciejgielnik@amu.edu.pl (M.G.); mtaube@amu.edu.pl (M.T.); mkozak@amu.edu.pl (M.K)
2 Institute of Biochemistry and Biophysics, Polish Academy of Sciences, Warszawa, Poland; lilia@ibb.waw.pl (L.Z.); igor@ibb.waw.pl (I.Z.)
3 Department of Biochemistry and Biophysics, Stockholm University, 10691 Stockholm, Sweden; seb.warmlander@gmail.com (S.K.T.S.W.); astrid@dbb.su.se (A.G.)
4 Department of Biotechnology, University of Rijeka, HR 51000, Rijeka, Croatia; zeljko.svedruzic@biotech.uniri.hr (Ž.S.)
5 Institute of Nuclear Physics Polish Academy of Sciences, Krakow, Poland; kwiatek@ifj.edu.pl (W.M.K.)
6 National Synchrotron Radiation Centre SOLARIS, Jagiellonian University, PL 30-392 Kraków, Poland

*Correspondence to: mkozak@amu.edu.pl, sebastian.warmlander@protonmail.com

Table S1. Estimation of the different secondary structure components (in %) of *apo* and Zn(II)-bound PrP^{C}, based on CD spectra (Fig. 2) analyzed with the BeStSel software[42]. 1QLX corresponds to the NMR structure proposed by Zahn[13]. NRMSD = normalized root-mean-square deviation.

	Helix 1	**Helix 2**	**Antiparallel β-sheet 1**	**Antiparallel β-sheet 2**	**Antiparallel β-sheet 3**	**Parallel β-sheet**	**Turn**	**Others**	**NRMSD**
1QLX	20.9	5.7	0	0	1.9	0	2.4	69	
apo-PrPC	20.6	8.33	0.96	7.1	5.97	4.24	9.29	43.51	0.0051
PrPC :Zn(II) 1:20	19	9.57	1.68	8.41	5.59	0.89	10.78	44.07	0.0054

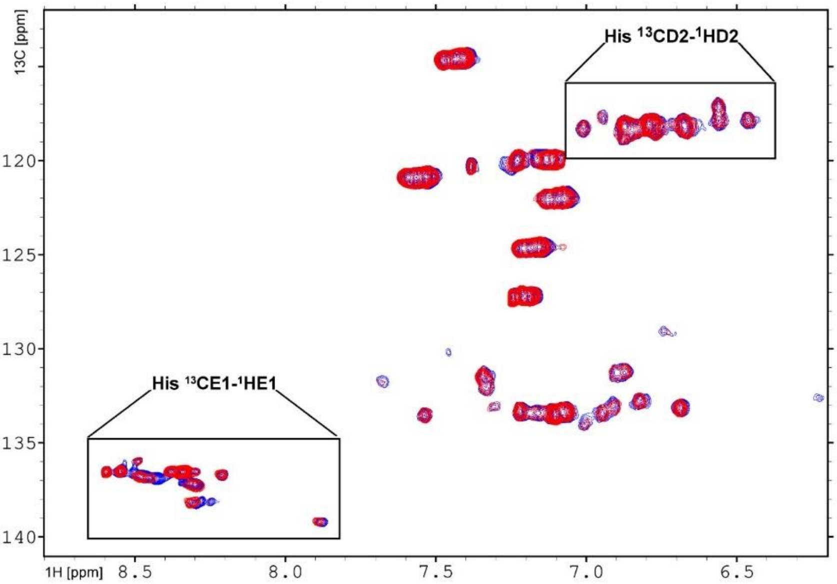

Figure S1. The overlay of the 2D ^{1}H-^{13}C HSQC spectra of the aromatic region of *apo* (blue) and Zn(II)-bound (red) PrP^{C} protein, acquired at 298 K on an Agilent DDR2 800 MHz NMR spectrometer. The regions of the ^{13}Cε1-^{1}Hε1 and ^{13}Cδ2-^{1}Hδ2 cross-peaks from histidine imidazole rings are shown as inserts.

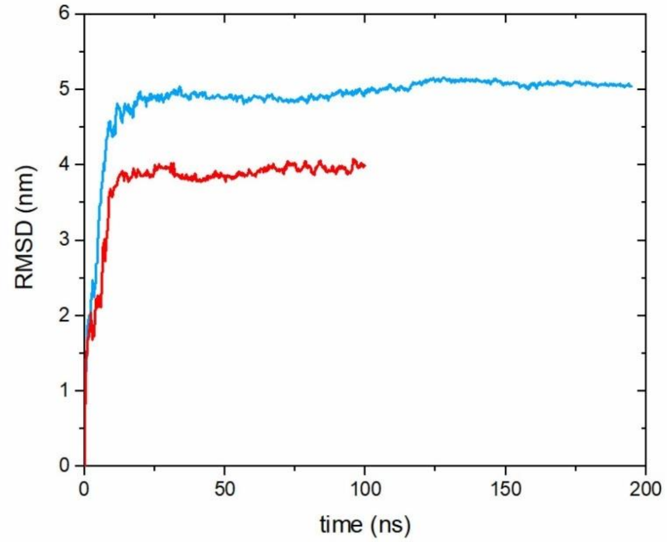

Figure S2. RMSD plot for apo (blue) and holo (red) PrP^{C}. Both systems converged after ~25 ns.

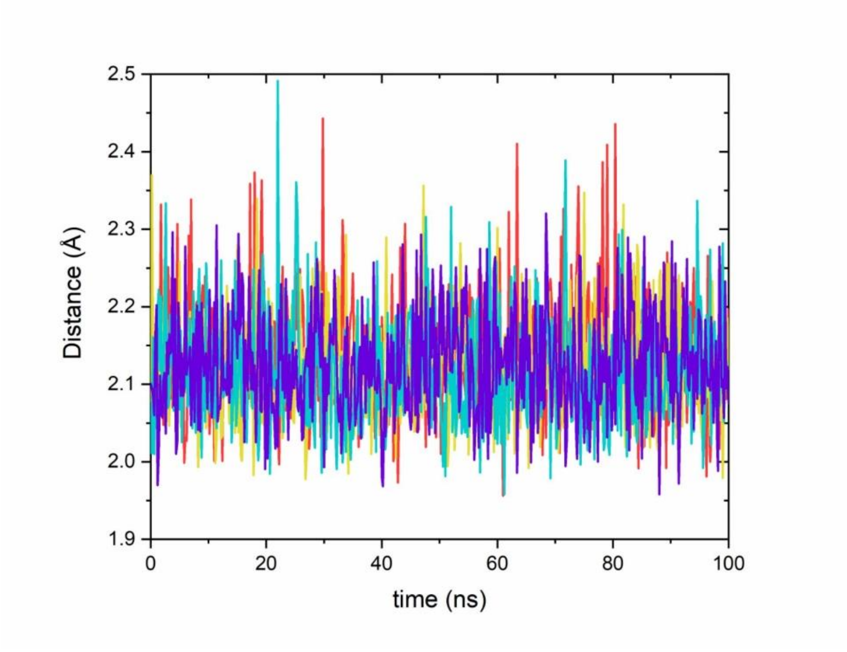

Figure S3. Computed distances between the Zn(II) ion and histidine ε2 nitrogen atoms, over 100 ns simulation time: His61 violet, His69 yellow, His77 blue, His85 red.

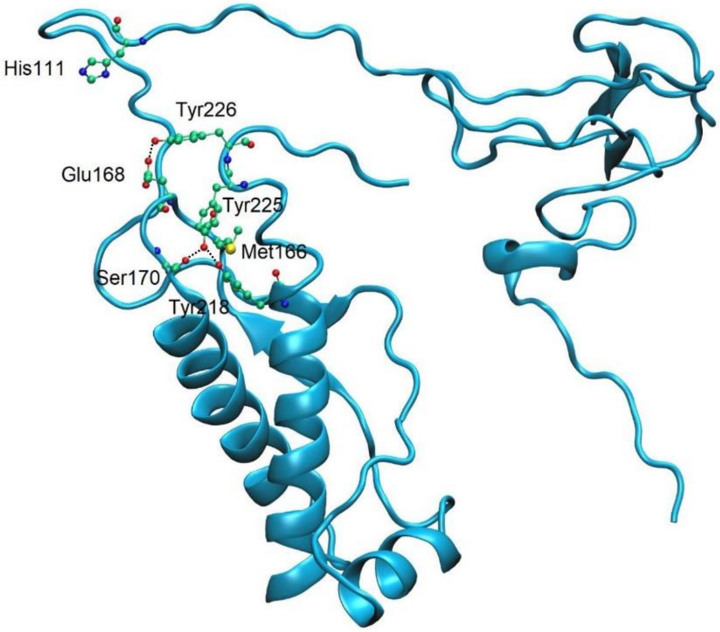

Figure S4. Possible mechanism of α-helix 3 C-terminal fragment unfolding. Initially C-terminal fragment of α-helix 3 is stabilized by hydrogen bonds between Glu168-Tyr226, Ser170-Tyr225 and Tyr225-Tyr218.

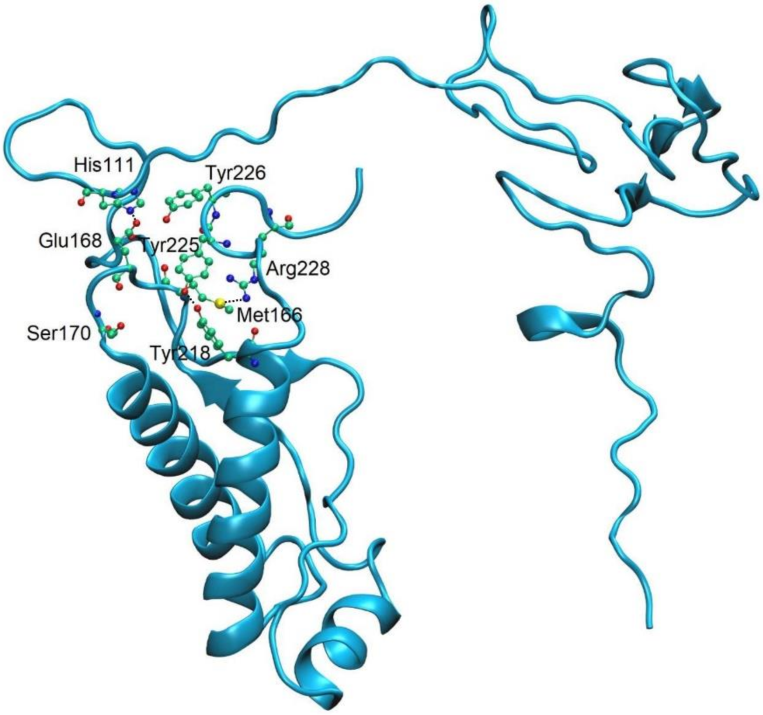

Figure S5. Possible mechanism of α-helix 3 C-terminal fragment unfolding. Newly formed hydrogen bond between H111-Glu168 allows Met166 to rotate and form hydrogen bond with Arg228.

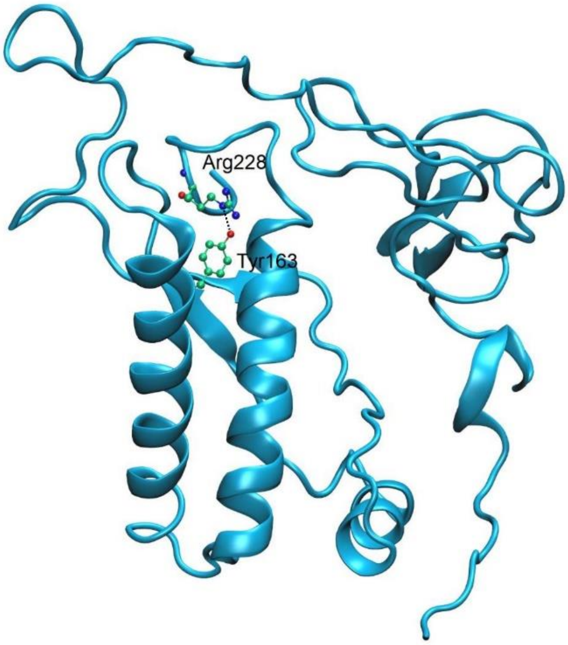

Figure S6. Possible mechanism of α-helix 3 C-terminal fragment unfolding. Arg228 form hydrogen bond with Tyr163 unfolding C-terminal fragment of α-helix 3.

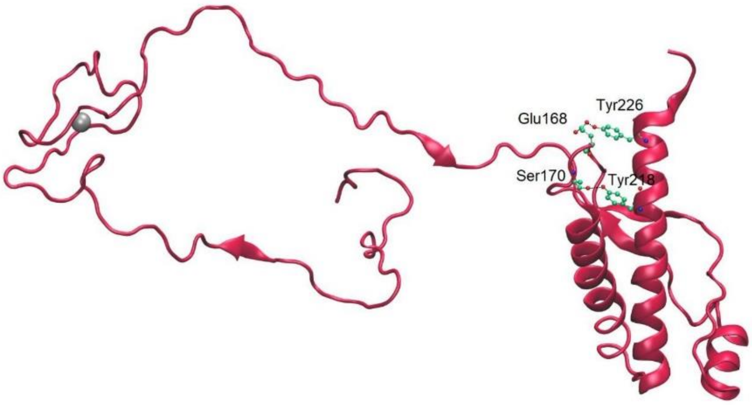

Figure S7. Possible mechanism of α-helix 3 C-terminal fragment stabilization in Zn(II)-PrP^{C} complex. Initially C-terminal fragment of α-helix 3 is stabilized by hydrogen bonds between Glu168-Tyr226 and Ser170-218.

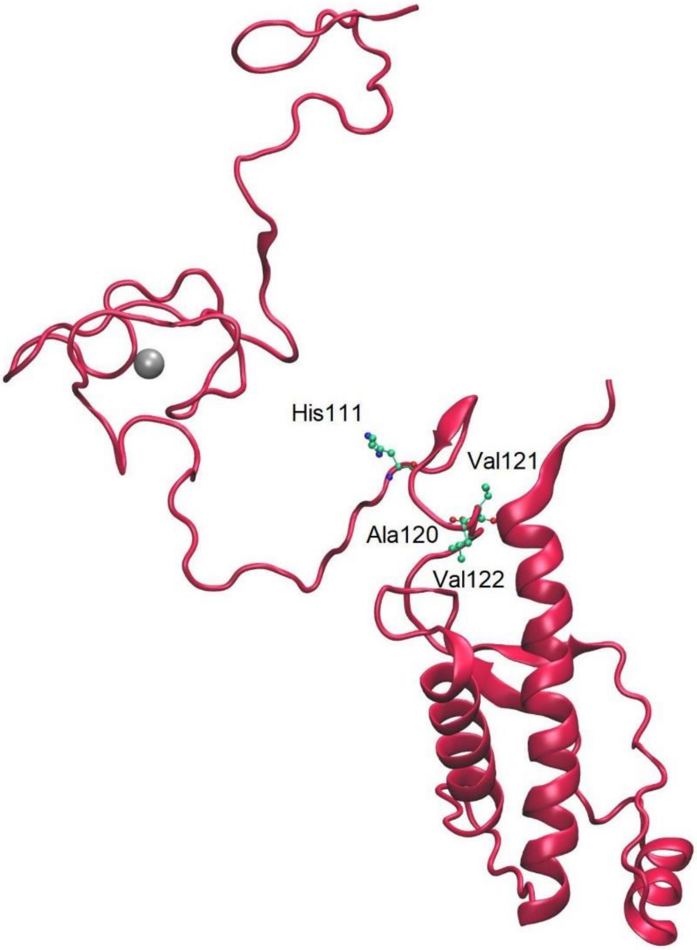

Figure S8. Possible mechanism of α-helix 3 C-terminal fragment stabilization in Zn(II)-PrP^C complex. Three hydrophobic residues Ala120, Val121, Val122 intercalate between β2-α2 loop and α-helix 3.

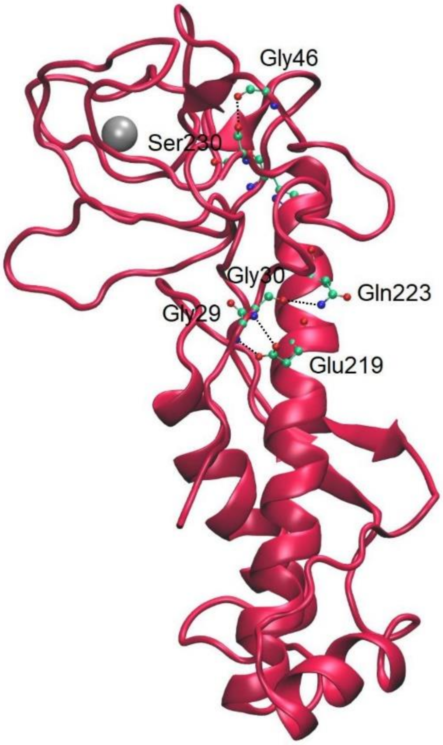

Figure S9. Possible mechanism of α-helix 3 C-terminal fragment stabilization in Zn(II)-PrP^{C} complex. N-terminal domain forms hydrogen bonds between Gly46-Ser230, Gly30-Gln223, Gly30-Glu219 and Gly29-Glu219.

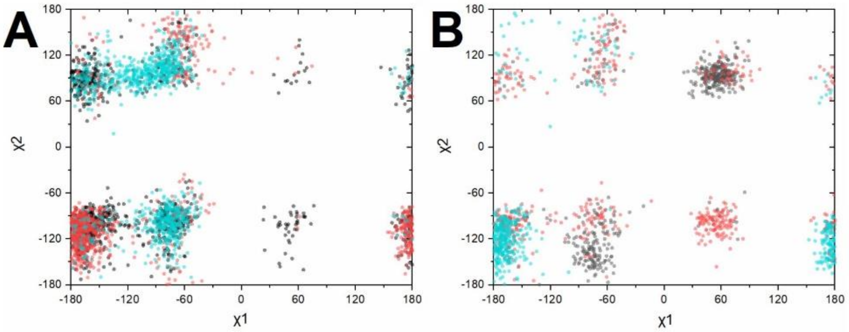

Figure S10. (A) Computed torsion angles χ2 versus χ1 for the side chains of tryptophan residues from the N-terminal domain of the PrP^C protein, in *apo* form (A) and with a bound Zn(II) ion (B). Trp31 black, Trp57 red, Trp99 blue.

The engineered peptide construct NCAM1-Aβ inhibits aggregation of the human prion protein (PrP)

Maciej Gielnik [1], Lilia Zhukova [2], Igor Zhukov [2], Astrid Gräslund [3], Maciej Kozak [1,4], Sebastian K.T.S. Wärmländer [3,*]

[1] Department of Macromolecular Physics, Adam Mickiewicz University, Poznań, Poland; maciejgielnik@amu.edu.pl (M.G.); mkozak@amu.edu.pl (M.K.)
[2] Institute of Biochemistry and Biophysics, Polish Academy of Sciences, Warszawa, Poland; lilia@ibb.waw.pl (L.Z.); igor@ibb.waw.pl (I.Z.)
[3] Department of Biochemistry and Biophysics, Arrhenius Laboratories, Stockholm University, 106 91 Stockholm, Sweden; astrid@dbb.su.se (A.G.); seb@dbb.su.se (S.W.)
[4] National Synchrotron Radiation Centre SOLARIS, Jagiellonian University, Kraków, Poland.

***** Correspondence: seb@dbb.su.se; Tel.: +46-8-16 24 44

Abstract: In prion diseases, the prion protein (PrP) becomes misfolded and forms fibrillar aggregates, which are resistant to proteinase degradation and become responsible for prion infectivity and pathology. So far, no drug or treatment procedures have been approved for prion disease treatment. We have previously shown that engineered cell-penetrating peptide constructs can reduce the amount of prion aggregates in infected cells. The molecular mechanisms underlying this effect are however unknown. Here, we use atomic force microscopy (AFM) imaging to show that the aggregation of the human PrP protein can be inhibited by equimolar amounts of the 25 residues long engineered peptide construct NCAM1-Aβ.

Keywords: Creutzfeldt-Jakob disease; AFM imaging; amyloid; drug design; drug transport; protein-peptide binding

1. Introduction

Prion and amyloid diseases are both characterized by aggregation of misfolded proteins or peptides (Jaunmuktane and Brandner, 2019; Miller, 2009; Sengupta and Udgaonkar, 2018; Verma et al., 2015), such as the prion (PrP) protein (Creutzfeldt-Jakob disease), α-synuclein (Parkinson's disease), and amyloid-β (Aβ) and tau (Alzheimer's disease). Many of these proteins and peptides may co-aggregate or at least influence each other's aggregation (Luo et al., 2016, 2017; Ren et al., 2019; Wallin et al., 2018). Factors that modulate the aggregation of one of these proteins, such as small molecules, potential drug compounds, lipids, and metal ions, can often modulate also the aggregation processes of other proteins in this family (Ambadi Thody et al., 2018; Chemerovski-Glikman et al., 2016; Gielnik et al., 2019; Owen et al., 2019; Richman et al., 2013; Robinson and Pinheiro, 2010; Wallin et al., 2017; Wärmländer et al., 2013; Wärmländer et al., 2019; Österlund et al., 2018). This suggests that the underlying mechanisms may be the same in prion and amyloid diseases (Jaunmuktane and Brandner, 2019; Jucker and Walker, 2018; Miller, 2009). Prion aggregates are however particularly infectious, as they spread between cells (Jaunmuktane and Brandner, 2019; Jucker and Walker, 2018), and are not degraded by cellular processes such as proteinase digestion (Jaunmuktane and Brandner, 2019; Löfgren et al., 2008; Söderberg et al., 2014).

The toxic species in amyloid and prion diseases are generally considered to be small toxic oligomeric aggregates (Sengupta and Udgaonkar, 2018; Verma et al., 2015), but so far no drugs or treatments that target such aggregates have been approved against prion diseases (Hyeon et al., 2020; Lee et al., 2019; Mashima et al., 2020). Potential drug molecules may interfere with oligomer formation in various ways: by reducing production of the protein, by inhibiting its aggregation, by diverting the aggregation pathway(s) towards non-toxic forms, or by reducing the lifetime of the toxic forms, for example by promoting rapid aggregation into larger non-toxic aggregates.
We have previously demonstrated anti-prion properties in short peptide constructs (up to 30 residues) with sequences derived from the unprocessed N-termini of mouse and

bovine prion proteins: such PrP-derived peptides induced lower amounts of prion aggregates resistant to proteinase K in prion-infected cells (Löfgren et al., 2008; Söderberg et al., 2014).

The PrP-derived peptides consisted of an N-terminal signal peptide segment (different for mouse and bovine PrP), together with a conserved positively charged and hydrophobic hexapeptide (KKRPKP) corresponding to the first six residues of the processed PrP protein. Our earlier studies had shown that peptides with such sequences were able to interact with and penetrate cell membranes (Lundberg et al., 2002; Magzoub et al., 2005; Magzoub et al., 2006; Oglecka et al., 2008). The anti-prion effects of the PrP-derived peptides were lost when the KKRPKP hexapeptide was coupled to various peptides with cell-penetrating properties (Söderberg et al., 2014). The anti-prion effects were however retained when KKRPKP was coupled to the signal sequence of the Neural cell adhesion molecule-1 (i.e., NCAM1$_{1\text{-}19}$) (Söderberg et al., 2014).

The mouse PrP$_{1\text{-}28}$ segment and the NCAM1$_{1\text{-}19}$-KKRPKP construct are both amyloidogenic in themselves, as they form amyloid fibrils by self-aggregation (Mukundan et al., 2017; Pansieri et al., 2019). The NCAM1$_{1\text{-}19}$-KKRPKP construct was recently shown to inhibit aggregation of the amyloid-β peptide involved in Alzheimer's disease (Henning-Knechtel et al., 2020), and to promote *in vitro* aggregation of the amyloid protein S100A9 (Pansieri et al., 2019), which is involved in amyloid-related and other inflammatory processes (Horvath et al., 2018; Wang et al., 2019; Wang et al., 2014). Almost identical results were obtained for a similar amyloidogenic 25 residue-construct, i.e. NCAM1$_{1\text{-}19}$-KKLVFF (from here onwards: NCAM1-Aβ) (Pansieri et al., 2019). The KLVFF sequence originates from the hydrophobic core (residues 16-20) of the Aβ peptide: this pentapeptide is known to inhibit aggregation of the full-length Aβ peptide (Tjernberg et al., 1996). In the NCAM1-Aβ construct, an additional lysine residue was added to the KLVFF sequence for increased solubility (Pansieri et al., 2019). The molecular properties of the NCAM1-Aβ sequence and its segments are shown in Table 1, including hydrophobicity values calculated according to the Wimley-White whole residue hydrophobicity scale (Wang et al., 2016; Wimley and White, 1996).

As the NCAM1-Aβ construct inhibits fibrillation of the Aβ peptide (Henning-Knechtel et al., 2020), but promotes (co-)aggregation of the S100A9 protein (Pansieri et al., 2019), it is unclear how the construct may affect the aggregation of the PrP protein (if at all). Here, we use Atomic Force Microscopy (AFM) imaging to investigate if there is a direct effect of the NCAM1-Aβ construct on the *in vitro* aggregation of the human PrP protein. Answering this question might help clarify the mechanisms underlying the previously observed beneficial effects of such peptide constructs on PrP infectivity (Löfgren et al., 2008; Söderberg et al., 2014).

Table 1. Primary sequences and molecular properties of the human PrP protein, the NCAM1-Aβ peptide construct, and its parts.

Protein	**Sequence**	**Isoelectric point (pI)**	**Molecular weight [g mol^{-1}]**	**Net charge at pH 7**	**Theoretical hydrophobicity [kcal mol^{-1}]**
huPrP$_{23-231}$	UniProt ID: P04156 (209 aa)	9.39	22747	+7	-
NCAM1$_{1-19}$-K-Aβ$_{16-20}$ (NCAM1-Aβ)	**NH$_2$**-MLRTKDLIWTLFFLGTAVSKKLVFF-**NH$_2$**	11.67	2974.7	+4	-3.83
NCAM1$_{1-19}$ (NCAM1)	**NH$_2$**-MLRTKDLIWTLFFLGTAVS-**NH$_2$**	11.39	2211.7	+2	-3.06
KKLVFF	**NH$_2$**-KKLVFF-**COOH**	10.69	781	+2	-0.77

2. Materials and Methods

2.1 Sample preparation

Human recombinant prion protein (huPrP) was prepared according to a previously published protocol (Morillas et al., 1999; Zahn et al., 1997), albeit with some modifications. The plasmid contained the full-length (23-231)huPrP protein in fusion with an N-terminal HisTag, and the thrombin cleavage site was cloned into the pRSETB vector (Invitrogen, USA). The construct was expressed in E. Coli (BL21-DE3) grown in LB growth medium with 100 µg/mL ampicillin. Expression was induced by isopropyl β-D-galactopyranoside (IPTG) at $OD_{600} = 0.8$. Sonication of the lysates was performed in a buffer containing 100 mM Tris at pH 8, 10 mM K_2HPO_4, 10 mM glutathione (GSH), 6 M GuHCl, and 0.5 mM phenylmethane sulfonyl fluoride (PMSF). The solution was centrifuged and the supernatant loaded to Ni-NTA resin (GE Healthcare) and eluted with buffer E (100 mM Tris at pH 5.8, 10 mM K_2HPO_4, and 500 mM imidazole). After washing the resin, the protein was purified with two-step dialysis, initially against 10 mM phosphate buffer with 0.1 mM PMSF at pH 5.8, and then against Milli-Q H_2O with 0.1 mM PMSF. After thrombin cleavage, the pure huPrP protein (i.e., with the HisTag removed) was concentrated using an Amicon Ultra 0.5 ml centrifugal filter (Merck & Co., USA) with an NMWL cutoff of 3 kDa. The final protein concentration was determined by spectrophotometry using an extinction coefficient of $\varepsilon_{280} = 57995\ M^{-1}cm^{-1}$ (Gasteiger et al., 2005). The quality of the final protein was controlled by mass spectrometry (molecular mass 22747 Da - Table 1).

The NCAM1-Aβ peptide (Table 1) was purchased as a custom order from the PolyPeptide Group (France) in lyophilized form. The peptide was dissolved in Milli-Q water, and its concentration was determined via triplicate UV absorption measurements at 280 nm, using a DS-11 spectrophotometer (DeNovix, USA) and an extinction coefficient of $\varepsilon_{280} = 5500\ M^{-1}cm^{-1}$ (Gasteiger et al., 2005).

2.2 Sample incubation

The initial buffer in the huPrP solution was exchanged to ultrapure water by triplicate diafiltration using an Amicon Ultra 0.5 ml centrifugal filter (Merck & Co., USA) with an NMWL cutoff of 3 kDa. Samples of 0.5 μM NCAM1-Aβ, 2.5 μM NCAM1-Aβ, 0.5 μM huPrP, and 0.5 μM NCAM1-Aβ + 0.5 μM huPrP were then prepared in 10 mM sodium phosphate buffer, pH 7.5, with 100 mM NaCl and 2 M urea. The urea was added as it has previously been shown to promote unfolding of the native PrP structure, which is the first step towards aggregation (Julien et al., 2009; Swietnicki et al., 2000). The samples were incubated for 72 hours at 50 °C with magnetic stirring at 400 rpm. Subsamples were taken out for AFM imaging (below) after 8 and 72 hours, respectively.

2.3 Atomic force microscopy (AFM) imaging

Incubated samples (5 μl) were transferred to freshly cleaved mica plates and left to absorb for 1 min, rinsed three times with 300 μl of pure water, and then dried under a gentle flow of nitrogen. AFM imaging was performed on a JPK Nanowizard 4 (Bruker, Germany) AFM unit using Tap150Al-G cantilevers (Ted Pella Inc., USA) in air intermittent contact mode. The scan rate was 0.3 - 0.7 Hz, the scan area size was 5 μm x 5 μm or 10 μm x 10 μm, with 512 x 512 or 1024 x 1024 pixel resolution respectively. The AFM images were analyzed using the Gwyddion 2.54 software (Necas and Klapetek, 2012).

3. Results and Discussion

AFM images of the aggregation products present in the samples after 8 hours of incubation are shown in Figs. 1A-D. The sample of 0.5 μM huPrP readily self-aggregated into long fibrils (Fig. 1A) that are approximately 3 - 4 nm thick (judged by their measured height, as width is not accurately represented in AFM images). This is somewhat thinner but still in line with the results of previous studies on PrP fibrils (Terry and Wadsworth, 2019; Vazquez-Fernandez et al., 2017; Yamaguchi and Kuwata, 2018). A few very large aggregate clumps, over 10 nm high, can also be seen (Fig. 1A). For NCAM1-Aβ, the 0.5 μM sample shows small aggregate clumps (Fig

1B). Some of them are relatively large, with heights over 6 nm, and may or may not be early stages of fibrillar aggregates (Luo et al., 2014). The 2.5 μM NCAM1-Aβ sample shows numerous mature fibrils, about 2 – 3 nm high, together with aggregate clumps (Fig. 1C). The more abundant amount of fibrils for 2.5 μM of NCAM1-Aβ confirms earlier results showing that NCAM1-Aβ self-aggregates faster at higher concentrations (Pansieri et al., 2019).

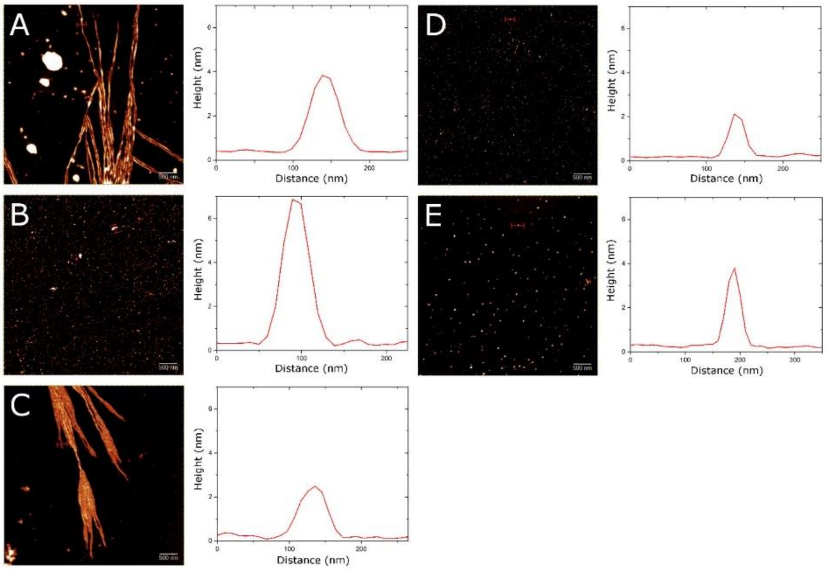

Figure 1. AFM images of: (A) 0.5 μM huPrP protein; (B) 0.5 μM NCAM1-Aβ peptide; (C) 2.5 μM NCAM1-Aβ peptide; and (D) 0.5 μM huPrP protein + 0.5 μM NCAM1-Aβ peptide. All samples in A-D were incubated for 8 hours. (E) 0.5 μM huPrP protein + 0.5 μM NCAM1-Aβ peptide, incubated for 72 hours. All studied samples were incubated at 50 °C in 10 mM sodium phosphate buffer, pH 7.5, with 100 mM NaCl and 2 M urea, and with magnetic stirring at 400 rpm. The white scale bars are 500 nm.

Interestingly, the sample containing both 0.5 μM NCAM1-Aβ and 0.5 μM huPrP displays no fibrils, but only numerous small aggregate clumps, about 2 nm high (Fig. 1D). Even after 72 hours no fibrils can be seen, but the aggregate clumps are then fewer and larger, around 3 – 4 nm high (Fig 1E). As it cannot be ruled out that these small aggregate clumps will eventually form fibrils, it is not possible to tell if fibrillation is completely inhibited, or if the fibrillation rate merely is significantly reduced. Nonetheless, the absence of fibrillar aggregates of huPrP in the presence of equimolar concentrations of NCAM1-Aβ clearly shows that the peptide construct directly interacts with the huPrP protein and interferes with its aggregation. As both molecules are positively charged (Table 1), it stands to reason that they interact mainly via hydrophobic forces.

The aggregation-inhibiting effect of NCAM1-Aβ (Fig. 1) appears to provide an explanation, at a molecular level, to our earlier observations that such peptide constructs significantly reduce the levels of prion aggregates in prion-infected cells (Löfgren et al., 2008; Söderberg et al., 2014). As both the NCAM1-Aβ peptide and the huPrP protein can form amyloid fibrils by themselves (Figs. 1A and 1C), the two molecules may interact via cross-aggregation, to form smaller non-fibrillar co-aggregates (Fig. 1E) that could be less toxic than pure huPrP aggregates (Luo et al., 2016, 2017). If so, the huPrP/NCAM1-Aβ interactions would be similar to the interactions between Aβ and NCAM1-Aβ (Henning-Knechtel et al., 2020). In any case, the huPrP/NCAM1-Aβ interactions are very different from the interactions between NCAM1-Aβ and S100A9 protein, where amyloid aggregation is promoted (Pansieri et al., 2019). Because the NCAM1-Aβ construct has different effects on different aggregating proteins, it would be interesting to study how this construct might affect the aggregation of other disease-related prion proteins, such as those involved in animal diseases like bovine spongiform encephalopathy (BSE), chronic wasting disease in cervids, and sheep scrapie (Vazquez-Fernandez et al., 2017).

4. Conclusions

Our atomic force microscopy images show that the *in vitro* aggregation of the human PrP protein is inhibited by equimolar amounts of the 25 residues long engineered peptide NCAM1-Aβ. Thus, a very likely molecular-level explanation to our previous observation that such cell-penetrating peptide constructs can reduce the amount of prion aggregates in infected cells, is that these peptide constructs directly interact with the PrP protein and prevent its fibrillation.

Funding: The research of MG, IZ, LZ and MK was supported by an OPUS research grant (2014/15/B/ST4/04839) from the National Science Centre (Poland). AG was supported by grants from the Swedish Research Council and from Byggmästare Engkvist´s Foundation.

Conflicts of Interest: The authors declare no conflict of interests.

References

Ambadi Thody, S., Mathew, M.K., Udgaonkar, J.B., 2018. Mechanism of aggregation and membrane interactions of mammalian prion protein. Biochim Biophys Acta Biomembr.

Chemerovski-Glikman, M., Rozentur-Shkop, E., Richman, M., Grupi, A., Getler, A., Cohen, H.Y., Shaked, H., Wallin, C., Wärmländer, S.K., Haas, E., Gräslund, A., Chill, J.H., Rahimipour, S., 2016. Self-Assembled Cyclic d,l-alpha-Peptides as Generic Conformational Inhibitors of the alpha-Synuclein Aggregation and Toxicity: In Vitro and Mechanistic Studies. Chemistry 22, 14236-14246.

Gasteiger, E., Hoogland, C., Gattiker, A., Duvaud, S.e., Wilkins, M.R., Appel, R.D., Amos, B., 2005. Protein Identification and Analysis Tools on the ExPASy Server, in: Walker, J.M. (Ed.), The Proteomics Protocols Handbook. Humana Press, pp. 571-607.

Gielnik, M., Pietralik, Z., Zhukov, I., Szymańska, A., Kwiatek, W.M., Kozak, M., 2019. PrP (58–93) peptide from unstructured N-terminaldomain of human prion protein forms amyloid-likefibrillar structures in the presence of Zn2+ions. RSC Advances 9, 22211–22219.

Henning-Knechtel, A., Kumar, S., Wallin, C., Król, S., Wärmländer, S., Jarvet, J., Esposito, G., Kirmizialtin, S., Gräslund, A., Hamilton, A.D., Magzoub, M., 2020. Designed cell-penetrating peptide inhibitors of amyloid-beta aggregation and cytotoxicity. Cell Reports Physical Science 1, 100014.

Horvath, I., Iashchishyn, I.A., Moskalenko, R.A., Wang, C., Wärmländer, S.K.T.S., Wallin, C., Gräslund, A., Kovacs, G.G., Morozova-Roche, L.A., 2018. Co-aggregation of pro-inflammatory S100A9 with alpha-synuclein in Parkinson's disease: ex vivo and in vitro studies. J Neuroinflammation 15, 172.

Hyeon, J.W., Noh, R., Choi, J., Lee, S.M., Lee, Y.S., An, S.S.A., No, K.T., Lee, J., 2020. BMD42-2910, a Novel Benzoxazole Derivative, Shows a Potent Anti-prion Activity and Prolongs the Mean Survival in an Animal Model of Prion Disease. Exp Neurobiol 29, 93-105.

Jaunmuktane, Z., Brandner, S., 2019. The role of prion-like mechanisms in neurodegenerative diseases. Neuropathol Appl Neurobiol.

Jucker, M., Walker, L.C., 2018. Propagation and spread of pathogenic protein assemblies in neurodegenerative diseases. Nat Neurosci 21, 1341-1349.

Julien, O., Chatterjee, S., Thiessen, A., Graether, S.P., Sykes, B.D., 2009. Differential stability of the bovine prion protein upon urea unfolding. Protein Sci 18, 2172-2182.

Kristensen, M., Birch, D., Morck Nielsen, H., 2016. Applications and Challenges for Use of Cell-Penetrating Peptides as Delivery Vectors for Peptide and Protein Cargos. Int J Mol Sci 17.

Lee, S.M., Kim, S.S., Kim, H., Kim, S.Y., 2019. THERPA v2: an update of a small molecule database related to prion protein regulation and prion disease progression. Prion 13, 197-198.

Lundberg, P., Magzoub, M., Lindberg, M., Hallbrink, M., Jarvet, J., Eriksson, L.E., Langel, U., Gräslund, A., 2002. Cell membrane translocation of the N-terminal (1-28) part of the prion protein. Biochem Biophys Res Commun 299, 85-90.

Luo, J., Wärmländer, S.K., Gräslund, A., Abrahams, J.P., 2014. Alzheimer peptides aggregate into transient nanoglobules that nucleate fibrils. Biochemistry 53, 6302-6308.

Luo, J., Wärmländer, S.K., Gräslund, A., Abrahams, J.P., 2016. Reciprocal Molecular Interactions between the Abeta Peptide Linked to Alzheimer's Disease and Insulin Linked to Diabetes Mellitus Type II. ACS Chem Neurosci 7, 269-274.

Luo, J., Wärmländer, S.K., Gräslund, A., Abrahams, J.P., 2017. Cross-interactions between the Alzheimer disease amyloid-beta peptide and other amyloid proteins. A FURTHER ASPECT OF THE AMYLOID CASCADE HYPOTHESIS. J Biol Chem 292, 2046.

Löfgren, K., Wahlström, A., Lundberg, P., Langel, U., Gräslund, A., Bedecs, K., 2008. Antiprion properties of prion protein-derived cell-penetrating peptides. FASEB J 22, 2177-2184.

Magzoub, M., Oglecka, K., Pramanik, A., Eriksson, G.L.E., Gräslund, A., 2005. Membrane perturbation effects of peptides derived from the N-termini of unprocessed prion proteins. Biochim Biophys Acta 1716, 126-136.

Magzoub, M., Sandgren, S., Lundberg, P., Oglecka, K., Lilja, J., Wittrup, A., Eriksson, G.L.E., Langel, U., Belting, M., Gräslund, A., 2006. N-terminal peptides from unprocessed prion proteins enter cells by macropinocytosis. Biochem Biophys Res Commun 348, 379-385.

Mashima, T., Lee, J.H., Kamatari, Y.O., Hayashi, T., Nagata, T., Nishikawa, F., Nishikawa, S., Kinoshita, M., Kuwata, K., Katahira, M., 2020. Development and structural determination of an anti-PrP(C) aptamer that blocks pathological conformational conversion of prion protein. Sci Rep 10, 4934.

Miller, G., 2009. Neurodegeneration. Could they all be prion diseases? Science 326, 1337-1339.

Morillas, M., Swietnicki, W., Gambetti, P., Surewicz, W.K., 1999. Membrane environment alters the conformational structure of the recombinant human prion protein. J Biol Chem 274, 36859-36865.

Mukundan, V., Maksoudian, C., Vogel, M.C., Chehade, I., Katsiotis, M.S., Alhassan, S.M., Magzoub, M., 2017. Cytotoxicity of prion protein-derived cell-penetrating peptides is modulated by pH but independent of amyloid formation. Arch Biochem Biophys 613, 31-42.

Necas, D., Klapetek, P., 2012. Gwyddion: an open-source software for SPM data analysis. Central European Journal of Physics 10, 181-188.

Oglecka, K., Lundberg, P., Magzoub, M., Eriksson, G.L.E., Langel, U., Gräslund, A., 2008. Relevance of the N-terminal NLS-like sequence of the prion protein for membrane perturbation effects. Biochim Biophys Acta 1778, 206-213.

Owen, M.C., Gnutt, D., Gao, M., Wärmländer, S.K.T.S., Jarvet, J., Gräslund, A., Winter, R., Ebbinghaus, S., Strodel, B., 2019. Effects of in vivo conditions on amyloid aggregation. Chem Soc Rev 48, 3946-3996.

Pansieri, J., Ostojic, L., Iashchishyn, I.A., Magzoub, M., Wallin, C., Wärmländer, S., Gräslund, A., Nguyen Ngoc, M., Smirnovas, V., Svedruzic, Z., Morozova-Roche, L.A., 2019. Pro-Inflammatory S100A9 Protein Aggregation Promoted by NCAM1 Peptide Constructs. ACS Chem Biol 14, 1410-1417.

Ren, B., Zhang, Y., Zhang, M., Liu, Y., Zhang, D., Gong, X., Feng, Z., Tang, J., Chang, Y., Zheng, J., 2019. Fundamentals of cross-seeding of amyloid proteins: an introduction. J Mater Chem B 7, 7267-7282.

Richman, M., Wilk, S., Chemerovski, M., Wärmländer, S.K., Wahlström, A., Gräslund, A., Rahimipour, S., 2013. In vitro and mechanistic studies of an antiamyloidogenic self-assembled cyclic D,L-alpha-peptide architecture. J Am Chem Soc 135, 3474-3484.

Robinson, P.J., Pinheiro, T.J., 2010. Phospholipid composition of membranes directs prions down alternative aggregation pathways. Biophys J 98, 1520-1528.

Santuccione, A., Sytnyk, V., Leshchyns'ka, I., Schachner, M., 2005. Prion protein recruits its neuronal receptor NCAM to lipid rafts to activate p59fyn and to enhance neurite outgrowth. J Cell Biol 169, 341-354.

Schmitt-Ulms, G., Legname, G., Baldwin, M.A., Ball, H.L., Bradon, N., Bosque, P.J., Crossin, K.L., Edelman, G.M., DeArmond, S.J., Cohen, F.E., Prusiner, S.B., 2001. Binding of neural cell adhesion molecules (N-CAMs) to the cellular prion protein. J Mol Biol 314, 1209-1225.

Sengupta, I., Udgaonkar, J.B., 2018. Structural mechanisms of oligomer and amyloid fibril formation by the prion protein. Chem Commun (Camb) 54, 6230-6242.

Swietnicki, W., Morillas, M., Chen, S.G., Gambetti, P., Surewicz, W.K., 2000. Aggregation and fibrillization of the recombinant human prion protein huPrP90-231. Biochemistry 39, 424-431.

Söderberg, K.L., Guterstam, P., Langel, U., Gräslund, A., 2014. Targeting prion propagation using peptide constructs with signal sequence motifs. Arch Biochem Biophys 564, 254-261.

Terry, C., Wadsworth, J.D.F., 2019. Recent Advances in Understanding Mammalian Prion Structure: A Mini Review. Front Mol Neurosci 12, 169.

Tjernberg, L.O., Näslund, J., Lindqvist, F., Johansson, J., Karlström, A.R., Thyberg, J., Terenius, L., Nordstedt, C., 1996. Arrest of beta-amyloid fibril formation by a pentapeptide ligand. J Biol Chem 271, 8545-8548.

Vazquez-Fernandez, E., Young, H.S., Requena, J.R., Wille, H., 2017. The Structure of Mammalian Prions and Their Aggregates. Int Rev Cell Mol Biol 329, 277-301.

Verma, M., Vats, A., Taneja, V., 2015. Toxic species in amyloid disorders: Oligomers or mature fibrils. Ann Indian Acad Neurol 18, 138-145.

Wallin, C., Hiruma, Y., Wärmländer, S., Huvent, I., Jarvet, J., Abrahams, J.P., Gräslund, A., Lippens, G., Luo, J., 2018. The Neuronal Tau Protein Blocks in Vitro Fibrillation of the Amyloid-beta (Abeta) Peptide at the Oligomeric Stage. J Am Chem Soc 140, 8138-8146.

Wallin, C., Luo, J., Jarvet, J., Wärmländer, S.K.T.S., Gräslund, A., 2017. The Amyloid-b Peptide in Amyloid Formation Processes: Interactions with Blood Proteins and Naturally Occurring Metal Ions. Israel Journal of Chemistry 57, 674-685.

Wang, C., Iashchishyn, I.A., Kara, J., Fodera, V., Vetri, V., Sancataldo, G., Marklund, N., Morozova-Roche, L.A., 2019. Proinflammatory and amyloidogenic S100A9 induced by traumatic brain injury in mouse model. Neurosci Lett 699, 199-205.

Wang, C., Klechikov, A.G., Gharibyan, A.L., Wärmländer, S.K.T.S., Jarvet, J., Zhao, L., Jia, X., Narayana, V.K., Shankar, S.K., Olofsson, A., Brännström, T., Mu, Y., Gräslund, A., Morozova-Roche, L.A., 2014. The role of pro-inflammatory S100A9 in Alzheimer's disease amyloid-neuroinflammatory cascade. Acta Neuropathol 127, 507-522.

Wang, G., Li, X., Wang, Z., 2016. APD3: the antimicrobial peptide database as a tool for research and education. Nucleic Acids Res 44, D1087-1093.

Wimley, W.C., White, S.H., 1996. Experimentally determined hydrophobicity scale for proteins at membrane interfaces. Nat Struct Biol 3, 842-848.

Wärmländer, S.K.T.S., Tiiman, A., Abelein, A., Luo, J., Jarvet, J., Söderberg, K.L., Danielsson, J., Gräslund, A., 2013. Biophysical studies of the amyloid beta-peptide: interactions with metal ions and small molecules. Chembiochem 14, 1692-1704.

Wärmländer, S.K.T.S., Österlund, N., Wallin, C., Wu, J., Luo, J., Tiiman, A., Jarvet, J., Gräslund, A., 2019. Metal binding to the amyloid-beta peptides in the presence of biomembranes: potential mechanisms of cell toxicity. J Biol Inorg Chem 24, 1189-1196.

Yamaguchi, K.I., Kuwata, K., 2018. Formation and properties of amyloid fibrils of prion protein. Biophys Rev 10, 517-525.

Zahn, R., von Schroetter, C., Wüthrich, K., 1997. Human prion proteins expressed in Escherichia coli and purified by high-affinity column refolding. FEBS Lett 417, 400-404.

Österlund, N., Kulkarni, Y.S., Misiaszek, A.D., Wallin, C., Kruger, D.M., Liao, Q., Mashayekhy Rad, F., Jarvet, J., Strodel, B., Wärmländer, S.K.T.S., Ilag, L.L., Kamerlin, S.C.L., Gräslund, A., 2018. Amyloid-beta Peptide Interactions with Amphiphilic Surfactants: Electrostatic and Hydrophobic Effects. ACS Chem Neurosci 9, 1680-1692.

10. Contribution statements

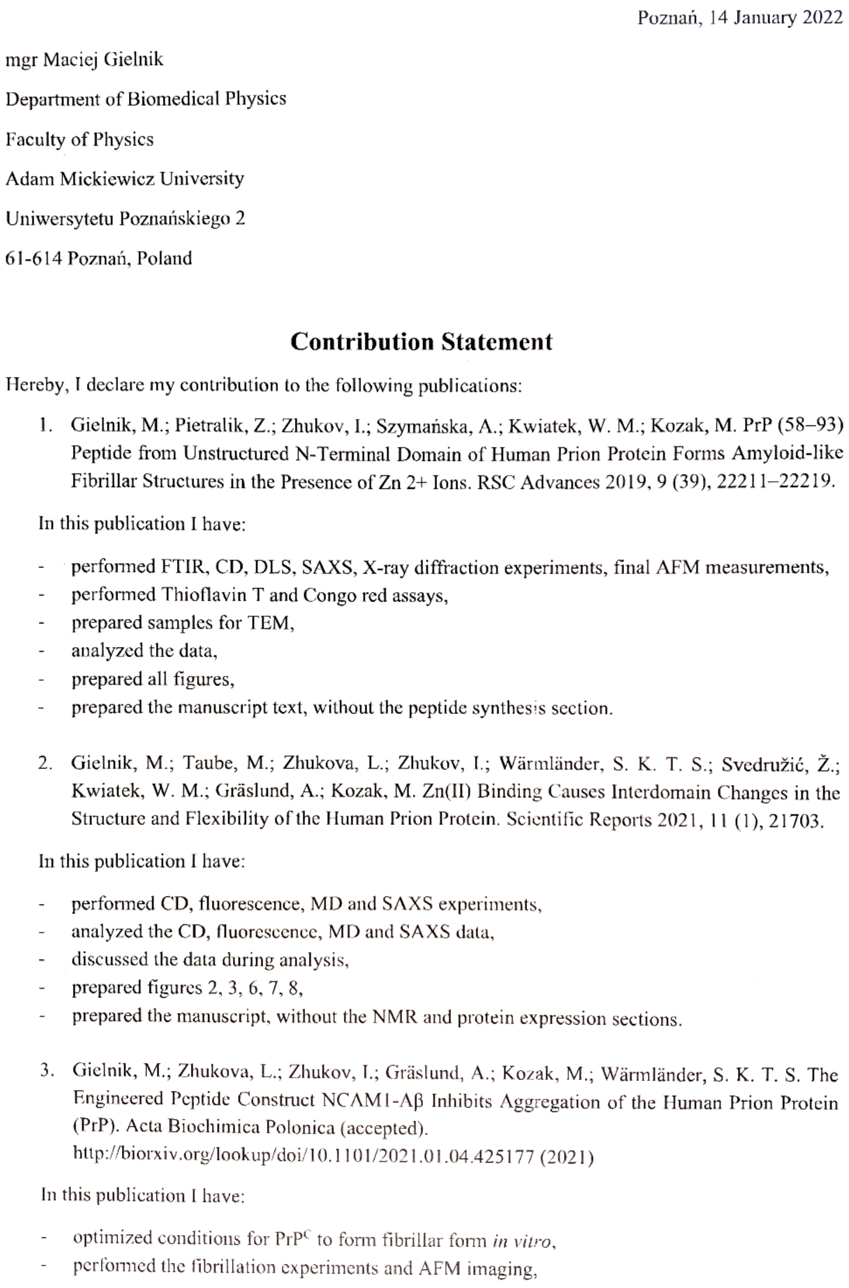

Poznań, 14 January 2022

mgr Maciej Gielnik
Department of Biomedical Physics
Faculty of Physics
Adam Mickiewicz University
Uniwersytetu Poznańskiego 2
61-614 Poznań, Poland

Contribution Statement

Hereby, I declare my contribution to the following publications:

1. Gielnik, M.; Pietralik, Z.; Zhukov, I.; Szymańska, A.; Kwiatek, W. M.; Kozak, M. PrP (58–93) Peptide from Unstructured N-Terminal Domain of Human Prion Protein Forms Amyloid-like Fibrillar Structures in the Presence of Zn 2+ Ions. RSC Advances 2019, 9 (39), 22211–22219.

In this publication I have:

- performed FTIR, CD, DLS, SAXS, X-ray diffraction experiments, final AFM measurements,
- performed Thioflavin T and Congo red assays,
- prepared samples for TEM,
- analyzed the data,
- prepared all figures,
- prepared the manuscript text, without the peptide synthesis section.

2. Gielnik, M.; Taube, M.; Zhukova, L.; Zhukov, I.; Wärmländer, S. K. T. S.; Svedružić, Ž.; Kwiatek, W. M.; Gräslund, A.; Kozak, M. Zn(II) Binding Causes Interdomain Changes in the Structure and Flexibility of the Human Prion Protein. Scientific Reports 2021, 11 (1), 21703.

In this publication I have:

- performed CD, fluorescence, MD and SAXS experiments,
- analyzed the CD, fluorescence, MD and SAXS data,
- discussed the data during analysis,
- prepared figures 2, 3, 6, 7, 8,
- prepared the manuscript, without the NMR and protein expression sections.

3. Gielnik, M.; Zhukova, L.; Zhukov, I.; Gräslund, A.; Kozak, M.; Wärmländer, S. K. T. S. The Engineered Peptide Construct NCAM1-Aβ Inhibits Aggregation of the Human Prion Protein (PrP). Acta Biochimica Polonica (accepted). http://biorxiv.org/lookup/doi/10.1101/2021.01.04.425177 (2021)

In this publication I have:

- optimized conditions for PrP^C to form fibrillar form *in vitro*,
- performed the fibrillation experiments and AFM imaging,

- analyzed the AFM data,
- read the manuscript and introduced minor changes.

4. Gielnik, M.; Szymańska, A.; Dong, X.; Jarvet, J.; Svedružić, Ž. M.; Gräslund, A.; Kozak, M.; Wärmländer, S. K. T. S. The Prion Protein Octarepeat Domain Forms Transient β-sheet Structures Upon Residue-Specific Cu(II) and Zn(II) Binding. http://biorxiv.org/lookup/doi/10.1101/2021.12.12.472308 (2021)

In this publication I have:

- performed CD and fluorescence titrations,
- performed MD experiments,
- analyzed and discussed the CD, fluorescence and MD data,
- prepared figures 2, 3, 4, 5, 6, 7, 8,
- prepared the manuscript text, without the peptide synthesis section.

mgr Maciej Gielnik

Maciej Gielnik

ADAM MICKIEWICZ UNIVERSITY IN POZNAŃ
Department of Biomedical Physics
Uniwersytetu Poznańskiego 2, 61-614 Poznań, Poland

Prof. dr hab. Maciej Kozak
Head of Department of Biomedical Physics
Adam Mickiewicz University

Poznań, January 14th, 2022

Contribution Statement

Hereby, I declare my contribution to the following publications:

1. Gielnik, M.; Taube, M.; Zhukova, L.; Zhukov, I.; Wärmländer, S. K. T. S.; Svedružić, Ž.; Kwiatek, W. M.; Gräslund, A.; Kozak, M. Zn(II) Binding Causes Interdomain Changes in the Structure and Flexibility of the Human Prion Protein. *Scientific Reports* 2021, **11 (1)**, 21703.

My role in the studies leading to this paper focused on:

- conceptualization of the research within the NCN OPUS project, leaded by me,
- obtaining the synchrotron beam time and participation in SAXS data collection in DESY (Hamburg, Germany),
- participation in discussion during the data analysis,
- participation in the critical reading and final editing of the manuscript,
- correspondence with the editors as one of the two corresponding authors.

2. Gielnik, M.; Zhukova, L.; Zhukov, I.; Gräslund, A.; Kozak, M.; Wärmländer, S. K. T. S. The Engineered Peptide Construct NCAM1-Aβ Inhibits Aggregation of the Human Prion Protein (PrP). *Acta Biochimica Polonica* (accepted).
http://biorxiv.org/lookup/doi/10.1101/2021.01.04.425177 (2021)

My role in the studies leading to this paper focused on:

- participation in discussion during AFM data analysis,
- critical reading and participation in the final edit of the manuscript.

3. Gielnik, M.; Szymańska, A.; Dong, X.; Jarvet, J.; Svedružić, Ž. M.; Gräslund, A.; Kozak, M.; Wärmländer, S. K. T. S. The Prion Protein Octarepeat Domain Forms Transient β-sheet Structures Upon Residue-Specific Cu(II) and Zn(II) Binding.
http://biorxiv.org/lookup/doi/10.1101/2021.12.12.472308 (2021)

My role in the studies leading to this paper focused on:

- conceptualization of the research within the NCN OPUS project, leaded by me,
- participation in discussion during the data analysis,
- critical reading of the manuscript.

4. Gielnik, M.; Pietralik, Z.; Zhukov, I.; Szymańska, A.; Kwiatek, W. M.; Kozak, M. PrP (58–93) Peptide from Unstructured N-Terminal Domain of Human Prion Protein Forms Amyloid-like Fibrillar Structures in the Presence of Zn 2+ Ions. *RSC Advances* 2019, **9 (39)**, 22211–22219.

My role in the studies leading to this paper focused on:

- conceptualization of the research within the NCN OPUS project, leaded by me,
- obtaining the synchrotron beam time and participation in SAXS data collection in DESY (Hamburg, Germany),
- participation in discussion during the data analysis,
- critical reading and participation in editing of the manuscript,
- correspondence with the editors as corresponding author.

prof. dr hab. Maciej Kozak

ul. Uniwersytetu Poznańskiego 2, Collegium Physicum, 61-614 Poznań
email: mkozak@amu.edu.pl

Stockholm, 22 December 2021

Dr Sebastian K. T. S. Wärmländer
Department of Biochemistry and Biophysics
Arrhenius Laboratories
Stockholm University
SE-106 91 Stockholm, Sweden

Contribution Statement

Hereby, I declare my contribution to the following publications:

1. Gielnik, M.; Taube, M.; Zhukova, L.; Zhukov, I.; Wärmländer, S. K. T. S.; Svedružić, Ž.; Kwiatek, W. M.; Gräslund, A.; Kozak, M. Zn(II) Binding Causes Interdomain Changes in the Structure and Flexibility of the Human Prion Protein. Scientific Reports 2021, 11 (1), 21703.

In this publication I have:

- analyzed the CD, fluorescence, and NMR data,
- discussed the data during analysis,
- edited and reviewed the manuscript,
- served as one of the two corresponding authors.

2. Gielnik, M.; Zhukova, L.; Zhukov, I.; Gräslund, A.; Kozak, M.; Wärmländer, S. K. T. S. The Engineered Peptide Construct NCAM1-Aβ Inhibits Aggregation of the Human Prion Protein (PrP). Acta Biochimica Polonica (accepted). http://biorxiv.org/lookup/doi/10.1101/2021.01.04.425177 (2021)

In this publication I have:

- conceptualized the study,
- prepared and edited the manuscript,
- served as a corresponding author.

3. Gielnik, M.; Szymańska, A.; Dong, X.; Jarvet, J.; Svedružić, Ž. M.; Gräslund, A.; Kozak, M.; Wärmländer, S. K. T. S. The Prion Protein Octarepeat Domain Forms Transient β-sheet Structures Upon Residue-Specific Cu(II) and Zn(II) Binding. http://biorxiv.org/lookup/doi/10.1101/2021.12.12.472308 (2021)

In this publication I have:

- designed the study,
- analyzed the CD and fluorescence data,
- edited and reviewed the manuscript,
- served as a corresponding author.

Sebastian Wärmländer

Dr Sebastian K. T. S. Wärmländer

Stockholm, 21 December 2021

Prof. Astrid Gräslund
Department of Biochemistry and Biophysics
Stockholm University
Svante Arrhenius väg 16C
SE-106 91 Stockholm, Sweden

Contribution Statement

Hereby, I declare my contribution to the following publications:

1. Gielnik, M.; Taube, M.; Zhukova, L.; Zhukov, I.; Wärmländer, S. K. T. S.; Svedružić, Ž.; Kwiatek, W. M.; Gräslund, A.; Kozak, M. Zn(II) Binding Causes Interdomain Changes in the Structure and Flexibility of the Human Prion Protein. Scientific Reports 2021, 11 (1), 21703.

In this publication I have:

- analyzed the CD, fluorescence, and NMR data,
- discussed the data during analysis,
- reviewed the manuscript,

2. Gielnik, M.; Zhukova, L.; Zhukov, I.; Gräslund, A.; Kozak, M.; Wärmländer, S. K. T. S. The Engineered Peptide Construct NCAM1-Aβ Inhibits Aggregation of the Human Prion Protein (PrP). Acta Biochimica Polonica (accepted). http://biorxiv.org/lookup/doi/10.1101/2021.01.04.425177 (2021)

In this publication I have:

- conceptualized the study,
- reviewed the manuscript,

3. Gielnik, M.; Szymańska, A.; Dong, X.; Jarvet, J.; Svedružić, Ž. M.; Gräslund, A.; Kozak, M.; Wärmländer, S. K. T. S. The Prion Protein Octarepeat Domain Forms Transient β-sheet Structures Upon Residue-Specific Cu(II) and Zn(II) Binding. http://biorxiv.org/lookup/doi/10.1101/2021.12.12.472308 (2021)

In this publication I have:

- designed the study,
- analyzed the CD and fluorescence data,
- discussed the data during analysis,
- reviewed the manuscript
-
-
-
- Prof. Astrid Gräslund

Kraków, 21 December 2021

Prof. dr. hab. Wojciech M. Kwiatek
Institute of Nuclear Physics
Polish Academy of Sciences
Radzikowskiego 152
31-342 Kraków, Poland

Contribution Statement

Hereby, I declare my contribution to the following publications:

1. Gielnik, M.; Pietralik, Z.; Zhukov, I.; Szymańska, A.; Kwiatek, W. M.; Kozak, M. PrP (58–93) Peptide from Unstructured N-Terminal Domain of Human Prion Protein Forms Amyloid-like Fibrillar Structures in the Presence of Zn 2+ Ions. RSC Advances 2019, 9 (39), 22211–22219.

In this publication I have:

In this publication I have:

- conceptualized the study,
- discussed the results,
- read, corrected and accepted to publish the final version of the manuscript.

2. Gielnik, M.; Taube, M.; Zhukova, L.; Zhukov, I.; Wärmländer, S. K. T. S.; Svedružić, Ž.; Kwiatek, W. M.; Gräslund, A.; Kozak, M. Zn(II) Binding Causes Interdomain Changes in the Structure and Flexibility of the Human Prion Protein. Scientific Reports 2021, 11 (1), 21703.

In this publication I have:

- conceptualized the study,
- discussed the results,
- read, corrected and accepted to publish the final version of the manuscript.

Prof. dr. hab. Wojciech M. Kwiatek

Rijeka, 21 December 2021

Prof. Željko M. Svedružić
Department of Biotechnology
University of Rijeka
University Campus Trsat,
HR-51000 Rijeka, Croatia

Contribution Statement

Hereby, I declare my contribution to the following publications:

1. Gielnik, M.; Taube, M.; Zhukova, L.; Zhukov, I.; Wärmländer, S. K. T. S.; Svedružić, Ž.; Kwiatek, W. M.; Gräslund, A.; Kozak, M. Zn(II) Binding Causes Interdomain Changes in the Structure and Flexibility of the Human Prion Protein. Scientific Reports 2021, 11 (1), 21703.

In this publication I have:

- designed the MD experiments,
- provided the functional computing resources,
- analyzed the CD, fluorescence, and MD data,
- read and agreed to publish the final version of the manuscript.

2. Gielnik, M.; Szymańska, A.; Dong, X.; Jarvet, J.; Svedružić, Ž. M.; Gräslund, A.; Kozak, M.; Wärmländer, S. K. T. S. The Prion Protein Octarepeat Domain Forms Transient β-sheet Structures Upon Residue-Specific Cu(II) and Zn(II) Binding. http://biorxiv.org/lookup/doi/10.1101/2021.12.12.472308 (2021)

In this publication I have:

- performed pKa calculations,
- provided text for the pKa calculations,
- provided the functional computing resources,
- analyzed the CD, fluorescence, and MD data,
- read and agreed to publish the final version of the manuscript.

Željko Svedružić

Prof. Željko M. Svedružić

Gdańsk, 21 December 2021

Prof. UG dr hab. inż. Aneta Szymańska
Department of Biomedical Chemistry
Faculty of Chemistry
University of Gdańsk
Wita Stwosza 63
80-308 Gdańsk, Poland

Contribution Statement

Hereby, I declare my contribution to the following publications:

1. Gielnik, M.; Pietralik, Z.; Zhukov, I.; Szymańska, A.; Kwiatek, W. M.; Kozak, M. PrP (58–93) Peptide from Unstructured N-Terminal Domain of Human Prion Protein Forms Amyloid-like Fibrillar Structures in the Presence of Zn 2+ Ions. RSC Advances 2019, 9 (39), 22211–22219.

In this publication I have:

- designed, synthetized and purified the peptide,
- provided text for the peptide synthesis and purification,
- read and agreed to publish the final version of the manuscript.

2. Gielnik, M.; Szymańska, A.; Dong, X.; Jarvet, J.; Svedružić, Ž. M.; Gräslund, A.; Kozak, M.; Wärmländer, S. K. T. S. The Prion Protein Octarepeat Domain Forms Transient β-sheet Structures Upon Residue-Specific Cu(II) and Zn(II) Binding. http://biorxiv.org/lookup/doi/10.1101/2021.12.12.472308 (2021)

In this publication I have:

- designed, synthetized and purified the peptide,
- provided text for the peptide synthesis and purification,
- read the manuscript and introduced minor corrections.

Prof. UG dr hab. inż. Aneta Szymańska

Aneta Szymańska

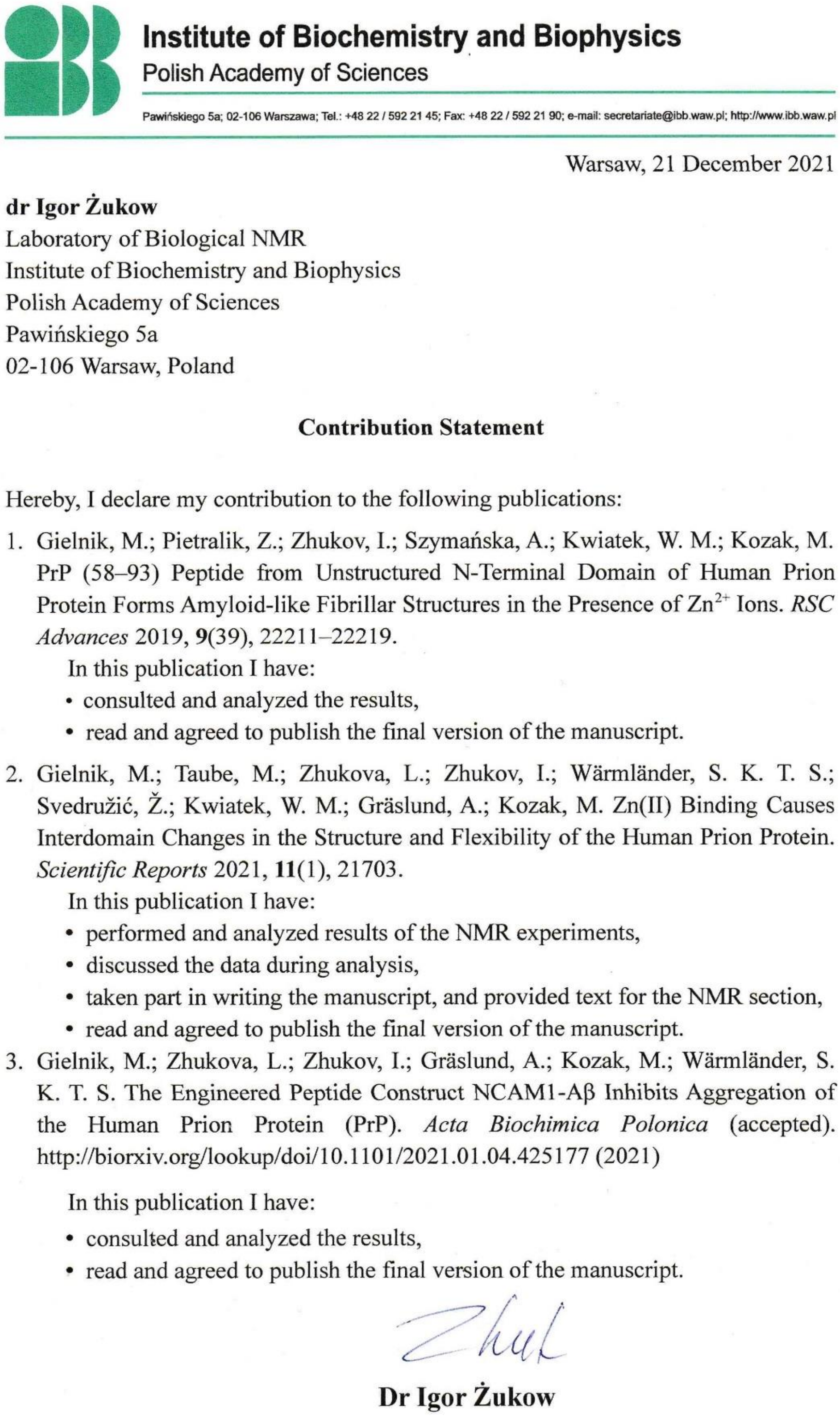

Institute of Biochemistry and Biophysics
Polish Academy of Sciences
Pawińskiego 5a; 02-106 Warszawa; Tel.: +48 22 / 592 21 45; Fax: +48 22 / 592 21 90; e-mail: secretariate@ibb.waw.pl; http://www.ibb.waw.pl

Warsaw, 21 December 2021

dr Igor Żukow
Laboratory of Biological NMR
Institute of Biochemistry and Biophysics
Polish Academy of Sciences
Pawińskiego 5a
02-106 Warsaw, Poland

Contribution Statement

Hereby, I declare my contribution to the following publications:

1. Gielnik, M.; Pietralik, Z.; Zhukov, I.; Szymańska, A.; Kwiatek, W. M.; Kozak, M. PrP (58–93) Peptide from Unstructured N-Terminal Domain of Human Prion Protein Forms Amyloid-like Fibrillar Structures in the Presence of Zn^{2+} Ions. *RSC Advances* 2019, **9**(39), 22211–22219.
   In this publication I have:
   - consulted and analyzed the results,
   - read and agreed to publish the final version of the manuscript.
2. Gielnik, M.; Taube, M.; Zhukova, L.; Zhukov, I.; Wärmländer, S. K. T. S.; Svedružić, Ž.; Kwiatek, W. M.; Gräslund, A.; Kozak, M. Zn(II) Binding Causes Interdomain Changes in the Structure and Flexibility of the Human Prion Protein. *Scientific Reports* 2021, **11**(1), 21703.
   In this publication I have:
   - performed and analyzed results of the NMR experiments,
   - discussed the data during analysis,
   - taken part in writing the manuscript, and provided text for the NMR section,
   - read and agreed to publish the final version of the manuscript.
3. Gielnik, M.; Zhukova, L.; Zhukov, I.; Gräslund, A.; Kozak, M.; Wärmländer, S. K. T. S. The Engineered Peptide Construct NCAM1-Aβ Inhibits Aggregation of the Human Prion Protein (PrP). *Acta Biochimica Polonica* (accepted). http://biorxiv.org/lookup/doi/10.1101/2021.01.04.425177 (2021)

   In this publication I have:
   - consulted and analyzed the results,
   - read and agreed to publish the final version of the manuscript.

Dr Igor Żukow

Institute of Biochemistry and Biophysics
Polish Academy of Sciences

Pawińskiego 5a; 02-106 Warszawa; Tel.: +48 22 / 592 21 45; Fax: +48 22 / 592 21 90; e-mail: secretariate@ibb.waw.pl; http://www.ibb.waw.pl

Warsaw, 21 December 2021

dr Lilia Żukowa
Institute of Biochemistry and Biophysics
Polish Academy of Sciences
Pawińskiego 5a
02-106 Warsaw, Poland

Contribution Statement

Hereby, I declare my contribution to the following publications:

1. Gielnik, M.; Taube, M.; Zhukova, L.; Zhukov, I.; Wärmländer, S. K. T. S.; Svedružić, Ž.; Kwiatek, W. M.; Gräslund, A.; Kozak, M. Zn(II) Binding Causes Interdomain Changes in the Structure and Flexibility of the Human Prion Protein. *Scientific Reports* 2021, **11**(1), 21703.

   In this publication I have:

   - expressed and purified the PrP^C protein,
   - taken part in writing the manuscript, and provided text for the sample preparation section,
   - read and agreed to publish the final version of the manuscript.

2. Gielnik, M.; Zhukova, L.; Zhukov, I.; Gräslund, A.; Kozak, M.; Wärmländer, S. K. T. S. The Engineered Peptide Construct NCAM1-Aβ Inhibits Aggregation of the Human Prion Protein (PrP). *Acta Biochimica Polonica* (accepted). http://biorxiv.org/lookup/doi/10.1101/2021.01.04.425177 (2021)

   In this publication I have:

   - expressed and purified the PrP^C protein,
   - taken part in writing the manuscript, and provided text for the sample preparation section,
   - read and agreed to publish the final version of the manuscript.

Lilia Żukowa

Stockholm, 21 December 2021

Dr Jüri Jarvet

Department of Biochemistry and Biophysics

Stockholm University

Svante Arrhenius väg 16C

SE-106 91 Stockholm, Sweden

Contribution Statement

Hereby, I declare my contribution to the following publications:

1. Gielnik, M.; Szymańska, A.; Dong, X.; Jarvet, J.; Svedružić, Ž. M.; Gräslund, A.; Kozak, M.; Wärmländer, S. K. T. S. The Prion Protein Octarepeat Domain Forms Transient β-sheet Structures Upon Residue-Specific Cu(II) and Zn(II) Binding. http://biorxiv.org/lookup/doi/10.1101/2021.12.12.472308 (2021)

In this publication I have:

- analyzed the CD and fluorescence data,
- read and agreed to publish the final version of the manuscript.

Dr Jüri Jarvet

Poznań, 21 December 2021

Dr Michał Taube

Department of Macromolecular Physics

Faculty of Physics

Adam Mickiewicz University

Uniwersytetu Poznańskiego 2

61-614 Poznań, Poland

Contribution Statement

Hereby, I declare my contribution to the following publications:

1. Gielnik, M.; Taube, M.; Zhukova, L.; Zhukov, I.; Wärmländer, S. K. T. S.; Svedružić, Ž.; Kwiatek, W. M.; Gräslund, A.; Kozak, M. Zn(II) Binding Causes Interdomain Changes in the Structure and Flexibility of the Human Prion Protein. Scientific Reports 2021, 11 (1), 21703.

In this publication I have:

- analyzed the SAXS data,
- prepared Figure 1,
- read and agreed to publish the final version of the manuscript.

M. Taube

Dr Michał Taube

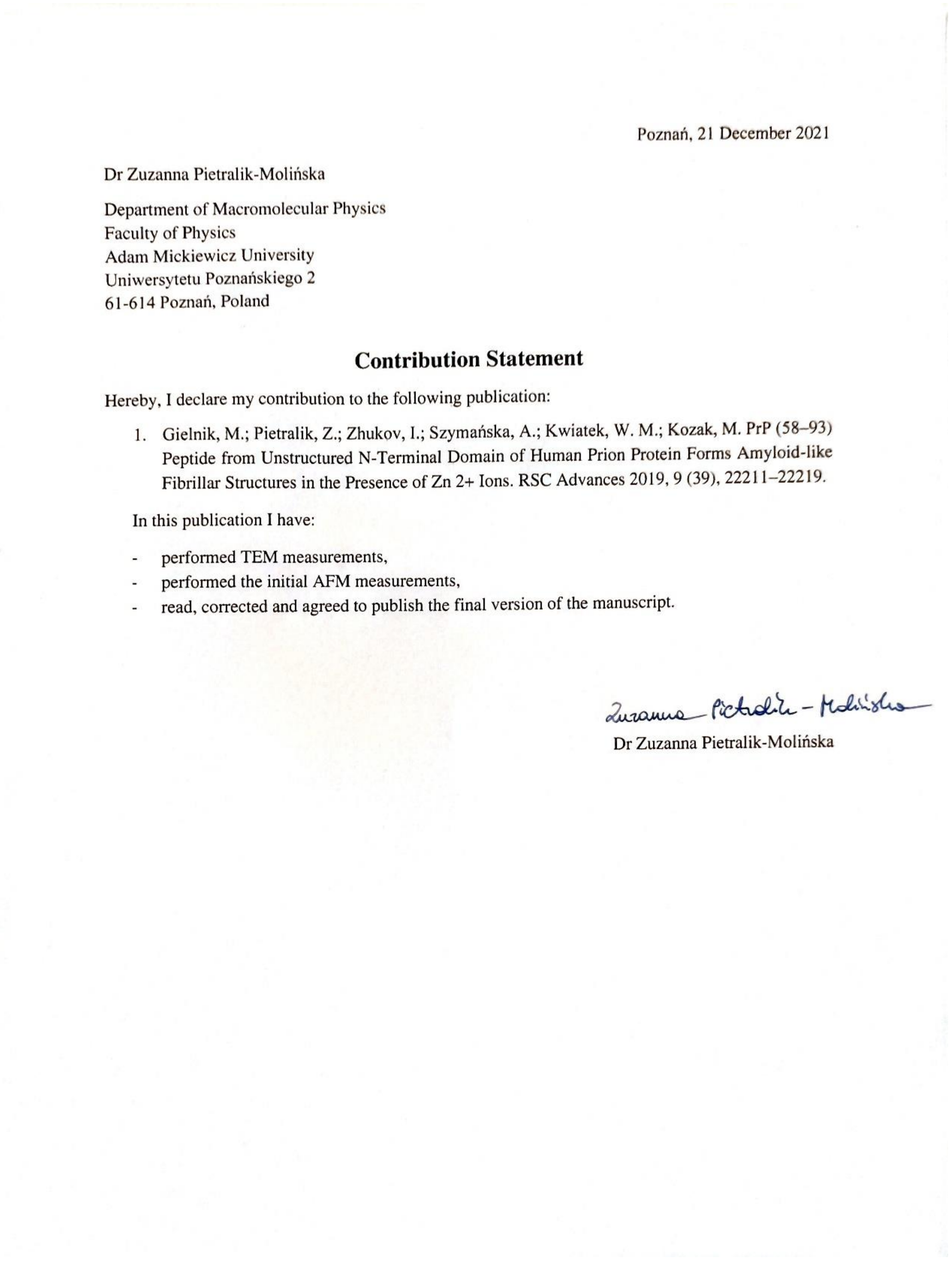

Poznań, 21 December 2021

Dr Zuzanna Pietralik-Molińska

Department of Macromolecular Physics
Faculty of Physics
Adam Mickiewicz University
Uniwersytetu Poznańskiego 2
61-614 Poznań, Poland

Contribution Statement

Hereby, I declare my contribution to the following publication:

1. Gielnik, M.; Pietralik, Z.; Zhukov, I.; Szymańska, A.; Kwiatek, W. M.; Kozak, M. PrP (58–93) Peptide from Unstructured N-Terminal Domain of Human Prion Protein Forms Amyloid-like Fibrillar Structures in the Presence of Zn 2+ Ions. RSC Advances 2019, 9 (39), 22211–22219.

In this publication I have:

- performed TEM measurements,
- performed the initial AFM measurements,
- read, corrected and agreed to publish the final version of the manuscript.

Zuzanna Pietralik-Molińska

Dr Zuzanna Pietralik-Molińska